Impact of the Wireless Channel on the Performance of Ultrawideband Communication Systems

A thesis submitted in partial fulfilment of the requirements for the degree of Doctor of Philosophy at the University of Oxford

Vit Sipal

Balliol College

September, 2012

Department of Engineering Science
University of Oxford
Parks Road, OX1 3PJ Oxford

Vit Sipal, Balliol College, University of Oxford, September 2012

Impact of the Wireless Channels on the Performance of Ultrawideband Communication Systems

ABSTRACT

Ultrawideband (UWB) wireless systems employ signals with bandwidths in excess of 500 MHz or with relative bandwidth more than 20%. The radiated signals have low power spectral density. A decade ago, UWB wireless systems were deemed to be the technology that will deliver 'Gigabit-wireless' for short range communications. However, the performance of current systems is significantly below the initial expectations. This thesis explores the UWB wireless channel and shows how its properties limit the performance of current UWB systems. Furthermore, it is shown that if the knowledge of the channel is fully exploited a significant performance improvement of UWB systems can be achieved.

The thesis begins with exploration of the channel properties. Unlike previous work, that has investigated either the 'classical narrowband' channel with bandwidth <100 MHz or the UWB channel with bandwidth >1 GHz, this work studies the transition between the narrowband channels with bandwidth of 1 MHz to the extremely wideband channels with bandwidths of up to 10 GHz. The thesis concludes that for signals with bandwidth <1 GHz UWB antennas and antenna arrays can be described by the classical means of gain and array factor, i.e. they treat such signals as 'narrowband'. In contrast, wireless propagation for signals with bandwidth >100 MHz has properties 'like UWB channels' with bandwidths in the GHz range.

Additionally, the thesis suggests a correction to the IEEE802.15.4a model for channel impulse response because as will be shown in the thesis many multipaths in the model are manifestations of the antenna impulse response. Hence multiple multipaths in the IEEE802.15.4a model actually represent a single multipath component. This reduces the number of multipath components in the model by approximately factor of five.

The understanding of the transition between narrowband and ultrawideband channel is used to improve the spectral efficiency of impulse radio systems which traditionally use signals with bandwidth >1 GHz. It is shown that the optimum signal bandwidth for impulse radio systems is in the range 150-450 MHz. Such systems balance the robustness against frequency selective fading with the reduction of duty cycle. Hence, the data-rate of impulse radio systems can be significantly improved.

The frequency selective fading is shown to be the main limiting factor for the performance of the commercial UWB WiMedia systems with OFDM. It is shown that adaptive loading of OFDM subcarriers, which is compatible with the frequency selectivity of the channel, is more suitable for UWB OFDM systems than the use of strong Forward-Error-Correction measures. The introduction of the adaptive OFDM is not a significant change to the design of the scheme because the commercial WiMedia standard already foresees pilot OFDM symbols for channel estimation. The adaptive OFDM for UWB has already been considered by some authors. Unlike previous works, this thesis explores the performance of such a system in a large number of measured wireless channels.

Finally, the thesis studies the MIMO techniques for UWB systems. Suitable schemes for fixed and adaptive OFDM are discussed. A realistic simulation using measured wireless channel shows that a 4×1 system with a low complexity beam-steering and adaptive OFDM can deliver a data-rate of 400 Mbps over a range of 9 m. This performance is for a system with bandwidth 528 MHz (like in the WiMedia standard). A further increase can be achieved with the increase of the system's bandwidth.

Acknowledgements

First and foremost I would like to thank to my supervisor, Prof. David Edwards, for giving me the opportunity to pursue the DPhil. qualification and the chance to be part of this exciting project. I would like to thank him for his patient guidance and helping hand he offered me whenever needed. I should also thank Prof. Ben Allen from the University of Bedfordshire for his advice and insightful comments that always steered me in the correct direction.

I also would like to express my appreciation to the Defense Science and Technology Laboratory and Her Majesty's Government Communications Centre for their generous funding. The regular meetings with their representatives, namely Dan Esdale, Dene Hedges, Amar Soon, and Chris Worral, always turned into a lively discussions which introduced new perspectives to the project.

An important contribution to the project has been done also by all members of the Communications Research Group. I really enjoyed their feedback to my work the provided during our weekly seminars. I should especially mention Grahame Faulkner whose help with administrative management of the project and his experience with practical designs helped me to overcome numerous hurdles. Next I should mention Dr. Christopher Stevens and Dr. Javier Gelabert for their help and comments to the work on frequency selectivity in confined environments. Finally I should name Dr. Pithawat 'Tan' Vachiramon, Dr. Zein Khan, and Chris Chan who were the centre of the group's social life.

Next I should thank the Oxford University Judo Club for the opportunity to forget problems from the office whilst doing the sport I love. I should also mention my friends James Maynard, Ian Coulter, Ed Latter, and Simon Jones from the Balliol MCR Darts Team. Throughout the last three years I have hugely benefited from our stimulating discussions on a variety of academic and non-academic topics.

Finally, I want to thank to my parents, my sister Michaela and her family for the inspiration and support I have received from them not only in the last three years but during my entire life. Last but not least I shall thank Maria Loshuertos for her endless support and patience especially during the final stages of the project.

List of Publications

Bookchapter

[BC1] Sipal, V.; Allen, B.; Edwards, D.; ”Wideband Channels,” chapter in *LTE-A and Next Generation Wireless Networks*, to be published by John Wiley & Sons in 11/2012

Journal papers and Letters

[J1] Sipal, V.; Allen, B.; Edwards, D.; Honary, B.; ”20 Years of Ultrawideband: Opportunities and Challenges,” *IET Communications* , vol.6, no.10, pp.1147-1162, July 3 2012, *invited review*

[J2] Sipal, V.; Allen, B.; Edwards, D.; ”Empirical study of Multi-tone Frequency Shift Keying for Ultrawideband Wireless Communications,” *IET Communications*, vol.6, no.10, pp.1170-1178, July 3 2012

[J3] Sipal, V.; Allen, B.; Edwards, D.; ”Exploration of Nakagami fading in ultra-wideband wireless channels,” *Electronics Letters*, vol.47, no.8, pp.520 -521, April 14 2011

[J4] Sipal, V.; Gelabert, J.; Allen, B.; Stevens, C.; Edwards, D.; ”Frequency-selective fading of ultrawideband wireless channels in confined environments,” *IET Microwaves, Antennas* & *Propagation*, vol.5, no.11, pp.1328-1335, August 19 2011

[J5] Sipal, V.; Allen, B.; Edwards, D.; ”Analysis and mitigation of antenna effects on wideband wireless channel,” *Electronics Letters*, vol.46, no.16, pp.1159-1160, August 5 2010

[J6] Sipal, V.; Ajami, A.; Heberling, D.; ”Miniaturisation of ϵ-negative transmission line based zeroth-order resonator antenna,” *IET Microwaves, Antennas* & *Propagation*, vol.5, no.1, pp.10-16, January 12 2011

[J7] Sipal, V.; Ajami, A.; Heberling, D.; ”Effect of Substrate Dimensions on Zeroth-Order Resonator Antennas,” *IEEE Antennas and Wireless Propagation Letters*, vol.9, no., pp.107-109, 2010

Conference papers

[C1] Sipal, V.; Allen, B.; Edwards, D.; "Bandwidth Requirement for Suppression of Grating Lobes in Ultrawideband Antenna Arrays," *International Conference on UWB, ICUWB 2012*, Syracuse , 17-20 Sep. 2012

[C2] Sipal, V.; Allen, B.; Edwards, D.; "On the Range of WiMedia OFDM UWB Wireless," *International Conference on UWB, ICUWB 2012*, Syracuse , 17-20 Sep. 2012

[C3] Sipal, V.; Allen, B.; Edwards, D.; "Subcarrier Fading in UWB OFDM Symbols," *IEEE Antennas and Propagation Symposium and USNC/URSI National Radio Science Meeting, APS-URSI 2012*, Chicago , 9-13 Jul. 2012

[C4] Sipal, V.; Allen, B.; Edwards, D.; "Limits for Low Comlexity Beam-Steering for UWB Antenna Arrays," *IEEE Antennas and Propagation Symposium and USNC/URSI National Radio Science Meeting, APS-URSI 2012*, Chicago , 9-13 Jul. 2012

[C4] Sipal, V.; Edwards, D.; "Radiomyography - Feasibility Study," *European Conference on Antennas and Propagation EUCAP 2012*, Prague,pp. 3643-3645, 26-30 Mar. 2012

[C6] Sipal, V.; Allen, B.; Edwards, D.; "Descriptor Choice for UWB Antenna Arrays," *European Conference on Antennas and Propagation EUCAP 2012*, Prague, pp. 603-606, 26-30 Mar. 2012

[C7] Sipal, V.; Allen, B.; Edwards, D.; "Low Complexity MIMO for WiMedia UWB," *European Conference on Antennas and Propagation, EUCAP 2012*, Prague, pp. 1427-1430, 26-30 Mar. 2012

[C8] Sipal, V.; Gelabert, J.; Stevens, C.J.; Allen, B.; Edwards, D.; "Low Complexity Free Space Impedances Measurement of UWB Antennas," *European Conference on Antennas and Propagation EUCAP 2012*, Prague, pp. 2095-2098, 26-30 Mar. 2012

[C9] Sipal, V.; Gelabert, J.; Stevens, C.J.; Allen, B.; Edwards, D.; "Impact of Confined Environments on WiMedia UWB Systems," *Antennas and Propagation Conference, LAPC 2011*, Loughborough, pp. 1-4, 14-15 Nov. 2011

[C10] Sipal, V.; Allen, B.; Edwards, D.; "Optimisation of Low Power Radio-over-Fibre Links for UWB Systems," *Int. Conference on UWB, ICUWB 2011*, Bologna , 14-16 Sep. 2011

[C11] Sipal, V.; Gelabert, J.; Stevens, C.J.; Allen, B.; Edwards, D.; "Frequency selectivity in confined environments," *European Conference on Antennas and Propagation, EUCAP 2011*, Rome, pp. 201-205, 11-15 April 2011

[C12] Sipal, V.; Allen, B.; Edwards, D.; "Exploration and analysis of fade depth scaling," *Antennas and Propagation Conference, LAPC 2010*, Loughborough , pp. 125-128, 8-9 Nov. 2010

[C13] Sipal, V.; Allen, B.; Edwards, D.; "Effects of antenna impulse response on wideband wireless channel," *Antennas and Propagation Conference, LAPC 2010*, Loughborough, pp. 129-132, 8-9 Nov. 2010

[C14] Sipal, V.; Allen, B.; Edwards, D.J.; "Modelling Of Antenna Pattern Descriptors For Antenna Performance Evaluation," *Int. Conf. Modelling and Simulation, AMSE 2010*, Prague, 22-25 Jun. 2010

[C15] Sipal, V.; Allen, B.; Edwards, D.J.; "Enhanced Fade Depth Model for Extremely Wideband Channels," *Int. Conf. Modelling and Simulation, AMSE 2010*, Prague, 22-25 Jun. 2010

List of Acronyms

ADC	Analogue-Digital-Converter
AoA	Angle-of-Arrival
AoD	Angle-of-Departure
AWGN	Additive White Gaussian Noise
BER	Bit-Error-Rate
CDF	Cumulative Distribution Function
CDMA	Code Division Multiple Access
CSLA	Coupled Sectorial Loop Antenna
DAA	Detect-and-Avoid
DCM	Dual Carrier Modulation
DVB	Digital Video Broadcasting
EAM	Electro-Absorption Modulator
EIRP	Equivalent Isotropic Radiated Power
FFT	Fast Fourier Transform
IFFT	Inverse Fast Fourier Transform
LMMSE	Linear Minimum Mean Squared Error
LOS	Line-of-Sight
MAC	Media Access Control Layer
MIMO	Multiple-Input-Multiple-Output
MISO	Multiple-Input-Single-Output
MMSE	Minimum Mean Square Error
NLOS	Non-Line-of-Sight
OFDM	Orthogonal Frequency Division Multiplexing
OOK	On-Off-Keying
QAM	Quadrature Amplitude Modulation
QPSK	Quadrature Phase Shift Keying
PDF	Probability Distribution Function
PER	Packet-Error-Rate

PHY	Physical Layer
RMS	Root-Mean-Square
RoF	Radio-over-Fibre
SIMO	Single-Input-Multiple-Output
SISO	Single-Input-Single-Output
SNR	Signal-to-Noise-Ratio
VNA	Vector Network Analyser
US FCC	US Federal Communications Commission
UWB	Ultrawideband
VLC	Visible Light Communications
VSWR	Voltage Wave Standing Ratio
WiFi	Wireless Fidelity
WLAN	Wireless Local Area Network

List of Symbols

A	minimum fade depth for ultrawideband channels, parameter in fade depth scaling model
A_{eR}	effective aperture of receive antenna
A_{eT}	effective aperture of transmit antenna
α_i	gain of i-th multipath in channel impulse response
$b(t)$	baseband signal of $s(t)$
B	increase of fade depth for narrowband channels, parameter in fade depth scaling model
B_{UL}	upper bandwidth limit for use of narrowband array descriptors
BER, PER, SER	Bit-, Packet-, Symbol-Error-Rate
$BP(1\text{dB})$	break point at which fade depth is 1 dB above A
BW, B	bandwidth
c	speed of light
c_{xy}	correlation coefficient between signals $x(t)$, $y(t)$
C	parameter for fade depth scaling with bandwidth, parameter in fade depth scaling model
$CE(f)$	normalised channel energy
d	element spacing in antenna array
$\delta(t)$	Dirac delta impulse
$\mathbf{E}(.)$	is vector of electric field strength
$\mathrm{E}\{x\}$	mean of x
E_s/N_0	signal to noise ratio - energy per symbol vs. noise spectral density
E_b/N_0	signal to noise ratio - energy per bit vs. noise spectral density

$\epsilon(\varphi,\varphi_0)$	beampattern for azimuth ϕ with mainlobe in direction ϕ_0
f	frequency
f_c	centre frequency of $s(t)$
F	fading
FD	fade depth
G	guard interval length in [s]
$G_p(.)$	path gain as a function of distance and frequency
G_T	realised gain of transmit antenna
G_R	realised gain of receive antenna
$H(f)$	channel transfer function in the frequency domain
$h(t)$	channel impulse response in the time domain
$\mathbf{h^T}(\hat{\mathbf{r}},\tau)$	antenna impulse response for transmission. $\mathbf{h^T}(\hat{\mathbf{r}},\tau)$ is a vector where each one of its dimensions is linked to polarisation
$\mathbf{h^R}(\hat{\mathbf{r}},\tau)$	the antenna impulse response for reception
$I^+(\tau)$	input current wave
$I_L(t)$	current to the load of receiver antenna
$J_A(t)$	surface current distribution on antenna
k, θ	parameters of Gamma probability distribution function
Λ, λ_1, λ_0	'lambda'-parameters of Poisson probability distribution
λ_0	wavelength in free space
m, ω	parameters of Nakagami probability distribution function
μ	magnetic permeability of free space
N, M, K	number of 'elements', e.g. antennas in array, bits in packet etc.
η	impedance of free space
Ω_l	mean energy of l-th cluster

$p(.)$	probability density function
P_e	probability of erroneous decision in Multitone-FSK receiver
ϕ	azimuth angle
$\mathbf{r}$	vector of the position of point of interest in relation to the antenna or array
$r = \lvert\mathbf{r}\rvert$	length of $\mathbf{r}$
$\hat{\mathbf{r}}$	normalized $\mathbf{r}$ denoting the direction of $\mathbf{r}$
$R_{xy}(\tau)$	correlation between signals $x(t)$, $y(t)$ delayed by τ
$\mathbf{R_i}(\tau)$	3-by-3 matrix corresponding to the reflection of i-th ray
$\Re[x]$	real part of x
$s(t)$	bandpass signal
$S_R(.)$	power spectral density at receiver
$S_T(.)$	power spectral density at transmitter
t	time
T_p, b	parameters defining the length of $b(t)$ see Appendix A
T_b	effective duration (-10dB) of signal $b(t)$
τ_i, T_i , Δ_i	signal delays of various causes, e.g. i-th ray/cluster, i-th antenna element
ϑ	elevation angle
θ	phase of i-th multipath in channel impulse response
$V^-(t)$	outgoing voltage wave at the port of the receiving antenna
V	volume
V_g	voltage pulse at the generator connected to the transmit antenna
$y(t)$	signal received by antenna array
Z_{0T}	impedance of the transmit antenna
Z_{0R}	load of the receiver antenna

CONTENTS

CHAPTER 1

Introduction

1.1 Motivation and Concept of Ultrawideband Communications

The history of wireless communication systems dates back almost 125 years. In 1888 Heinrich Hertz demonstrated the existence of electromagnetic waves which supported the theoretical work of James Clerk Maxwell [1]. Despite the fact that Hertz "saw no practical use in his discovery" [1], already in 1895 Guglielmo Marconi demonstrated wireless telegraphy over a distance of 1.5 km [2]. Six years later Marconi succeeded with wireless transmission across the Atlantic ocean [2]. The catastrophe of Titanic in 1912 helped to increase the public awareness of Marconi's work as it is believed that the survivors owed their lives to Marconi's wireless telegraph [3]. Since then, wireless communications has been developed at an impressive rate. In 1941 the US Federal Communications Commission (US FCC) licensed TV broadcasting. In 1981, the first generation of mobile phones was introduced and IEEE 802.11, the current Wireless Local Area Network (WLAN) standard, was first released in 1997.

As a result of this rapid development, current radio engineers have to face a new issue: the frequency band most suitable for wireless communication is almost fully allocated; there is not much new bandwidth available for additional wireless services but the demand for further expansion of wireless communications services continues [4].

However, even though the spectrum is almost fully allocated, it is not fully used [5]. Henceforth, re-usage of the frequency spectrum was recognised as an opportunity to break the spectrum gridlock. Two approaches have emerged and attracted a lot of attention: White Space Cognitive Radio and Ultrawideband (UWB) radio. White Space Cognitive radio uses active spectrum sensing to detect unused bands in the spectrum [4]. If such band is detected, it can be utilised for communication. Therefore, no interference to the primary spectrum users appears. UWB, on the other hand, re-uses the spectrum elegantly by transmitting an extremely wideband signal ($B > 500$ MHz) with a low power spectral density. For the primary licensed narrowband users, a UWB transmission appears as white noise. Conversely, the narrowband user represents only a narrowband interference to the UWB system and this interference can be resolved using the inherent frequency diversity of the UWB system as long as the front-end of the UWB receiver is not overloaded.

These two concepts are not competing with each other; in fact they are complementary. The transmission range of UWB is limited to approximately 10 m due to the low power spectral density [6]. Thus it allows extremely dense frequency re-usage. Also, due to its immense bandwidth it offers extremely high available channel capacity even for low Signal-to-Noise-Ratio (SNR). As a result, it is the candidate for short-range high speed wireless networks (data-rates in the magnitude of hundreds or thousands of Mbps) [6]. White Space Cognitive Radio does not offer sufficient bandwidth to compete with UWB in the field of data-rate, but it outperforms UWB in terms of transmission range. Hence, it is the candidate for wireless services over longer distance, e.g. future generations of mobile phones.

1.2 History of Ultrawideband Communications

1.2.1 Early Days and Regulation

The term 'ultrawideband' was published in 1991 by Fullerton [7] (it is noted that some military projects about UWB started already in the 1960s [8]). However, in the IEEExplore™ database, there are been only 35 papers on the topic from 1991-97. The real breakthrough started in 1998 when Win and Scholtz showed that time hopping codes enable the avoidance of catastrophic collision of multiple users using impulse radio communication [9]. The interest raised by reference [9] has been further fueled by part 15 ruling of the US Federal Communication Commission in 2002 that has allowed unlicensed UWB radiation in the frequency band 3.1 - 10.6 GHz. Similar ruling by many regulatory bodies across the world have followed soon after. The regulations for Equivalent Isotropic Radiated Power (EIRP) spectral density for indoor UWB communications for Europe, USA, Korea and Japan are introduced in Fig. 1. This introduction is essential as it defines the basic framework for UWB systems and many conclusions in later chapters of this thesis will be stated as a result of system optimisation within this regulatory framework.

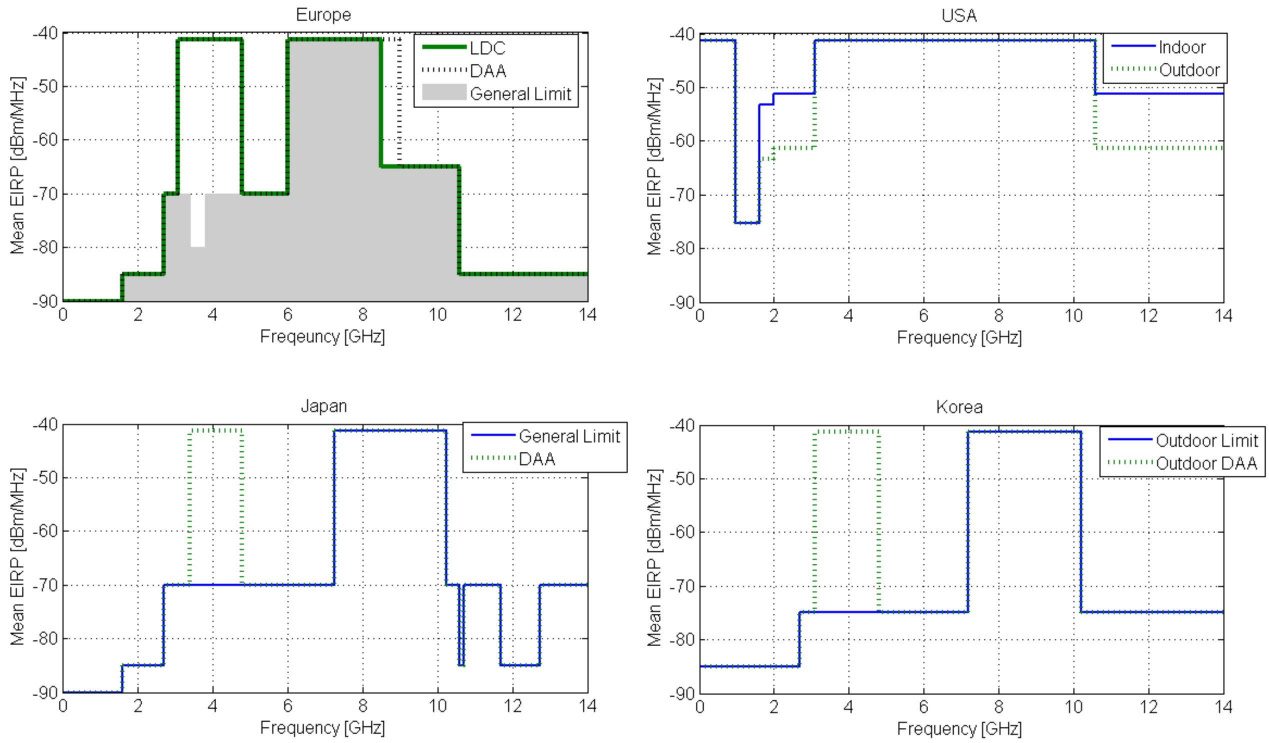

Figure 1.1: UWB EIRP spectral masks for Europe, USA, Korea and Japan

In Europe, the regulation was changed in 2009. Now it defines a 'general limit' for UWB transmission. The 'general limit' applies to any indoor wireless device. Outdoor devices are subject to additional constraints [10]. The 'general limit' allows to use the frequency range of 6 - 8.5 GHz with a mean EIRP spectral density of -41.3 dBm/MHz [10]. The regulation also allows emissions in the 3.1 - 4.8 GHz band with a mean EIRP density of -41.3 dBm/MHz but only under the assumption that Low Duty Cycle (LDC) mitigation techniques will be used. This regulation specifies that the duration of all signals is less than 5% of the time averaged over each second and less than 0.5% of the time averaged over each hour, and no transmitted signal can last longer than 5 ms [10]. Alternatively, if Detect-and-Avoid (DAA) is employed, a mean EIRP density of -41.3 dBm/MHz is allowed (on top of the general limit) in the bands of 3.1 - 4.8 GHz and 8.5 - 9.0 GHz [10]. The objective of DAA is to avoid a frequency band if a device can detect spectrum used by other services. The details of the European requirements on DAA can be found in [11] or in the ETSI norm EN 302 065.

The regulations in the USA are the most liberal compared to other areas. UWB radiation for communication is allowed in the band 3.1 - 10.6 GHz with an average EIRP density of -41.3 dBm/MHz [12]. The rules for out-of-band radiation are stricter for outdoor emissions. Transmission at low frequencies is allowed for applications such as ground penetrating radar.

Japan, in contrast, has strict rules. UWB is allowed indoors only and it is specified that there has to be a mains powered 'host' device and a battery powered 'client' [13]. This sets additional constraints on power consumption of UWB devices. In terms of frequency spectra, the allocated frequency spectrum is 7.25 - 10.25 GHz at a mean EIRP density of -41.3 dBm/MHz. The 3.4 - 4.8 GHz band is allowed for devices using DAA [13].

The regulation in South Korea allows indoor and outdoor operation. The approved frequency bands are similar to the ones in Japan. A mean EIRP density of -41.3 dBm/MHz is allowed in the band 7.2 - 10.2 GHz. The band 3.1 - 4.8 GHz with mean EIRP density of -41.3 dBm/MHz can be used if DAA is employed [13].

After the part 15 ruling by the US FCC, the interest of academia and industry has exploded. In the first years after the US FCC part 15 ruling, UWB was treated as the new wonder child in the world of wireless communication. It was the technology that was about to change the world. In 2004, Parks Associates Research Consultants estimated that the market for UWB chips and gear will top $1,000,000,000 by 2008 [14]. In the same year the TIME magazine selected UWB as one of the technologies to remember for 2005 [15].

1.2.2 Standardisation, the Beginning of the Decline

Soon after the part 15 ruling, the IEEE 802.15.3a standardisation task group was created. From several proposals for the physical layer implementation, two proposals, both backed by strong industrial alliances, were selected. These approaches were Direct Sequence CDMA (DS-CDMA) supported by the alliance called the UWB Forum, and Multi Band Orthogonal Frequency Division Multiplexing (OFDM) which was the proposal of the WiMedia alliance [13]. Both alliances never managed to reach a compromise, and as a result the 802.15.3a task group ceased its existence in early 2006. Each of the Alliances was expected to create their own standards and let the marketplace make the decision [13].

The WiMedia alliance finalised their proposal and submitted it to ECMA (European association for standardising information and communication). The Physical Layer (PHY) and Media Access Control Layer (MAC) specifications were incorporated in the ECMA-368 document [13]. Meanwhile, Motorola's spin-off company, Freescale, abandoned the UWB Forum. Soon after Freescale, other members started leaving the body [13]. At the present time, the UWB Forum is effectively lifeless.

However, the expected market success of WiMedia devices did not occur. Reference [16] claims that the chip costs were too high and prevented a successful market entry. As a result, in March 2009 the WiMedia alliance announced the transfer of its specifications to two partner groups (USB Implementors Forum and Bluetooth SIG) and published plans to disband [16]. A month later (April 2009) another UWB start up, Radiospire, that used the OFDM approach announced bankruptcy which prompted commentators to go as far to claim that "UWB is dead in consumer electronics..." [17].

1.3 Thesis - Aim and Structure

The events described in section 1.2 would suggest that there is no future for UWB. Doubts about the meaning of any research into UWB communication can be cast. However, hunger for more wireless technology increases and it is likely to accelerate due to the shift towards cloud services [18]. To meet this demand, new technologies will have to be introduced. The main aim of this thesis is to show that UWB , despite commercial failure, remains a feasible technical contender with other candidate technologies such as 60 GHz communication [18], or the Visible Light Communications (VLC) [19].

The commercial failure of the technology does not necessarily imply it is without potential (in fact, Radiospire was able to develop a commercial device providing 1.6 Gbps over a range of 5 metres [20]). Thus this thesis aims to demonstrate that if the properties of the ultrawide-band wireless channel (including antennas) are considered in the system design, it is possible to achieve reliable high-data-rate short-range communication because UWB systems posses some properties that might provide a performance edge. Compared to the communication in the 60 GHz band, UWB does not need to rely on complex antenna arrays for beam-steering that compensates for high path loss. The VLC does not have the potential to provide symmetric channel, it provides fast downlink from a base-station but the uplink's performance is at best limited, if not impossible [19]. Thus, VLC does not seem feasible for fast peer-to-peer connections among devices in the cloud (e.g. TV set, tablet, smartphone).

To achieve its main objective, the thesis starts with the analysis of the wireless channel in chapters 2 and 3. Unlike many other works, the thesis does not focus solely on channels with bandwidth of several GHz. Instead it studies the transition between the narrowband and the UWB channel. This investigation is motivated by the fact that practical WiMedia UWB systems have bandwidth of 528 MHz [13]. Such a channel is not narrowband but at the same time it does not quite have the properties of a channel with bandwidth 7.5 GHz spreading across the entire US UWB spectrum. Chapters 4-7 then discuss the impact of the channel on practical UWB systems.

Chapter 2 discusses the challenges for design and description of antennas for UWB wireless systems. It also discusses the descriptors of UWB arrays and some specific properties of these arrays are introduced. Some of these properties will be of interest for understanding of the wave propagation in the wireless channel that is discussed in chapter 3. Chapter 3 firstly introduces the IEEE802.15.4a channel model [21]. The model for channel impulse response from the IEEE802.15.4a channel model is discussed and a correction considering the impact of antenna impulse responses on the UWB channel measurements is suggested. The core of chapter 3 is exploration of frequency selective fading in the wireless channel, and the scaling of impact when the bandwidth increases from narrowband to UWB channels.

Chapter 4 investigates impulse radio. It is known that impulse radio is robust against frequency selective fading because the duration of the employed impulses enables to resolve individual multipath components in the propagation channel, but the repetition rate of the symbols is limited by the Root-Mean-Square (RMS) delay spread of the wireless channel. Furthermore, processing of extremely short pulses (duration of less than few nanoseconds) proves extremely challenging. Hence, chapter 4 shows that the understanding of the bandwidth scaling of frequency selective fading allows alleviation of some of these issues.

Frequency selective fading is studied in great detail because it also plays a pivotal role in limitation of performance of OFDM systems (in terms of range and/or throughput), which will be discussed in chapter 5. Chapters 6 and 7 then introduce some enhancements to the existing OFDM concepts for UWB that increase its robustness against frequency selective fading and can be employed to improve the range and/or data-rate of the systems.

The appendices include information relevant for the thesis but not necessarily novel. Appendix A introduces the waveform of baseband pulses used for many investigations in chapter 2. Appendix B presents the experimental setup used for the sounding of the wireless channels. The setup is introduced since measurements of the wireless channel represent an important part of this thesis and were used to derive many of its conclusions. Thus, it is deemed important to include a detailed review of the setup so that limitations related to this setup are fully understood. Appendix C introduces the plan of the laboratory, where most of the channel measurement were conducted, and the relative position of the measurement points to the room. Finally, appendix D introduces a UWB WiMedia development kit that was used to investigate the performance of WiMedia systems in chapter 5.

CHAPTER 2

Ultrawideband Antennas and Antenna Arrays

Antennas represent an integral part of the wireless channel and they have an important impact on the performance of the communication system as a whole. The objective of this chapter is to introduce some properties and descriptors of UWB antennas and antenna arrays. The properties of antennas and antenna arrays transmitting or receiving UWB signals often differ significantly from the properties known for their narrowband counterparts [8]. For instance, the dispersive properties of antennas are of interest when designing impulse radio systems that employ sub-nanosecond pulses as pulse distortion represents a challenge for the receiver [8]. Similarly, UWB antenna arrays for impulse radio systems posses some highly remarkable properties: they are reported not to manifest grating lobes [22]. It is important to fully comprehend these properties in order to either asses their impact on communication systems or to design communication systems that would capitalise on these properties.

In order to provide a full understanding of the impact on system performance, this chapter focuses first on the **UWB antenna** elements. Some basic antenna structures for radiation over extreme bandwidths are introduced and their properties are discussed. Due to the specific properties of UWB antennas the descriptors used for narrowband systems do not provide sufficient information about signal distortion, thus alternative descriptors from the literature are introduced and the bandwidth limit for the usage of narrowband descriptors is investigated.

The properties of **UWB antenna arrays** are explored next. Array factors [23], the classical array descriptors, are not suitable descriptors for UWB antenna arrays because they are related to a single frequency. Therefore alternative descriptors in the time domain are introduced and the bandwidth limit for the use of narrowband descriptors is explored. The literature reports that UWB antenna arrays manifest some remarkable properties such as non-existence of grating lobes [22]. These properties are investigated and the bandwidth limits for them are introduced.

2.1 UWB Antennas

Design of wide-band antennas has always been one of the main challenges for antenna engineers and wide-band antennas were designed long before the concept of UWB started. This can be illustrated by classical DuHamel's works on log-periodic antennas from the late 1950s [24], [25]. The term 'UWB antenna' is typically associated to any antenna capable of covering the UWB assigned bandwidth 3.1-10.6 GHz. However as pointed out in [26], quite often the description relates only to return loss and the radiation properties are not investigated. However, low return loss does not equal to good radiation. The energy can be dissipated by lossy materials in the structure or it might leak in the form of surface waves that do not contribute to radiation. Thus, [26] proposes that "it makes sense to use realized gain and radiation pattern to define the bandwidth".

However, the realized gain and constant radiation pattern over a wide bandwidth are not the only parameters used to describe UWB antennas [8]. Many works, e.g. [27], go even further and claim that the classical description of antennas used in narrow-band systems, using gain, beamwidth, Voltage Wave Standing Ratio (VSWR) etc., is "often incorrect for evaluating antennas with baseband-pulse excitations" because they do not include phase information [27]. In other words, they define the amount of energy radiated in a direction with no information about the distortion of the actual signal. As a result, many alternative descriptors such as correlation pattern descriptors ([28]), and fidelity ([29], [30]) have been introduced. These descriptors are application specific because they describe the antenna performance when using a specific signal template. Therefore, the most general antenna descriptor, the antenna impulse response, is introduced in section 2.1.1. It is also employed to evaluate the signal distortion by an antenna as a function of bandwidth in order to determine the limit for the use of narrowband descriptors. Finally, some basic wideband antenna structures will be introduced.

2.1.1 Antenna Impulse Response

2.1.1.1 Definition

For a transmitting antenna, the antenna impulse response describes a relationship between the forward wave at the current (or voltage) wave incoming to an antenna's port and the electric field around the antenna [31]. For a receiving antenna, it is the relationship between the incident electric field strength and the outgoing voltage wave at the antenna port. Arguably the best theoretical study on the antenna impulse response was published by Shlivinski et.al. in [31]. In their paper, the antenna impulse response is called 'effective height'. Even though there is a good reason for this name originating in the basic antenna theory (see e.g. [23]), it may be confusing for system engineers who are not familiar with this theory. Therefore in this work, this descriptor will be referred as 'antenna impulse response' because this name seems to be more likely to be understood even by experts outside of the field of antenna engineering.

Fig. 2.1 introduces the quantities of interest for both transmit and receive antenna. According to [31], the antenna impulse response of a transmitting antenna is defined as follows:

$$\mathbf{E}(\mathbf{r},t) = -\frac{\mu}{4\pi r}\left[I^{+}(\tau) * \mathbf{h}^{\mathbf{T}}(\hat{\mathbf{r}},\tau)\right], \qquad \tau = t - \frac{r}{c} \tag{2.1}$$

where $\mathbf{E}(\mathbf{r},t)$ stands for the vector of electric field strength; $I^{+}(\tau)$ stands for the input current

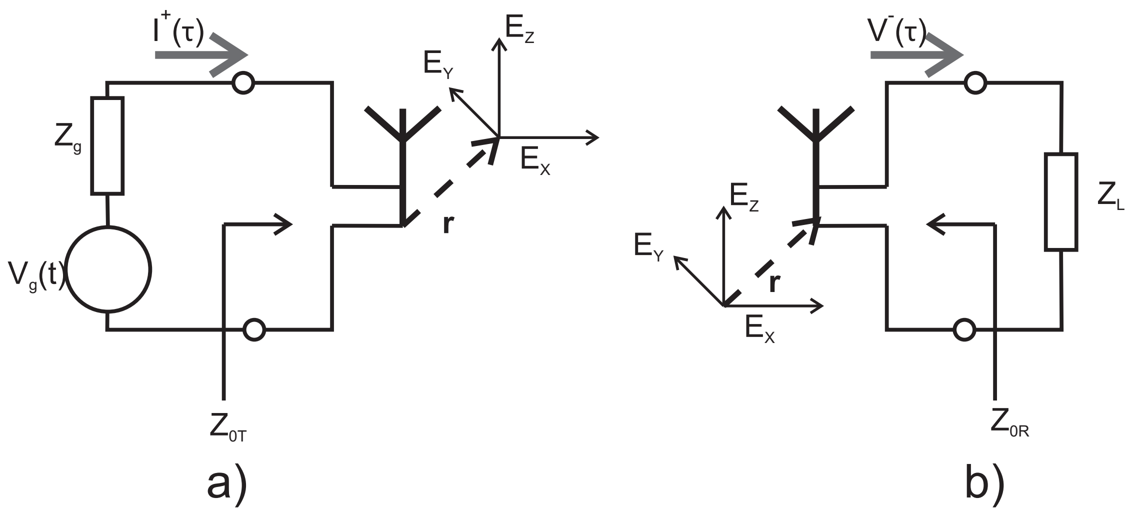

Figure 2.1: Equivalent circuits for definition of antenna impulse response for a) transmitting antenna b) receiving antenna.

wave, $\mathbf{h^T}(\hat{\mathbf{r}},\tau)$ for the antenna impulse response for transmission, $\mathbf{h^T}(\hat{\mathbf{r}},\tau)$ is a vector where each one of its dimensions is linked to polarisation of $\mathbf{E}(\mathbf{r},t)$; t stands for time; $\mathbf{r}$ defines the position of point of interest in relation to the antenna, $r = |\mathbf{r}|$, and $\hat{\mathbf{r}}$ is normalized $\mathbf{r}$ denoting the direction of the outgoing electromagnetic wave; μ is magnetic permeability of free space; $*$ defines the standard convolution.

The receiver impulse response of an antenna is according to [31] defined as follows:

$$V^{-}(t) = -\mathbf{E_0}(t) \star \mathbf{h^R}(\hat{\mathbf{r}},t) \tag{2.2}$$

where $V^{-}(t)$ stands for the outgoing voltage wave at the port of the receiving antenna, $\mathbf{E_0}(t)$ stands for electric field of incident wave with arbitrary waveform, $\mathbf{h^R}(\hat{\mathbf{r}},t)$ for the antenna impulse response for transmission, $\hat{\mathbf{r}}$ is a unit vector defining the direction of the incident wave, $\star$ denotes a temporal convolution concurrent with spatial scalar product [31]:

$$\begin{pmatrix} a_1(t) \\ a_2(t) \\ a_3(t) \end{pmatrix} \star \begin{pmatrix} b_1(t) \\ b_2(t) \\ b_3(t) \end{pmatrix} = a_1(t) * b_1(t) + a_2(t) * b_2(t) + a_3(t) * b_3(t) \tag{2.3}$$

where $*$ is the standard convolution.

Due to the reciprocity theorem, the relationship between $\mathbf{h^T}$ and $\mathbf{h^R}$ is as follows [31]:

$$\frac{1}{2}\mathbf{h^T}(\hat{\mathbf{r}},t) = \frac{\partial \mathbf{h^R}(\hat{\mathbf{r}},t)}{\partial t} \tag{2.4}$$

2.1.1.2 Examples

So far, the concept of antenna impulse response has been introduced theoretically. In this section, we present the impulse responses for three example antennas. The antenna impulse responses were modelled using CST Microstripes™, which is a commercial full-wave simulation package. The selected antennas were: a discone antenna with lower cut-off frequency of 2.4 GHz; a printed circular monopole antenna from [32]; a Coupled Sectorial Loop Antenna (CSLA) presented in [33]. The results are presented in Fig. 2.2.

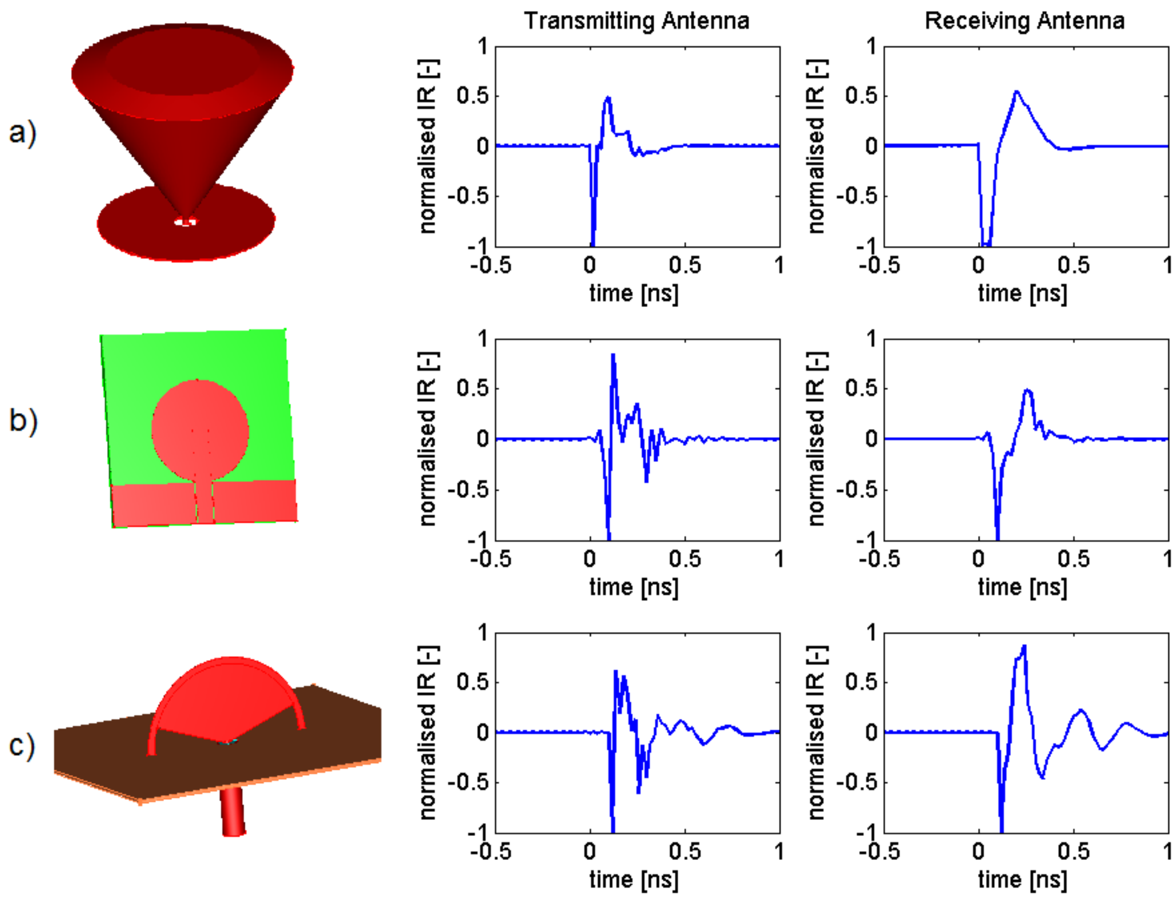

Figure 2.2: Examples of antenna impulse responses $\mathbf{h}^{\mathbf{T}}(\tau)$ for transmitting and $\mathbf{h}^{\mathbf{R}}(\tau)$ for receiving antenna for a) discone antenna b) printed circular monopole antenna [32] in boresight c) CSLA antenna [33] in boresight. For all three cases, the impulse response is presented for the main polarisation of the antenna, which is vertical polarisation in the antenna pictures. It was determined for a distance of 1 m from the antenna, which satisfies the far-field requirements.

2.1.1.3 Transmission between two antennas

Assuming perfect matching of the transmitter's voltage generator V_g to the impedance Z_{0T} of the transmit antenna, and perfect matching of the receiver's antenna to its load Z_{0R} the current to the load $I_L(t)$ is then given as [31]:

$$I_L(t) = \frac{1}{4\pi r}\frac{\eta}{2cZ_{0T}Z_{0R}}\left[\left(\mathbf{h}^{\mathbf{T}}_{\mathbf{T}}(\hat{\mathbf{r}}^{\mathbf{TR}},\tau) \star \mathbf{h}^{\mathbf{R}}_{\mathbf{R}}(\hat{\mathbf{r}}^{\mathbf{RT}},\tau)\right) * V_g(\tau)\right], \qquad \tau = t - \frac{r}{c} \tag{2.5}$$

Eq. (2.5) represents the most general description of a transmission in a wireless channel with only one direct path between the transmitter and receiver. For a more general case with several multipath components (2.5) can be expanded as follows:

$$I_L(t) = \sum_{i=1}^{N} \frac{1}{4\pi r_i} \frac{\eta}{2cZ_{0T}Z_{0R}} \left[\left(\mathbf{h_T^T}(\mathbf{\hat{r}_i}^{\mathbf{TR}}, \tau_i) \star \mathbf{R_i}(\tau_i) \bigstar \mathbf{h_R^R}(\mathbf{\hat{r}_i}^{\mathbf{RT}}, \tau_i) \right) * V_g(\tau_i) \right], \qquad \tau_i = t - \frac{r_i}{c} \quad (2.6)$$

where i is the index of the i-th ray out of a total N rays. $\bigstar$ represents a convolution concurrent with matrix-vector multiplication:

$$\begin{pmatrix} A_{11}(\tau) & A_{12}(\tau) & A_{13}(\tau) \\ A_{21}(\tau) & A_{22}(\tau) & A_{23}(\tau) \\ A_{31}(\tau) & A_{32}(\tau) & A_{33}(\tau) \end{pmatrix} \bigstar \begin{pmatrix} a_1(\tau) \\ a_2(\tau) \\ a_3(\tau) \end{pmatrix} = \begin{pmatrix} A_{11}(\tau) * a_1(\tau) + A_{12}(\tau) * a_2 + A_{13}(\tau) * a_3(\tau) \\ A_{21}(\tau) * a_1(\tau) + A_{22}(\tau) * a_2 + A_{23}(\tau) * a_3(\tau) \\ A_{31}(\tau) * a_1(\tau) + A_{32}(\tau) * a_2 + A_{33}(\tau) * a_3(\tau) \end{pmatrix} \quad (2.7)$$

$\mathbf{R_i}(\tau)$ is a 3-by-3 matrix corresponding to the reflection of i-th ray. The time dependency represents the fact that the reflection coefficient may include frequency dependency. As can be seen in (2.7), each line in the matrix corresponds to one polarisation direction. The diagonal elements describe the reflections coefficients of selected polarisation. The non-diagonal elements correspond to the cases when the reflective surface also rotates the polarisation.

For the first ray, there are no reflections, so :

$$\mathbf{R_1}(\tau) = \begin{pmatrix} \delta(\tau) & 0 & 0 \\ 0 & \delta(\tau) & 0 \\ 0 & 0 & \delta(\tau) \end{pmatrix} \quad (2.8)$$

where $\delta(\tau)$ stands for the Dirac Delta impulse. For further rays, the delays τ_i as well as the weighting factors corresponding to the reflections are given by the propagation properties of the channel. $\mathbf{R_i}(\tau)$ for later rays will typically, but not necessarily, be a purely diagonal matrix.

2.1.1.4 Impact of Antenna Impulse Response on Transmitted Signals

So far, the antenna impulse response has been discussed. However, expressions such as (2.6) are not very suitable for practical system design because it does not provide an intuitive understanding as what happens to the waveform of the transmitted pulse. For instance, for narrowband signals, the distortion of the pulse waveform is negligible, therefore the description by the means of transmitted energy (gain) is sufficient [8],[28]. In this section we aim to explore to what extent this can be extended towards the UWB signals, i.e. the transition between the narrowband and UWB extreme cases will be explored. As will be shown in chapter 3.2, the channel model can be significantly simplified if the impact of antenna impulse responses can be neglected. The objective of this section is not to provide an analytical expression that would encompass any antenna structure. The aim is to show that in many practical cases, the signal distortion can be neglected even for UWB signals with bandwidths below 1 GHz. This provides justification for neglecting of the channel impulse response in subsequent chapters 3 - 7.

To start the investigations, we first discuss the impulse responses of an 'ideal electrically small antenna' and its impact on transmitted bandpass signals. This will then be followed by empirical investigations of the performance of the example antennas introduced in 2.2.

For the **ideal electrically small antenna** the antenna impulse response for the transmit case is often assumed as $h^T(t) \propto \frac{\partial}{\partial t}$ [31]. In other words the transmit antenna acts as a differentiator. The reasoning for this is as follows: there is a differentiation relationship between the electric field $\mathbf{E}(\mathbf{r},t)$ and the vector field potential $\mathbf{A}(\mathbf{r},t)$ (at time t in position $\mathbf{r}$): $\mathbf{E}(\mathbf{r},t) = \frac{\partial \mathbf{A}(\mathbf{r},t)}{\partial t}$ (e.g. [31]). Furthermore, the vectorial potential is a retarded potential and can be obtained as an integration over the current density $\mathbf{J}(t)$ on the antenna surface. For an ideal electrically small antenna, it is assumed that this density is constant over the small volume of antenna and that it is proportional to the incoming current wave $\mathbf{J}_A(t) \propto I^+(\tau)$. These assumptions result in the fact that transmitting antennas are idealised as differentiators.[1] Due to the Lorentz reciprocity (see (2.4)) the antenna impulse response of such an ideal antenna is then an integration of the differentiation, thus $h^R(t) \propto \delta(t)$, where $\delta(t)$ stands for a Dirac Delta impulse. A transmission between two such ideal antennas in free space as shown in (2.5) results in the case that the ideal received impulse has the waveform of a differential of the input

[1] It is noted here that this assumption does not hold for practical antennas. The assumption that $\mathbf{J}_A(t) \propto I^+(\tau)$ can be correct for a stationary state with excitation at a single frequency but not for impulse excitation. Strictly speaking there is a finite delay between the moment when the wave arrives at the antenna port and the moment when it is manifested as a current density $\mathbf{J}_A(t)$ somewhere on the antenna and the delay differs for various point on the antenna. Furthermore, in larger antenna structures, antenna designers aim to control the surface current in order to achieve desired radiation properties. As a result, the current distribution is often very complex and the simplistic assumption that the transmitting antenna acts as a differentiator is not valid.

impulse.

In this paragraph, we will discuss the relationship between the signal bandwidth B and its distortion, assuming the transmission between two ideal electrically small antennas. Let us assume a bandpass signal $s(t)$:

$$s(t) = b(t) \cdot \cos(2\pi f_c t) \tag{2.9}$$

where $b(t)$ is the baseband envelope signal defining the bandwidth B, f_c is the centre frequency[2]. If such signal is differentiated one obtains:

$$\frac{\partial s(t)}{\partial t} = -2\pi f_c [b(t) \cdot \sin(2\pi f_c t)] + \frac{\partial b(t)}{\partial t} \cdot \cos(2\pi f_c t) \tag{2.10}$$

Eq. (2.10) contains two terms. The first term has the same envelope as the original signal, it is scaled by $-2\pi f_c$ and the cos-term has been turned into a sin-term. In the second term the cos-function remained but its envelope is now the derivative $\frac{\partial b(t)}{\partial t}$. Now we compare the amplitudes of both terms for a narrowband and UWB case. In both cases $\frac{\partial b(t)}{\partial t}$ represents the rate at which the original envelope signal $b(t)$ changes. The steepest slopes in signal yield maximum $\frac{\partial b(t)}{\partial t}$ and the steepest slopes also define the bandwidth. Hence in the narrowband case, where changes of $b(t)$ are slow, the second term in (2.10) can be neglected because $\frac{\partial b(t)}{\partial t} << -2\pi f_c b(t)$ (because for UWB communications f_c is in the GHz range) leaving this approximation:

$$\frac{\partial s(t)}{\partial t} \approx -2\pi f_c [b(t) \cdot \sin(2\pi f_c t)] \tag{2.11}$$

As a result, the pulse received in such an ideal case would equal the original pulse only with the change of the phase of the carrier. As the bandwidth of the baseband pulse $b(t)$ increases, the envelope distortion $\frac{\partial b(t)}{\partial t}$ increases and the envelope of the received pulse manifests distortion. Therefore, even an ideal electrically small antenna can significantly distort the waveform of the baseband pulse, if the pulse's bandwidth is sufficiently large.

Now, the bandwidth for which **practical antennas** do not distort the pulse envelope $b(t)$

[2] It is noted that many initial works about UWB considered the use of baseband pulses. However, the recent changes in the regulations in Europe, Japan and Korea (see chapter 1) reduced the available band. For Europe with the general limit enabling only the band from 6-8.5 GHz, it is believed that even in impulse radio systems, it will be possible to use (2.9) to describe the signals employed by practical systems.

will be investigated. The outgoing pulse was calculated using the simulated antenna impulse responses according to (2.5) for three example antennas and five different input pulses with variable bandwidth. In all cases the centre frequency was selected as 7.25 GHz (centre of the EU UWB band).

Following three antennas, as described in Fig. 2.2, were used for the investigation:

- discone antenna (described in detail in Appendix B)
- circular monopole from [32]
- Coupled-Sectorial Loop Antenna (CSLA) from [33]

The transmission between two antennas of the same type in the horizontal plane ($\theta = 90°$ for antenna orientation as in Fig. 2.2) was investigated. For the monopole antenna and the CSLA antenna, the communication between the boresights of the antennas was evaluated, similarly to Fig. 2.2.

As mentioned, five types input baseband pulses $b(t)$ were investigated:

- Gaussian Pulse $b(t) = e^{-\pi\left(\frac{t}{T_P}\right)^2}$
- Rectangular pulse $b(t) = \mathrm{rect}(bt)$
- Raised Cosine pulse $b(t) = \mathrm{rect}(bt)\cos(\pi bt)$
- Triangular pulse $b(t) = \mathrm{tri}(bt)$
- Double Exponential pulse $b(t) = e^{-\frac{|t|}{T_p}}$

where t stands for time, and b and T_p are parameters defining pulse length/bandwidth. The pulses are well known and described in open literature (e.g. [34]-[37]). The full definition of the waveform and bandwidth properties of these pulses is presented in Appendix A.

As will be shown here, the pulse distortion is almost independent on the pulse waveform and is given mainly by its bandwidth, centre frequency and the bandwidth of the employed antenna. The distortion was evaluated using correlation analysis. The waveform of a received pulse $y(t)$ was calculated using (2.5) and it was compared a sample pulse $x(t)$:[3]

$$c_{xy} = \frac{\max_t \left\{ \int_{-\infty}^{\infty} x(\tau) y(\tau - t) d\tau \right\}}{\sqrt{\int_{-\infty}^{\infty} |x(\tau)|^2 d\tau} \sqrt{\int_{-\infty}^{\infty} |y(\tau)|^2 d\tau}} \tag{2.12}$$

[3]This is similar to fidelity analysis presented e.g. in [28]

The delay t between the signals was selected to maximise the value of the correlation coefficient c_{xy}. Two sample pulses $x(t)$ were investigated:

- the input pulse $s(t)$ described in (2.9)
- the approximate differential of this pulse $\frac{\partial s(t)}{\partial t} = -2\pi f_c[b(t) \cdot \sin(2\pi f_c t)]$.

The results of this analysis for the bandwidth of the baseband signal varied from 5 MHz to 11 GHz are presented in Fig. 2.3 for the Gaussian pulse and the raised cosine pulse. A number of observations that can be drawn from the figure.

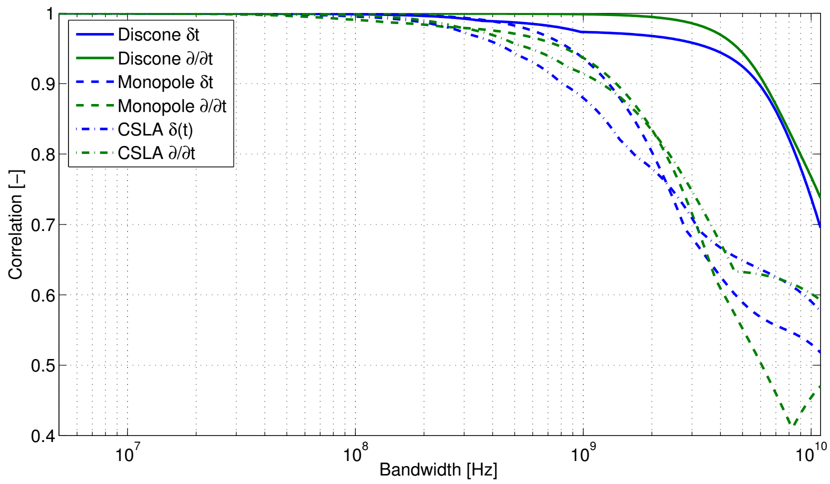

a)

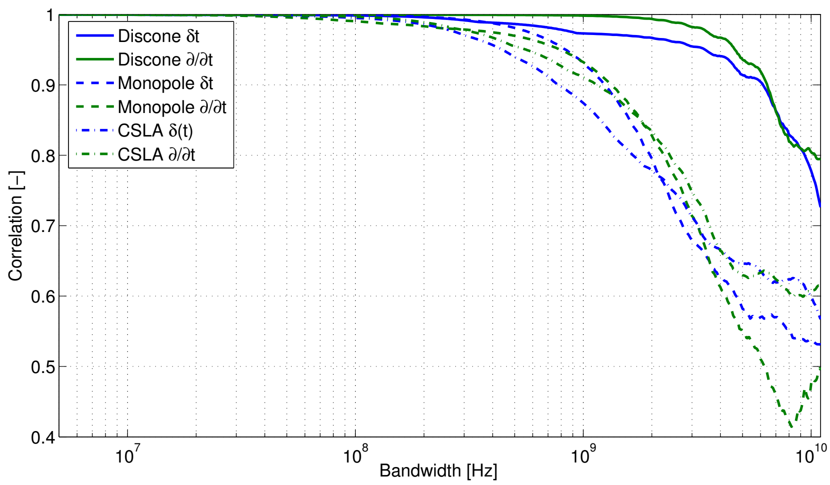

b)

Figure 2.3: The correlation between the received pulse $y(t)$ and the two input pulses. $\delta(t)$ relates to comparison to the input pulse $s(t)$ (the communication link acts just as a delay), $\partial/\partial t$ relates to correlation with derivative with neglecting the second term distorting the envelope. The envelopes $b(t)$ of input pulses are: a) Gaussian pulse b) Raised cosine

The first observation is that the correlation decreases with bandwidth as theoretically predicted. However, the theory above does not explain the differences between different antennas. This is due to the fact that the decrease of the correlation with bandwidth is caused not only by the relative increase of the term $\frac{\partial b(t)}{\partial t}$ in (2.10). There is also the impact of the current distribution $\mathbf{J}_A(t)$. The current distribution changes continuously with the frequency. For a narrow bandwidth B the distribution can be assumed to be the same across the entire frequency range $f_c - B/2$ to $f_c + B/2$. As the bandwidth B increases, the difference between current distribution at the lower edge of the frequency band $f_c - B/2$ and at the upper edge $f_c + B/2$ becomes starker and leads to different properties of the associated electric field at the lower and the upper end of the frequency band.

This is depicted in Fig. 2.4 which shows how the surface current distribution on a circular monopole from [32] changes within the frequency range 5.5 - 9 GHz. It can be seen that the number of current maxima along the circumference of the monopole increases with frequency. It can be also seen that within the band from 6.75 - 7.75 there is not much change which corresponds to high correlation values in Fig. 2.3 for bandwidths below 1 GHz. In contrast, there is a significant difference for the band 5.75 - 8.75 GHz which corresponds to a low correlation coefficient of 0.7 in Fig. 2.3. This result also suggests that the current distribution contributes more to the distortion of the pulse envelope than the term $\frac{\partial b(t)}{\partial t}$.

The second observation is the fact that the correlation coefficient c almost does not differ between either of the input pulses. This suggests that the main factor for distortion is the bandwidth of $b(t)$ rather than its actual waveform. This conclusion can be confirmed by comparison with the further three pulse types. This can be explained by the fact that the antennas' radiation for each frequency is given by the term $\frac{\partial b(t)}{\partial t}$ in (2.10) and by current distribution $\mathbf{J}_A(t)$ on the antennas. Both contributions are approximately the same for the pulses with the same -10 dB bandwidth regardless the pulse shape.

It is noted here that the statement that the distortion is independent of the pulse waveform is not strictly correct. The statement is valid for practical pulses occuppying their -10 dB bandwidth with a reasonable spectral efficiency. It is possible to derive an 'artificial' signal for which the distortion curves differ significantly from the ones plotted in Fig. 2.3 , for instance a

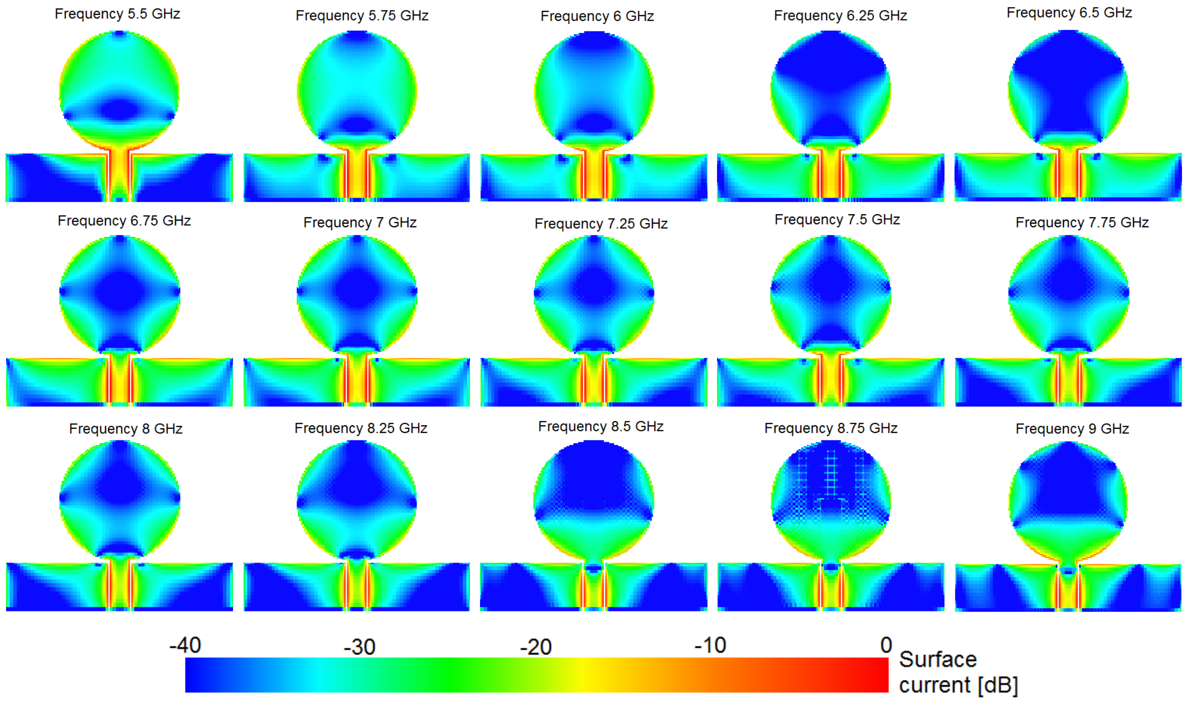

Figure 2.4: Examples of surface current distribution for the monopole antenna from [32].

pulse with Fourier transform: $B(f) = 0.64\text{rect}(b_1 f) + 0.36\text{rect}(b_2 f)$ with $b_1 >> b_2$. For such a pulse the -10 dB bandwidth is given as $1/b_2$, however the level of $20\log(|B(f)|) = -8.9\text{dB}$ for the majority of the bandwidth with the exception of the narrow bandwidth given as $1/b_1$. In investigation, as in Fig. 2.3, such pulse would have the properties of a pulse with bandwidth $1/b_1$ rather than its actual -10 dB bandwidth if $1/b_2 >> 1/b_1$.

The third observation is that the assumption that real antennas cannot be generally assumed to act as a differentiator for the transmit case ($h^T(t) \propto \frac{\partial}{\partial t}$). Such assumption can seems to be valid for the discone antenna (the correlation coefficient is larger for the case of correlation with the derivative of the input signal). For the monopole antenna and the CSLA antenna the correlation coefficients comparing the received signal to the original template $s(t)$ and to the approximate differentiation yield approximately the same results.

In either case it can be stated that the envelope of the signals have low distortion even for UWB bandwidths because for all three investigated antennas the correlation coefficients remain above the 0.9 for bandwidths $B < 1\text{GHz}$. As demonstrated in Fig. 2.5, the distortion for correlation coefficient above 0.9 can be neglected because for these cases the real output signal is qualitatively identical to the approximated signals. Even for the correlation coefficient of

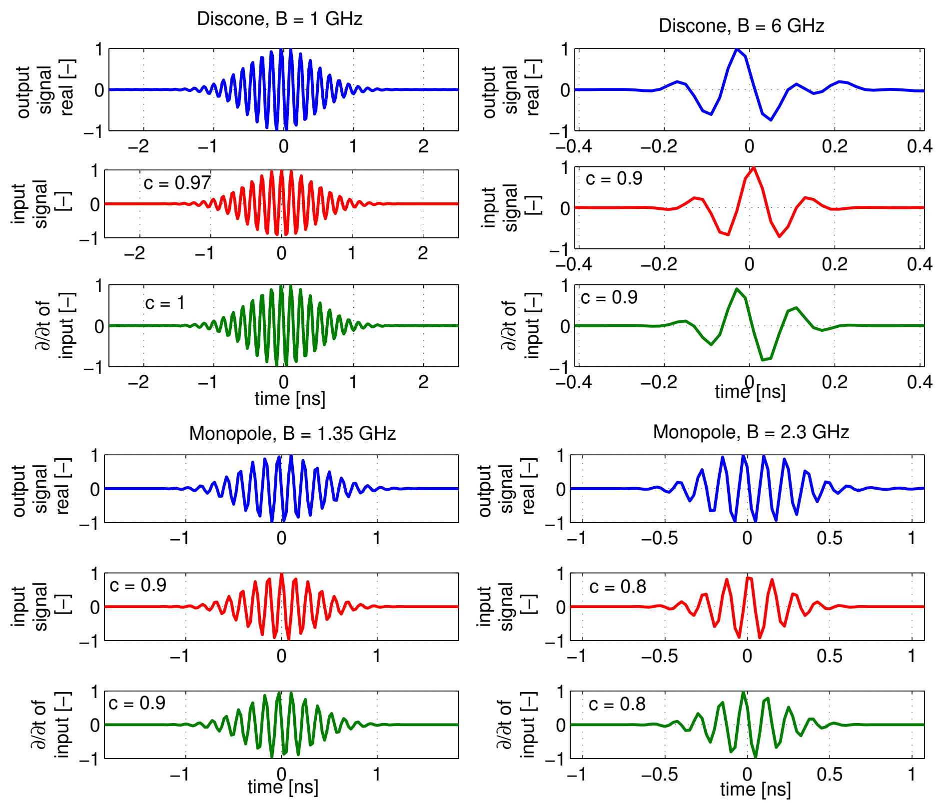

Figure 2.5: Examples of pulse distortion for transmission between the discone antennas and between the monopole antennas. The blue line displays the received signal. The red line is the input signal and the green line shows the approximate differentiation. The correlation coefficient c, (2.12), between the red/green and the blue curve is plotted in respective subplots.

$c = 0.8$ there is a significant similarity between the real distorted signal and the approximated signal outputs.

The final conclusion based on the three previous observation is following. Whilst one should be aware of the possible distortion introduced by antennas, Figs. 2.3-2.5 show that the distortion of the envelope of the transmitted pulses can be neglected for practical cases with signal bandwidth below 1 GHz. This statement holds as long as the current distribution on the antenna remains constant over the bandwidth of operation. Once it begins to differ, distortion of pulse envelope occurs.

This requires a careful and application-specific design, but as shown on three example UWB antennas, such a behaviour for signals with bandwidths of up to 1 GHz can be achieved. In the case of the discone antenna, the envelope distorion was negligible up to the bandwidth of 6 GHz. Such bandwidth is sufficient for most practical existing and near future UWB systems.

The bandwidth WiMedia OFDM system is 528 MHz [13]. Even the impulse radio systems discussed in chapter 4, will operate with pulses within this limit. Also, the current regulations in Europe, Japan and Korea (see Fig. 1.1) do not even allow radiation with bandwidths above 3 GHz.

2.1.1.5 Summary

This section described in detail the time domain properties of antennas for UWB wireless communication systems. The insight into the properties and behavior of antennas processing the UWB signal will prove useful in chapter 3 when the antenna impulse responses will be identified in the measurements of UWB wireless channel. Furthermore, the knowledge of the antenna impulse response and its impact on pulse distortion as a function of bandwidth is important. This knowledge enables the signal distortion in chapters 4-7 to be neglected.

2.1.2 Antenna Structures for UWB Radiation

There are many approaches and many papers on the topic of UWB antennas. An exhaustive summary of all designs is to not the objective of this thesis. Thus, only a short summary of the main approaches towards UWB radiation is presented here. A very good classification of antennas can be found in [26]. According to this reference, there are three basic types of antennas:

- Broadband dipoles and monopoles
- Log-periodic structures
- Traveling wave antennas

Broadband dipoles and monopoles are a very popular type of antenna because of their low cost and simple manufacturing. These antennas, in general, change the standard shape of thin wire dipole into a more complex 2D or 3D structure.

A typical example of a 2D structure is the bowtie antenna. However, other shapes have been investigated by various researchers - e.g. elliptical dipole [38], diamond dipole [39] or circular monopole [32]. Most used 3D structure is the bicone or discone antenna or variation on this concept.

In general, 3D and 2D structures use 2 types of radiation. At the lower edge of the frequency spectrum a standing wave is caused with $\lambda/4$ close to the characteristic dimension of the antenna structure [8]. For higher frequencies the waves tend to be traveling waves along the dipole structure, however, with a node at the end of the structure [32], [8]. As a result, the radiation pattern of the antenna is frequency dependent. The gain in the main direction of radiation increases. This happens at the cost of reduced beam width.

Log-periodic structures are based on repetition of a basic structure which is scaled in size by a constant factor. One obtains a number of elements each of which radiates at a different frequency. A typical example is the Yagi-Uda antenna consisting of wire dipoles or the classical DuHamel's antennas [24], [25]. These antennas show a constant radiation pattern and a very good return loss over theoretically infinite frequency range (given only by the number of employed elements). However, reference [26] also points out that these antenna structures are dispersive. This means that they distort the waveform of transmitted pulses. For each frequency, the antenna structure radiates from a different part of its structure. Which is the main cause for distortion of the pulse envelope as described in preceding section. Thus the antennas are not suitable for impulse radios, but Multiband OFDM systems such as the WiMedia standard [13] can well profit from the constant radiation patterns. However, the dimension of these antennas may become a concern for mobile applications.

Typical examples of **traveling wave antennas** are structures such as tapered-slot antennas (e.g. Vivaldi antenna), rolled-edge horns or ridged horns [26]. These antennas use absorptive loading or carefully shaped arms to control the diffraction on the antenna, especially at its ends [26]. Hence, they show very good broadband behavior in terms of return loss [26]. But their drawback is the fact that they are very directive which is not advantageous for many deployment scenarios of short-range wideband mobile systems where the Angle-of-Arrival of the signal is unknown and variable. Therefore, the use of travelling wave antennas in UWB communication systems is typically not considered [8] but they are often considered in UWB imaging applications [40]-[42].

2.2 UWB Antenna Arrays

Antenna arrays have been investigated since the emergence of wireless communications. The earliest papers listed in the database IEEExplore^{TM} are from the period 1928-1930, e.g. [43]-[45]. These papers already list the advantages of antenna arrays such as increased gain and steerable beam. Since then, the interest in antenna arrays has been enormous. IEEExplore^{TM} registers more than 42,000 scientific publications about antenna arrays published over the past 85 years, which is almost 500 papers per year. The theory of antenna arrays has matured accordingly and is well described in standard textbooks [23] or many engineering handbooks, e.g. in [8], [46]. The benefits for antenna arrays for applications ranging from radars and imaging [8] to the advantages of Multiple-Input-Multiple-Output (MIMO) communication systems are well known. Antenna arrays in MIMO systems enable an increased SNR by suppressing the interferers, by the use of spatial filtering, or by the use of spatial diversity [8],[47]. Recently the advantages of MIMO systems for cryptography have also been discussed [48].

The advantages that antenna arrays offer to UWB systems are the same as in the narrowband cases [8], [22]. However, the immense available bandwidth represents both a challenge and opportunity. This is illustrated by the reference [49], which has the title: "UWB antenna arrays: it is a different world."

The structure of this section is following. Section 2.2.1 firstly explains why the classical array descriptors for narrowband arrays are not suitable for UWB antenna arrays and alternative descriptors suitable for UWB antenna arrays are introduced. Antenna descriptors for UWB arrays have been studied by a number of authors, e.g. [22],[49]-[51], but to our best knowledge no one has studied the transition between the narrowband and the UWB case to determine the bandwidth limits for the choice of appropriate descriptor. This transition is studied in section 2.2.2. Finally, references [22],[49]-[50] report that UWB arrays manifest a remarkable property that even sparse arrays do not manifest, i.e. grating lobes. This property will be discussed in detail in Section 2.2.3.

2.2.1 Array Descriptors - Introduction

The standard way of describing antenna arrays is by the means of array factors. This method is well known and described in a number of standard textbooks, e.g. in [23]. Hence, here only a brief summary is presented. Antenna arrays sum the signals received by individual elements after signals from individual antennas are weighted in amplitude and phase. The radiation pattern of such an antenna array (consisting of identical elements) is given as a multiplication of element radiation pattern and the array factor [23]. For each Angle-of-Arrival/Departure, the array factor describes the amplitude of the signal received/transmitted in that direction if the antennas were ideal isotropic elements [23]. For the classical array factors, the signal is a periodic signal at a single frequency. As a result, the array factor is defined by the phase shifts introduced by the array geometry, by the phase shifters at each antenna element, and by the amplitude weight of each element. However, this approach cannot be directly used in UWB systems. Quite simply, the phase shifts are not frequency independent. Thus, between two frequencies the superposition can change from destructive into constructive [22],[49].

The phase shifts caused by the array geometry and/or by phase shifters change with frequency. However the phase shifts correspond to a single time delay. Furthermore, the duration of the processed signals can often be comparable to the delay introduced by the array geometry [22],[49]-[51]. In such a case, the received signal can be pulse-train rather than a single impulse. Therefore, the description of UWB antenna arrays is typically performed in the time domain [22],[49]-[51]. An example of such an antenna array is in Fig 2.6. The array in Fig. 2.6 is a uniform linear array with element spacing d. The array is uniform because received signals $y_i(t)$ are only delayed but the amplitude is the same and the elements spacing is constant. Fig. 2.6 shows only the receiving array which will be discussed in this section but the same descriptors can be used for transmitting array as well.

All descriptors in [22],[49]-[51] begin with investigation of received the signal $y(t)$:

$$y(t,\tau,\varphi) = \sum_{i=0}^{N-1} y_i(t - \tau_i,\varphi) \tag{2.13}$$

where N stands for the number of elements; τ_i stands for the delay introduced in the branch

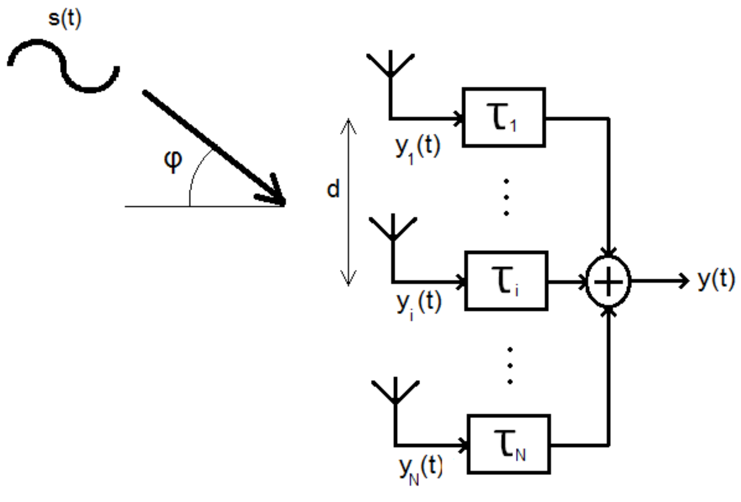

Figure 2.6: Uniform linear antenna array with element spacing d

of i-th antenna element; τ is a vector of all τ_i and $y_i(t,\varphi)$ represent the received signals from Angle-of-Arrival φ. As discussed in the preceding section 2.1 the waveforms of received electric signal $y_i(t)$ and the electromagnetic wave $s(t)$ may differ. However, section 2.1 concluded that for UWB antennas designed well for specific $s(t)$, the distortion of the signal is minimal. Hence (2.13) can be rewritten as:

$$y(t,\tau,\varphi) = \sum_{i=0}^{N-1} s\left(t - i\frac{d}{c}\sin\varphi - \tau_i\right) \tag{2.14}$$

where d is element spacing, c is the speed of light, the term $\left(i\frac{d}{c}\sin\varphi\right)$ represents the path delay caused by the array geometry.

For the sake of simplicity we assume far-field beam-steering in direction φ_0 with a constant increment $\Delta\tau = \frac{d}{c}\sin\varphi_0$ between τ_i and τ_{i+1} [22],[49]. Thus, (2.13) can be further simplified as:

$$y(t,\varphi_0,\varphi) = \sum_{i=0}^{N-1} s\left(t - i\frac{d}{c}(\sin\varphi - \sin\varphi_0)\right) \tag{2.15}$$

The array descriptors, called beampatterns in [22] and [49], then analyse the energy, power, or amplitude properties of $y(t,\varphi,\varphi_0)$. Reference [50] observes the total energy of $y(t)$, amplitude of $y(t)$, or the peak power of the signal $y(t)$. References [22] and [49] observe the total energy of $y(t)$, the maximum energy of $y(t)$ integrating over the duration of $s(t)$, or the peak power of $y(t)$. To a large extent the results provided by all descriptors are similar. Here, we focus on the descriptor using the total energy because we believe that this descriptor corresponds the most to a practical communication systems considering equalizing receivers as well as inter-symbol interferences. Such beampattern is given as [22],[49]:

$$\epsilon(\varphi,\varphi_0) = \frac{\int_{-\infty}^{\infty} |y(t)|^2 \mathrm{d}t}{\int_{-\infty}^{\infty} |s(t)|^2 \mathrm{d}t} \tag{2.16}$$

when (2.15) is substituted in (2.17), one obtains:

$$\epsilon(\varphi_0,\varphi) = \frac{\sum_{i=0}^{N-1} \sum_{j=0}^{N-1} R_{ss}\left((i-j)\frac{d}{c}(\sin\varphi - \sin\varphi_0)\right)}{R_{ss}(0)} \tag{2.17}$$

where $R_{ss}(\tau) = \int_{-\infty}^{\infty} s(t) \cdot s^*(t-\tau)\mathrm{d}t$ is the autocorrelation function of signal $s(t)$, with $s^*(t)$ standing for complex conjugate of $s(t)$.

If we similarly as in (2.9) in section 2.1 assume a bandpass signal $s(t)$:

$$s(t) = b(t) \cdot \cos(2\pi f_c t) \tag{2.18}$$

Equation (2.17) can be rewritten as:

$$\epsilon(\varphi_0,\varphi) = \frac{\sum_{i=0}^{N-1} \sum_{j=0}^{N-1} R_{bb}\left((i-j)\frac{d}{c}(\sin\varphi - \sin\varphi_0)\right) \cos\left(2\pi f_c (i-j)\frac{d}{c}(\sin\varphi - \sin\varphi_0)\right)}{R_{bb}(0)} \tag{2.19}$$

where $R_{bb}(\tau)$ is the autocorrelation function of the baseband signal $b(t)$.

$R_{bb}(\tau)$ is a purely real even function for real bandpass signals $b(t)$ [34]. For complex signals $b(t)$ the $R_{bb}(\tau)$ is a Hermitian function[4] [34], then further simplification of (2.19) is possible:

$$\epsilon(\varphi_0,\varphi) = N + \frac{2\sum_{i=1}^{N-1}(N-i)\Re\left[R_{bb}\left(i\frac{d}{c}(\sin\varphi - \sin\varphi_0)\right)\right] \cos\left(2\pi f_c i\frac{d}{c}(\sin\varphi - \sin\varphi_0)\right)}{R_{bb}(0)} \tag{2.20}$$

where $\Re[\bullet]$ stands for real part. Note that $R_{bb}(0)$ is purely real in for all functions $b(t)$ thus the operator $\Re[\bullet]$ could be left out. For real bandpass signals $b(t)$ (as is the case for all the signals listed in the appendix A) the operator $\Re[\bullet]$ can be left out of (2.20)

Equation (2.20) can be used to show how the energy beampattern can be linked to the narrow-

[4]Hermitian function is a function $f(x)$ for which $f(x) = f^*(-x)$ with * stating complex conjugate [34]

band array factor and also to explain why the array factor is not suitable as a descriptor for UWB arrays.

Firstly, consider a signal with a single frequency which is assumed for calculation of array factors [8],[23], the bandpass signal $b(t) = 1$. Its autocorrelation function can be rewritten: $R_{bb}(\tau) = R_{bb}(0) = \infty$. As a result, the R_{bb} terms can be canceled out of (2.20) leaving:

$$\epsilon(\varphi_0,\varphi) = N + 2\sum_{i=1}^{N-1}(N-i)\cos\left(2\pi f_c i\frac{d}{c}(\sin\varphi - \sin\varphi_0)\right) \tag{2.21}$$

This yields the same results as the square of the array factor. This is because the array factor is an 'amplitude' function where as $\epsilon(\varphi_0,\varphi)$ is an 'energy function'.

Equation (2.21) can also be used for narrowband arrays for which the signal duration $T_b >> (N-1)\frac{d}{c}|\sin\varphi - \sin\varphi_0|$ (where $i = (N-1)$ is chosen as it represents the maximum delay) because for such cases $\Re\left[R_{bb}(|\tau| < |(N-1)\frac{d}{c}(\sin\varphi - \sin\varphi_0)|)\right] \approx R_{bb}(0)$.

However, as the bandwidth of the signal $b(t)$ increases, the autocorrelation function $R_{bb}(\tau)$ changes because it is linked to $B(f)$, the Fourier transform of $b(t)$, in the following way $\mathcal{F}\left[R_{bb}(\tau)\right] = |B(f)|^2$ [34]. For band limited signals $b(t)$ the signal duration T_b is proportional to the inverse of their bandwidth B. This is also true about their autocorrelation function $R_{bb}(\tau)$ which can be approximated as having duration $2T_b$.[5] As a result, with the increase of bandwidth, the cos-terms in (2.20) are not weighted by the factor $(N-i)$, as in the narrowband case (2.21), but with a lower factor $(N-i)\frac{\Re\left[R_{bb}\left(i\frac{d}{c}(\sin\varphi - \sin\varphi_0)\right)\right]}{R_{bb}(0)}$ instead. Especially for cases when the signal delays $i\frac{d}{c}(\sin\varphi - \sin\varphi_0)$ become comparable to the signal duration T_b the beampattern differs significantly from the array factor.

Having introduced the beampattern $\epsilon(\varphi_0,\varphi)$, few examples of how the beam pattern changes with bandwidth are shown in Fig. 2.7. Fig. 2.7 presents beampatterns according to (2.20) calculated for excitation with a Gaussian pulse (introduced in Appendix A) at the centre frequency of 7.25 GHz. Several conclusions about the beampattern properties can be made.

Firstly, it can be observed that the beampattern begins to change significantly after the band-

[5]Here it is noted that there are signals $b(t)$which are not time and/or band limited in the strict mathematical sense, e.g. Gaussian pulse. However, practical signals used for communication purposes and certainly all signals considered in this thesis (listed in Appendix A), following is true for their limits $\lim_{|t|\to\infty} b(t) = 0$ and $\lim_{|f|\to\infty} B(f) = 0$. As a result, the bandwidth of the signals can be described by the means of -10 dB bandwidth B and similarly defined -10 dB effective duration T_b.

width exceeds 1 GHz. Then the array factor can no longer be used for description of UWB arrays. This has been predicted in the theoretical discussion of beampatterns. The transition between the narrowband case and the ultrawideband case with focus on the choice of correct descriptor is presented in more detail in subsequent section 2.2.2.

Secondly, it is noted that the main beam remains approximately independent on the bandwidth. This is due to the fact that for the main beam the term $|\sin\varphi - \sin\varphi_0|$ remains very

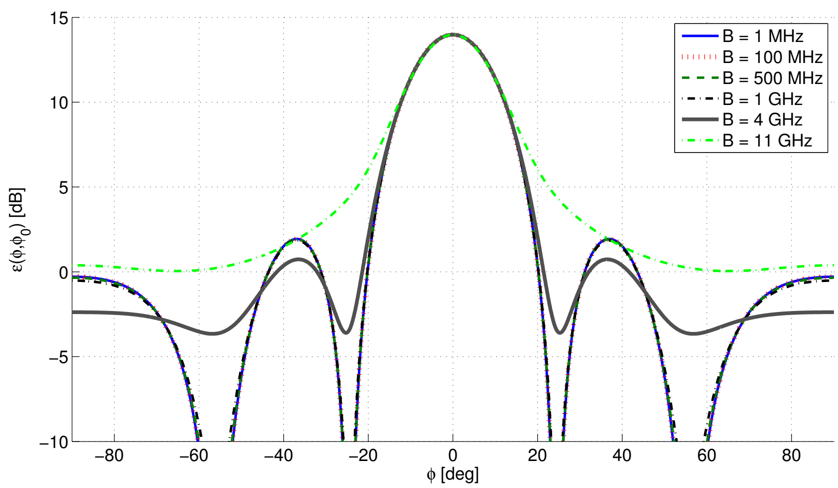

a)

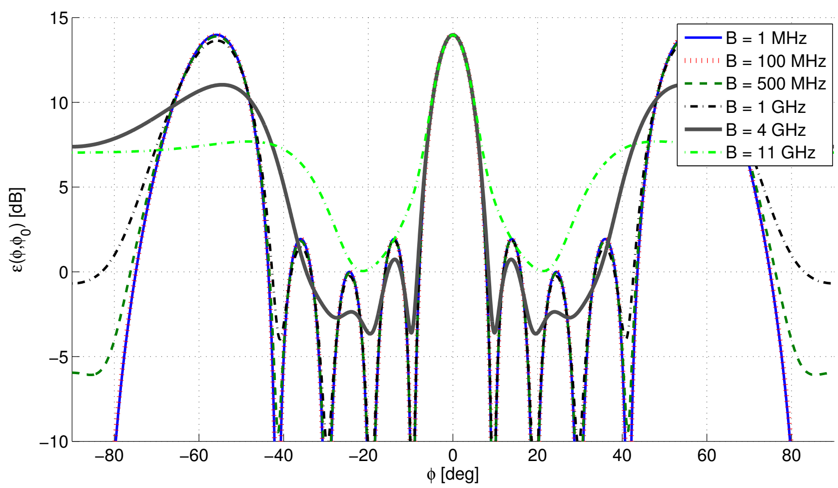

b)

Figure 2.7: Uniform linear antenna array with 6 elements calculated using (2.20). The element spacing d is a) 2 cm and b) 5 cm. The baseband signal $b(t)$ is a Gaussian pulse with centre frequency of 7.25 GHz. The beampatterns for the lowest bandwidth of 1 MHz correspond to the classical array factor.

small, ensuring that $T_b >> (N-1)\frac{d}{c}|\sin\varphi - \sin\varphi_0|$ remains fulfilled even for large bandwidths[6]. However, as $|\sin\varphi - \sin\varphi_0|$ increases the differences between the array factor and the beampattern increases. Ultimately, for sufficient bandwidths $\epsilon(\varphi_0,\varphi)$ the beampattern assumes value $10\log N[dB]$, where N is the number of elements, as can be observed for the case of a sparse array, bandwidth of 4 GHz and $\varphi = \pm 90°$ in Fig. 2.7 b). Practically this corresponds to the fact that for this combination of Angle-of-Arrival and bandwidth, the array receives a train of N pulses rather than a single pulse amplified/attenuated by the array. This means that with the increase of the bandwidth, the directivity of an array is reduced and ultimately the beampattern consists only of a main beam with $\epsilon(\varphi_0,\varphi = \varphi_0) = 20\log N \quad [\text{dB}]$ and $\epsilon(\varphi_0,\varphi) = 10\log N \quad [\text{dB}]$ for φ outside of the main beam. The beamwidth of the main lobe remains a function of the physical size of the array as shown in [22],[49].

Lastly, the effect described in the preceding paragraph applies also to grating lobes which eventually disappear. This can be observed in Fig. 2.7 b). Such property is potentially interesting for many applications, e.g. for low-complexity Angle-of-Arrival localisation systems with sparse arrays. Hence, the conditions for the disappearance of grating lobes are studied in more detail in section 2.2.3.

2.2.2 Array Descriptors - Choice

The reasons why the array factors are not suitable descriptors for the UWB antenna arrays was discussed in the preceding section. However in Fig. 2.7, it can be noticed that for both cases there is no stark difference between the beampattern for the narrowband case and for beampatterns for bandwidths $B = 500$ MHz and $B = 1$ GHz. This suggests that even for many UWB cases the description by the array factor may well be sufficient. Hence, this section aims to investigate the transition between the narrowband and UWB array and to find an empirical bandwidth limit for which the array factors can still be used. The knowledge of such limit is believed to be beneficial because there is a large fundamental knowledge of array design linked to the theory using array factors, e.g. in [23], [46]. If the use of array factors for some UWB cases can be justified, it also justifies the use of this body of knowledge to the design UWB

[6]Here it is noted that considering the bandpass signal $b(t)$ from (2.18), the maximum possible bandwidth is double the centre frequency f_c, $B = 2f_c$

arrays.

The bandwidth limit will be explored using correlation analysis. The correlation coefficient $c_{\epsilon(\varphi,\varphi_0,B=0)\epsilon(\varphi,\varphi_0,B)}(B)$ between the narrowband beampattern in dB scale $\epsilon_{dB}(\varphi,\varphi_0,B_0 \to 0)$ and its wideband counterpart $\epsilon_{\mathrm{dB}}(\varphi,\varphi_0,B)$ is observed:

$$c_{\epsilon(\varphi,\varphi_0,B=0)\epsilon(\varphi,\varphi_0,B)}(B) = \frac{\mathrm{E}\{\epsilon_{\mathrm{dB}}(\varphi,\varphi_0,B_0 \to 0)\epsilon_{\mathrm{dB}}(\varphi,\varphi_0,B)\} - \mathrm{E}\{\epsilon_{\mathrm{dB}}(\varphi,\varphi_0,B_0 \to 0)\}\mathrm{E}\{\epsilon_{\mathrm{dB}}(\varphi,\varphi_0,B)\}}{\mathrm{std}\{\epsilon_{\mathrm{dB}}(\varphi,\varphi_0,B_0 \to 0)\}\mathrm{std}\{\epsilon_{\mathrm{dB}}(\varphi,\varphi_0,B)\}} \tag{2.22}$$

The bandwidth B is increased and once the correlation coefficient $c(B_{UL}) = 0.9$ the upper bandwidth limit for the use of arrayfactor is given B_{UL}. The procedure is repeated for a large number of arrays and the bandwidth are evaluated as a function of array parameters.

Before, the analysis is started, the theoretical expectation for the properties of the bandwidth limit based on (2.20) is discussed. Then reasons for correlating the beam pattern in the dB-scale and the choice of the limit $c = 0.9$ are explained. Finally, the bandwidth limit is explored.

2.2.2.1 Theoretical expectations

The theoretical limit for the use of array factor is given by (2.20) and has already been briefly discussed in the preceding section. The array factors can be used as long as the effective duration of the signal autocorrelation function $R_{bb}(|\tau|) \approx R_{bb}(0)$ for $|\tau| \leq (N-1)\frac{d}{c}|\sin\varphi - \sin\varphi_0|$. In other words the duration of the signal is longer than the maximum delay experienced by the signal when traveling along the array. Based on this, the following can be concluded for the bandwidth limit.

Firstly, it will not depend on the actual centre frequency f_c. This might be surprising at first, because centre frequency defines the properties of array factors (the position of nulls, the existence and position of grating lobes) [23]. Whilst this is true, this investigation aims to observe the change of the beam pattern with increasing bandwidth, not the shape of the beampattern. This change is given in (2.20) only by $R_{bb}(\tau)$.

Secondly, with increased size of the array the upper bandwidth limit for the use of array factors will be reduced as longer pulses will be required to increase the effective duration of $R_{bb}(\tau)$. As a result the bandwidth limit B_{UL} is expected to be inversely proportional to the array size

$B_{UL} \propto \frac{1}{(N-1)d}$.

Lastly, there will be an impact of the pulse shape on the bandwidth limit, but the assumption is that for most pulses that 'efficiently' occupy the bandwidth, the difference will not be significant. (For details, see the discussion about pulse distortion by antennas in section 2.1)

2.2.2.2 Choice of Correlation

The upper limit for bandwidth investigated here aims to define when the beam pattern does and does not differ significantly from the narrowband array factor. Therefore, the correlation analysis has been chosen. The correlation in (2.22) is performed on the beam patterns in dB scale. This is chosen for the following reason. The array factors often include nulls with attenuation more than 30 dB compared to the main lobe. These nulls are often utilised by the beam-steering algorithms [47]. However, in the linear scale they are negligible compared to the main lobe. As a result, correlation analysis on the linear scale would not necessarily evaluate the disappearance of the nulls as a significant change. In dB scale, all the changes are weighted similarly.

The selection of $c(B_{UL}) = 0.9$ as the definition for the upper bandwidth limit B_{UL} is a heuristic choice. A large number of beam patterns and their correlation coefficients were observed. $c(B_{UL}) = 0.9$ appeared as the correct choice for the upper limit. For $c(B_{UL}) = 0.9$ the nulls in the pattern are less deep but remain significant and if grating lobes are present, $c(B_{UL}) = 0.9$ means that they are typically attenuated by less than 1 dB. This is illustrated by Fig. 2.8 which shows beam patterns for six different arrays. For each array two beam patterns are shown: the narrowband beam pattern and the beam pattern for $c(B_{UL}) = 0.9$. As can be seen there is a significant similarity between the beam patterns. Thus Fig. 2.8 justifies the choice of $c(B_{UL}) = 0.9$ as a limit.

2.2.2.3 Bandwidth limit - Exploration

As outlined in the theory, it is expected that the bandwidth limit will depend inverse proportionally on the array size. This section aims to confirm the theory and to quantify the inverse proportionality. Therefore, the dependency on the following parameters will be explored -

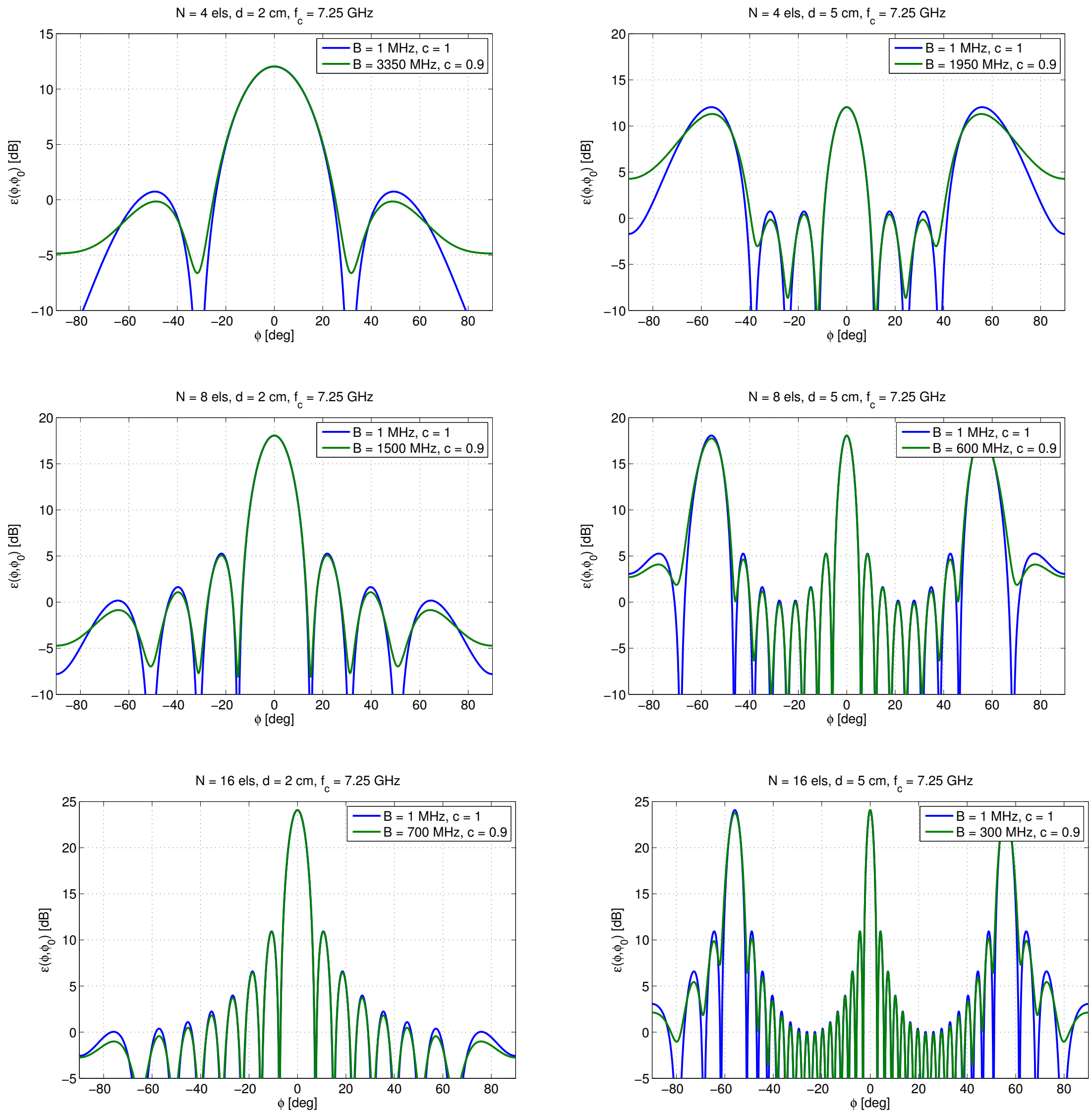

Figure 2.8: Examples of array beampatterns with various spacing and their beampatterns for $c = 1$ and $c = 0.9$. The beam patterns were calculated according to (2.20). The details about the arrays are in the titles of each graph.

dependency on centre frequency, on pulse type, on element spacing, and on the number of elements.

The first dependency that is explored is presented in Fig. 2.9 and shows the dependency of the upper bandwidth on the element spacing. It plots the dependency for arrays with 3 and 15 elements. For each array the bandwidth limit was explored for four different centre frequencies. The baseband pulses $b(t)$ are Gaussian pulses, introduced in the Appendix A. Fig. 2.9 allows three conclusions. Firstly, it can be seen that the bandwidth limit decreases with element spacing. Secondly, it decreases with the number of elements. These two conclusions are an

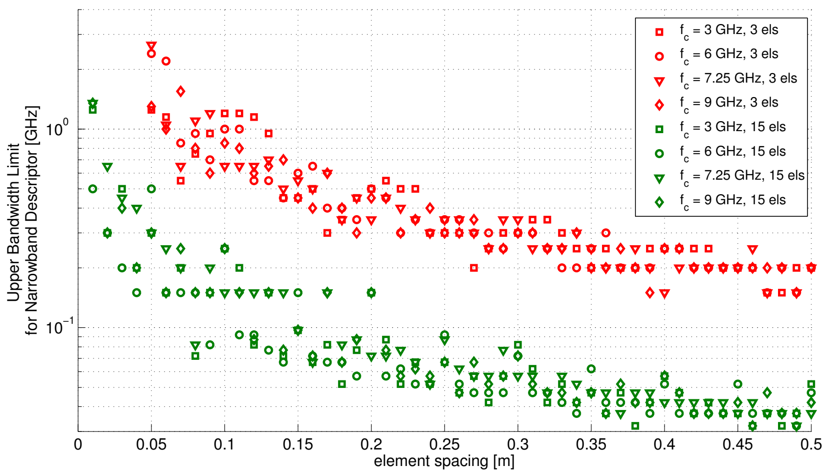

Figure 2.9: The upper bandwidth limit for arrays with variable spacing for variable number of elements and centre frequency. The main objective is to show the independency on centre frequency. This is documented by the points of same colour following the same trend. The baseband pulse $b(t)$ is Gaussian pulse. Logarithmic scale for the bandwidth-axis was chosen to demonstrate that bandwidth limit is lower for the arrays with more elements even for large element spacing. In linear scale this difference would not be as apparent.

initial confirmation of the theoretical expectation. In terms of dependency on centre frequency, there are slight differences but it can be observed that for all 4 frequencies the data points oscillate around a 'mean' trend. This is believed to be caused by the fact that for different centre frequencies the arrays often have a different number of grating lobes and different position of nulls in the pattern. The first changes for the shape of the beampattern appear for angles most distant from the angle of the main lobe φ_0 as can be seen in Fig. 2.8 and by analysis of (2.20). The impact of these changes on the correlation is not the same for all beampatterns and partly depends on the actual beampattern energy value for these angles.

However as all curves follow the same trend and the objective is to determine an engineering limit for the applicability of array factor on UWB arrays, it seems sufficient to assume that there is no dependency on the centre frequency. This simplifies subsequent investigation that will be limited only to a single centre frequency f_c. The centre frequency of $f_c = 7.25$ GHz was chosen as it corresponds to the centre of the UWB band in the EU.

Fig. 2.10 displays the same dependency as Fig. 2.9 but only for the case of 4-element array and it explores the impact of the baseband pulse type. It explores the dependency for the

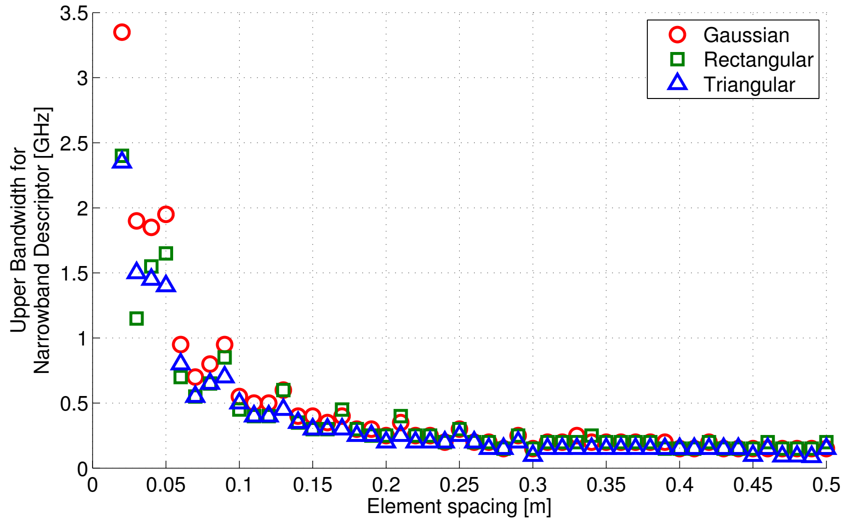

Figure 2.10: The upper bandwidth limit for arrays with variable spacing for variable waveform of baseband pulse $b(t)$. The number of antenna elements is $N = 4$, centre frequency $f_c = 7.25$GHz. The pulse bandwidth is defined by the bandwidth limit.

Rectangular, Gaussian and Triangular pulse, all defined in Appendix A.[7]

The upper bandwidth limit displayed in Fig. 2.10 corresponds to the 10 dB bandwidth for each pulse type. As can be seen, the upper bandwidth limit does not change significantly with the pulse type. This is due to the fact that as mentioned in the theory the effective duration of the autocorrelation function $R_{bb}(\tau)$ is approximately given by the 10 dB bandwidth. Hence, for all three pulses the bandwidth for which the approximation of constant $R_{bb}(\tau) \approx R_{bb}(0)$, as required for the use of array factor, is approximately the same. This statement is also applicable to other practical baseband pulse waveforms. Similarly as in the discussion in the Antenna section 2.1, this statement is not generally applicable to all pulses. It might well be possible to design an 'obscure' pulse for which the array properties will differ significantly. However, it is believed that for most practical pulses that aim to utilise the 10 dB bandwidth efficiently the choice of the array descriptor depends on the pulse bandwidth but not on its type. Thus, only the Gaussian pulse will be used in the subsequent analysis.

Finally, the dependency on the array size is investigated. The theory suggests that the band-

[7]The remaining pulses - the raised cosine and double exponential pulse are not presented here because there seem to be no simple closed analytical expression for their autocorrelation function $R_{bb}(\tau)$. Numerical evaluation was not performed because it is computationally complex and based on the results of the first three pulse types, it does not seem that it would provide any additional information.

width limit will be inversely proportional to the array size. The bandwidth limit was determined for multiple arrays with different number of elements and using the Least-Square curve fitting it was fit by a curve $B_{UL} = A/d$[GHz] where d is the spacing and A is a coefficient. Some example curve fits are presented in Fig. 2.11, which shows a good fit between the data points and the curve for arrays with 3,5,7 and 9 elements. Then, the coefficient A and it's dependency on the number of elements is shown in Fig. 2.12. The coefficient decreases as the number of elements increase and a fit with a curve $\propto 1/(N-1)$ is plotted and a good agreement between the data points and the fit is shown. These two fits confirm that the bandwidth limit is inversely proportional to the array size and they enable to quantify it as follows:

$$B_{UL} = \frac{0.16}{d \cdot (N-1)}[\mathrm{GHz}] \tag{2.23}$$

2.2.2.4 Conclusion

In this subsection the bandwidth limit for the use of the array factors as suitable descriptors for UWB arrays is explored and quantified by (2.23). The conclusions itself are not very surprising and confirmed the theoretical expectations based on the theory of beampatterns introduced in section 2.2.1. More surprising than the nature of the dependency of the bandwidth limit is its quantification which shows that for many arrays smaller than 20 cm (which is size that might be expected for most indoor UWB applications) the bandwidth limit is approximately 800 MHz, which means that many UWB applications can use array designs considering the classical array factors.

2.2.3 UWB Antenna Arrays - Existence of Grating Lobes

In Fig. 2.7 which showed some examples of the beampatterns it could be noticed that in the case of a sparse array the grating lobes become suppressed. This is a very interesting property, described e.g. in [22],[49], and in [50], because it might appear that in UWB, sparse arrays provide a narrow beam (given by the array size) with no grating lobes. This would be advantageous e.g. for low-complexity localisation systems or low-complexity beamformers. However, Fig. 2.7 also reveals that the grating lobes remain present even for bandwidth of 1

GHz. This suggests that the general statement: "In UWB arrays there are no grating lobes" from [22] needs a revision. The statement is not incorrect, but it only applies to UWB systems with sufficient bandwidth. Thus here it is quantified what bandwidth is needed to suppress the grating lobe in sparse antenna arrays. Firstly, the reasons for the presence of grating lobes are briefly summarised. Then, then the mechanism of their suppression in UWB arrays is presented and finally, the mechanism is quantified.

Grating lobes appear in narrowband antenna arrays with element spacing d larger than $\lambda_0/2$, where λ_0 is the free-space wavelength of the electromagnetic wave [23]. A pair of grating lobes appear symmetrically around the main lobe because the superposition of the incoming waves

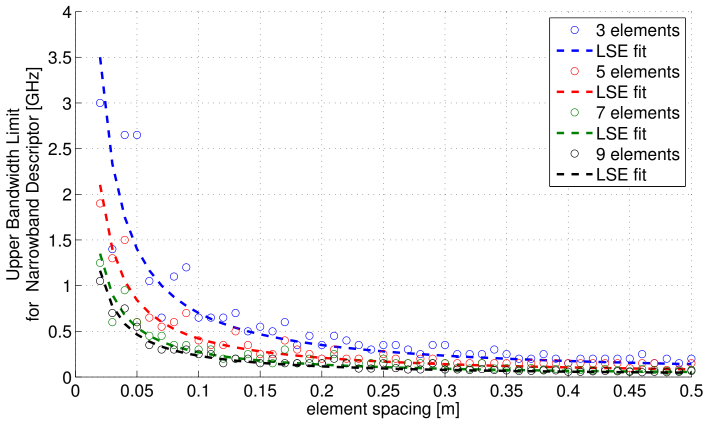

Figure 2.11: The upper bandwidth limit for arrays with variable spacing and corresponding Least Square Error fits $B_{UL} = A/d[GHz]$. The fits and their data points are colour-matched.

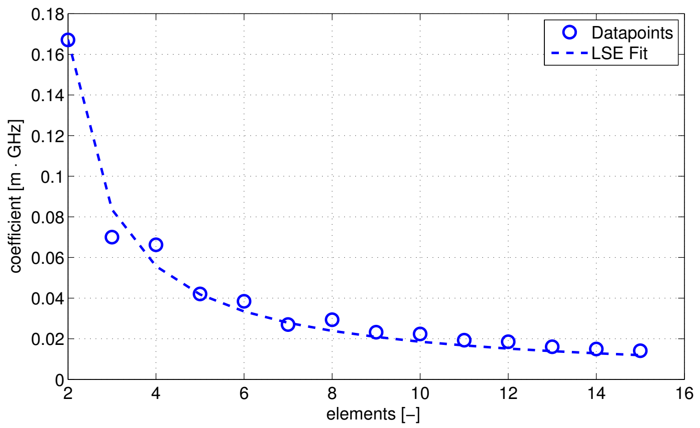

Figure 2.12: The data-points in the graph show the coefficient A (determined from fits in 2.11) for a variable number of elements and the Least Square Error fits $\propto 1/(N-1)$

becomes constructive even for angles other than the direction of the main lobe [23]. If the element spacing exceeds the wavelength of the wave ($d \geq \lambda_0$), the grating lobes have the same power level as the main lobe [23]. If the size of the array increases further, another pair of grating lobes appear.[8] In general for $d \geq n \cdot \lambda_0$ where $n \geq 1$ is an integer, n pairs of grating lobes appear in each hemisphere [23]. For arrays with the main lobe in the bore-side direction ($\tau_i = 0$ for all delay elements in Fig. 2.6) the position φ_{GL} of the first grating lobes is given as [23]:

$$\sin \varphi_{GL} = \frac{\lambda_0}{d} \tag{2.24}$$

As can be seen in (2.24) the first grating lobes are positioned in angles for which the path difference for a wave between adjacent elements is equal to λ_0 [23]. For the $n-$th grating lobe, the path difference for a wave between adjacent elements is $n\lambda_0$ [23]. This can be used to substitute into (2.20). With $\lambda_0 = \frac{c}{f_c}$, where c is the speed of light for the first grating lobes one obtains:

$$\epsilon(\varphi_{GL},\varphi_0) = N + \frac{2\sum_{i=1}^{N-1}(N-i)\Re\left[R_{bb}\left(\frac{i}{f_c}\right)\right]}{R_{bb}(0)} \tag{2.25}$$

This is true for any first grating lobe regardless the main-lobe direction φ_0 (assuming conditions for the existence of grating lobes are met). Equation (2.25) leads to a conclusion that the energy level of the grating lobe is independent of the array size (assuming $d > \lambda_0$). This might seem surprising at first but it is a correct conclusion because the spacing determines only the direction of the grating lobe. The energy is given by the superposition of the signals shifted among each other by integer multiples of λ_0 and this is independent of the actual angle of the grating lobe.

The mechanism of grating lobe suppression is the same as was the reason why array factor cannot be used to describe UWB arrays. In general $\Re\left[R_{bb}\left(\frac{i}{f_c}\right)\right] \leq R_{bb}(0)$ for all integers $i \geq 1$. For a narrowband signal, it is valid that $\Re\left[R_{bb}\left(\frac{i}{f_c}\right)\right] \approx R_{bb}(0)$. As a result the grating

[8] It is not entirely correct to claim that a pair of grating lobes appears. For an array with the main lobe in bore-side direction and $d = \lambda_0$ a pair of grating lobes exists in the end-fire direction. As the spacing increases each grating lobe may be divided into two grating lobes because the array represents a plane of symmetry. Thus, 4 grating lobes exist but a pair in each hemisphere.

lobe has the same energy level as the main lobe.

$$\epsilon(\varphi_{GL},\varphi_0) = N + 2\sum_{i=1}^{N-1}(N-i) = N^2 \tag{2.26}$$

For UWB signals the approximate equality does not hold anymore and the energy is reduced. As the bandwidth increases the energy decreases further. Ultimately the bandwidth reaches a level for which $\Re\left[R_{bb}\left(\frac{i}{f_c}\right)\right] = 0$ for all integers $i \geq 1$. Then the grating lobe fully disappears and the beampattern energy is:

$$\epsilon(\varphi_{GL},\varphi_0) = N \tag{2.27}$$

This is shown in Fig. 2.13 that shows the narrowband beampattern with 2 pairs of grating lobes and the UWB case where the grating lobes are fully suppressed.

Now the transition between the narrowband and UWB case is studied in more detail. Observing (2.25), it can be noticed that the energy of the grating lobe depends effectively only on three variables. The number of elements N, the centre frequency of the signal f_c, and on the signal waveform and bandwidth which is reflected by the $R_{ss}(\tau)$. The impact of these will be investigated here.

The impact of the number of elements is studied in Fig. 2.14. Fig. 2.14 plots the energy of the

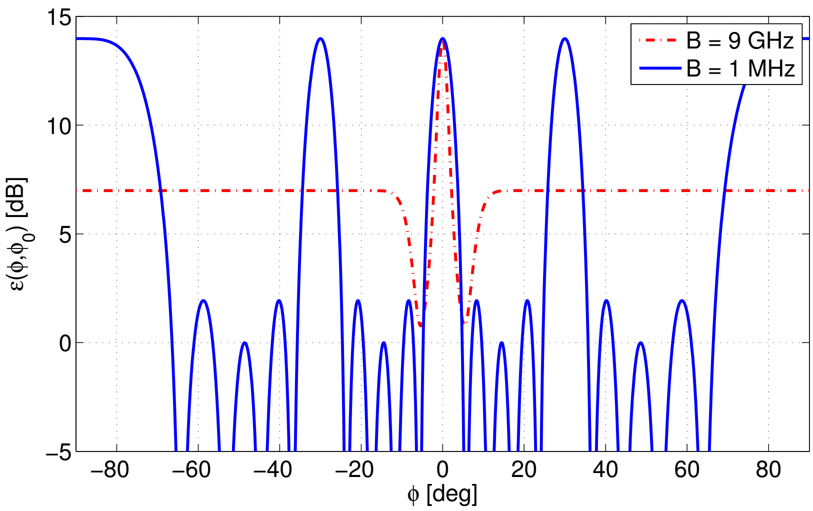

Figure 2.13: The example beampattern for 5-element antenna array excited by Gaussian pulse modulated at centre frequency of 6 GHz. The array spacing is 10 cm. © 2012 IEEE. Reprinted, with permission, from our work [52].

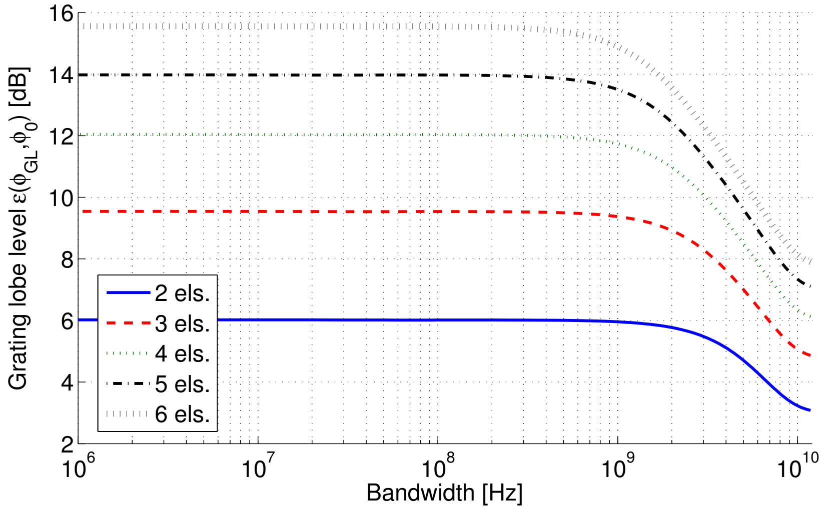

Figure 2.14: The energy level of grating lobe for arrays with variable number of elements. The centre frequency $f_c = 6$GHz and the baseband pulse $b(t)$ is Gaussian. The element spacing is 10 cm but as noted in the text it is irrelevant for the grating lobe energy for $d > \lambda_0$. © 2012 IEEE. Reprinted, with permission, from our work [52].

grating lobe in the beampattern according to (2.25) for a variable number of elements. The different levels for narrowband and UWB cases correspond to what was expected according to (2.26) and (2.27), and this observation is neither surprising nor very important.

The first important conclusion is the observation of the bandwidths for which the grating lobe energy begins to drop. This bandwidth decreases with the increasing number of elements. The explanation of this is the same as for the dependency of the bandwidth limit for the use of array factors. As the number of elements increases, (2.25) considers $\Re\left[R_{bb}\left(\frac{i}{f_c}\right)\right]$ with increasing values of i. Thus the approximation used for (2.26) stops being valid for lower bandwidths.

The second important observation is the fact that the bandwidth for which the energy achieves the UWB level of $\epsilon(\varphi_{GL},\varphi_0) = N$ is the same regardless of the number of elements. This is due to the fact that this corresponds to a bandwidth for which $\Re\left[R_{bb}\left(\frac{1}{f_c}\right)\right] \approx 0$. In other words, the bandwidth for which the pulses received by two adjacent antenna elements from the direction of the grating lobe effectively do not overlap in the time domain. This means that if the full suppression of grating lobes is required, the minimum required bandwidth cannot be changed by the number of elements.

The second factor that is evaluated is the impact of centre frequency. This is explored in

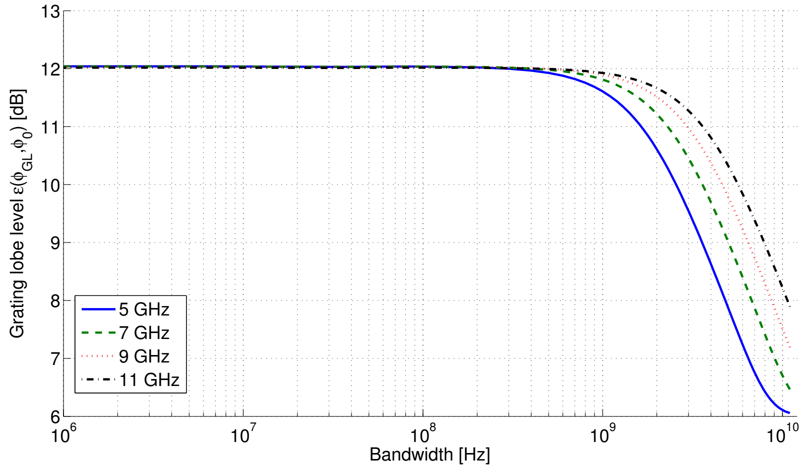

Figure 2.15: The energy level of grating lobe for arrays with variable centre frequency for a 4 element array. The baseband pulse $b(t)$ is Gaussian at centre frequency of 6 GHz. The element spacing is 10 cm but as noted in the text it is irrelevant for the grating lobe energy for $d > \lambda_0$. © 2012 IEEE. Reprinted, with permission, from our work [52].

Fig. 2.15 and in 2.16. In Fig. 2.15 can be seen that the bandwidth required to suppress the grating lobes increases with the centre frequency. This is explored in more detail in Fig. 2.16 where the bandwidth for grating lobe suppression by 3 dB compared to the narrowband case is plotted as a function of the centre frequency. It is shown that the bandwidth increases linearly with the centre frequency. The small discrepancies from the perfect linear fit in Fig. 2.16 are noted but are believed to originate from the fact that the numerical evaluation was performed at discrete bandwidth steps.

The reasons for the linear dependency can be explained by the analysis of (2.25). For a full suppression, it is needed that $\Re\left[R_{bb}\left(\frac{1}{f_c}\right)\right] \approx 0$ as stated in previous paragraph. As f_c increases, the term $\frac{1}{f_c}$ is reduced requiring the autocorrelation function to 'disappear' faster. In other words, the signal bandwidth needs to increase proportionally with f_c. Thus the conclusion is that **the relative bandwidth required for grating lobe suppression is independent of the centre frequency**. This is a very important conclusion especially if one would want to exploit the grating lobe suppression for antenna arrays for 60 GHz systems. It can be concluded that such approach would not be feasible simply because, as can be seen e.g. in Fig. 2.13, the relative bandwidth required for full suppression of grating lobes exceeds 100%, which is not feasible for a 60 GHz system.

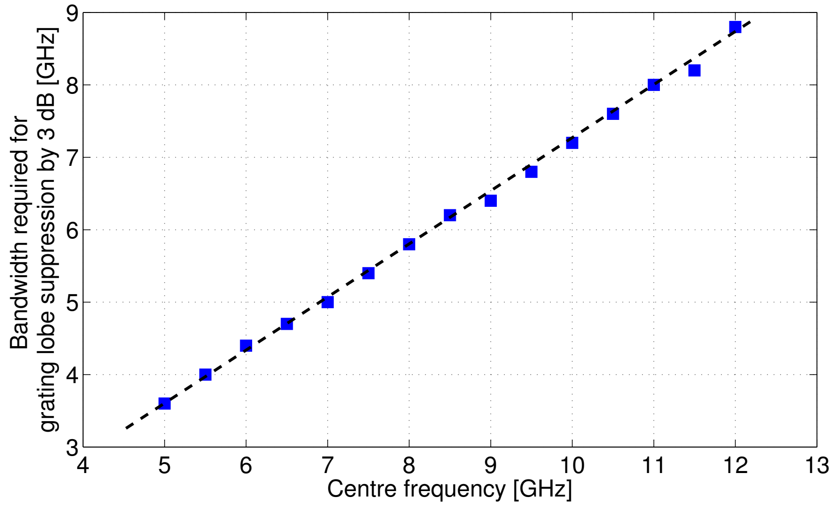

Figure 2.16: The dependency of the bandwidth required for grating lobe suppression by 3 dB as a function of centre frequency, as can be read in Fig. 2.15. © 2012 IEEE. Reprinted, with permission, from our work [52].

Finally, the impact of pulse shape has been studied and is presented in Fig. 2.17. As can be seen, the impact of pulse shape is almost negligible, which is not surprising because as mentioned in the preceding section the length of autocorrelation function $R_{bb}(\tau)$ is given more by the 10dB bandwidth of the baseband pulse $b(t)$ than by its specific waveform, which results in similar grating lobe levels for all pulses.

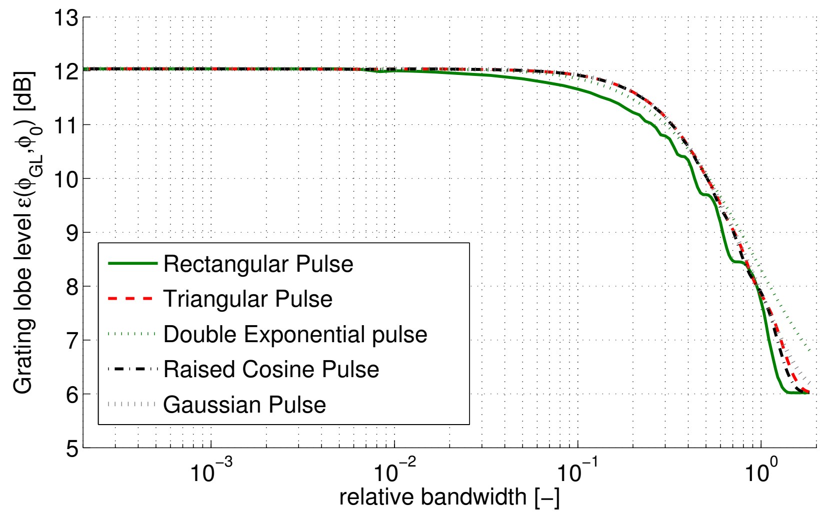

Figure 2.17: The energy level of grating lobe for arrays with variable waveform of the baseband pulse $b(t)$. This figure shows that the bandwidth required for grating lobe suppression is practically independent of the pulse waveform. © 2012 IEEE. Reprinted, with permission, from our work [52].

To conclude, this section studied the conditions for suppression of grating lobes in UWB arrays. The section confirms the conclusions of previous works that UWB arrays can suppress grating lobes. It also explores how the grating lobe suppression increases with increasing bandwidth. It is concluded that to achieve full suppression of grating lobes, the relative bandwidth of the signal has to be above 100% and it is independent on the type of pulse and the number of elements in the array. This effectively means that most of UWB systems do not have sufficient bandwidth to exploit the grating lobe suppression in sparse arrays. For instance, the regulations in EU, Japan, and Korea do not allow relative bandwidth of 100%, as discussed in chapter 1.

2.3 Conclusions Antennas and Antenna Arrays

In this chapter, the UWB antennas and Antenna Arrays were discussed. The antenna section introduced antenna impulse response as a full time-domain descriptor of UWB antennas and its impact on distortion of transmitted signals was discussed. The understanding of the nature and of the impact of the antenna impulse response will be important in chapter 3 where the concept of antenna impulse responses will be used to simplify the IEEE802.15.4a model of UWB channel impulse response [21].

In the section about antenna arrays, the specific properties and descriptors of UWB antenna arrays were introduced. It was explained why the classical narrowband descriptors are not suitable for the description of UWB arrays. Additionally, the property of sparse UWB arrays that suppress grating lobes is discussed. The bandwidth limit for the use of narrowband array descriptors and the bandwidth required for the grating lobe suppressions for UWB arrays were presented. The understanding of these limits will be useful especially in chapter 7 where UWB MIMO systems are discussed and the understanding of array properties and the selection of the correct descriptor will be of essence.

The main conclusion of this chapter is that it was shown that for UWB systems with signal bandwidths below 1 GHz, it is possible to use the standard narrowband descriptors without any significant error compared to the results obtained when the general UWB descriptors are used. This simplifies the handling of many UWB systems such as the practical WiMedia system.

CHAPTER 3

Ultrawideband Wireless Channel

This chapter introduces wave propagation in the UWB wireless channels. The understanding of the properties of wave propagation in wireless channel are essential for the understanding of the limitations of modulation schemes for UWB wireless communication, and for the design of superior schemes as will be shown in the remaining chapters. This chapter starts with the description of the path-gain, which is the most important large scale channel parameter in wireless channel models. The impulse response of wireless UWB from the IEEE802.15.4a channel model [21] is then critically studied and a new corrected model of the channel impulse response is suggested. Finally, the small scale fading of the wireless UWB channel is explored in great detail as this will be of use in chapters 4-7.

3.1 Path-Gain

The most significant large scale channel property is the path-gain/loss. This defines the expected received energy and is therefore one of the main parameters defining the transmission range of a wireless communication system because it can directly be used to estimate the receiver's SNR and/or Bit-Error-Rate (BER). The path-gain, G_p, is typically defined as follows [53], [54]:

$$G_p(r,f) = E\left\{\int_{f_c-B/2}^{f_c+B/2} |H(r,f)|^2 \mathrm{d}f\right\} \tag{3.1}$$

where r represents range; f stands for frequency; f_c is the centre frequency of the channel; B is the channel bandwidth; and $H(r,f)$ represents the transfer function of the wireless channel. Path-gain and path-loss are fully equivalent quantities and their relationship is an inversion. As a result, path-gain decreases with range whilst path-loss increases. In this chapter, we choose path-gain because the fact that the integration in (3.1) is not in the denominator will prove useful in some subsequent investigations, but the conclusions are fully equivalent.

Eq. (3.1) sums the energy carried by all multipath components. As a result, in indoor environments the path-gain will be typically larger than in free-space where path-gain decreases with the square of range [8]. The mean $E\{\bullet\}$ in (3.1) reflects the fact that the superposition of multipath components can be constructive or destructive which varies the composite received energy. This effect is called 'fading' and is studied in detail in section 3.3 of this chapter. For path-gain measurements, averaging over a local area is performed to eliminate the impact of fading.

Another conclusion from (3.1) is that the path-gain is a function of range and frequency. Whilst most researchers typically agree on the range dependency of the channel's path-gain, the frequency dependency of path-gain in a UWB channel is a more controversial topic because it strongly reflects the impact of antennas. The IEEE802.15.4a channel model [21] defines path-gain as a product of range and frequency [21]:

$$G_p(r,f) = G_p(r) \cdot G_p(f) \tag{3.2}$$

Both dependencies will be discussed in separate subsections.

3.1.1 Path-gain - Range Dependency

The distance part of the expression (3.2) can be modeled with the conventional formula known for narrowband wireless propagation [21]:

$$G_p(r)|_{dB} = G_0|_{dB} - 10n \cdot log_{10}\left(\frac{r}{r_0}\right) \tag{3.3}$$

where $G_0|_{dB}$ represents the path-gain in dB at reference distance r_0, r is the range and n is path-gain coefficient. In the IEEE802.15.4a channel model, the choice of r_0 is 1 m [21].

The value of the path-gain coefficient n depends on the environment and on the condition Line-of-Sight (LOS) or Non-Line-of-Sight (NLOS). For LOS free space, $n = 2$ which is also a path-gain coefficient applicable when individual rays are observed. As shown in (3.1) the path-gain is defined as a sum over all multipath components. Thus, for a dense multipath indoor environment the actual path-gain is higher than in free space, in other words the path-gain coefficient is typically lower than 2. Its actual value depends on the type of environment, its geometry and the physical properties of the scatterers and reflectors. For instance, an industrial environment with large number of metallic scatterers differs from a residential area. Furthermore, there is an impact of the relative positions of the transmitter and receiver to walls and scatterers. As a result, reported values of path-gain coefficient from different reports may vary significantly as illustrated below.

In **office areas**, the value of the path-gain exponent varies between measurement sets reported by various researchers. For the LOS scenario, the following results are reported: 1.9 in [55] or 1.3 in [56]. For the NLOS scenarios, the reported values are: 3.6 in [55] or 2.3-2.4 in [56].

The variations between the individual measurements can be explained with results from [57] - [59], where **residential areas** were investigated and it was found that the path-gain exponent, n, is in fact a Gaussian random variable with standard deviation σ_n. References [57]-[59] propose to use n = 1.7 with standard deviation 0.3 for the case of LOS and n = 3.5 with standard deviation 0.97 in the case of NLOS.

The random nature of the path-gain coefficient, n, as well as G_0 is generally accepted and mentioned in the IEEE802.15.4a UWB channel model [21]. If the random nature is considered in simulations, the computational complexity increases, which removes one of the main advantages of empirical models over complex deterministic models (ray-tracing). Henceforth for the sake of low computational complexity, the IEEE802.15.4a UWB channel model [21] proposes values for path-gain parameters as summarised in Table 3.1.

Environment	n	$G_0[dB]$
Office LOS	1.63	-35.4
Office NLOS	3.07	-57.9
Residential LOS	1.79	-43.9
Residential NLOS	4.58	-48.7
Industrial LOS	1.2	-56.7
Industrial NLOS	2.15	-56.7
Outdoor LOS	1.76	-45.6
Outdoor NLOS	2.5	-73.0

Table 3.1: path-gain parameters according to IEEE802.15.4a channel model [21]

3.1.2 path-gain - Frequency Dependency

The frequency dependency of path-gain in UWB wireless channels is a topic well studied. It often depends to what extent the antennas are included in the channel. In [60], the waveform of a pulse transmitted in free space between two antennas is studied. It is shown that the waveform does not change as the distance increases. As a result, [60] argues that the propagation itself is not frequency selective and that the frequency selectivity is caused by the antennas. Furthermore [60] explores the Friis formula for power spectral density at the receiver $S_R(r,f)$ for free space [60]:

$$S_R(r,f) = S_T(f) \cdot G_T(f) \cdot G_R(f) \cdot \left(\frac{c}{4\pi r f}\right)^2 \tag{3.4}$$

where $S_T(r,f)$ is the transmitted power spectral density; $G_T(f)$ and $G_R(f)$ represent the gains of transmit and receive antennas.

In (3.4), the antenna gains are presented as a function of frequency. Reference [60] argues that the standard assumption of path-gain $G_p(f) \propto f^{-2}$ is valid for the assumption of constant gain of antennas $G_T(f) = G_T$ and $G_R(f) = G_R$. This is not always true for UWB antennas. In fact, (3.4) can be rewritten by means of affective apertures $A_{eT}(f)$, $A_{eR}(f)$ as [60]:

$$S_R(r,f) = S_T(f) \cdot A_{eT}(f) \cdot A_{eR}(f) \cdot \left(\frac{f}{rc}\right)^2 \tag{3.5}$$

If it is assumed that the effective aperture of antennas is constant, i.e., $A_{eT}(f) = A_{eT}$ and $A_{eR}(f) = A_{eR}$, then (3.4) yields a completely different frequency dependency of path-gain $G_p(f) \propto f^2$.

These observations make the frequency dependency of path-gain quite complex. As pointed out in [8], the gain of practical antennas for UWB communication is neither constant nor is their effective apperture constant. As a result, the frequency dependency for free space caused by the antennas will be somewhere between $G_p(f) \propto f^2$ and $G_p(f) \propto f^{-2}$. In a practical multipath channel, this frequency dependency is experienced individually by each multipath because of the angular variation of antenna gain.

Furthermore, the assumption that propagation itself is frequency independent is valid only for direct rays. In [61], the physical propagation of individual rays is studied and it is shown that, if the antennas are excluded the path-gain of the i-th ray, $G_{p,i}(f)$, depends on the physical propagation experienced by the ray [61]:

$$G_{p,i}(f) \propto f^{2\alpha(i)} \tag{3.6}$$

The frequency dependence factor $\alpha(i)$ depends on the physical mechanisms that are applicable to the i^{th} ray. Table 3.2 from [61] summarises the frequency dependencies for typical physical mechanisms.

Physical Mechanism	Frequency Dependence Factor α
Line of sight	0
Reflection	0
Diffraction from smooth or flat surface	0
Diffraction by edge	-0.5
Diffraction by corner or tip	-1
Diffraction by axial cylinder face	0.5
Diffraction by broadside of a cylinder	1

Table 3.2: Frequency selectivity for different diffraction mechanisms according to [61]

In a summary, there is a frequency dependency of the path-gain for UWB channels. This is given by the combination of antenna effects (frequency and angular dependency of antenna gain) and physical propagation. These mechanisms are well understood and can be implemented in a deterministic channel model. However, for an empirical model a 'typical' scenario is taken into account by the IEEE802.15.4a UWB channel model [21] to provide a low-complexity dependency:

$$G_p(f) \propto f^{\kappa} \tag{3.7}$$

where κ depends strongly on the propagation scenario. The measured values for various environments are listed in Table 3.3 based on data taken from [54].

Environment	κ for LOS	κ for NLOS
Residential	-1.12±0.12	-1.53±0.32
Office	-0.03	-0.71
Industrial.	+1.103	+1.427
Outdoor	-0.12	-0.13

Table 3.3: Frequency dependency coefficient κ according to [21]

3.2 Channel Impulse Response

The knowledge of the channel impulse response is important for the design of a robust wireless communication system. For instance, energy carried by multipath components can contribute to inter-symbol interference and it determines the frequency selectivity of a wireless channel. The standard assumption is to model the channel impulse response as a sequence of Dirac impulses [8] but it is important to know the statistics of the wireless channel for the deployment scenario, i.e., the number of multipath components, the mean delay between the components, and the attenuation coefficient etc. In this section, we firstly introduce the channel impulse response adopted by the IEEE802.15.4a channel model [21]. This is later critically discussed and a correction is suggested in order to integrate the impact of the antennas.

3.2.1 Impulse Response According to IEEE802.15.4a

The IEEE802.15.4a channel model recommends the Saleh-Valenzuela model that defines the rays arriving in clusters. As a result, the channel impulse response is given as [62]:

$$h(t) = \sum_{l=0}^{\infty}\sum_{k=0}^{\infty} \alpha_{kl} e^{j\theta_{kl}} \delta(t - T_l - \tau_{kl}) \tag{3.8}$$

where index l stands for the cluster number, index k stands for ray number in the l-th cluster. Accordingly, index T_l is the cluster arrival time and index τ_{kl} relates to the ray delay in the l-th cluster. α_{kl} represents the ray amplitude and θ_{kl} its phase.

The cluster arrival times are given by the Poisson Probability Distribution Function (PDF) [21]:

$$p(T_l|T_{l-1}) = \Lambda e^{-\Lambda(T_l - T_{l-1})}, \qquad l > 0 \tag{3.9}$$

$T_0 = 0$ by definition, for modelling it corresponds to the delay of the direct path for LOS or to the delay of the shortest path for NLOS. Λ is a parameter of the Poisson PDF.

For the arrival of rays within a cluster, the IEEE802.15.4a channel deviates from the original Saleh-Valenzuela model and suggests a mixture of two Poisson processes [21]:

$$p(\tau_{kl}|\tau_{(k-1)l}) = \beta\lambda_1 e^{-\lambda_1(\tau_{kl} - \tau_{(k-1)l})} + (1-\beta)\lambda_2 e^{-\lambda_2(\tau_{kl} - \tau_{(k-1)l})}, \quad k > 0 \tag{3.10}$$

$\tau_{0l} = 0$ by definition.

This high number of multipath components in the model of channel impulse response caused by the fact that for a UWB channel, the immense bandwidth allows resolution more multipath components.

The mean energy of a cluster, Ω_l, has an exponential decay [21]:

$$10\log(\Omega_l) = 10\log(e^{-T_l/\Gamma}) \tag{3.11}$$

where Γ is a model parameter specific for the deployment scenario. The total energy of all clusters (sum of Ω_l) is given by the total path-gain as specified in (3.1). The mean power delay profile of individual rays also follows an exponential decay with a model parameter [21]:

$$E\left\{|\alpha_{kl}|^2\right\} = \Omega_l \frac{1}{\gamma_l[(1-\beta)\lambda_1 + \beta\lambda_2 + 1]} e^{-\tau_{kl}/\gamma_l} \tag{3.12}$$

Reference [21] notes that the γ_l that might depend on the cluster number l and that the normalisation in (3.12) is only approximate.

3.2.2 Impact of Antenna Impulse Response in Free Space

The IEEE802.15.4a channel model specifies the set of model parameters $\Lambda, \lambda_1, \lambda_2, \Gamma$, and γ_l for various environments. However, our work [63], [64] point out some fundamental errors in the assumption that the Saleh-Valenzuela model from (3.8) is a suitable descriptor of the UWB channel. Firstly, it is pointed out that the mean delays between rays given by the coefficient λ_1 correspond to a path difference of 10-15 cm. These path loss differences might be justifiable for the reflected rays but there seems to be no physical reason for them for the direct path. Secondly, the model does not consider the impulse response of the antennas (e.g. [31]) that are manifested in the channel measurements. Based on these discrepancies an alternative explanation is offered.

In [63] we begin with the hypothesis that the clusters in the channel impulse response are not individual random rays but they are manifestation of antenna impulse responses. Quite simply, antennas are spatial filters. A communication between two antennas in free space, with one direct path only, can be modelled as a band-pass filter. Thus an impulse response of such a channel will correspond to an impulse response of a bandpass filter which explains the peaks in the cluster.

In narrowband channels, it is common to use a transformation into the equivalent baseband channel. Many UWB measurements, including the ones used for the IEEE802.15.4a channel model [21], do not use this transformation. One justification of that is the fact that baseband pulses have been the initial waveforms considered for UWB communications see e.g. [8],[65]. For such wideband baseband signals the channel transformation into baseband does not provide the same advantage as in the narrowband systems because an equivalent transformation would have to be applied on the signals themselves. It is noted, though, that the baseband transformation is well suited for some other UWB signals. All bandpass signals, such as OFDM signals, can benefit from the same advantages of baseband transformation as the narrowband systems.

To confirm the hypothesis that multiple rays in the IEEE802.15.4a channel model [21] represent a manifestation of the anntenna impulse responses, in [63] we use a commercial fullwave simulation software to determine the antenna impulse response of a discone antenna using the

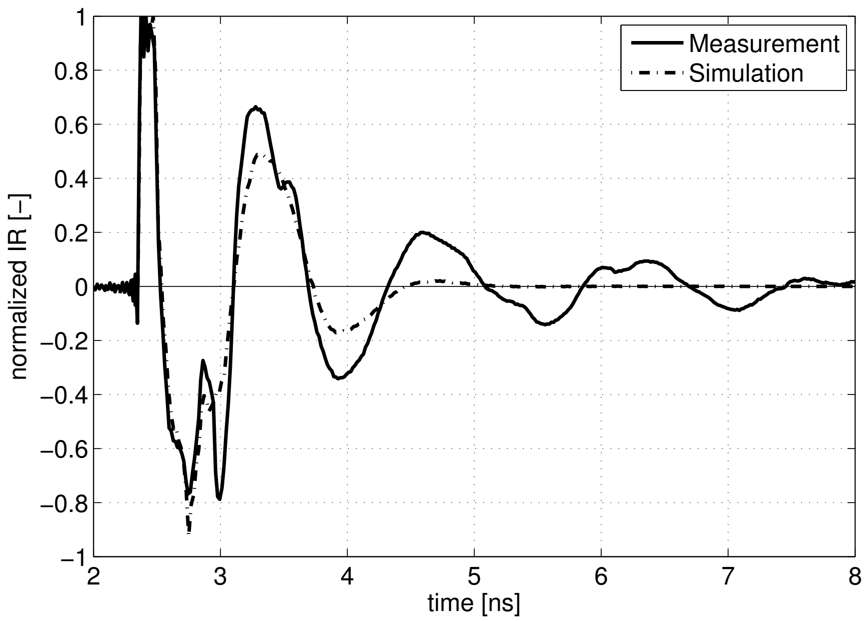

Figure 3.1: Simulated and measured normalised impulse response of a single path channel, the measurement bandwidth spans from 3 - 20 GHz and transformation into the equivalent baseband was not used

algorithm introduced in [66]. The antenna impulse response for the transmit and the receive case then models the ideal free space channel with two discone antennas, as described in section 2.1. This result is compared to a measurement of the same antennas in an aneachoic chamber. The resulting impulse responses are shown in Fig. 3.1. (If the framework from chapter 2.1 is used, Fig. 3.1 effectively represents the $I_L(t)$ in (2.5).)

From Fig. 3.1, firstly, a good agreement of theory and measurement can be observed. The small discrepancy can be attributed to simulation errors and non-ideal measurement conditions. Secondly, even though there is only one ray present in the measurement and simulation, the channel impulse response does not resemble a single Dirac impulse, but it resembles well a manifestation of an impulse response of a bandpass filter. Therefore, Fig. 3.1 supports the hypothesis that ray clusters are actually a manifestation of the antenna impulse responses.

It is believed that the reason why the individual non-zero values within a cluster are often attributed to individual multipath components, arises from the insufficient bandwidth of channel measurements (often less than 3 GHz [54]), and also because the concept of antenna impulse response is not yet used as a standard antenna descriptor, and the antenna impulse response is not manifested in narrowband systems that use the equivalent baseband representation of the channel.

Additionally, the assumption that rays within a cluster originate from the antenna impulse response can also explain the differences among measurements carried out by different research groups, simply because they used different antennas. To illustrate this, the simulated impulse response of the free space channel for three different types of UWB antennas is presented in Fig. 3.2 to explore the effect of antenna type. In terms of the framework introduced in section 2.1, Figs. 3.1 and 3.2 show the normalised result of (2.5).

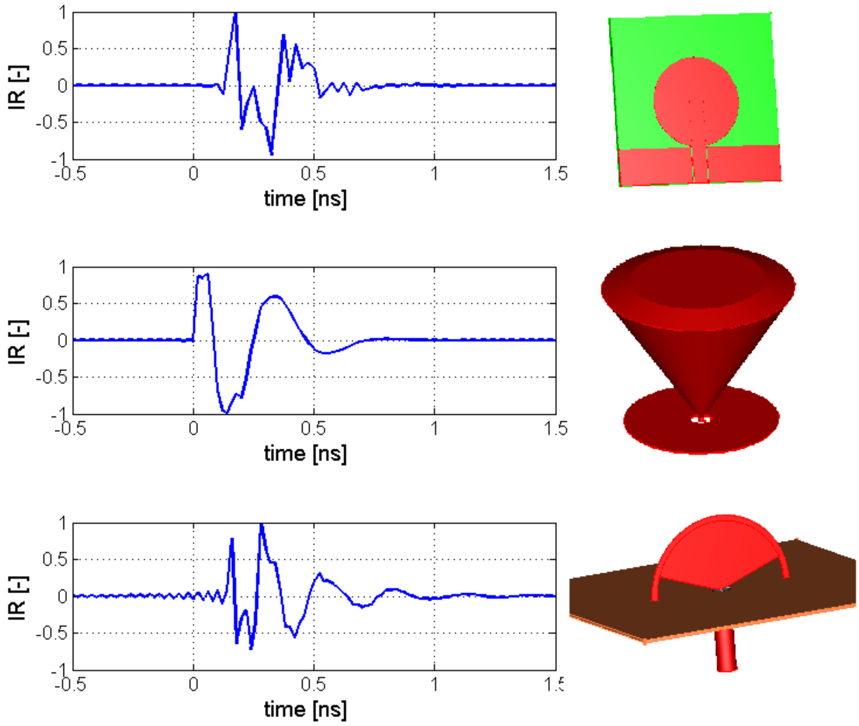

Figure 3.2: Simulated impulse response of a free space UWB channel for three different types of antennas. © 2010 IEEE. Reprinted, with permission, from our work [64].

3.2.3 Manifestation of Antenna Impulse Response in Realistic Indoor Channels

In [63], a simulation and measurement for an ideal free space channel with only one multipath was presented. Reference [64] presents measurements in a laboratory environment with several multipath components. These show that antenna impulse responses manifest themselves not only for the line-of-sight case, but for later reflected rays as well. The distance between the transmitter and receiver was chosen to be 120 cm. The experiment used discone antennas with vertical polarisation. The details about the experimental setup as well as about the plan of the laboratory can be found in appendices B and C. An example of such a measured channel impulse response is presented in Fig. 3.3. [1]

In Fig. 3.3, three detectable multipath components are highlighted. It can be seen that rays 1 and 2 are similar, except for the sign caused by the reflection in the case of ray 2. Ray 3, however, is shorter. The reason for this was obtained by an analysis of the specific channel.

[1]The channel impulse responses presented in this chapter were obtained using the Fourier transform of the complex channel transfer function measured by a VNA. Assumption that the frequency response of the channel is a Hermitian function was made.

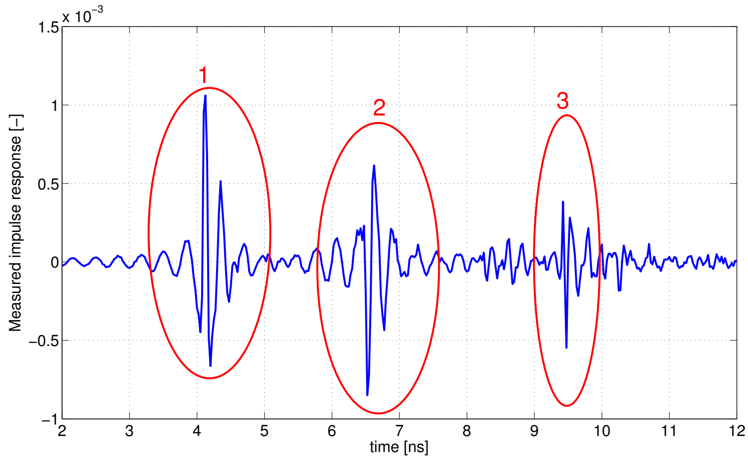

Figure 3.3: Measured channel impulse response for an example realistic wireless channel.© 2010 IEEE. Reprinted, with permission, from our work [64].

Delays of the rays were compared to real distances in the channel setup to determine the ray paths. Ray 1 is the direct path, ray 2 represents a reflection in the horizontal plane. Due to the rotational symmetry of discone antennas its shape remains the same and the sign is determined by the reflection coefficient. Ray 3 represents a ceiling reflection with an elevation angle of 60°. This is also the reason for its different waveform. As already mentioned, the antennas act as spatial filters and therefore the impulse response of such filter changes with the direction. For higher frequencies the elevation angle of the radiation maximum of a discone antenna increases, e.g. [8], [64], which impacts the waveform of the antenna impulse responses.

To confirm this claim, in [64] we simulate the antenna impulse responses (transmit and receive case) for the discone antennas for direct paths corresponding to elevations of 0° ($\theta = 90°$) and 60° ($\theta = 30°$). These are presented in Fig. 3.4. The simulated antenna impulse response for 0° is then de-convolved from ray 1 and ray 2 in Fig. 3.3 whereas the simulated antenna impulse response for 60° is de-convolved from ray 3.[2] The results are collated together to represent the channel impulse response without the impact of the antennas. This is presented in Fig. 3.5 where the channel is manifested as three Dirac impulses. This evidence supports the initial hypothesis that some clusters in the IEEE802.15.4a channel model are in manifestations of antenna impulse responses, and suggest the need for its revision.

[2]The deconvolution of antenna impulse responses was performed as a division in the frequency domain separately for the two antenna impulse responses. The two results were transformed back to the time domain and collated into Fig. 3.5. The result for deconvolution of antenna impulse response for $\theta = 90°$ is plotted for the time 0-7.8 ns. The times after 7.8 ns are for the deconvolution of antenna impulse response for $\theta = 30°$.

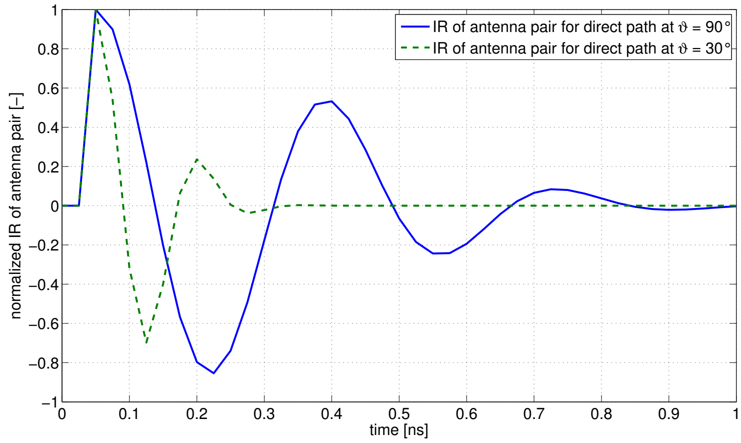

Figure 3.4: Manifestation of antenna impulse response of small discone antenna for two elevation angles. © 2010 IEEE. Reprinted, with permission, from our work [64].

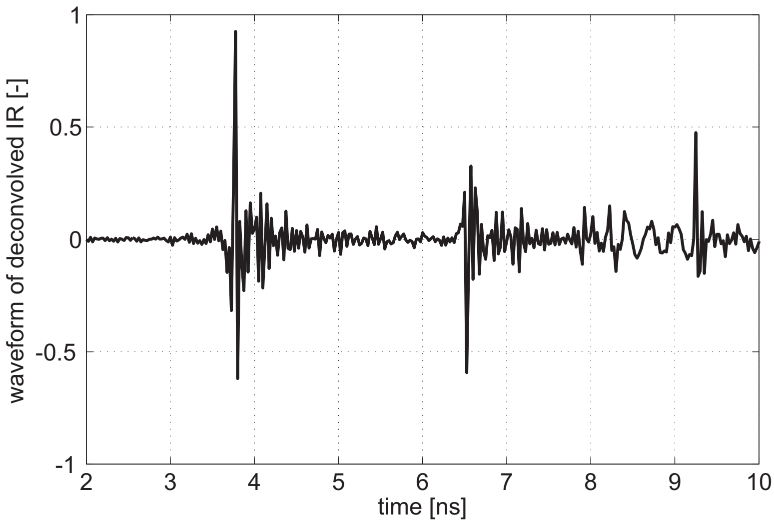

Figure 3.5: Channel impulse response after de-convolution of antenna impulse responses.© 2010 IEEE. Reprinted, with permission, from our work [64].

3.2.4 New Model for Impulse Response of the UWB Channel

Further comparison of Fig. 3.5 with Eq. (3.10) defining the probability of ray arrival in clusters reveals the reason for the use of the mixture of two Poisson processes in Eq. (3.10), whilst the standard Saleh-Valenzuela model for narrowband systems uses a single Poisson process [62]. For the indoor office environment and LOS measurements the IEEE802.15.4a model suggests $\lambda_1 = 0.19[1/\text{ns}]$ and $\lambda_2 = 2.97[1/\text{ns}]$. These values correspond to a mean ray arrival delay of 5.26 ns and 0.33 ns respectively. Using the data presented above, the Poisson process with mean ray arrival delay of 0.33 ns can be linked to the antenna impulse response (see Fig. 3.3) whereas the second Poisson process corresponds to the actual multipath propagation (see the Fig. 3.5). The same can be shown for the parameters for the outdoor environment, indoor residential and indoor industrial environments as listed in [21]. In other words, there are ray clusters in the model of antenna impulse response, but the number of rays in each cluster is significantly lower and it corresponds to the original Saleh-Valenzuela model. The difference is that for UWB bandwidths without baseband transformation, the antenna impulse response is resolvable.

This leads to a proposal of the following change to the model of channel impulse response of UWB channels:

$$h(t) = \sum_{l=0}^{\infty} \sum_{k=0}^{\infty} h_{kl}(t) * \alpha_{kl} e^{j\theta_{kl}} \delta(t - T_l - \tau_{kl}) \tag{3.13}$$

where $h_{kl}(t)$ represents the manifestation of antenna impulse responses associated with the antenna type and specific ray kl and will be discussed in more detail below; $*$ stands for convolution.

The definition of inter-cluster parameters remains the same as in Eqs. (3.9), (3.11). For the intra-cluster parameters, Eq. (3.10) is simplified as follows:

$$p(\tau_{kl}|\tau_{(k-1)l}) = \lambda e^{-\lambda(\tau_{kl} - \tau_{(k-1)l})}, \qquad k > 0 \tag{3.14}$$

where for λ, the smaller parameters out of the pair λ_1 and λ_2 offered by IEEE802.15.4a model is selected.

In (3.13) $h_{kl}(t)$, is normalised to have unit energy as the path energy is included in α_{kl}. Therefore in the framework introduced in chapter 2.1, specifically in Eq. (2.6) $h_{kl}(t)$ can be introduced as follows:

$$h_{kl}(t) = \frac{\mathbf{h}_{\mathbf{T}}^{\mathbf{T}}(\hat{\mathbf{r}}_{kl}^{TR}, \tau) \star \mathbf{R_i}(\tau_{kl}) \bigstar \mathbf{h}_{\mathbf{R}}^{\mathbf{R}}(\hat{\mathbf{r}}_{kl}^{RT}, \tau_{kl})}{\sqrt{\int_{-\infty}^{\infty} \left| \mathbf{h}_{\mathbf{T}}^{\mathbf{T}}(\hat{\mathbf{r}}_{kl}^{TR}, \tau) \star \mathbf{R_i}(\tau_{kl}) \bigstar \mathbf{h}_{\mathbf{R}}^{\mathbf{R}}(\hat{\mathbf{r}}_{kl}^{RT}, \tau_{kl}) \right|^2 \mathrm{d}\tau_{kl}}}, \qquad \tau_{kl} = t - \frac{r_{kl}}{c} \tag{3.15}$$

The parameters as well as the different convolutions $\star$ and $\bigstar$ are defined in Eq. (2.6).

According to the framework from chapter 2.1 α_{kl} yields:

$$\alpha_{kl} = \frac{1}{4\pi r_{kl}} \frac{\eta}{2cZ_{0T}Z_{0R}} \sqrt{\int_{-\infty}^{\infty} |\mathbf{h}_{\mathbf{T}}^{\mathbf{T}}(\hat{\mathbf{r}}_{kl}^{TR},\tau) \star \mathbf{R}_{\mathbf{i}}(\tau_{kl}) \bigstar \mathbf{h}_{\mathbf{R}}^{\mathbf{R}}(\hat{\mathbf{r}}_{kl}^{RT},\tau_{kl})|^2 \, \mathrm{d}\tau_{kl}}, \qquad \tau_{kl} = t - \frac{r_{kl}}{c} \quad (3.16)$$

Expressions (3.15) and (3.16) are presented here to link the antenna theory from section 2.1 and the channel impulse response. For practical applications, empirical expressions for α_{kl}, as shown in (3.11) and (3.12), or as will be discussed in subsequent subsection, are used.

So far, the new model presented in Eq. (3.13) seems more complex and less suitable for practical use in channel simulations. However, it can be further simplified, as described in the following subsection.

3.2.5 UWB Channel Impulse Response - Simplified Model for Practical Use

The first simplification of the model can be achieved if the practical dynamic range of the UWB system is considered. This dynamic range is typically around 70 dB (EIRP limit is -41.3 dBm/MHz and the noise floor is -114 dBm/MHz). As a result, rays with delays of more than 100 ns do not need to be considered. Rays with delay more than 100 ns have a path length of 30 m. A simple path loss calculation for free space at frequency of 3.1 GHz (lower end of the US FCC spectrum for UWB) yields a path-loss of 71.5 dB ($PL = (4\pi r/\lambda_0)^2$). This path loss increases for higher frequencies and whilst the antenna gain might reduce it, it does not include the reflection losses. For typical indoor environments, path lengths of 30 m correspond to multiple reflections. Such a consideration reduces the number of clusters that need to be considered. For instance, for an indoor office environment the IEEE802.15.4a suggests mean inter-cluster delay $E\{T_l - T_{l-1}\}$ of 62.5 ns, and an average of 5.4 clusters. It is apparent that for practical UWB systems there is no need to consider more than two clusters.

Furthermore, for LOS scenarios in residential areas the mean inter cluster delay is $E\{T_l - T_{l-1}\}$ reported to be 21.3 ns. The mean intra-cluster delay between rays $E\{\tau_{k,l} - \tau_{k-1,l}\}$ given by λ is 6.7 ns which is about one third of the inter-cluster delay. This suggests that the clusters actually be reduced by a sequence of rays with delay given by Eq. 3.14.

If these two points are combined, the model can be simplified into the following form:

$$h(t) = \sum_{k=0}^{K_{DR}} h_k(t) * \alpha_k e^{j\theta_k} \delta(t - \tau_k) \tag{3.17}$$

where K_{DR} is the number of rays that need to be considered given the dynamic range of the system. The value of K_{DR} is selected based on the system architecture. For instance, it is lower for a non-coherent impulse radio receiver with low dynamic range, whereas it will be larger for direct sequence Code Division Multiple Access (CDMA) with good noise suppression capabilities. The ray arrival time is then given as:

$$p(\tau_k|\tau_{k-1}) = \lambda e^{-\lambda(\tau_k - \tau_{k-1})}, \qquad k > 0 \tag{3.18}$$

For the energy of rays $E\{\alpha_k^2\}$, Eq. (3.11) can be transformed and used as:

$$E\{\alpha_k^2\} = e^{-\tau_k/\Gamma} \tag{3.19}$$

Alternatively, a path-loss estimate for a given frequency band can be employed.

Here it is noted that (3.17) remains a description of a bandpass system which is the general description of a UWB channel. $h_k(t)$ defines the properties of the antenna as a band-pass filter. As shown in section 2.1, in most practical cases the antennas do not distort the transmitted pulse because the antennas are designed for a specific type of application and for a specific type of pulse. This is valid with the exception of the inherent derivation which for modulated pulses will mainly affect the phase term $e^{j\theta_k}$ since sin-terms are turned into cos-terms and vice versa, see discussion in section 2.1. However, the signal envelope remains unchanged. In other words, the antennas in practical systems are designed in such a way that the signal is in their pass-band and is not distorted. Thus, (3.17) can be simplified as[3]:

$$h(t) = \sum_{k=0}^{K_{DR}} \alpha_k e^{j\theta_k} \delta(t - \tau_k) \tag{3.20}$$

[3]This simplification can also be seen as exclusion of the antennas so that the resulting model describes solely the wave propagation.

3.2.6 UWB Channel Impulse Response - MIMO Channels

So far, only the channel impulse response of a Single-Input-Single-Output (SISO) channel has been discussed. This section will discuss the Single-Input-Multiple-Output (SIMO), Multiple-Input-Single-Output (MISO), and MIMO channels and their impulse responses. The knowledge of the properties of such channel is important for the beam-steering algorithm discussed in chapter 7. It is known that for small spatial distance between the antennas in the MIMO systems, the number of rays or their amplitude in the channel impulse response in narrowband wireless channels does not change [67]. What changes are the delays of the individual rays in the model. The changes in the delay are related to the Angle-of-Arrival (AoA) and/or Angle-of-Departure (AoD) for individual rays and by the spacing between array elements.

Intuitively this is also applicable to the UWB channel impulse response. Here this hypothesis is tested especially observing the changes in the $h_k(t)$ as a function of displacement. Therefore, the measurements presented in Fig. 3.3 were repeated for a grid of 40×40 points spaced by 6 mm and the impulse responses were analyzed. The analysis is presented in Figs. 3.6 and 3.7.

Fig. 3.6 shows the channel impulse response for five grid points spaced by 42 mm along the x-axis of the measurement grid. The red dashed line shows that the temporal shift of corresponding rays changes linearly with the displacement and that there is almost no change in the waveform of $h_k(t)$. Fig. 3.7 then shows two time snapshots across the measurement grid and the energy of the channel impulse response at that time instances is shown (in dB scale). From the snapshots it is apparent that multipath components in Fig. 3.6 can be modelled as a plane wave propagating across the grid with no significant change in the waveform of $h_k(t)$. These two figures document that the assumption of plane waves from [67] is applicable also to UWB channels. Since, Figs. 3.6 and 3.7 do not show any significant changes in $h_k(t)$ it can be concluded that the $h_k(t)$ does not change for a small displacement of the transmitter or receiver as was shown in our work [64].

It is noted that Figs. 3.6 and 3.7 show only a single grid location. Therefore, the measurement was repeated for five more different positions in the same laboratory with the same outcome for each. The details about the position of the measurements are in Appendix C. Similar results were also obtained for the SIMO channel measurements in an office environment, which

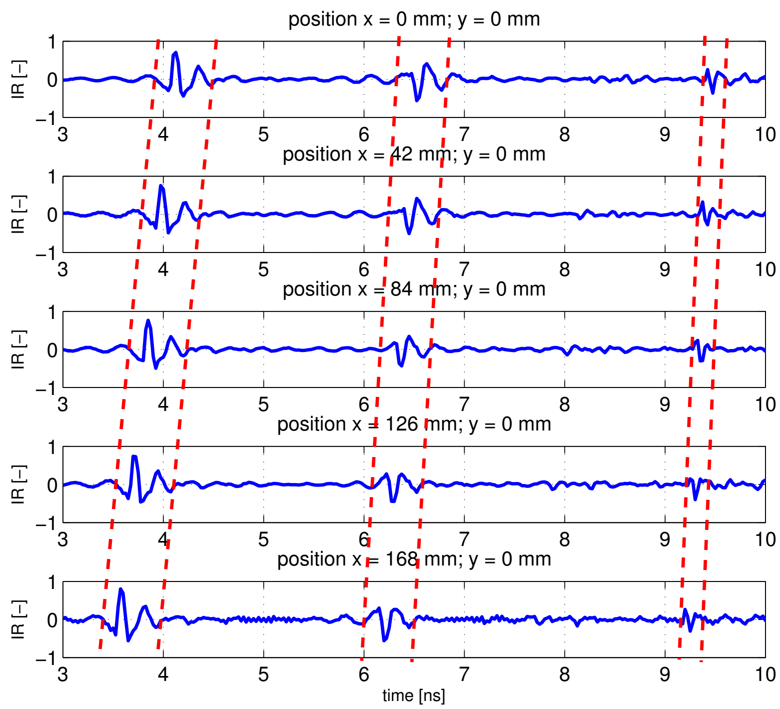

Figure 3.6: Impulse response of 5 real channels spaced by 42 mm along the x-axis demonstrating that multipath components can be approximated as planar waves and the displacement defines the changes in the multipath delays.

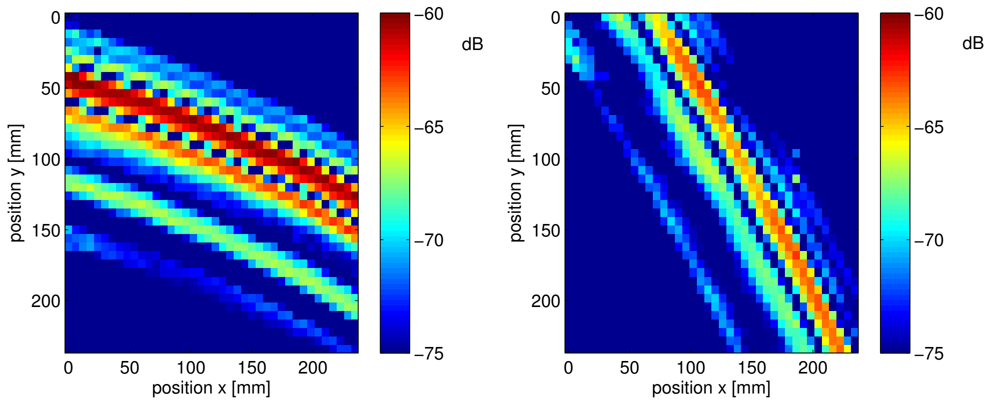

Figure 3.7: Two instant snapshots of energy of channel impulse response across the measurement grid demonstrating that multipath components can be approximated as planar waves and the displacement defines the changes in the multipath delays.

are presented in chapter 5. These additional measurements provide confidence that the plane wave assumption is valid and can be used. As a result, the channel impulse response for $h_{i,j}(t)$ between the i-th transmitter and the j-th receiver in a $M \times N$ MIMO channel can be described as:

$$h_{i,j}(t) = \sum_{k=0}^{K_{DR}} h_k(t) * \alpha_k e^{j\theta_k} \delta(t - \tau_k - \tau_{k,i,j}) \tag{3.21}$$

where $\tau_{k,i,j}$ represents the delay incurred due to the AoA and AoD of the k-th ray between the receiver and transmitter arrays and the geometry of the array compared to the case $h_{1,1}(t)$. Hence it is apparent that $\tau_{k,1,1} = 0$ for all k; otherwise the variables are the same as in (3.17).

As in the preceding section, for most practical application of (3.21), where signals have bandwidths below 1 GHz, it is possible to neglect the impact of $h_k(t)$, similarly for (3.17) and (3.20), yielding:

$$h_{i,j}(t) = \sum_{k=0}^{K_{DR}} \alpha_k e^{j\theta_k} \delta(t - \tau_k - \tau_{k,i,j}) \tag{3.22}$$

The confirmation that MIMO channels can be described using the plane wave assumption and geometrical displacements will be important for the work presented in section 7.3 where (3.22) will be used to study the performance of a low complexity beam-steerer.

3.2.7 Channel Impulse Response - Summary

This section has suggested a novel model of channel impulse response for UWB wireless channels. It is shown that the immense bandwidth of channel measurements allows us to resolve and identify the impulse response of an antenna which is a deterministic waveform. As a result, rays that were assumed random in the IEEE802.15.4a channel model are shown to be deterministic. This is useful for practical system considerations because the reduced number of independent multipaths can reduce the design complexity of communication systems.

Investigation of multiple channels in a close proximity enabled the expansion of the model of the channel impulse response into the MIMO case. General models for SISO (3.17) and MIMO (3.21) which still include the antenna impulse responses $h_k(t)$ have been presented, but it is noted that in many cases the pulse distortion can be neglected and $h_k(t)$ can be replaced by $\delta(t)$ as was discussed in greater detail in section 2.1.

3.3 Frequency Selective Fading in Wireless Channels

Frequency selective fading in a wireless channel is caused by the superposition of multipath components. As a result, the path loss of a channel may vary significantly even for a small displacement of transmitter or receiver. Consequently, the link budgets of wireless communication systems plan a fade margin to overcome this issue [8]. As will be shown in chapters 4 and 5, fading has an enormous impact on the performance of UWB systems and good knowledge of the frequency selective fading can be utilised to optimise the system performance.

The actual path-gain on a specific point is a random variable. The typical probability distribution functions suggested by the literature are: Rayleigh (no dominant line-of-sight), Rice (dominant line-of-sight) or Nakagami (combination of both suitable for dense multipath environments).

One of the major advantages of UWB wireless communications is the robustness against the impact of fading because the available bandwidth allows us to resolve individual multipath components in the time domain [8]. This is illustrated by Fig. 3.8 which shows the variation of empirical normalised channel energy, CE, (3.23):

$$CE(r,f) = \frac{\int_{f_c-B/2}^{f_c+B/2} |H(r,f)|^2 df}{E\left\{\int_{f_c-B/2}^{f_c+B/2} |H(r,f)|^2 \mathrm{d}f\right\}} \tag{3.23}$$

where the variable definition is the same as in (3.1).

The channel energy was measured within a square grid of 40 × 40 measurement points spaced by 6 mm. The measurement was performed in a laboratory environment with discone antennas and channel sounder described in detail in appendix B and the laboratory environment in appendix C. The presented data were obtained for measurement position 2). The individual points in Fig. 3.8 correspond to the same position of a receiver but different bandwidths.

As can be seen in Fig. 3.8, the variation of channel energy, CE, for UWB channels is within 1 dB while for the narrowband case it changes by up to 25 dB. This section aims to characterise the transition between fading in the narrowband and the UWB case in terms of spread and probability distribution function.

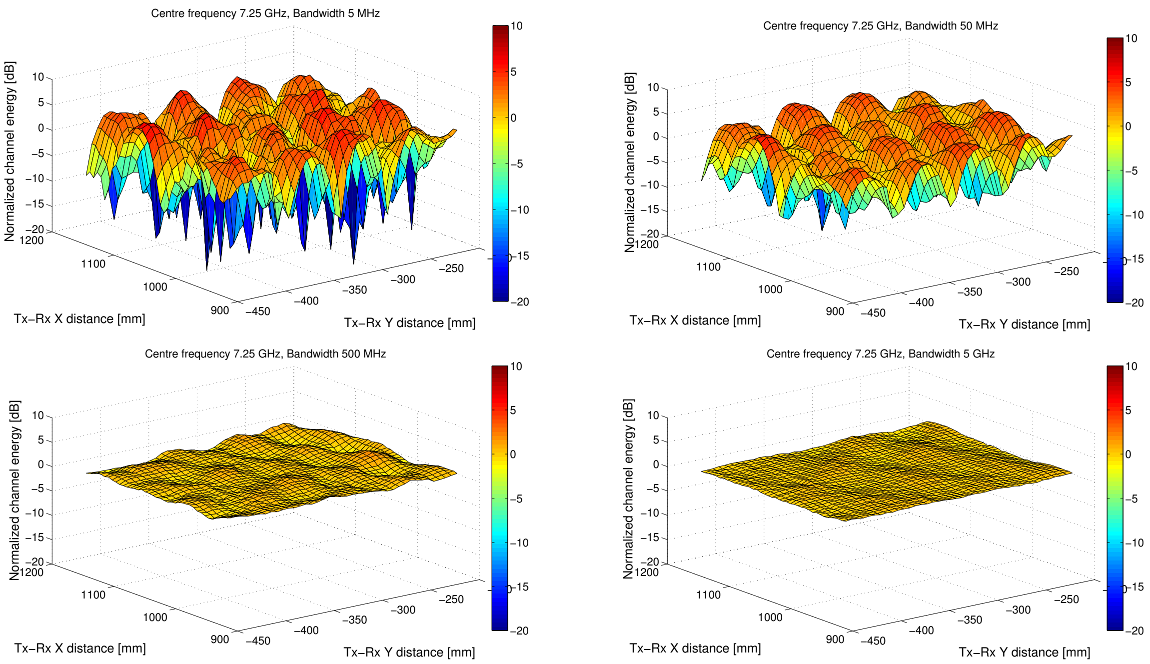

Figure 3.8: Empirical spatial variation of path loss (Eq. 3.1) normalised to a local mean for a channel with centre frequency of 7.25 GHz for bandwidths of 5 MHz, 50 MHz, 500 MHz, and 5 GHz.

Firstly, the transition in fading severity between narrowband and wideband channel, called fade depth scaling, is studied. Then the link between the type of environment and the severity of fading is discussed. Lastly, the probability distribution function of fading is discussed, we specifically focus on the change of the probability distribution function with channel bandwidth between the narrowband and UWB case.

3.3.1 Fade Depth Scaling

3.3.1.1 Fade Depth Scaling - Cause

The analytical reason for the scaling of fading with bandwidth has been published in our work [68]. Here we use a very similar approach. For the sake of readability, referencing to our paper [68] is omitted in this section. We begin the investigation of fade depth with the simplified channel model from Eq. (3.20) and perform a Fourier transformation in order to have an expression compatible with (3.23):

$$H(f) = \sum_{k=0}^{K_{DR}} \alpha_k e^{j\theta_k} e^{-j2\pi f \tau_k} \tag{3.24}$$

where all the variables are the same as in (3.20) and (3.23).

Using (3.24) in (3.23) one obtains:

$$CE(f_c) = \frac{\int\limits_{f-B/2}^{f_c+B/2} \left(\sum_{k=0}^{K_{DR}} \alpha_k^2 + \sum_{k=0,k\neq l}^{K_{DR}} \sum_{l=0}^{K_{DR}} \alpha_k \alpha_l e^{-j(2\pi f \tau_k - \theta_k)} e^{j(2\pi f \tau_l - \theta_l)} \right) \mathrm{d}f}{E\left\{ \int\limits_{f_c-B/2}^{f_c+B/2} |H(f)|^2 \mathrm{d}f \right\}} \tag{3.25}$$

$$CE(f_c) = \frac{B \sum_{k=0}^{K_{DR}} \alpha_k^2 + \sum_{k=0,k\neq l}^{K_{DR}} \sum_{l=0}^{K_{DR}} \int\limits_{f_c-B/2}^{f_c+B/2} \alpha_k \alpha_l \cos\left(2\pi f(\tau_k - \tau_l) - (\theta_k - \theta_l)\right) \mathrm{d}f}{E\left\{ \int\limits_{f_c-B/2}^{f_c+B/2} |H(f)|^2 \mathrm{d}f \right\}} \tag{3.26}$$

The integration and few operations with the trigonometric functions yield:

$$CE(f_c) = \frac{B\left[\sum_{k=0}^{K_{DR}} \alpha_k^2 + \sum_{k=0,k\neq l}^{K_{DR}} \sum_{l=0}^{K_{DR}} \alpha_k \alpha_l \mathrm{sinc}\left(B(\tau_k - \tau_l)\right) \cos\left(2\pi f_c(\tau_k - \tau_l) - (\theta_k - \theta_l)\right) \right]}{E\left\{ \int\limits_{f_c-B/2}^{f_c+B/2} |H(f)|^2 \mathrm{d}f \right\}} \tag{3.27}$$

where $\mathrm{sinc}(x) = \frac{\sin(\pi x)}{\pi x}$.

The mean operation in the denominator is performed over the same integral as in the numerator. Here, only the double sum varies for small displacements. Due to the random nature of delays between multipaths $(\tau_k - \tau_l)$ and of phase components θ_k,θ_l, Eq. (3.27) can be simplified as:

$$CE(f_c) = 1 + \frac{\sum_{k=0,k\neq l}^{K_{DR}} \sum_{l=0}^{K_{DR}} \alpha_k \alpha_l \mathrm{sinc}\left(\pi B(\tau_k - \tau_l)\right) \cos\left(2\pi f_c(\tau_k - \tau_l) - (\theta_k - \theta_l)\right)}{\sum_{k=0}^{K_{DR}} \alpha_k^2} \tag{3.28}$$

Eq. (3.28) illustrates the issue of fading. There are two terms, the one represents the mean energy of the normalised channel carried by all the multipath components. The fraction and specifically double-sum in its numerator represents the energy fluctuations caused by the superposition of band-limited signals in the time domain. For a UWB signal with large $B(\tau_k - \tau_l)$ the second term goes to zero. Hence, all multipaths are resolved and no fluctuations appear, as illustrated in the wideband plot in Fig. 3.8.

For a narrowband channel in a dense multipath environment $B(\tau_k - \tau_l) \rightarrow 0$ and the sinc-term equals one. For a small displacement change, the $(\tau_k - \tau_l)$-term in the cos-term will cause a change in amplitude. Due to the high centre frequency f_c, even a small change of $(\tau_k - \tau_l)$ can induce a phase shift of π in the cos-term. As a result, a rather large variation of the energy can occur, as shown in Fig. 3.8.

3.3.1.2 Fade Depth Scaling - Characterisation

An empirical way to express the variation of channel energy in [69]-[71] defines a quantity called fade depth FD. For a small displacement of antennas (compared to communication range) the fade depth is defined as three times the standard deviation of the channel energy (expressed in dB). According to Eq. (3.28), the fade depth is expected to be reduced in amplitude with increasing bandwidth and it is expected to approach 0 dB for an infinite bandwidth. The changes of fade depth with bandwidth is called fade depth scaling [69]-[71]. References [69]-[71] studied mainly the transitions of fade depth between the wideband and UWB channel.

References [68],[72], and [73] studied the transition from narrowband channels to UWB channels. Reference [73] studied this using the IEEE802.15.4a channel model. At the same time, our works [68] and [72] empirically explored the transition with the same conclusions about fade depth scaling as [73]. Reference [72] also introduced a three parameter model for fade depth scaling [72]:

$$FD = A + \frac{B}{1 + C \cdot BW} \tag{3.29}$$

where A, B, and C are model parameters and BW stands for bandwidth. For a visualisation, the model and its fit to empirical data is presented is presented in Fig. 3.9.

The parameter A represents the minimum fade depth for a channel with infinite bandwidth. It is typically just above 0 dB due to the fact that the small changes of path loss are inevitably associated with any spatial displacement. The parameter B represents the increase of fade depth for a narrowband channel. In terms of Eq. (3.29), it describes the contribution of the double sum for a zero bandwidth. C describes the transition between the narrowband and the UWB channel. Reference, [72] introduces another descriptor, BP(1dB), which is believed to provide better insight than C because BP(1dB) is a bandwidth for which the fade depth increases 1 dB above the minimum value for UWB channel. In other words, BP(1dB) bandwidth represents

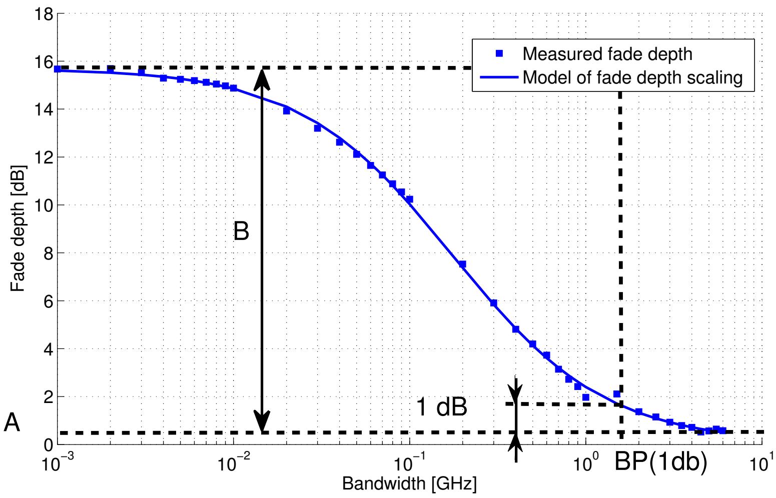

Figure 3.9: Empirical scaling of fade depth with bandwidth. © 2011 IET. Reprinted, with permission, from our work [68].

the minimum bandwidth required to resolve individual multipaths and to suppress the impact of fading on the variation of channel energy. It can be calculated as follows:

$$BP(1\text{dB}) = \frac{B-1}{C} \tag{3.30}$$

The aim of the model is to enable a comparison of fade depth scaling between different channels. For instance, our reference [68] uses these parameters to investigate the changes of fade depth scaling behaviour as a function of the volume of the room. In [72], we studied a total of 9,600 UWB wireless channels in a laboratory environment. This corresponds to six measurements of grids 40 $\times$ 40 datapoints (as shown Fig. 3.8). The details about the measurement positions in the laboratory are in appendix C. To introduce some example model values, the model parameters from (3.29) for these six measurement sets at the centre frequency of 7.25 GHz are presented in Table 3.4. As can be seen the paramaters A and B are similar for all the measurements. This helps to conclude that the fading penalty for narrowband channel compared to UWB channels is constant for an indoor channel. The bandwidth, BP(1dB), required to resolve individual multipath components is approximately 1.9 GHz for 5 out of 6 measurement positions. The change for one position is believed to be caused by increased delays between multipath components due to the distance from transmitter and receiver to the closest reflectors. The impact of these delays is studied in more detail in section 3.3.1.3.

Position ♯	TX-RX distance [m]	A [dB]	B [dB]	BP(1dB) [GHz]
1	1.93	0.21	13.7	0.85
2	1.05	0.08	15.2	1.76
3	1.26	0.03	14.4	1.81
4	1.56	0.03	15.8	2.09
5	2.36	0.19	13.7	1.99
6	2.78	0.51	13.0	1.98
average		0.18	14.3	1.75

Table 3.4: The parameters of model from (3.29) for six example data sets that differ by distance and position in the room. Centre frequency for the investigation is 7.25 GHz.

In [72] we show that the fade depth scaling model from (3.29) can be applied to a wide range of frequencies and that the model parameters A, B, and C are approximately independent of centre frequency and distance between transmitter and receiver. Apart from Table 3.4, this is also documented in Fig. 3.10 that shows the measured fade depth and model fit for three different centre frequencies. The decrease of parameter B with increasing frequency is believed to be caused by the increased path loss for higher frequencies [72]. Even though the path loss is normalised in (3.23) due to the fixed dynamic range of the measurement, with higher frequencies less individual multipath components are detected by the Vector Network Analyser (VNA). As

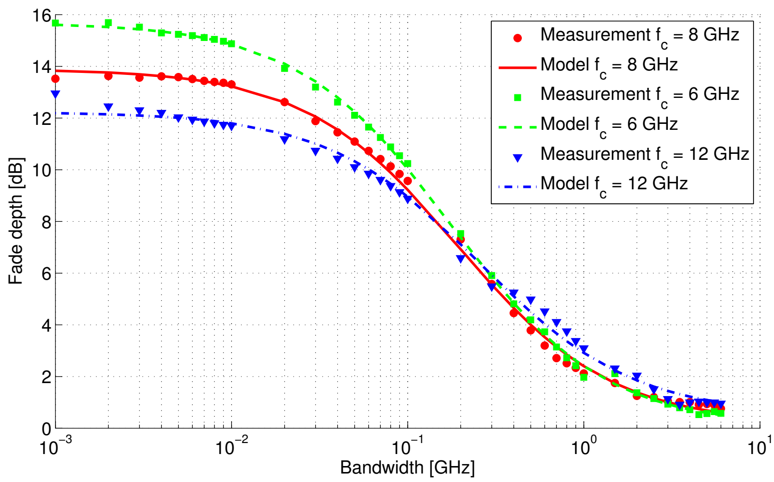

Figure 3.10: Example of empirical data and model fit from (3.30) for three different measurement conditions. © 2010 IEEE. Reprinted, with permission, from our work [72].

a result, the variation of the channel energy is expected to decrease [72].

3.3.1.3 Fade Depth Scaling in Confined Environments

The motivation for investigating how fading and fade depth changes for various volumes of confined environment is the desire to ensure robust deployment of wireless technology in environments such as airplanes [74]-[76], cars [77]-[79] or even inside computer cases [80]-[82].

Therefore in [68] we studied the impact of environment volume on fading and fade depth scaling. The investigation starts with an expression (3.28). In [68] we point out that the fade depth scaling is caused by the decrease of the sinc-term which removes the impact of the double sum (i.e. removes the impact of fading) for large products of $B(\tau_k - \tau_l)$. It is apparent that the product is the smallest for the consecutive rays, i.e. $k = l \pm 1$. Furthermore, it is expected that the delays, $\tau_k - \tau_l$, between the rays decrease as the volume of the environment decreases. Thus, the bandwidth required to resolve individual multipaths increases for a smaller volume. As a result, theoretical considerations suggest a dependency of $BP(1\text{dB})$ on volume of the environment V [68]:

$$BP(1\text{dB}) \propto V^{-\frac{1}{3}} \tag{3.31}$$

This theory was tested by means of ray-tracing simulations. A total of 21,200 environments were modelled, which were generated as follows. Each environment consisted of a rectangular box. The dimensions of the box were given as: $rand_1 \cdot b \times rand_2 \cdot b \times b$, where $rand_i$ are random variables with uniform distribution from the interval $\langle 1; 2 \rangle$. In total, 200 different pairs of $rand_1$ and $rand_2$ were generated. The length parameter, b, was swept in 106 steps from 0.5 to 30 m. The steps were logarithmically distributed in order to have similar number of data points for environments with small and large volume.

The reflection coefficient of the walls was assumed to be -0.9. This value was estimated using the assumption of a perfect electric conductor (reflection -1) with losses counting for the thin layer of fabric/plastic as a cover of the metal in a car or plane interiors. The attenuation was estimated using attenuation constants of materials presented in [8]. For the sake of simplicity, the reflection coefficient was assumed to be constant for the whole UWB range. In real scenarios, this is not the case but this simplification significantly reduces the computational effort with no significant impact on the results as for each ray its path loss is dominant over the reflection losses. Rays with up to six reflections were considered. The ray-tracer uses the tile algorithm, which uses copies of the rectangular room to determine the impulse response of the channel in the time domain. The ray-tracing algorithm is described in more detail in [83].

For the case of modelling cars, which have a significant proportion of windows, it should be noted that a different model for the reflection coefficient is required to produce meaningful results. However, modern higher-class vehicles already have metallic foils in windows to protect against heat [84]. It can be anticipated that such windows will soon appear in middle- and lower-class vehicles too. Moreover, according to Zuazola et al. [77], even standard glass represents a noticeable reflector. As mentioned above, the exact value of the reflection coefficient is not as important because, for high reflection coefficients (modulus 0.8), the power of each ray is dominated by the path loss associated with it. Therefore the approximation of the reflection coefficient as -0.9 is sufficient.

Another concern may be that real cars are not shaped as rectangular boxes, but as presented in the theoretical analytical model, the important factor is the delay between consecutive ray clusters. Intuitively, these delays depend mainly on the volume of the environment rather than on the actual shape. The fading severity is therefore believed to depend mainly on the volume of the environment.

The positions of the transmitter and receiver were selected as follows. The transmitter was placed at position $[0.25b; 0.3b; 0.6b]$. The receiver location was varied in a grid of 20×20 points spaced by 1 cm. The square was in the horizontal xy-plane. The centre of the grid was at $[0.75b; 0.7b; 0.2b]$. The inter-element spacing is approximately $\lambda_0/2$ for the highest frequency that was considered for analysis. This frequency is 12.75 GHz ($\lambda_0 = 2.35$ cm) and it corresponds to a centre frequency of 7.25 GHz and the total bandwidth of 11 GHz. The channel transfer functions were determined for the frequencies 1 - 16 GHz, then the fade depth scaling with bandwidth was studied at a centre frequency of 7.25 GHz. A single frequency of 7.25 GHz (centre frequency of the EU UWB band) was selected as our previous work [72] showed that the dependency on centre frequency can be neglected.

The investigation of fade depth scaling was performed as follows. The normalised channel energy CE for a selected bandwidth (swept logarithmically from to 1 MHz - 11 GHz) was calculated using (3.24) for each position of the receiver. Evaluation of the fade depth FD as a function of the bandwidth provided data for fit by the model from (3.29). The model parameters A and B, and BP(1dB) were recorded for each volume step. Finally, the dependency of the model parameters A, B, and BP(1dB) on the volume was explored.

The local area for energy normalisation in the denominator in (3.24) was defined by the displacement of 4 cm in both directions. Thus, the local area consisted of 81 simulation points. It is noted that the selection of the local area is essential. The maximum displacement in the local area has to be small to remove the impact of path loss. The movement by 4 cm is negligible for box size b larger than 2 m in terms of path loss, but it is significant for the smallest environment, that is, $b = 0.5$ m. On the other hand, it has to be sufficiently large to contain the full variation of the path loss caused by the multipath superposition. Selection of 4 cm for the maximum displacement of local environment appears to be a good compromise between both requirements so that the path loss is sufficiently removed from observations for a small box size b but the area remains large enough to include the full variation of the energy.

The simulation results were confirmed by real measurements. The office measurements presented in appendix C were compared to the simulation results. On top of that, two more measurements were performed in environments with volume 0.3 m^3 and 3 m^3. The environments are shown in Figs. 3.11 and 3.12. Both figures show the positioner table and the environment that was built as a wooden cage covered with metallic foil. The figures also show the position of the measurement grid which consisted of grids with 30×30 points for the 0.3 m^3 environment and 40×40 points for the 3 m^3 environment. In both cases the measurement points were spaced by 6 mm and the channel measurement was performed with the channel sounder and discone antennas introduced in appendix B.

All the simulation results and measurements were used to generate Figs. 3.13-3.15. Apart from the simulation and measurement data, Figs. 3.13-3.15 also present the Minimum Mean Square Error (MMSE) fits of the simulated data.

Several conclusions can be obtained from the figures. Firstly, it is apparent that the measured data correspond well to results obtained by the simulations which provides credibility for conclusions reached based on the simulations. Secondly, the dependencies of the individual parameters on the volume of the environment V can be studied through the MMSE fit. The fits are:

$$A = 0.96 \cdot V^{-0.171} [dB] \tag{3.32}$$

According to the theory, the minimum fade depth A should be widely independent of the volume of the environment. The dependency manifested in (3.32) may be attributed to the fact that for the small rooms, even the fixed local area of 81 points contains the impact of path loss dependency on distance, which does not occur for larger rooms.

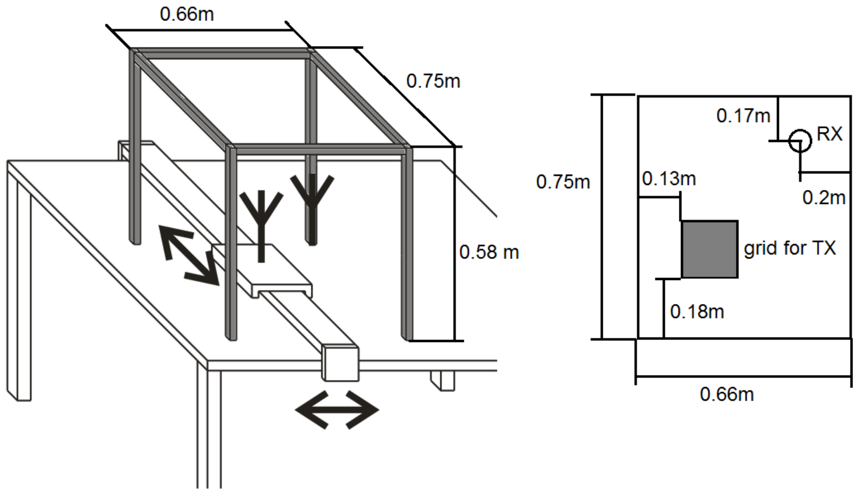

Figure 3.11: Environment with volume 0.3 m^3 for fading characterisation. © 2011 IET. Reprinted, with permission, from our work [68].

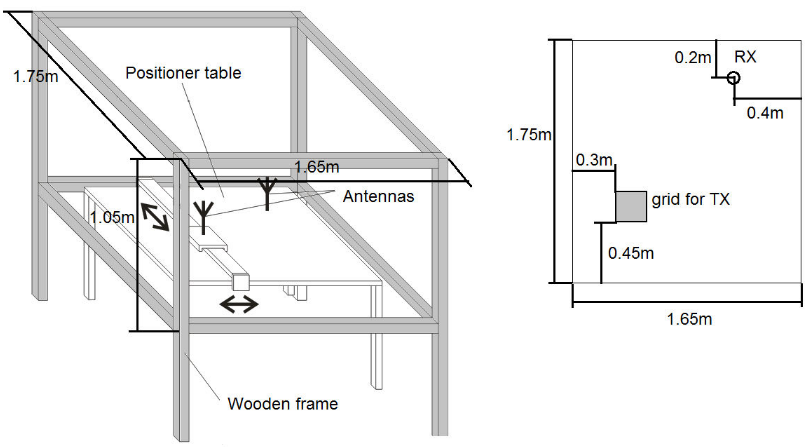

Figure 3.12: Environment with volume 3 m^3 for fading characterisation. © 2011 IET. Reprinted, with permission, from our work [68].

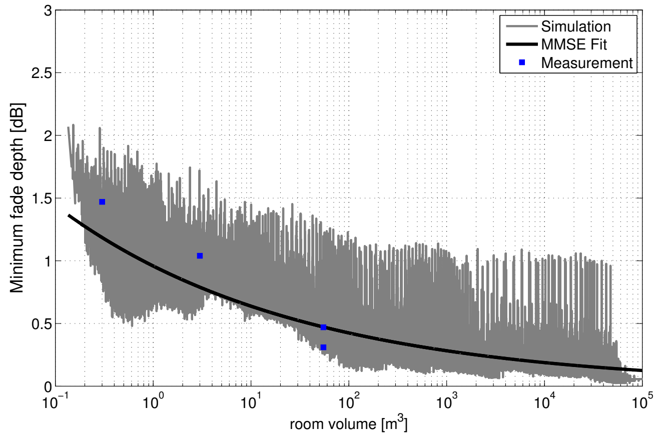

Figure 3.13: Dependency of parameter A from (3.29) on the room volume: simulation results, measurements, and the minimum-mean-square-error fit of the simulation results. © 2011 IET. Reprinted, with permission, from our work [68].

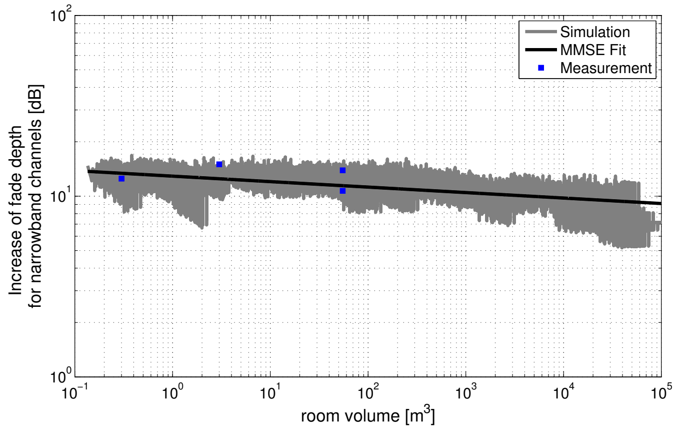

Figure 3.14: Dependency of parameter B from (3.29) on the room volume: simulation results, measurements, and the minimum-mean-square-error fit of the simulation results. © 2011 IET. Reprinted, with permission, from our work [68].

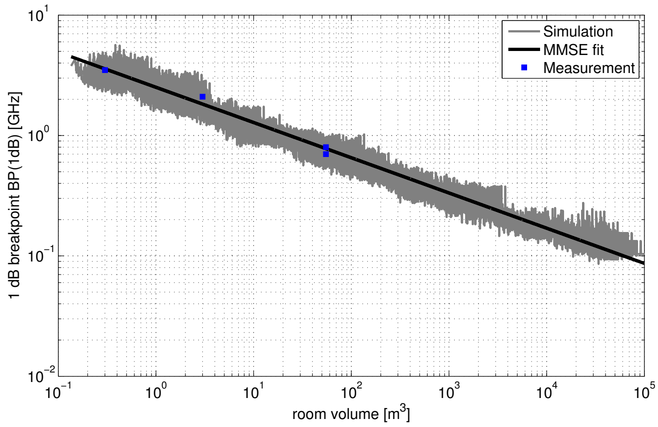

Figure 3.15: Dependency of parameter $BP(1dB)$ from (3.30) on the room volume: simulation results, measurements, and the minimum-mean-square-error fit of the simulation results. © 2011 IET. Reprinted, with permission, from our work [68].

The dependency for model parameter B yielded:

$$B = 12.9 \cdot V^{-0.029}[dB] \tag{3.33}$$

Similarly to A, the theory suggests that the difference between the fade depth for narrowband and wideband channels B should be independent on the volume. In our case presented in (3.33) the dependency is so weak that it can almost be neglected.

Finally, we observe the dependency of the bandwidth required to resolve individual multipath components (to minimise the impact of fading).

$$BP(1\text{dB}) = 2.5V^{-0.295}[GHz] \tag{3.34}$$

The theory expected a dependency $\propto V^{-\frac{1}{3}}$ (see (3.31)). The simulation results provide dependency of $\propto V^{-0.295}$ which is very close to the theoretical result and can therefore be assumed to be the confirmation of the theory.

To conclude this section, an extensive exploration of fade depth scaling revealed that the fade depth scaling is widely independent of the centre frequency and on the distance between transmitter and receiver, but there is a dependency on the volume of the environment. Smaller environments require more bandwidth to resolve individual multipath components. This bandwidth is inversely proportional to the cubic root of the volume of the environment as shown in (3.31). This conclusion was confirmed by simulations and experiments. In terms of the model for fade depth scaling introduced in Fig. 3.9, the change of the volume of the environment is manifested by the horizontal shift of the curve along the x-axis (bandwidth-axis).

This dependency also has interesting practical implications. For UWB systems the fading appears worse in smaller environment and can lead to the situation when mechanisms protecting it from fading in larger environments are not satisfactory. In [68] we use this to explain why the commercial WiMedia system designed for indoor operation fails to provide the highest data-rate of 480 Mbps in a small van [77] even though the link budget analysis suggests the opposite. More thorough discussion on the impact of fading on performance of OFDM systems will be presented in chapter 5.

3.3.2 Probability Distribution Function of Fading

The preceding section has studied the fade depth scaling in wireless channels. The conclusions of that can be used to predict the standard deviation of channel energy variations. Whilst our work in [68] shows that it is possible to link this parameter and the system performance, for many system considerations the full knowledge of the PDF of fading rather than just its spread is necessary to estimate system performance. For instance, the PDF can be used to estimate the mean expected BER of a system.

3.3.2.1 Choice of Distribution Function

To start the investigation we use (3.1) for mean path-gain to define the path-gain for a specific point in space using the mean path-gain and a non-negative random variable representing fading, $F(B)$, as follows:

$$G_p(r,f_c) = F(B)E\left\{\int_{f_c-B/2}^{f_c+B/2} |H(r,f)|^2 df\right\} \tag{3.35}$$

The fading $F(B)$ depends on the bandwidth as presented in the preceding subsection and it can posses any non-negative value. Different authors suggest various probability distributions of $F(B)$. The most popular ones are Rice, Rayleigh, Log-Normal and Nakagami. Nakagami fading is suggested by the IEEE802.15.4a model [21] and many other works, e.g. [53], [85]. Some works, e.g. [73] and [86], suggest Gamma distribution which is closely related to Nakagami. However, to our best knowledge the investigation is typically focused on finding PDF for a single bandwidth. Here, we aim to find the PDF scaleable with bandwidth so that the bandwidth of the transmitted signal can be optimised in chapter 4.

Fig. 3.16 compares empirical Cumulative Distribution Function (CDF) and PDF with CDFs of Ricean, Rayleigh, Log-Normal, Gamma, and Nakagami distribution. For the wideband channel, all distributions apart from the Rayleigh correspond well to the fading and fall within the 5% confidence bounds of the empirical CDF. For a narrowband channel, it is apparent that Nakagami distribution is the best fit to the measured data. Ricean, Rayleigh, Log-Normal do

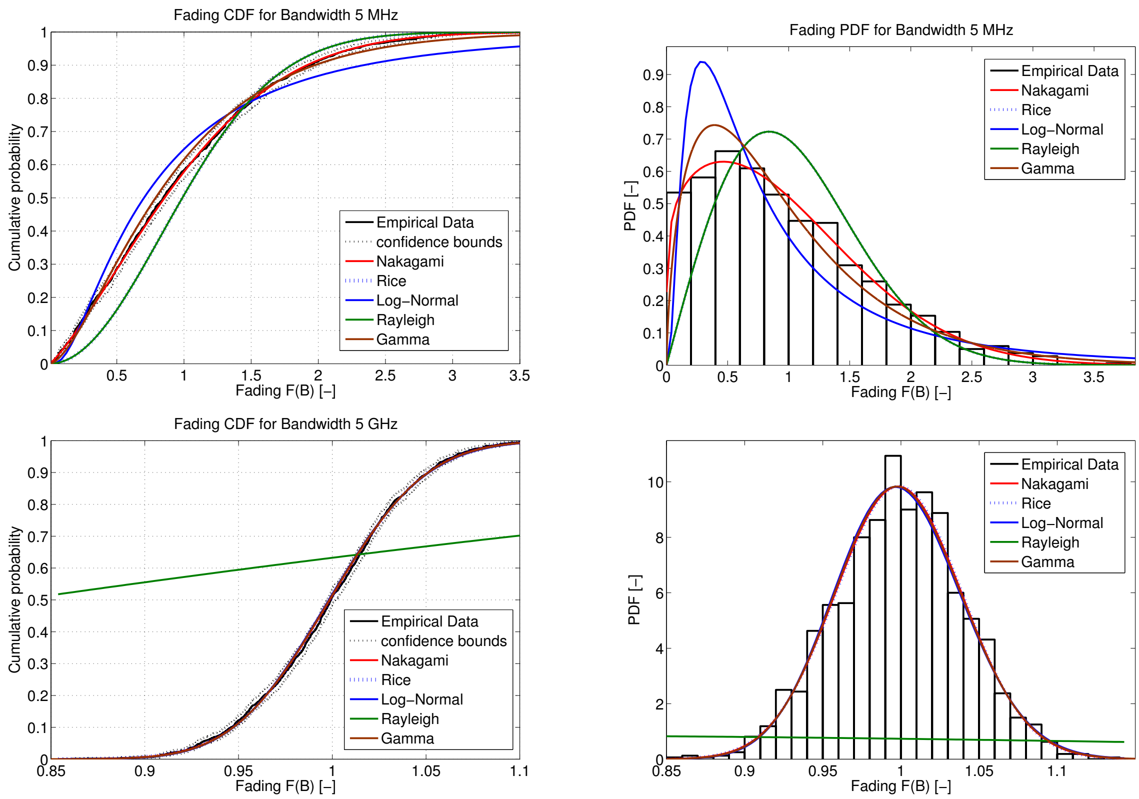

Figure 3.16: Empirical distribution of fading $F(B)$ defined in (3.35) for a channel with centre frequency of 7.25 GHz for bandwidth of 5 MHz and bandwidth of 5 GHz and corresponding fits of various fading distributions

not fit at all. Gamma distribution is worse than the Nakagami distribution but both seem to describe the fading reasonably well.

Therefore, for this subsection the Nakagami and the Gamma distributions will be investigated further as descriptors of fading $F(B)$ in (3.35) for more bandwidths than in Fig. 3.16. The PDFs $p_N(F)$ of Nakagami distribution is given as follows [21]:

$$p_N(F) = \frac{1}{\Gamma(m)} \left(\frac{m}{\omega}\right)^m F^{2m-1} e^{-\frac{m}{\omega}F^2} \tag{3.36}$$

where m and ω are distribution parameters and Γ stands for Gamma-Function.

The PDFs $p_\Gamma(F)$ of Gamma distribution is given as follows [73]:

$$p_\Gamma(F) = \frac{1}{k^\theta} \frac{1}{\Gamma(k)} F^{k-1} e^{-\frac{F}{\theta}} \tag{3.37}$$

where k and θ are distribution parameters and Γ stands for Gamma-Function.

The distributions were fitted on measurements of UWB channel. The same measurements as in section 3.3.1.2 were used. The channel was measured at 6 positions in the laboratory environment (see appendix C). For each distance, a grid of 40×40 channels spaced by 6 mm was measured. The variation of channel energy in Eq. (3.23) was studied and the parameters for Nakagami (3.36) and Gamma distributions (3.37) were calculated using maximum likelihood estimation. This was performed for a set of 35 bandwidths spaced logarithmically between 2 MHz and 5 GHz. The channel centre frequency was 7.25 GHz. The estimated parameters of the distributions were then used to calculate the theoretical CDF, which was then compared to the empirical CDF by the Kolmogorov-Smirnov Test with statistical significance of 5% and 2%. The results are summarised in Table 3.5.

Position ♯	TX-RX distance [m]	Nakagami 5% [%]	Gamma 5% [%]	Nakagami 2% [%]	Gamma 2% [%]
1	1.93	97.1	77.1	97.1	97.1
2	1.05	68.6	51.4	71.4	77.1
3	1.26	40.0	80.0	42.8	91.4
4	1.56	34.3	88.6	34.6	88.6
5	2.36	62.9	80.0	71.4	88.6
6	2.78	77.1	48.6	77.1	60.0
average		63.3	71.0	65.7	83.8

Table 3.5: Results of Kolmogorov-Smirnov test for using Nakagami and Gamma distributions to describe fading. The numbers represent the relative number of cases when the Kolmogorov-Smirnov test confirmed the null hypothesis (i.e. the empirical distribution matches the selected type of distribution).

As can be seen in Table 3.5, on average the Gamma distribution fits the fading in more cases and with the decrease of statistical significance the performance of Gamma distribution increases faster. Which suggests that despite Fig. 3.16 the Gamma distribution is more suitable to describe channels with varying bandwidth. We expand our investigation further and observe the result of the Kolmogorov-Smirnov test as a function of position and bandwidth. This is plotted in Fig. 3.17. Despite few exceptions, the following conclusions can be reached. The Gamma distribution is suitable for channels with bandwidths up to 100 MHz and with bandwidth above 1 GHz. In most cases it fails to describe properly channels with bandwidths between 100 MHz and 1 GHz. However for these bandwidths, the same can be stated about the Nakagami distribution. For the bandwidths of 100 MHz - 1 GHz a fitting with other distributions available

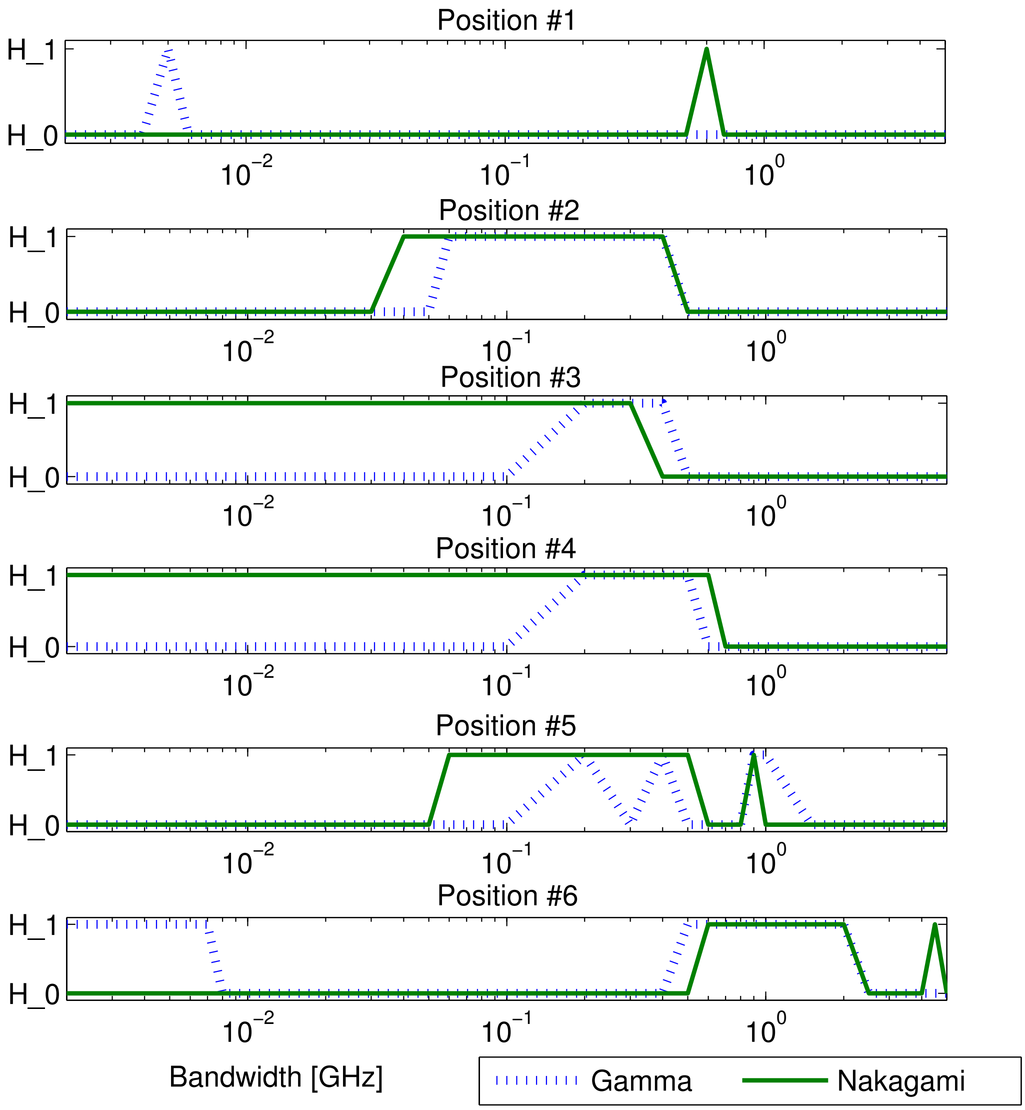

Figure 3.17: The result of Kolmogorov-Smirnov test applied on the empirical CDF as a function of Bandwidth. H_0 stands for null hypothesis (theoretical distribution matches the empirical one), H_1 stands for rejection of the null hypothesis. The plot is valid for test with statistical significance of 2%

in the Statistics Toolbox of Matlab^{TM} were attempted but none appeared to provide a better fit than Gamma or Nakagami. Thus we conclude this section with the statement that Gamma distribution appears to be the most suited one for description of fading in wireless channel for variable channel bandwidths.

3.3.2.2 Impact of Bandwidth on the Shape of PDF

Having selected the suitable distribution type, the change of the shape of the fading's PDF will now be explored in more detail. This exploration will further illustrate why the wideband signals are more robust against frequency selective fading than their narrowband counterparts and the results will later be used in chapter 4 to propose improvements to the Impulse Radio Systems.

The change of the shape of the PDF with the change of the bandwidth in (3.35) is illustrated in Figs. 3.18 and 3.19. Both figures display the PDF of fading $F(B)$ for eight different example bandwidths B chosen to spread from narrowband to UWB channel. These empirical PDFs are compared to the fitting by Nakagami and Gamma distributions. The Nakagami distribution is included only to further confirm conclusion made based on Table 3.5 and Fig. 3.17.

Fig. 3.18 shows the case for the position $\sharp 1$ for which both distributions fit well the empirical pdf (see Fig. 3.17). For all eight examples both Nakagami and Gamma distributions pass the Kolmogorov-Smirnov test. Fig. 3.19 on the other hand shows distribution for position $\sharp 3$. For this position, the Nakagami distribution fits well only for bandwidths above 400 MHz and Gamma fits well for all bandwidth except 200 - 400 MHz (see Fig. 3.17), but even for these bandwidths it is closer to the empirical data than Nakagami.

The fact that for narrowband channels fading can be very deep (relative attenuation by more than 20 dB compared to the mean value which) whilst it has limited impact for channels with bandwidth above 1 GHz is nicely illustrated by the PDFs in Figs. 3.18 and 3.19. This is a barely surprising conclusion given the discussion in section 3.3.1.2. Figs. 3.18 and 3.19, however, show the transition between the two states and it can be seen that for bandwidths of 200 MHz the probability of deep fading resulting in signal erasure is effectively zero.

A second conclusion that can be drawn from Fig. 3.19 is the fact even in the cases where Gamma distribution is not suitable according to the Kolmogorov-Smirnov test, it seems to match the actual distribution well at the extremities ($F \to 0$ and $F > 1.5$). Especially the $F \to 0$ area is very important because, as will be shown in chapters 4 and 5, it is the deep fades that represent the most significant contribution towards BER. Thus the fact that the Gamma distribution fits well for low F will prove crucial in performing BER estimates.

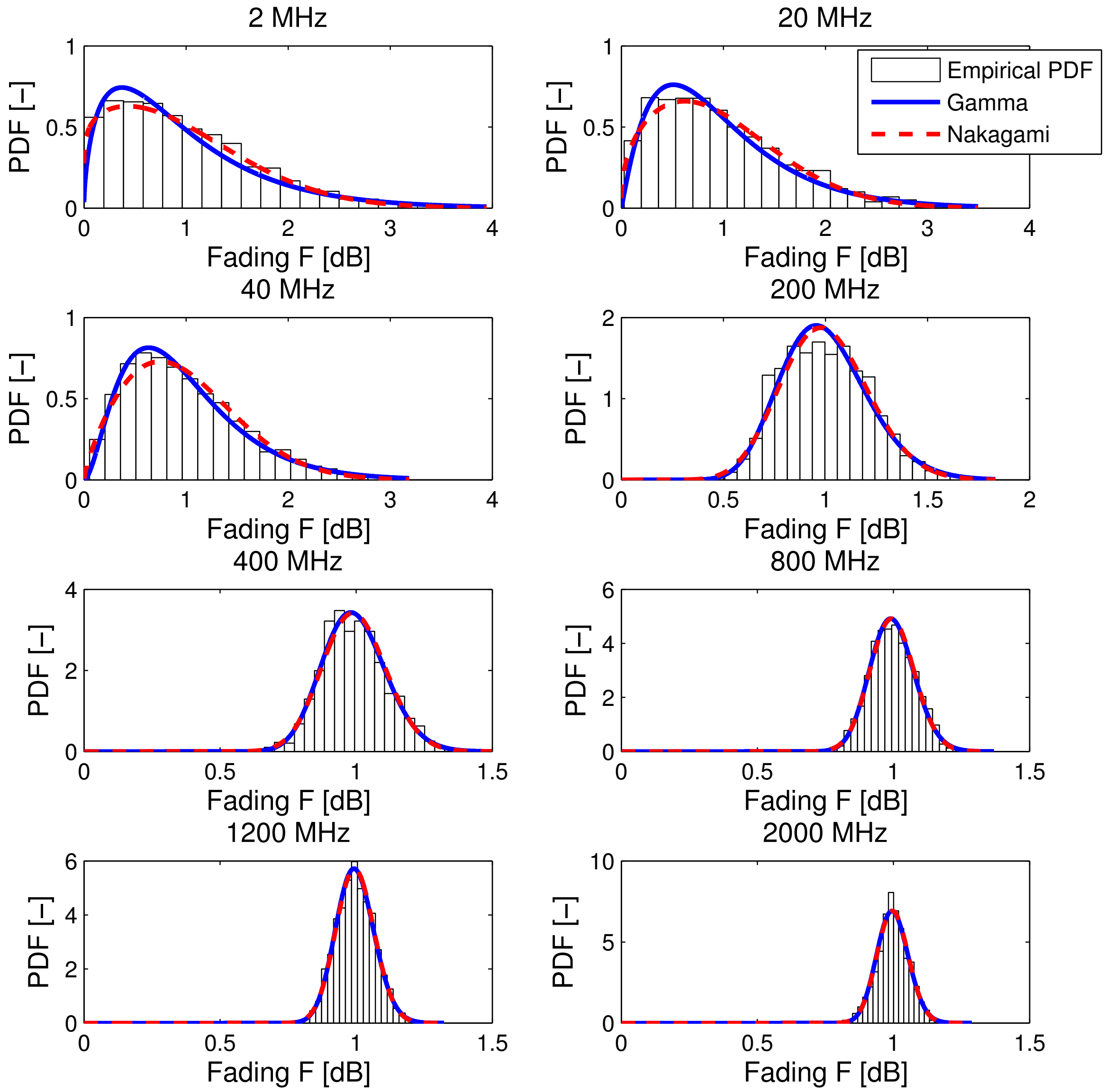

Figure 3.18: The change of shape of the empirical PDF (histogram) of fading $F(B)$ and the fitted distributions from 3.35 for eight example bandwidths for position 1

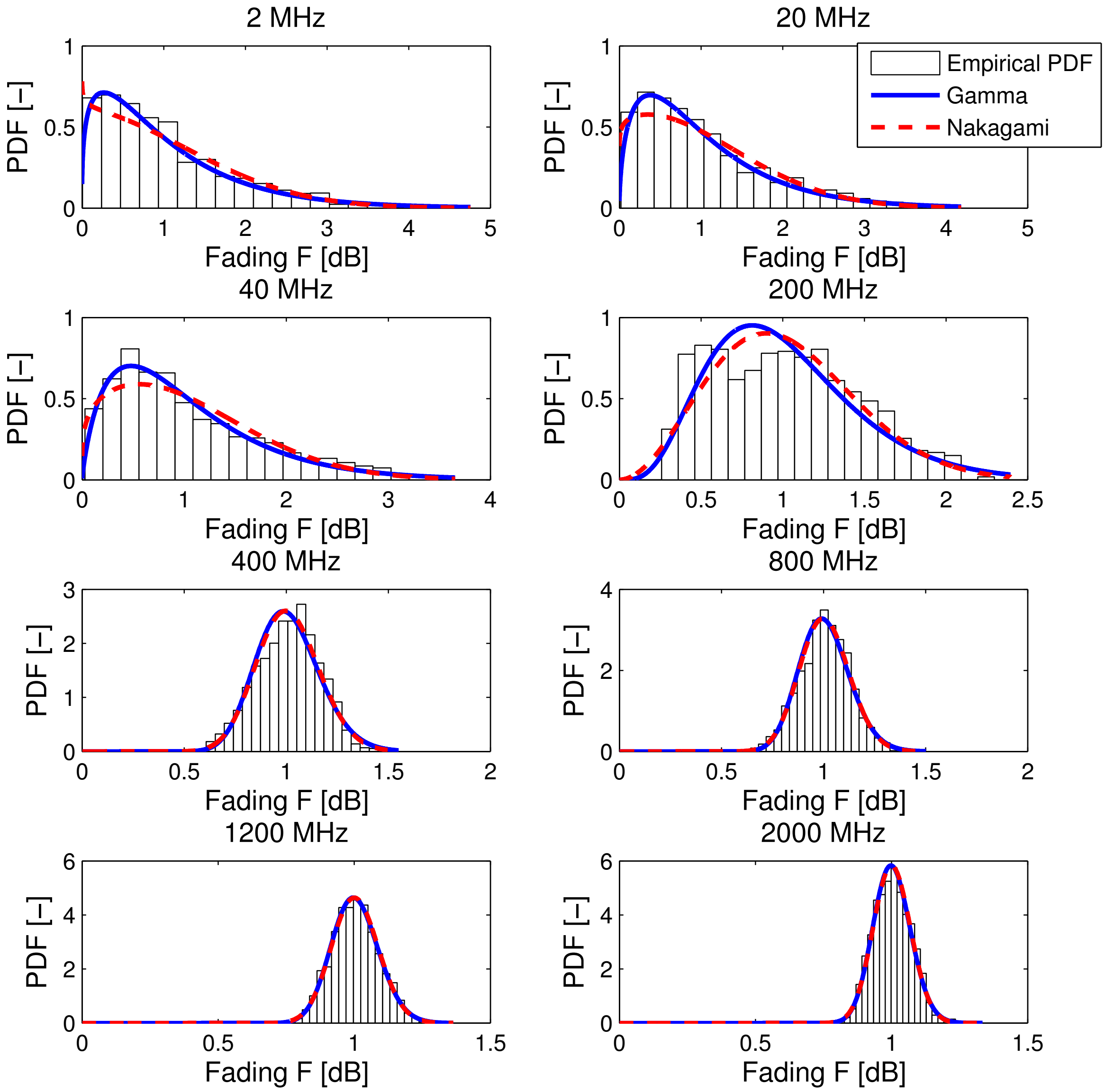

Figure 3.19: The change of shape of the empirical PDF (histogram) of fading $F(B)$ and the fitted distributions from 3.35 for eight example bandwidths for position 3

For calculation of BER estimates it will be necessary to use an analytical expression for $F(B)$, as presented in (3.37). Therefore the parameters for both distributions for all measurement positions and for all bandwidths are presented Fig. 3.20. It can be observed that, for all positions, the parameters differ but follow similar trend. This means that the trend in the change of the PDF shape is the same for all positions. Therefore, a mean has been calculated and is highlighted by the solid black line. This line represent the parameters that will be used

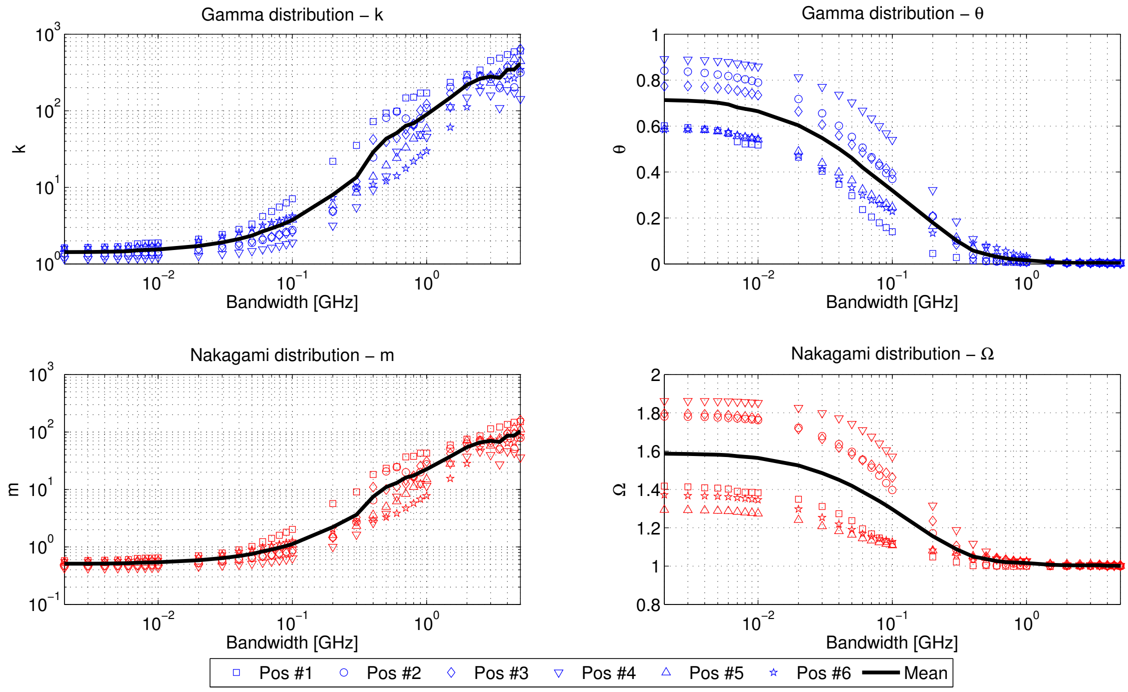

Figure 3.20: The change of the parameters of the PDFs as a function of bandwidth

for evaluation of system performances in chapters 4 and 5.

The data-sets in Fig. 3.20 also illustrate the change of the PDF with bandwidth. The fading has the narrowband nature until bandwidths of about 100 MHz. The UWB nature of the channel starts for bandwidths above 1 GHz. The range between 100 MHz - 1 GHz can be described as a transition range, where the channel does not quite have the properties of a UWB channel but it also does not have the properties of a narrowband channel anymore. As will be shown in chapter 4, it is this transition range that can be exploited to significantly improve the properties of impulse radio systems.

3.4 Wireless Channel - Summary

In this chapter, the wireless UWB channel has been introduced and explored in detail. This knowledge will be applied in chapters 4-7 to evaluate the performance of impulse radio and OFDM systems. The novel contributions of this chapter are the correction of the IEEE802.15.4a model of the channel impulse response and the exploration of fading.

The chapter shows that many independent rays in the IEEE802.15.4a model of the channel impulse response are actually a manifestation of the antenna impulse responses. This finding enabled simplification of the channel model and reduction of the number of independent multipath components in the model.

Frequency selective fading is a well-known phenomenon in wireless channel propagation. The novelty of this chapter is the fact that it contains a complete description from cause to its manifestation in a wireless channel. Unlike many other works the observations are performed over a wide range of bandwidths from 1 MHz to up to 10 GHz. To the author's best knowledge, most other works have typically focused either on the narrowband or on the UWB bandwidths. The full description of fading (fade depth and PDF parameters) for the entire bandwidth spectrum is novel and it will be used to discuss what is the optimum signal bandwidth for wireless communications.

CHAPTER 4

Impact of Channel on Impulse Radio Systems

Impulse radio was suggested in some of the first UWB works from the 1990s e.g. [9],[7]. The main idea of impulse radio is the use of extremely short sub-nanosecond pulses. These pulses are shorter than the distance between multipath components in the channel impulse response, thus individual multipaths can be resolved and no frequency selective fading occurs [8]. In the UWB works of Wine and Scholtz [9], [65] it was shown that it is possible to accommodate multiple users by using using code division multiple access techniques based on randomising the pulse repetition rates of individual users. Since then, there has been an ongoing interest in UWB impulse radio. For instance, the search for 'IR UWB' in IEEExplore^{TM} currently returns more than 750 conference papers and 175 journal papers.[1]

In this chapter we discuss the performance and challenges of impulse radio systems. We start by summarising the receiver techniques and the main challenges of impulse radio systems. Then we show how our study from chapter 3 on the scaling of fading properties with bandwidth can be applied to alleviate some of these issues, and to select the properties of transmitted signals. Finally, the findings are used to improve the performance of impulse radio schemes. The content of this chapter significantly overlaps with our work presented in [87].

4.1 Impulse Radio - Challenges

The challenges for impulse radios can be categorised as: transceiver implementation; impact of the rms delay spread; and the regulations. This section will be started with a short discussion about the transceiver design which is followed by the discussion of other challenges.

4.1.1 Implementation Challenges

The main issue for implementation of impulse radio systems is undoubtedly the task to receive and process extremely short low power pulses [13],[37]. Before discussing the implementation

[1] IR in the search stands for Impulse Radio

architectures, the modulation schemes for impulse radio systems are briefly introduced because they somewhat differ from the classical modulation schemes known from the narrowband systems [37]. There is a plethora of modulation schemes that can be utilised for impulse radio communications [37]:

- **On-Off-Keying (OOK)** is the most simple modulation scheme in terms of complexity in which a bit is encoded by the presence/absence of a pulse. [37]
- **Frequency Shift On-Off-Keying** encodes bits by the selection of pulse centre frequencies. [37]
- **Pulse-Amplitude-Modulation** transmits pulses with different amplitude levels to modulate multiple bits on a single pulse. [37]
- In **Pulse-Position-Modulation** the bit(s) are coded by the relative position of the pulse within a frame. [37]

The list of modulation schemes is not exhaustive and combinations of the schemes in the list can be used [37]. These modulation schemes can also be used to explain the differences between the coherent and non-coherent UWB receivers.

Coherent receivers correlate the received signals with a carefully-designed template signal. It outperforms non-coherent receivers in minimising the BER for Additive White Gaussian Noise (AWGN) channel without inter-symbol interference [88]. They do not operate as traditional narrowband coherent receivers that aim to demodulate the phase of the carrier [34], instead UWB coherent receivers focus on precise estimation of the Time-of-Arrival of all multipath components [88].

Reference [88] shows that for perfect synchronisation, the gap between coherent and non-coherent in UWB systems is 9 dB which is "more than the 3 dB gap known from narrowband systems" [88]. This seems to be a huge drawback of non-coherent receivers because the 9 dB penalty in SNR represents a significant difference in the UWB landscape where the available dynamic range is between the limited EIRP of -41.3 dBm/MHz and the noise floor at -114 dBm/MHz [6]. This dynamic range of 72.7 dBm is further reduced by mean path loss (approx. 45 dB for a distance of 1 m e.g. [21]) and the noise figure of the receiver (realistic assumption of 4-5 dB or more [6]).

On the other hand, the correlation receiver is associated with extremely high implementation complexity because it requires almost perfect synchronisation [89]. Consequently, it requires precise and complex channel estimation [90] which is not suitable for low-complexity low-cost applications, the primary target marketplace for impulse radio UWB. Furthermore, to capture the energy spreaded into many multipaths, coherent receivers have to employ the rake architecture with many fingers. This further increases the complexity, especially because high sampling rate Analogue-Digital-Converters (ADCs) are required [91].

For the non-coherent receivers the gain for their performance degradation is the use of low complexity architectures. Firstly, they are more robust against synchronization errors and do not require complex channel estimation [88], [92], [93]. Furthermore, they do not need the rake structure [88], [92], [93] and "only frame or symbol rate sampling" is sufficient [93]. Two designs most studied in the literature are energy detectors and the autocorrelation receivers. The energy detector has mainly been considered for OOK or Frequency Shift Keying-OOK systems as it can be implemented as a low complexity filter bank [92]. For Pulse-Position-Modulation systems, autocorrelation receivers are the suitable choice [93]. The autocorrelation receivers use the autocorrelation of the received signal to determine its position within a frame. Two techniques can be used: the transmitted reference and the differential scheme. For the sake of brevity, the reader interested in details on these schemes of autocorrelation receivers, their performance and challenges for synchronisation is referred to works [88],[93] and references therein.

To conclude, this section introduced the main modulation schemes and the main receiver architectures for impulse radio UWB systems. It shows the trade-off between high performance complex coherent receivers and their low-complexity non-coherent counterparts. The issue of wide bandwidth and its impact on the ADCs is mentioned. Next, the impact of the channel is discussed.

4.1.2 Impact of RMS Delay Spread of UWB Impulse Radio

The main advantage of impulse radio systems in terms of propagation in a wireless channel is their ability to resolve individual multipath components. As a result, they do not suffer from the impact of frequency selective fading in the way narrowband systems do. In other words, the received energy is approximately constant independent of small displacement as was shown in chapter 3.3.[2]

Unfortunately, the short duration of the pulses also represents an issue, because the problem of frequency selective fading has been traded for the issue of inter-symbol-interference. Inter-symbol-interference is caused by the late arriving multipath copies of the signal [13]. The inter-symbol-interference is typically resolved by the employment of guard interval between adjacent symbols [13]. If the guard intervals are longer than the typical RMS delay spread, no inter-symbol-interference can occur.

For narrowband services, the RMS delay is usually significantly shorter than the signal duration and is therefore not associated with a significant performance loss. For UWB impulse radio systems, however, the pulse duration is shorter than the RMS delay spread, as a result, the spectral efficiency is compromised. In UWB systems, the typical length of guard intervals is 50-70 ns [13],[88] for the reasons of limited dynamic range as discussed in the channel impulse response simplification in chapter 3.2. If a pulse with duration 1 ns is considered, the duty cycle is below 2%.

On one hand, it is this low efficiency that enables the multiple user access as proposed e.g. in [9], [65]. On the other hand, it limits the actual data-throughput. A guard interval of 50 ns corresponds to a symbol rate of 20 MSps.[3]. Due to the low dynamic range and the complexity of the reception, most real systems use a simple modulation where each symbol carriers one bit of information [37],[88]. As a result, impulse radio seems to be destined only for low-data-rate applications.

4.1.3 Impact of Regulations

The initial work on UWB communications, such as [7],[65], assumed baseband pulse communications. This idea was still considered even after the 2002 FCC ruling enabling UWB in the band from 3.1 to 10.6 GHz, and a lot of effort was invested into the design of pulses compliant to

[2] The small displacement is a displacement that is relatively small compared to the range. Hence, it does not significantly change the path loss. For more specific discussion, refer back to section 3.3.1.3.

[3] MSps stands for Mega-Symbols-per-Second

the US FCC spectral mask [37]. However, the recent regulatory changes in Europe, Japan and Korea, as discussed in the introduction of this thesis, have changed the UWB landscape. Quite simply, with the European's general limit enabling communication in the band of 6-8.5 GHz, it is more convenient to consider the traditional bandpass transmission with well described theory, e.g. [34],[94], than baseband communication.

On the one hand, the reduction of the available bandwidth effectively ruled out the possibility of frequency division multiple access. On the other hand, the European standard foresees an extra 500 MHz spectrum allocated for Low-Duty-Cycle services [10]. The definition of Low-Duty-Cycle further limits the data-rate of the service but it can be seen as an opportunity because it enables access to an additional spectral band. This band can be utilised by applications such as wireless sensor networks for which the data-rate is not critical and which could benefit from the low-complexity of impulse radio transmitters combined with localisation systems.

4.2 Optimum Signals for Transmission over Fading Channel

The preceding section introduced the major challenges for impulse radio systems: the complexity of processing of nanosecond pulses, and the low maximum data-rate. The limitations caused by the regulations were also discussed. This section aims to show how the understanding of the wireless channel can be employed to alleviate some of these issues. It discusses the optimisation of the pulse bandwidth for communications considering frequency selective fading, the selection of suitable guard interval, and the spectral efficiency of the system. This discussion facilitates the choice of the optimum signal bandwidth for OOK impulse radio.

4.2.1 Impact of Bandwidth on BER

Here the effect of bandwidth on BER in a fading channel is explored. The theoretical expectations are following. For a narrowband signal with a known mean SNR, the behaviour will correspond to the well known performance in such a fading channel, i.e. the BER will be significantly higher than for the case of a flat fading channel with the same mean SNR, e.g. [94]. If the bandwidth is sufficiently large, the spatial fading effectively disappears as shown in chapter 3. As a result, the channel will behave like a frequency flat channel. For this section, what is of interest is the behaviour for the transition between the two cases.

This is studied for a system with OOK. The closed form expression for the bit-error-rate, BER, is given as [34],[94]:

$$BER = \frac{1}{2}\mathrm{erfc}\sqrt{\frac{1}{4}\frac{E_b}{N_0}} \tag{4.1}$$

where erfc is the complementary error function; the $\frac{E_b}{N_0}$ (ratio of energy per bit to the mean spectral noise density) varies due to fading. Hence the performance in a fading channel is given as [94]:

$$BER = \int_0^\infty \frac{1}{2}\mathrm{erfc}\sqrt{\frac{1}{4}F\mathrm{E}\left\{\frac{E_b}{N_0}\right\}}\mathrm{p}(F)\mathrm{d}F \tag{4.2}$$

where F represents fading, a non-negative random variable with PDF $\mathrm{p}(F)$, and $\mathrm{E}\left\{\frac{E_b}{N_0}\right\}$ is the expectation of $\frac{E_b}{N_0}$ given by the link budget analysis and the path loss from the IEEE802.15.4a channel model [21].

Chapter 3 shows that the fading PDF in a UWB channel with variable bandwidth is best fitted by a Gamma-distribution. Hence, we perform our investigation with the Gamma distribution with bandwidth scaled parameters of $\mathrm{p}(F)$ as determined in chapter 3. The results are plotted

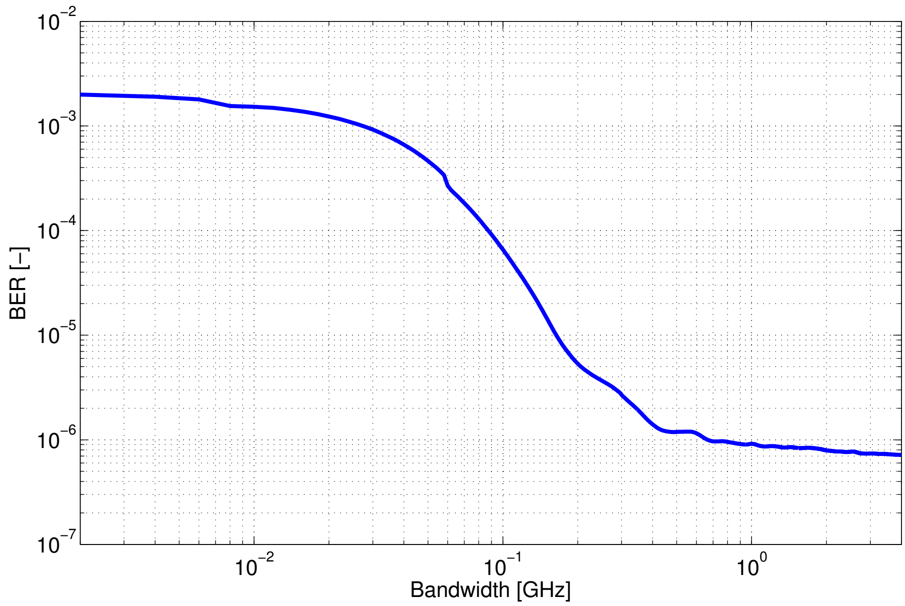

Figure 4.1: BER in an OOK system for $\mathrm{E}\left\{\frac{E_b}{N_0}\right\} = 10$ and variable bandwidth. The curve shows the transition between the fading channel for narrowband signals and a 'frequency flat' channel for UWB signals.

in Fig. 4.1. Fig. 4.1 shows evaluation of (4.2) for $\mathrm{E}\left\{\frac{E_b}{N_0}\right\} = 10$ for various signal bandwidths. As can be seen there is a BER improvement by a factor of almost 10^4 between the narrowband channel and the wideband channel. It is noted that the BER improvement between the case of bandwidth $B = 4$ GHz and $B = 200$ MHz is less than a factor of 10. This means that even signals with a bandwidth of 200 MHz can largely benefit from the same properties as extremely wideband signals. There is a penalty between the two cases, but for the pulses with 200 MHz bandwidth, this performance deterioration may well be compensated by the decrease of complexity as well as by the increase in spectral efficiency because the relative ratio of guard interval to signal duration increases approximately by factor of 10.

4.2.2 Choice of guard interval length

The length of the guard interval is essential for the performance of the system. If the guard interval is short, the system will be influenced by Inter-Symbol-Interference (ISI). On the other hand, long intervals reduce the achievable data-rate. The typical guard intervals in UWB systems have the length 50-70 ns [13],[88]. This choice can best be justified by considering the link budget. A delay of 50 ns corresponds to a ray-path length of 15 m. The free-space path loss, PL, at 7.25 GHz (the centre frequency of the EU band for UWB [10]) over 15 m is given as [8]:

$$PL = 20\log\left(\frac{\lambda_{7.25\mathrm{GHz}}}{4\pi r_{15\mathrm{m}}}\right) = -73 \text{ dB} \tag{4.3}$$

where $\lambda_{7.25\mathrm{GHz}}$ is free space wavelength at 7.25 GHz, $r_{15\mathrm{m}}$ is a range of 15 m.

The dynamic range for OOK impulse radio systems is given by the allowed EIRP of -41.3 dBm/MHz and by the sensitivity of the receivers. Here, we assume an energy detection receiver with a sensitivity of -100 dBm/MHz. This is a realistic estimation for state-of-the-art energy detectors. For instance, in 2007 reference [95] introduced an energy receiver with sensitivity of -97 dBm/MHz. It can be seen that in such a system, a signal delay of 50 ns would have energy 14 dB below the receiver sensitivity. This can be improved by the antenna gain but most UWB devices are targeted for mobile applications with omni-directional antennas, thus gains typically do not exceed 3 dBi, e.g. [6],[8],[13],[37]. This consideration limits the range of the system but it also shows that guard interval of 50 ns is more than sufficient for OOK systems with energy detection to avoid inter-symbol interference.

This is also shown in Fig. 4.2 which shows the simulated results of BER for an impulse radio system with OOK over empirical indoor channels, presented in chapter 3 and in appendix C. The system is assumed to use Gaussian baseband pulses with -10dB-bandwidth of 500 MHz modulated at a centre frequency of 7.25 GHz (see Appendix A for details about the pulse waveform). The plot is for positions 3 and 4 with mean distance between transmitter and receiver of 1.36 m and 1.56 m respectively (see appendix C). Each measurement position provides information about 1,600 channels in a 40×40 grid spaced by 6 mm. For each channel, perfect synchronisation was assumed in order to isolate only the impact of the repetition period. For each channel position 10^4 bits were transmitted and the information over 1,600 channels was collated to plot the BER as a function of pulse repetition frequency. The receiver was assumed to be an energy receiver with sensitivity of -100 dBm/MHz. Thus Additive White Gaussian Noise with power spectral density of -100 dBm/MHz was added to the received signal. The signals are transmitted with variable repetition period. The receiver integrates the received energy over the repetition period. If the received energy over the period is 3 dB above what corresponds to the integrated energy over the repetition period for power -73 dBm (power of signal with -100 dBm/MHz and bandwidth of 500 MHz), the receiver assumes to receive a '1', otherwise a '0' is received.

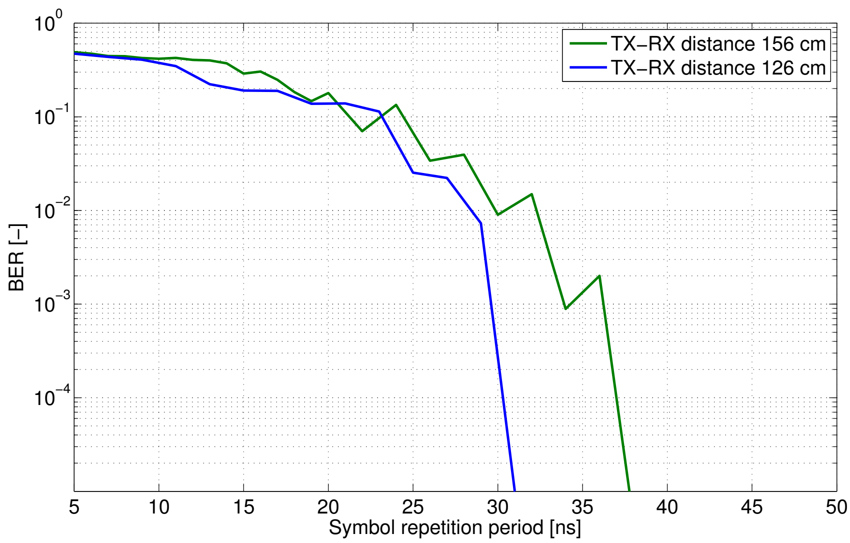

Figure 4.2: BER in an OOK system (specified in the text) as a function of symbol repetition period. © 2012 IET. Reprinted, with permission, from our work [87].

As can be seen in Fig. 4.2, the BER drops below 10^{-5} for repetition period larger than 40 ns. This suggests that such a repetition rate is sufficient protection against inter-symbol-interference for realistic channels. This is valid for the EU band from 6 to 8.5 GHz [10]. For lower frequencies (e.g. in the USA radiation around centre frequency of 3.3 GHz would be possible), the path loss is reduced and therefore more delay between pulses is required.

4.2.3 Bandwidth Optimisation using Spectral Efficiency

In section 4.2.1, the improvement of BER as a function of bandwidth was shown. It was shown that the difference between the performance of a system with $\mathrm{E}\left\{\frac{E_b}{N_0}\right\} = 10$ can differ by a factor of almost 10^4 between narrowband and UWB signal. It has also been shown that for a Gaussian pulse with a bandwidth of 500 MHz modulated into the EU UWB band, the symbol period required to suppress the inter-symbol-interference is 40 ns. This leads to an approximate expression for spectral efficiency SE [87]:

$$SE = \frac{\frac{1}{B}}{\frac{1}{B} + G} = \frac{1}{1 + B \cdot G} \tag{4.4}$$

where B is the bandwidth of the baseband signal, $1/B$ represents approximately the duration of the baseband signal, and G is the guard interval. Based on the preceding subsection the guard interval will be chosen as $G = 40$ ns.

For a narrowband system with $B \rightarrow 0$ the SE goes to 1. For a UWB system with bandwidth $B = 3$ GHz, $SE = 0.83 \cdot 10^{-2}$. In other words, it varies by a factor of approximately 10^2 and it improves with decreasing bandwidth, which is opposite to the BER dependency on bandwidth. Thus, in [87] we define a new performance measure, PM, that compares the BER performance and the spectral efficiency in order to see the optimum bandwidth:

$$PM = \frac{BER}{SE^2} = BER(1 + B \cdot G)^2 \tag{4.5}$$

The spectral efficiency is squared in order to have the same dynamic range for BER and SE so that they can be weighed equally. This measure is plotted in Fig. 4.3. The optimum bandwidth is the bandwidth for which the performance measure PM is minimised. For this bandwidth,

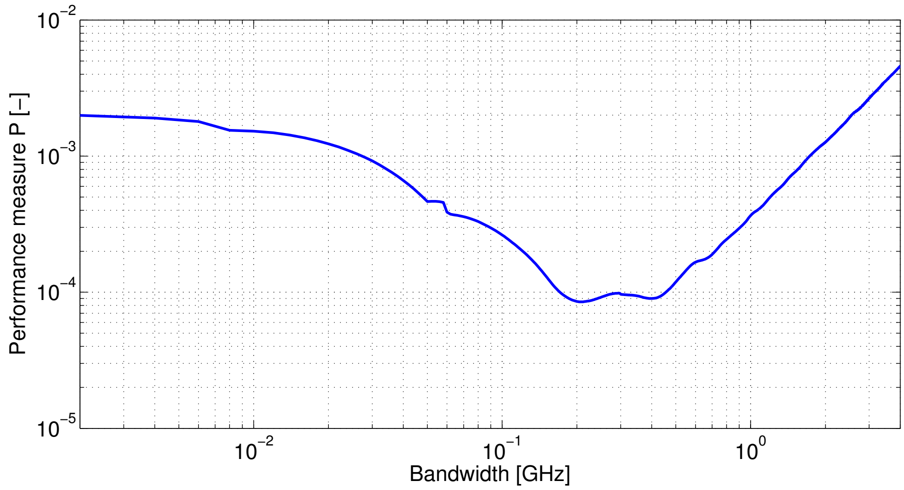

Figure 4.3: The performance measure specified in Eq. (4.5) as a function of bandwidth.

the BER is low whilst the spectral efficency is not compromised. As can be observed in Fig. 4.3, this can be achieved for bandwidths from 150 MHz to 450 MHz for which the $PM < 10^{-4}$.

4.2.4 Optimum Bandwidth

In the previous sections, the scaling of fading in wideband channels was balanced with the spectral efficiency in systems with a guard interval. It is concluded that the optimum performance is obtained for bandwidths of between 150 MHz and 450 MHz. These bandwidths are attractive from the implementation point of view because the reduced bandwidth (increased pulse duration) compared to the sub-nanosecond pulses typically used in UWB impulse radio systems mitigates many of the complexity issues of the reception.

From the regulatory point of view, such impulses do not qualify as a UWB waveform, and therefore use of such a pulse would violate the regulations which are binding for all users of the radio spectrum. Fortunately, the issue is insufficient bandwidth which can be easily addressed by a multi-carrier system transmitting multiple impulses in parallel. Not only would such a waveform satisfy the regulation requirement of bandwidths being wider than 500 MHz, but it would also increase the data-rate.

The drawback is the fact that the number of users would be limited by the available bandwidth. In the USA the 7.5 GHz bandwidth is sufficient to accommodate multiple users sharing the spectrum by the means of frequency division multiple access. However, with the about 2.5 GHz bandwidth available in Europe, Japan and Korea (see Introduction of this thesis), the number of users is very restricted. Hence, the subsequent section introduces the Multi-tone Frequency Shift Keying as an alternative, which enables the partial re-use of individual frequency slots by multiple users or the increase of the spectral efficiency by shortening the guard interval.

4.3 Multi-tone Frequency Shift Keying

For a single-tone FSK, the value of a bits is defined by the usage of one frequency out of the available set of frequencies [94]. Single-tone FSK has been considered for UWB wireless communication in reference [96], where it is used for a low complexity transceiver achieving bit rates of 1-15 Mbps. Compared to single-tone FSK, multitone FSK, introduced in [97] and [98], transmits simultaneously K active tones at a time out of the set of N available tones, thus bit blocks are represented by the combination of the frequencies. Authors of references [97] and [98] are the only ones who have considered multitone FSK for wideband radio channels. Their work, however, deals with information theoretical aspects of multitone FSK (MT-FSK) and its ability to approach the wideband channel capacity.[4] Here, we discuss some advantages of Multi-tone UWB systems and their performance in practical channels.

4.3.1 Advantages of Multi-tone FSK

One of the main features of the Multi-tone FSK is the fact that, to some extent, it can be used as 'coded modulation' [94]. If a communication link does not use the full alphabet of $\binom{N}{K}$ code words, the receiver can decide which K out of N tones are active using the *a priori* knowledge of the symbol assignments from the alphabet and discarding tones that would result in non-valid symbols. This feature is what makes Multi-tone FSK attractive as the next evolutionary stage of UWB impulse radios because of two main advantages.

Firstly, they enable frequency re-use among multiple users which addresses the problem of how to accommodate multiple impulse radio users using energy detection in a limited 2.5 GHz

[4] Multi-tone FSK is also discussed in [99] where it is used for ultrasonic communication.

spectrum when each has to occupy at least 500 MHz bandwidth.[5] There are N available tones and each user can use K tones. This gives a space of $\binom{N}{K}$ code words. The standard way would be to assign fully orthogonal codewords that do not re-use tones among users. However, in fact each user can be assigned a subset of these codewords and share some tones among each other but not the entire combination of tones defining the codeword. Then a receiver can use its *a priori* knowledge which code words are valid and which not to avoid the inter-user-interference.

Secondly, the guard interval between subsequent pulses can be reduced. The idea is to use the same property of the code-words within a single communication link. The link can switch between two (or more) code sets. Then the subsequent symbols never use the same code set and the inter-symbol-interference can be mitigated by the *a priori* knowledge of the code sets.

In summary, in both cases less bits per symbol than possible are transmitted but this provides with a Forward-Error-Correction capability and enables a system either to accommodate more users or to increase the duty cycle of the communication.

4.3.2 Number of Tones and Active Subcarriers

The size of the alphabet provided by N available tones and K active tones is $\binom{N}{K}$. This suggest that in terms of alphabet size, which is directly related to data-rate, it is best to choose a large N. For the bandwidth B this means the selection of $B = 150$ MHz. On the other hand such implementation is reflected by the transceiver complexity. Especially the receiver has to be implemented as N energy detectors in parallel. For the performance evaluation $N = 16$ is chosen to explore the maximum achievable data-rate. This means a total occupied bandwidth of 2,400 MHz which almost fully occupies the 2.5 GHz UWB band allocated in Europe [10].

In terms of K, the alphabet has the largest size $\binom{N}{K}$ for $K = N/2$ for even N and $K = (N \pm 1)/2$ for odd N, however, the selection of K also has an impact on the symbol-error-rate, SER. The symbol error rate is given as [87]:

$$SER = 1 - [(1 - P_e)^{N-K}]^K = 1 - (1 - P_e)^{NK-K^2} \tag{4.6}$$

[5]Sharing of the spectrum by time positioning codes as suggested by Win and Scholtz in [65] is not possible in cases when receivers use energy detection which integrates energy over time.

P_e is the probability that an in-active tone is selected over an active tone.

Eq. (4.6) calculates the probability that no in-active tone is selected over an active one and subtracts it from 1. Hence, $(1 - P_e)^{N-K}$ is the probability that none of the in-active tones are selected over one of the active tones. This probability is independent for each of K active tones.[6]

From Eq. (4.6) it can be observed that the symbol-error-rate reaches its maximum exactly for $K = N/2$ for even N and $K = (N \pm 1)/2$ for odd N, i.e. for the largest size of the alphabet. It can also be observed that Eq. (4.6) is symmetric around its maximum. $K < N/2$ is chosen here because whilst in terms of SER and data-rate, the performance is the same for both $K < N/2$ and $K > N/2$. For $K < N/2$ less tones are active at the transmitter thus less power is radiated and the transmitter is more power efficient.

Following (4.6) it can be concluded that K needs to be selected as a compromise between low K for low symbol-error-rate and optimum K in terms of data-rate. For the performance evaluation $K = 4$ was selected as a compromise for large alphabet and low SER.

4.3.3 Performance of a MT-FSK System over Empirical UWB Channels

The performance of a Multi-tone FSK system is investigated in this section. The system parameters are: $N = 16$ available tones, $K = 4$ active tones, the tones are baseband Gaussian pulses modulated with -10 dB bandwidth of 150 MHz modulated on the tone centre frequencies. The $\binom{N}{K}$ gives 1820 possible combinations which are used to code 10 bits. This approach almost fully exploits the capacity of the alphabet. It does not allow multiple-user access, but it enables estimation of the maximum throughput in the system. The symbol repetition period was selected as 40 ns. This enables us to achieve a gross data-rate of 250 Mbps (this data-rate includes protocol overheads, channel coding etc.).

The performance over empirical channels was evaluated as follows. The receiver was assumed to have a sensitivity of -100 dBm/MHz as explained above. Hence, after the transmission of the

[6]This formula is not entirely correct as it does not consider the self-correcting capability discussed in section 4.3.1. In reality, there is not a single probability P_e. Instead there are different probabilities based on combination of multiple factors such as the code, the tone in question, the active tones etc. However, Eq. (4.6) can still be used to illustrate the impact of K. Even though it is not precise dependency, the trend is similar and it provides an engineering insight into the problem.

signals were over the empirical channels presented in chapter 3, Additive White Gaussian Noise was added, and 16 energy detectors processed the data from each frequency. A soft decision was implemented, i.e. four tones with the most energy integrated over the repetition period of 40 ns were selected as active tones.

The simulation was run for 6 measurement distances, as presented in appendix C. For each measurement distance, the 40 channels out of the available grid of 1,600 channels were selected. The selected 40 channels are on the diagonal of the grid. The timing of the receiver was set perfect for the first position in the corner of the grid. With the displacement along the diagonal of the measurement grid, a timing mismatch occurred. For each channel position, 10^9 bits were simulated. The performance results are presented in Fig. 4.4 which shows 6 lines, each line corresponds to one mean distance between the transmitter and the receiver (to one grid in the measurements introduced in chapter 3). The lines also show the BER for various displacement from the initial position for which the receiver timing synchronisation was perfect.

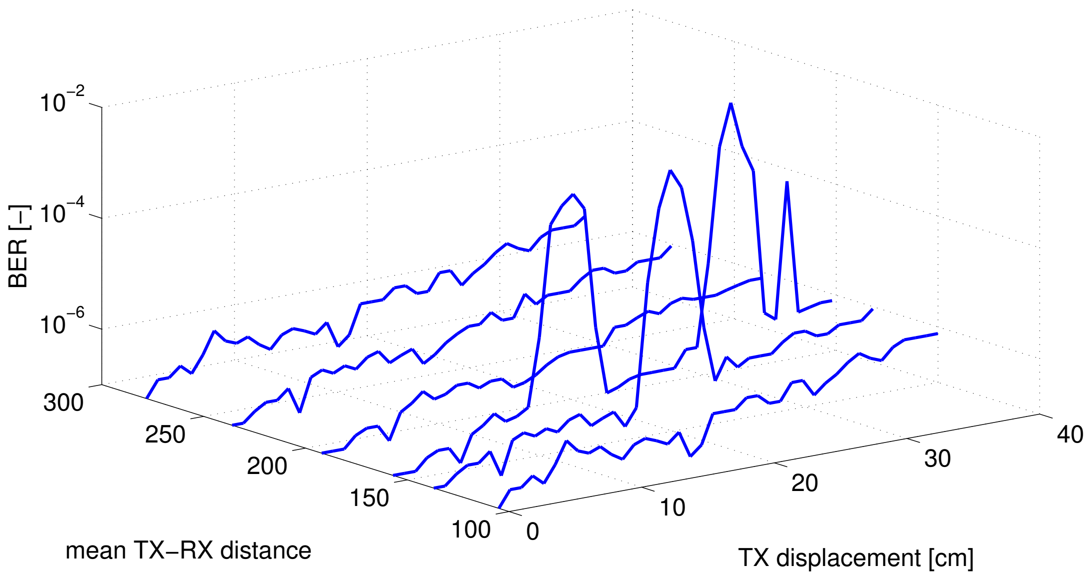

Figure 4.4: The BER performance of the example MT-FSK system for six measurement positions specified in Appendix C. © 2012 IET. Reprinted, with permission, from our work [87].

It can be seen that apart from a few outliers the BER is below the magnitude of 10^{-5} for almost all measurements. In fact, it is below 10^{-6} for all displacements smaller than 10 cm. If it is assumed that mobile terminals will have a velocity of up to 10 m/s.[7] The minimum corresponding to a 10 cm displacement is 10 ms. With a symbol repetition period of 40 ns, this corresponds to 250,000 symbols. Henceforth, it can safely be assumed that a practical system would correct its synchronisation before it moves farther than 10 cm. This shows that the system is robust against both spatial and temporal fading.

4.4 Summary

In this chapter, the performance of impulse radio UWB communication systems is studied. The chapter shows that in terms of communication in multipath environment, there are two extremes:

- Narrowband signals have high duty cycles but are affected by fading
- UWB impulse radio systems are immune to frequency selective fading but this immunity is available at the cost of low duty cycle.

Therefore, the chapter introduces a performance measure that enables one to balance the knowledge of fading as a function of bandwidth (and its impact on BER) with the spectral efficiency. It shows that for an indoor environment the optimum bandwidth for signal transmission compliant to the European UWB regulations on EIRP is in the range of 150-450 MHz. The robustness of such signals against the attenuation by frequency selective fading is comparable to the sub-nanosecond pulses whilst their duty cycle is higher. Due to the regulations, such pulses must be used in multi-carrier systems.

Performance of an example multicarrier system has been presented in the chapter. It utilises multi-tone frequency keying, which in the case of a carefully designed alphabet can be used as coded modulation which enables re-use of tones by multiple users or to shorten the guard interval. In a realistic simulation using empirical channels such a system provides a data-rate of 250 Mbps with BER below 10^{-6}. Due to the improved spectral efficiency, this performance

[7]At the time of writing this thesis, the fastest time for 100 m sprint was 9.58s. This corresponds to an average speed 10.44 m/s.

is superior to impulse radio systems reported in the literature, e.g. only 30 Mbps is reported in [88].

Unfortunately, even for multi carrier systems with a tone bandwidth of 150 MHz, the spectral efficiency due to simple OOK is the limiting factor. If all tones are used at all times, the maximum achievable throughput is 400 Mbps (16 bits transmitted with symbol period of 40 ns) when using 2,400 MHz. WiMedia OFDM systems can provide 480 Mbps whilst utilising only 528 MHz [13]. The main reason is the fact that WiMedia systems use higher order coherent modulations.

Considerations of the use of higher order modulation schemes in impulse radio systems with optimised bandwidth is an interesting research avenue for the future. However design of such receivers would go beyond the scope of this thesis which aims to show how the understanding of the UWB wireless channel can be used to explain and improve the performance of communication systems. Therefore, the next chapter will change the topic and discuss the impact of the channel on the performance of OFDM systems, which is another type of modulation popular within the UWB community.

Compared to impulse radio systems, the OFDM systems have the advantage of being well-understood and matured thanks to their employment in systems such as IEEE802.11 and DVB. As a result even though the OFDM systems are suboptimal in terms of the performance measure introduced in this chapter, this deficiency is compensated by the availability of signal processing and higher order modulations.

CHAPTER 5

Impact of the Channel on UWB OFDM Systems

This chapter aims to use the conclusions from the chapters 2 and 3 to investigate the impact of the channel on UWB OFDM systems. The chapter will mainly focus of WiMedia OFDM systems which represents the industrial standard for UWB OFDM systems [13]. The chapter has following structure. Firstly, the concept of OFDM and its advantages are introduced and implementation complexity is discussed. Secondly, the main features of the physical layer of the WiMedia standard are briefly introduced. Then the transmission range of practical WiMedia development kit is explored and compared to theoretical predictions. The frequency selective fading in UWB channel is identified as the main cause for the discrepancy between the theoretical and practical performance. Finally the conclusion of the chapter introduces some avenues that alleviate the limitations of the system and that will be further explored in subsequent chapters.

5.1 OFDM - Introduction

To the author's best knowledge the concept of OFDM has firstly been introduced by Chang in his work [100] from 1966 and in [101] from 1967. The main concept of the scheme is the division of a wideband frequency selective channel into a larger number of orthogonal narrowband channels (these are typically referred to as subcarriers [13],[94]) that can be used for parallel transmission. Each of these subcarriers can be treated as a frequency flat channel with AWGN. Properties of frequency flat channels with AWGN are well known and well described in standard textbooks, e.g. [34],[94]. Furthermore, the receivers for such channels are less complex than receivers for wideband frequency selective channels [13], [34], [94].

The main trigger for the success of the OFDM technique is most likely the 1971 paper from Weinstein and Ebert [102], which introduces the guard interval between symbols and also shows that the modulation and demodulation of the OFDM symbol can be performed by the means of Inverse Fast Fourier Transform (IFFT) and Fast Fourier Transform (FFT) [102]. The modulation and demodulation by the means of IFFT and FFT simplifies the computational complexity of the parallel transmission and it is deemed as the main reason for commercial success of OFDM for many digital communications systems, e.g. IEEE802.11 Wireless Fidelity (WiFi), Digital Video Broadcasting (DVB), and WiMedia UWB [13].

For the sake of brevity, the principle of operation of OFDM modulators is not described in this thesis because it is well known in the community and it is described in many standard textbooks, e.g. [13], [34], and [94]. Instead, the complexity of the OFDM chips will be briefly discussed. The complexity is mainly determined by the implementation of the FFT. To our best knowledge, the most efficient algorithm has been presented by Johnson and Frigo in [103]. With this approach, implementation complexity of an FFT with length N in $FLOP$ (floating-point operations) is given as [103]:

$$FLOP = \frac{34}{9} N \log_2 N - \frac{124}{27} N - 2\log_2 N - \frac{2}{9}(-1)^{\log_2 N} \log_2 N + \frac{16}{27}(-1)^{\log_2 N} + 8 \tag{5.1}$$

For the practical considerations that will follow in this section, the equation (5.1) is approximated as:

$$FLOP \approx \frac{34}{9} N \log_2 N \tag{5.2}$$

The repetition rate at which the FFT needs to be performed by a communication system with bandwidth B and N subcarriers is approximately B/N.[1] As a result, the approximate computational complexity of OFDM chips in $FLOPS$ (floating-point operations per second) yields:

$$FLOPS \approx \frac{34}{9} B \log_2 N \tag{5.3}$$

The main reason for presenting (5.3) is to show the scaling that is associated with the bandwidth and subcarrier increase in OFDM systems. For instance, if the complexity of a WiMedia system, with $B = 528$MHz and $N = 128$ [13], is compared to a IEEE802.11a-g system, with $B = 20$MHz and $N = 64$ [104], it can be observed that the complexity of WiMedia UWB is approximately 30-times higher than the complexity of IEEE802.11a-g systems. Despite recent development of low-complexity, low-power chips for UWB OFDM applications, e.g. [105]-[107], this complexity

[1] This repetition rate neglects the guard interval.

increase is reflected in the cost of the chip. Thus, such complexity increase has to be associated with performance improvement. As will be shown later in this chapter, this is not really the case for WiMedia OFDM. Thus the complexity/cost of the chips that do not provide significant performance improvement over IEEE802.11a-g systems is believed to be the main reason for commercial failure of WiMedia systems. However, as will be presented in subsequent chapters, it is believed that performance justifying the chip complexity increase can be achieved if a few changes are introduced to the WiMedia standard.[2]

5.2 Physical Layer of WiMedia OFDM Systems

The history of the development of the WiMedia standard has been briefly described in section 1.2.2. Here, we focus on the actual physical layer description which is described in the ECMA-368 standard [111]. The physical layer of the ECMA-368 standard has been described in a large number of research papers, e.g. [111]-[113]. The best description of the standard, including an in-depth explanation for any particular choices of the standard is presented in [13]. Here, we present an excerpt of the standard in order to list all the essential properties of the standard. The aim is to introduce the properties of the standard that are deemed important for the subsequent sections of this chapter. More details about the standard can be found e.g. in [13] or directly in the standard [111].

The block diagrams of the WiMedia transmitter and receiver are introduced in Fig. 5.1. The WiMedia standard is an OFDM system [13] with a symbol bandwidth of 528 MHz. The symbol consists of 128 subcarriers spaced by 4.125 MHz [13]. The system is a multiband OFDM system with 14 bands. These bands and their centre frequencies are introduced in Table 5.1. Considering the regulations for UWB emission limits introduced in the introduction in Fig. 1.1, it is apparent that all 14 bands are available only in the USA. In other territories, the number of available bands is typically 4, which reduces the potential for multiuser access.

[2]Recently, the 60 GHz systems have been investigated as potential successor of/replacement for UWB systems [18]. In fact, there already are three co-existing standards IEEE802.15.3c-2009 [108], ECMA-387 [109], and WirelessHD^{TM} [110]. All standards differ in detail but all include the implementation of OFDM with $N = 512$ over bandwidth $B \approx 2$GHz [108]-[110]. It is noted here that for such systems, the chip complexity implementation will further increase and the systems will face similar complexity vs. performance issues as UWB systems.

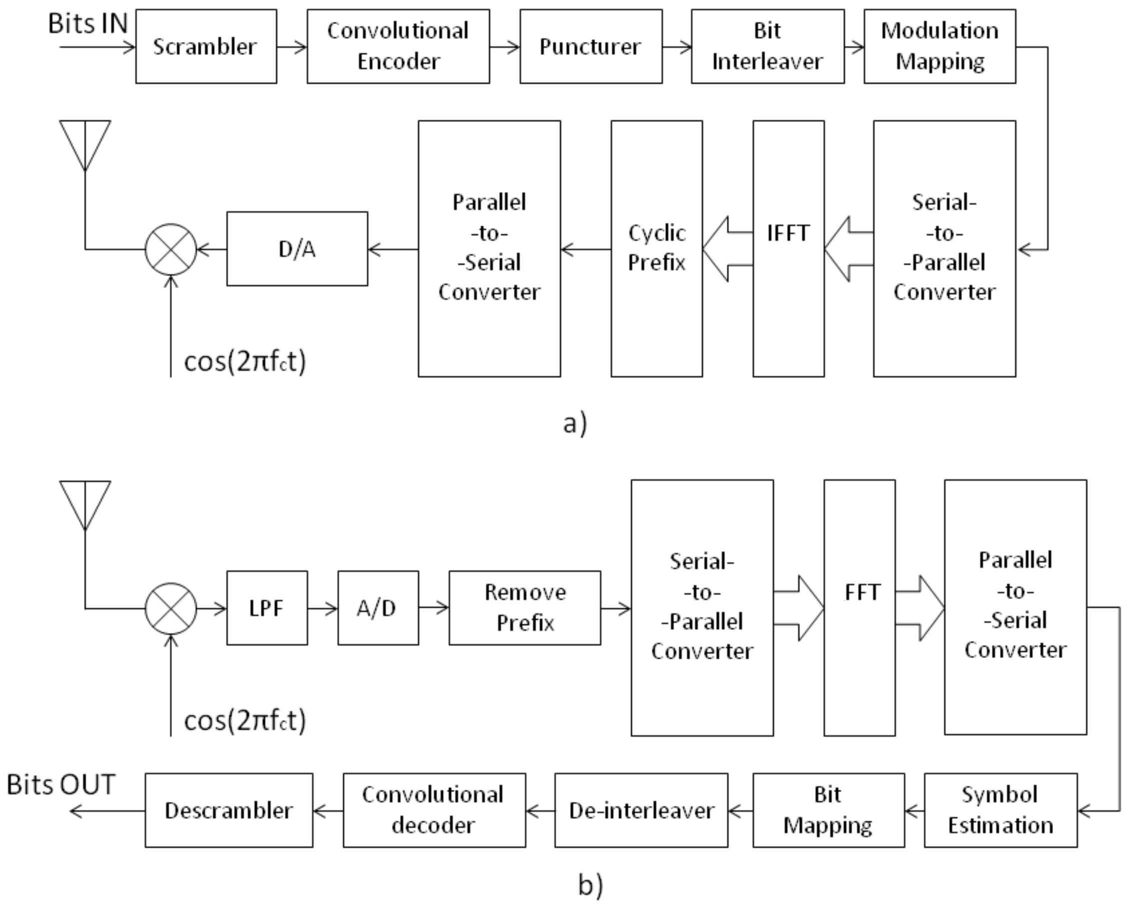

Figure 5.1: Block diagram of Wimedia transmitter (a) and receiver (b) inspired by [114]

Band ♯	frequency span [GHz]	centre frequency [GHz]
Band 1	3.168 - 3.696	3.432
Band 2	3.696 - 4.224	3.960
Band 3	4.224 - 4.752	4.488
Band 4	4.752 - 5.280	5.016
Band 5	5.280 - 5.808	5.544
Band 6	5.808 - 6.336	6.072
Band 7	6.336 - 6.864	6.600
Band 8	6.864 - 7.392	7.128
Band 9	7.392 - 7.920	7.656
Band 10	7.920 - 8.448	8.184
Band 11	8.448 - 8.976	8.712
Band 12	8.976 - 9.504	9.240
Band 13	9.504 - 10.032	9.768
Band 14	10.032 - 10.560	10.296

Table 5.1: The WiMedia Bands, taken from [13]

The OFDM symbol consists of 128 subcarriers spaced by 4.125 MHz. This yields a symbol duration of 242.4 ns which corresponds to 128 samples [13]. The system also includes a zero postfix of 70 ns (37 samples) which eliminates the impact of the Inter-Symbol-Interference [13]. In the receiver the zero postfix can either be removed or it can be used for overlap-add operation. However, the standard does not specify the overlap-add procedure and the manufacturers may or may not opt to use it [13]. Not all of the 128 subcarriers are used for data. The DC component is set to zero and the outer subcarriers are set to zero to minimise the interference to the adjacent band [13]. This leaves 122 active subcarriers out of which the 10 outer subcarriers are used as extension of the guard intervals [13]. To meet the regulatory requirements for emission limits, these subcarriers are copies of 4 closest subcarriers with actual payload [13]. This leaves 112 subcarriers, out of which 12 are used as pilots, leaving only 100 subcarriers for payload [13]. The pilot subcarriers are spaced by 41.25 MHz (corresponds to spacing by 10 subcarriers) throughout the OFDM symbol [13].

The transmission in WiMedia systems can benefit from frequency diversity and by the use of frequency hopping, when consecutive OFDM symbols are transmitted in different bands [13]. Apart from the gain in frequency diversity, the system with frequency hopping can increase the radiated power because the regulations average EIRP spectral density over a period longer than the duration of the OFDM symbol [13]. The standard defines 10 hopping patterns [13]. Four patterns hop over three frequency bands, three patterns hop over two bands only and three patterns have no hopping at all [13].

The WiMedia standard defines 8 data rates (53.3, 80, 106.7, 160, 200, 320, 400, and 480 Mbps) divided into three modes [13]. These rates/modes differ by the subcarrier modulation scheme, the strength of the punctured convolution coding, by bit spreading, and by the minimum required receiver sensitivity [13]. The properties of each data-rate are specified in Table 5.2 and described in detail in subsequent paragraphs.

The two lowest data-rates employ Quadrature Phase Shift Keying (QPSK) which modulates two bits on each subcarrier. The data is spread in frequency and time to reduce the impact of frequency selective fading [13]. This means that each bit is modulated onto four subcarriers. Firstly it is spread in frequency, i.e. each bit is modulated on two subcarriers within one

OFDM symbol [13]. The modulation is performed in such a way that the resulting OFDM symbol exhibits conjugate complex symmetry [13]. This enables simplified FFT analysis at the receiver as the resulting signal is purely real [13] and the imaginary part can be discarded. Secondly, the spreading in time means that the same OFDM symbol is transmitted twice at different centre frequencies (thanks to the frequency hopping) [13]. The receiver uses a maximum-ratio combiner to estimate the spreaded data [13]. The base-rate code used by all the data-rates is a convolutional code 1/3 which is punctured to yield better rates as shown in Table 5.2 [13].

The next three data-rates of the Mode 2 are almost identical to the Mode 1. They differ mainly in the fact that they employ only spreading in the time domain, which doubles the data-rate. On the other hand, this mode is less robust against frequency selective fading and the symbol after the FFT is not purely real which requires more complex processing [13].

The three highest data-rates in Mode 3 do not use any frequency spreading and the implementation of these data-rates is optional [13]. Furthermore, they employ a modulation scheme called Dual Carrier Modulation (DCM). This scheme takes 4 bits and modulates them on two subcarriers spaced by 50 subcarriers. Each subcarriers modulates the 4 bits into a 16-QAM mask (Quadrature Amplitude Modulation (QAM)) in a way that the symbols are neither the same nor conjugate complex [13]. As a result, the Mode 3 can enjoy similar frequency diversity as Mode 2 without spreading [13]. However it must be noted for the same BER, the decoding of 16-QAM symbols requires higher signal-to-noise ratio than decoding of QPSK. This is documented by the increasing requirement on minimum signal power (increase in minimum sensitivity level). Similarly to Mode 2, Mode 3 symbols are not conjugate complex and require

Data-rate	Mode	Modulation	Spreading	Code Rate	Receiver Sensitivity [dBm]
53.3	Mode 1	QPSK	Freq. and Time	1/3	-80.8
80	Mode 1	QPSK	Freq. and Time	1/2	-78.9
106.7	Mode 2	QPSK	Time	1/3	-77.8
160	Mode 2	QPSK	Time	1/2	-75.9
200	Mode 2	QPSK	Time	5/8	-74.9
320	Mode 3	DCM	None	1/2	-72.8
400	Mode 3	DCM	None	5/8	-71.5
480	Mode 3	DCM	None	3/4	-70.4

Table 5.2: The WiMedia data-rates at a glance, data taken from [13]

full FFT processing.

The final blocks in Fig. 5.1 that need to be introduced are the scrambler and interleaver. The objective of the interleaver is to mix the bits from multiple codewords in order to increase robustness of the code against bursts of errors [13]. The scrambler applies a pseudorandom code on the input bits through the logical operation exclusive-OR in order to minimise spectral artifacts in the spectrum of the transmitted signals [13]. If the same operation is applied at the receiver, the input data stream can be fully recovered [13].

Now, the packet structure is briefly discussed. The packets in the WiMedia PHY layer consist of a preamble, header and a payload. [13]. The preamble lasts 30 symbols for the normal mode and 18 symbols for burst mode [13].[3] Its main task is to ensure receiver synchronisation and channel estimation [13]. The header lasts for 12 symbols and contains information for the PHY and MAC layers. This data is further protected by additional channel coding [13]. Finally, the payload has 0-4095 Bytes of data transmitted with the mechanism described above [13]. The length is variable but the default length is 1024 Bytes [13].

5.3 Performance of Practical WiMedia systems

In this section, the range performance of a practical WiMedia system is explored. Firstly, the transmission range estimation using standard link budget analysis is presented and compared to actual range of the Wisair™ DV9110 Development Kit (details about the kit are given in Appendix D). The aim of this section is to show what aspects limit the performance of the WiMedia systems the most. The measures that can be taken to improve the performance are discussed in subsequent chapters.

5.3.1 Transmission Range of Practical WiMedia Systems

5.3.1.1 Discrepancy between Practical Range and Theoretical Estimates

In this section, the transmission range of WiMedia systems is estimated using link budget analysis. The results of the analysis are then compared to the range determined experimentally.

[3] The implementation of the burst mode is optional and differs mainly in the shorter preamble and shorter delay between subsequent packets.

A difference between the results of the estimated and measured range is shown.

Theoretical Range Estimation

The standard and accepted way of range estimation for wireless communication systems, used e.g. in [13],[115]-[117], is based on the analysis of the link budget. A detailed discussion of link budget analysis of WiMedia OFDM devices is presented in [117]. For the theoretical range estimation the same methodology was used. The approach from [117] compares the path-gain of the channel with the dynamic range of the system (given in Table 5.2) considering the effects of spectral flatness and code gains, which can be found in [13]. Resolving the formula yields the estimated range.

The path-gain for the office environment was determined using the IEEE802.15.4a channel model [21] as presented in (3.3), here the equation is repeated for the sake of readability:

$$G_p(r)|_{dB} = G_0|_{dB} - 10n \cdot log_{10}\left(\frac{r}{r_0}\right) \tag{5.4}$$

where $G_0|_{dB}$ represents the path-gain at a reference distance, r_0, and n is the path-gain coefficient. For UWB, the choice of r_0 is 1 m in the IEEE802.15.4a channel model [21]. For an indoor office environment the path-gain parameters are given as [21]: $G_0 = -36.6$dB; $n = 1.63$. The IEEE802.15.4a channel model gives frequency dependency of 3.5 dB/decade [21] which gives a variation of 0.6 dB over the lowest three WiMedia bands that are used by the Wisair$^{\text{TM}}$ DV9110 Development Kit (details in Appendix D) that was used for the performance evaluation of OFDM systems.

Measured Range

The range was determined with the Wisair$^{\text{TM}}$ DV9110 Development Kit (details in Appendix D) by measurement in an office environment. The plan of the office is presented in Fig. 5.2. There were 10 sets of measurements conducted for the LOS condition: five sets for horizontal polarisation and five sets for vertical polarisation of the In4Tel$^{\text{TM}}$ antennas (see Appendix B.3.2). Four measurements were performed across the office in between the tables (horizontal direction in Fig. 5.2) and one measurement was performed along the office (vertical direction in Fig. 5.2). All measurements were performed for the case of frequency hopping over three

WiMedia bands.

The range was determined as follows. The distance between the transmitter and receiver was increased and the Packet-Error-Rate (PER) of the system was measured. The range of the system was determined as the distance for which the PER reached 8%. This choice of PER is not arbitrary. In WiMedia systems, default packets consist of 8192 bits [13], thus PER of 8% corresponds to BER of approximately 10^{-5} [13]. Also according to [13], the WiMedia systems should manifest PER of 8% for the situation when the received signal energy corresponds to the receiver sensitivity as presented in Table 5.2. Our measurements also revealed that the PER of 8% marks a range beyond which the PER starts increasing rapidly.

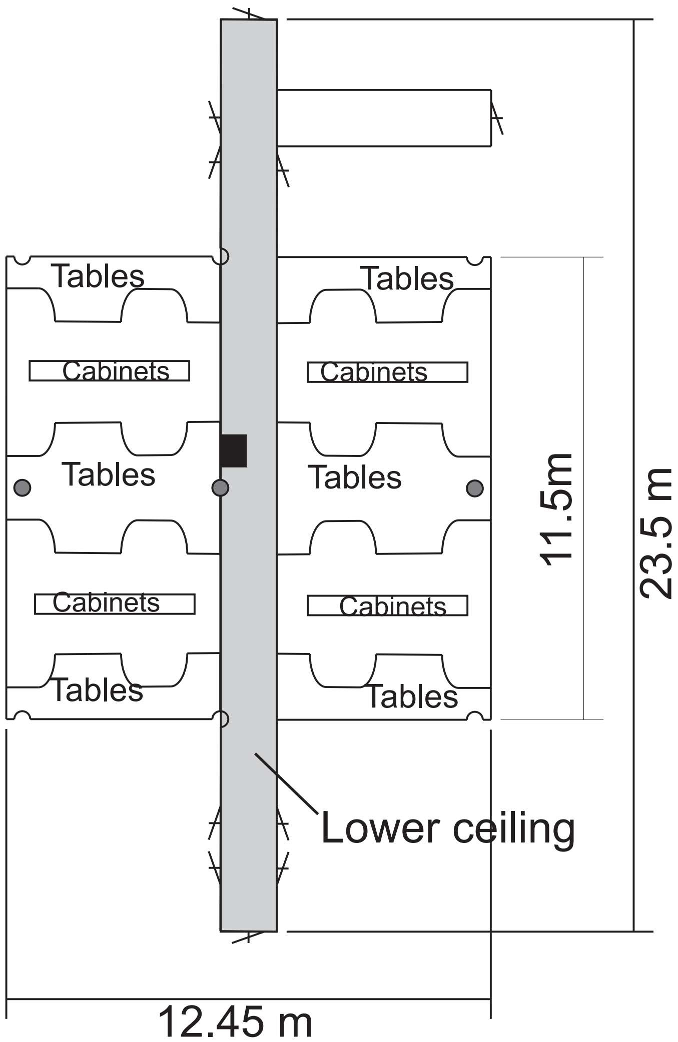

Figure 5.2: The plan of the office environment where the measurement was conducted. The windows are on the left and right hand side of the office, however the glass is covered with metallic foil making the windows similarly significant reflectors as the walls.

Comparison of Results

The results of the theoretical range estimation and of the measured data are presented in Table 5.3. The range for each polarisation was determined as the mean of the five measurements.

Data rate [Mbps]	Mean theoretical range [m]	Range for horizontal polarisation [m]	Range for vertical polarisation [m]
53.3	70.5	8.1	9
80	53.9	7.2	7.9
106.7	46.2	6.6	7.2
160	35.3	5.8	6.9
200	30.6	4.9	6.0
320	22.8	4.7	3.7
400	18.9	3.0	3.1
480	16.2	2.6	1.4

Table 5.3: The theoretical and measured range of WiMedia systems. After our work [118]

As can be seen in Table 5.3, there is a significant difference between the practical and theoretical range of WiMedia systems. On average, the theoretical range exceeds the practical performance by 675%. It may be noted that the path-gain model used in this estimation is optimistic. For instance, reference [115] uses a free space path-gain model with path-gain exponent $n = 2$. However, even these estimates significantly exceed the actual performance. In [115], the theoretical range is 7 m for the data-rate of 480 Mbps and 23 m for the data-rate of 53.3 Mbps. Such estimates are still more than 200% of the real performance.

Such a difference between the theoretical range and practical performance is not unusual. Reference [117] reports similar performance results as in Table 5.3. For instance, [117] notes that a multi-antenna UWB development kit using the lowest three frequency bands fails to provide the 200 Mbps data-rate for LOS condition and range of 6 m, but subsequent independent measurement of the Received Signal Strength Indicator suggests that signal is well above the minimum receiver sensitivity. Hence, the discrepancy between the theoretical and practical range will be investigated in more detail in the next subsection.

5.3.1.2 Frequency Selective Fading - The Range Limiting Factor of UWB OFDM Systems

In this subsection the reasons for the discrepancy between the theoretical and the practical range are discussed and the frequency selective fading is identified as the main range limiting factor. The identification of frequency selective fading as the main range limiter is performed in two steps. Firstly, the performance of the Wisair$^{\mathrm{TM}}$ UWB development kit DV9110 in free space is evaluated. In free space, there is no frequency selective fading as there are no multipath components, which are the reason for frequency selective fading as explained in chapter 3.3. Furthermore the path-gain can be exactly calculated which enables confirmation that the receiver sensitivity is compliant with the Wimedia specifications.

Receiver's Sensitivity

The range measurement of the Wisair$^{\mathrm{TM}}$ UWB development kit DV9110 was repeated in an anechoic chamber which simulates free-space environment. In a free space environment, the path-gain is given as [23]:

$$G_p(r)|_{dB} = -20 \cdot log_{10}\left(\frac{4\pi d}{\lambda_0}\right) \tag{5.5}$$

where λ_0 is the free-space wavelength. In our case, λ_0 was chosen as 7.58 cm which corresponds to the centre frequency of the lowest three WiMedia bands ($f_c = 3.96$ GHz).

To simulate free space transmission, the anechoic chamber available at the University of Oxford was used. This chamber is limited in range, therefore, the measurements could only be performed over a range of 2-3 meters. For longer ranges, the ranges were simulated by reduction of EIRP by calibrated attenuators because in free space, doubling of the distance corresponds to 6 dB increase of loss, as can be seen in (5.5). The measured and estimated range results are presented in Table 5.4.

As can be seen in Table 5.4, the discrepancy between theory and the measurement is significantly less than for the office environment. The average relative error is only 7% and the difference exceeds 10% only in two out of eight cases. The low discrepancy confirms that the receiver sensitivity of the Wisair$^{\mathrm{TM}}$ UWB development kit DV9110 is compliant with the WiMedia specifications on receiver sensitivity.

Data rate [Mbps]	Mean theoretical range [m]	Experimental range[m]
53.3	12.2	10.0
80	9.8	9.5
106.7	8.7	8.9
160	7.0	7.9
200	5.9	6.3
320	4.9	5.3
400	4.2	4.4
480	3.7	3.8

Table 5.4: The theoretical and measured range of WiMedia systems for free-space, table was also presented in [118]

In summary the same range estimation algorithm gives correct results for free space but incorrect results for the office environment. The main difference of the two environments is the presence of multipath components in the office environment. On one hand these components increase the path-gain but on the other hand they also introduce the frequency selective fading, which limits the range as will be shown next.

Frequency Selectivity within OFDM Symbols

In chapter 3.3 the frequency selective fading has been thoroughly described as a variation of the channel energy that occurs with small displacements of the transmitter or receiver. For a single OFDM symbol, it is of interest to what extent does the channel energy change with frequency, i.e. what are the energies of individual subcarriers at the receiver. However, this investigation can be started with equation (3.28) for the normalised channel energy which is for the sake of readability repeated here:

$$CE(f_c) = 1 + \frac{\sum_{k=0,k\neq l}^{K_{DR}} \sum_{l=0}^{K_{DR}} \alpha_k \alpha_l \mathrm{sinc}\left(\pi B(\tau_k - \tau_l)\right) \cos\left(2\pi f_c(\tau_k - \tau_l) - (\theta_k - \theta_l)\right)}{\sum_{k=0}^{K_{DR}} \alpha_k^2} \tag{5.6}$$

As explained in chapter 3.3, for narrowband channels (which is the applicable description of a single WiMedia subcarrier with bandwidth $B = 4.125$ MHz [13]) the term $\mathrm{sinc}\left(\pi B(\tau_k - \tau_l)\right) \rightarrow 1$ and the normalised channel energy is given by the random values of $(\tau_k - \tau_l)$ and $(\theta_k - \theta_l)$ which determine the magnitudes and signs of the cos-terms.

For a single OFDM symbol the $(\tau_k - \tau_l)$ and $(\theta_k - \theta_l)$ can be assumed to be the same for all subcarriers because as shown in Fig. 2.4 in chapter 2, well designed UWB antennas do not significantly change their current distribution (hence radiation properties) for a frequency change of up to 1 GHz. Similarly, the free-space path-gain (5.5) which has the main impact on the magnitude of α_k does not change much for a change in frequency of 500 MHz.[3] In other words, the channel can be assumed to be static across all the subcarriers.

However, for each subcarrier the cos-terms have different centre frequency f_c which causes a significant variance of $CE(f_c)$ across the entire 528 MHz of the OFDM symbol. Using the data from the IEEE802.15.4a channel model [21] and considering the modifications introduced in chapter 3.2 the mean $(\tau_k - \tau_{k-1})$ for an office environment is approximately 5 ns. If these 5 ns are multiplied with the 528 MHz bandwidth of the OFDM symbol, we can see that within the subcarriers of a single OFDM symbol, the argument of all cos-terms changes by 5.28π. Thus there will be significant variation of energies among the subcarriers as shown in Fig. 5.3.

Fig. 5.3 was obtained as a result of channel measurement in the office environment. The measurement was conducted with a Vector Network Analyser with wideband Radio-over-Fibre link as presented in appendix B with the In4Tel^{TM} antenna (see appendix B.3.2). The frequency range of the measurement was 3-6 GHz (but only the first three WiMedia bands were analysed). The measurement was performed for 10 different distances (1-10 m). For each distance it was repeated for four positions of the receiver (receiver positioned in corners of a square 5×5 cm, which was chosen as a half-wavelength at 3 GHz). The measurements were performed for vertical polarisation only.

Fig. 5.3 presents the spread of the power spectral densities corresponding to subcarriers. It shows the energies of the WiMedia Band 2 (3.696 - 4.224 GHz) and the data are combined for all four measurement positions. The spread is shown by the means of median and percentiles 2.5, 10, 90, and 97.5. The figure shows that the spectral density changes by 20 dB between the weakest and strongest subcarriers. Fig. 5.3 also plots the noise floor and the power spectral density corresponding to receiver sensitivities for data-rates 480 Mbps and 53.3 Mbps as

[3]The biggest change appears for the frequencies in the lowest WiMedia band but even for this case, the change of path-gain between the lower and upper frequency end of the Band 1 (see Table 5.1) according in Eq. (5.5) is 2.5 dB which is not so significant considering that free space path loss at 3 GHz and distance of 1 m is -42 dB. For the WiMedia bands complying to the EU emission limits, the change in α_k within the OFDM symbols above 6 GHz is below 0.7 dB.

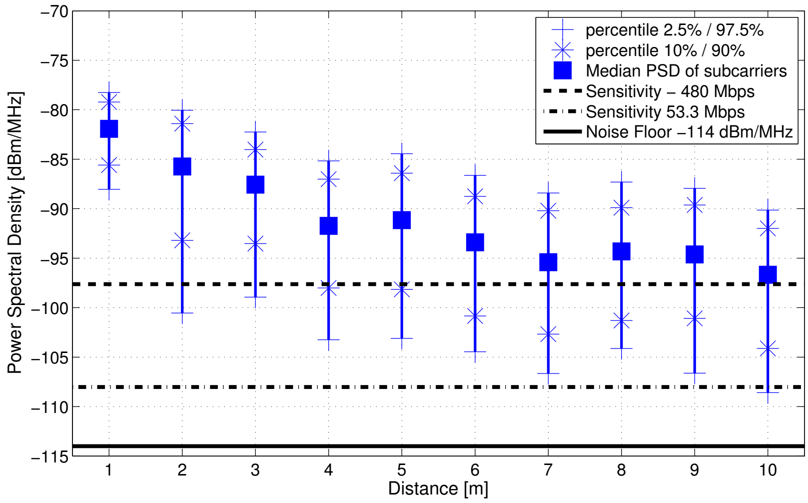

Figure 5.3: The measured spread of the subcarrier energies as a function of distance in the office environment. © 2012 IEEE. Reprinted, with permission, from our work [118].

specified by the WiMedia standard [13].

The analysis of data in Fig. 5.3 can firstly be used to show the following. The mean path-gain $G_0|_{dB}$ at 1 m is $G_0|_{dB} = -40$dB. This is less than the -36.6 dB for the office environment as listed in the IEEE802.15.4a model [21] but the path-gain index n of the measurement is approximately 1.5 which is less than the 1.63 predicted by the model [21]. In other words, in this specific office environment the path-gain is lower for short distances but it decreases slower than in the case of the IEEE802.15.4a. The discrepancy evens out over distance. Overall this discrepancy is not large enough to justify the difference between the theoretical range and the actual range of the development kit in Table 5.3.

In a nutshell, analysis of the path-gain refutes the possible hypothesis that the discrepancy between the theoretical and practical range of the WiMedia system shown in Table 5.3 is caused by the fact that the path-gain in this specific office is significantly lower than in an average office described by the IEEE802.15.4a channel model for offices.

Secondly, the analysis shows that frequency selectivity causes spread of subcarrier energies by about 20 dB and that many of the weak subcarriers have energy below or comparable to the receiver's sensitivity. These subcarrier then contribute the most to the gross BER before channel coding. The channel coding [13] (and the spreading of information for the lower data-rates [13]) helps to mitigate the net BER. However, the mitigation is often not sufficient to provide net BER yielding an acceptable PER. This is caused by the choice of the packet size. In WiMedia the default packet size is 8192 bits. If ideal interleaving of the bits is assumed the PER can be expressed as follows [13]:

$$PER = 1 - (1 - BER)^N \tag{5.7}$$

where $N = 8192$ is the number of bits in the packet. It can be shown that for this large number of bits per packet, the PER reaches significant values even for a BER acceptable for most wireless services. For instance, $BER = 10^{-6}$ yields $PER = 0.01$, $BER = 10^{-5}$ yields $PER = 0.08$, and $BER = 10^{-4}$ yields $PER = 0.56$.

This issue is illustrated in Fig. 5.4, which analyses one set of measurements of subcarrier energies presented in Fig. 5.3. For the subcarrier energies, the gross BER was calculated for the bit rates of 53.3 and 200 Mbps using the WiMedia specifications from [13] and the well known formulas for BER dependency on SNR for QPSK included in standard textbooks, e.g. [34], [94]. Then, the net error rates were calculated considering code specifications in the WiMedia standard [13]. Finally, the PER was calculated using (5.7).

As can be seen on the results, the channel coding can significantly mitigate the gross-error rates. However, even then the PER yields quite large values. For the data-rate of 53.3 Mbps the range for which PER becomes 1 corresponds well to the empirical range determined in Table 5.3. The same applies to the data-rate of 200 Mbps, if the peak for a distance of 4 m is neglected. The peak at the distance of 4 m can be explained as follows. The gross BER for 4 m yielded $1.06 \cdot 10^{-2}$ and for 5 m it yielded $1.04 \cdot 10^{-2}$. These values are at the limit of the strength of the channel coding. As a result, if the channel coding is applied, the net BER yields $4 \cdot 10^{-3}$ for 4 m and $1.6 \cdot 10^{-9}$ for 5 m. This has an enormous impact on the PER but the actual relative difference in the gross BER is about 2%. The measurements of the channel with the VNA and the range measurement with the development kit were not performed at the same time hence the channel was not exactly the same for both experiments (minor movements of the computer monitor, presence of the VNA etc.). As a result, it is perfectly plausible that for the experiment with the development kit, the gross BER could have been just below the

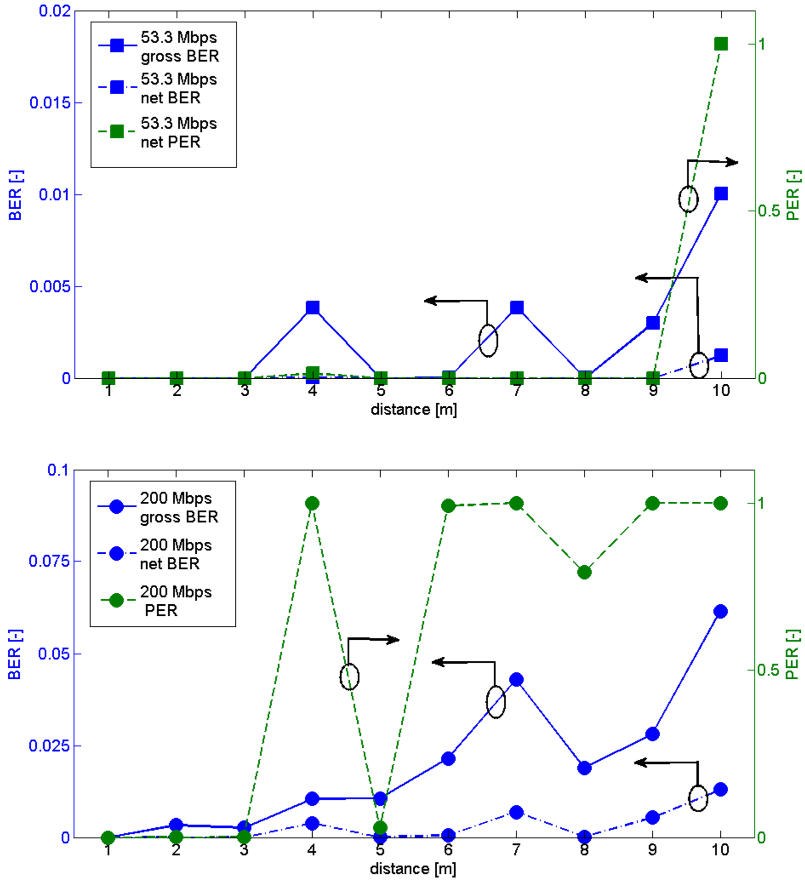

Figure 5.4: The analytical BER and PER as a function of the distance calculated using channel measurement. The vertical axis is in linear scale as in many cases the net BER (after channel coding) can yield a zero value. As a result, the PER can also assume zero value. Only the gross BER is always non-zero. © 2012 IEEE. Reprinted, with permission, from our work [118].

strength of the code and no significant increase in PER was observed.

The summary of this analysis is following. The frequency selective fading causes significant variation of the energies of individual subcarriers. These variations are up to 20 dB and result in the fact that the subcarrier with the lowest energy contribute significantly towards the gross BER of OFDM symbol. This is mitigated by the channel coding but even small net BER can yield significant PER due to the large packet size. Before, proceeding to the proposal on how to mitigate this issue, the following question arises. Why are other OFDM systems such as the IEEE802.11 or DVB so successful with OFDM even if they are subject to similar fading?

This question is answered by Fig. 5.5 which was obtained in the same way as Fig. 5.3 but the measurement was performed with the discone antenna in the frequency band 5 - 6GHz. The

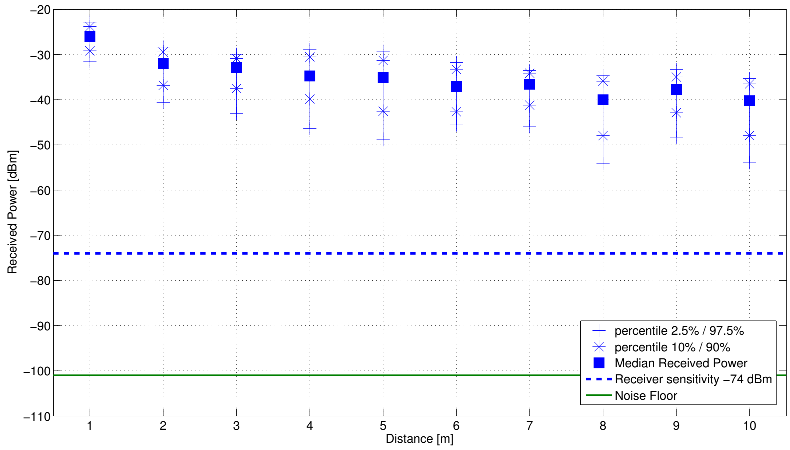

Figure 5.5: The measured spread of the subcarrier energies for a 5 GHz IEEE 802.11 system as a function of distance in office environment.

operation of a IEEE802.11 system [104] in the UN-II band, i.e., 5.15-5.35 GHz was analysed. The EIRP was selected to be 150 mW, which is well within regulatory limits. Fig. 5.5 shows also the noise floor, which yields -101 dBm for 20 MHz bandwidth, and a receiver sensitivity of -74 dBm, which according to a market study is the standard sensitivity for systems operating at 54 Mbps. As can be seen, the spread of the subcarrier energies remains approximately the same as in the UWB case (up to 20 dB), but due to the available dynamic range even the weakest subcarriers posses SNR in the magnitude of about 20 dB. Hence, the fading does not impact the performance because the weakest subcarriers do not manifest as stark increase of BER as in the case of UWB. As a result, the range of IEEE802.11 is dominated mainly by the path-loss. Especially since for ranges $>$ 10m in indoor environments, the path-loss is typically dominated by the penetration through walls between transmitter and receiver.

5.4 Performance of WiMedia systems: Conclusions

To conclude this section it has been shown that the range of WiMedia UWB OFDM system is significantly below the range estimated by the standard link budget analysis. It is shown that this is caused by the combination of low dynamic range and frequency selective fading. As a result, the subcarriers with the lowest energy contribute the most towards the gross BER. Even when the channel coding can remove a large number of errors, its performance is mitigated by the the large packet size. As a result, it can be stated that the frequency selective fading limits the performance.

The conclusion for an end-user considering range of 4-10m is that WiMedia systems do not significantly outperform IEEE802.11 systems. In fact, considering IEEE802.11n devices, WiMedia systems provide inferior performance. If this conclusion about performance is combined with the complexity of the WiMedia systems, which exceeds the complexity of IEEE802.11 systems by a factor of 30 as discussed in Section 5.1, it explains the commercial failure of UWB described in the introduction of this thesis and earlier in this chapter.

However, the understanding of the causes of performance limitations may enable us to make improvements. In the rest of the thesis, it will be shown that the knowledge of the UWB wireless channel, as introduced in chapter 3, and the understanding of how it limits performance of the wireless channel can be utilised to significantly enhance the performance of UWB OFDM systems. There are three main ways to improve the performance of UWB OFDM systems.

- **Reduce the packet size** This is an apparent choice based on equation (5.7), however it must be noted that reducing the packet size increases the relative size of the overhead and reduces the relative payload. The packet size optimisation will not be discussed in this thesis. It is noted that it might help to improve the system's performance but it does not address the underlying issue which is the impact of frequency selectivity.
- **Use adaptive OFDM** Adaptive OFDM changes the subcarrier modulation based on its energy. Subcarriers with high energy use high order modulation and subcarriers with low energy might not be used at all. This approach is discussed in Chapter 6
- **MIMO UWB systems** MIMO UWB systems can be used to either increase the received energy, to reduce the spread of the energies of received subcarriers or a combination of both. Two examples of MIMO UWB systems are discussed in chapter 7.

It is noted here that the main aim of chapters 6 and 7 is not to propose the 'optimal' UWB OFDM scheme, instead the chapters explore performance improvements associated with modifications to the existing WiMedia scheme so that the experience and know-how acquired during the development of WiMedia systems can be re-used to develop competitive systems at feasible costs.

CHAPTER 6

Adaptive OFDM Systems for UWB

The idea of adaptive OFDM systems is not new. In fact there is a large number of publications that investigate adaptive OFDM schemes for wideband systems, e.g., [119]-[121]. There is also a significant amount of work focusing on adaptive OFDM in UWB systems [122]-[125]. The conclusions of the references cited above indicate that the performance of OFDM systems with adaptive loading of subcarriers is more power efficient and achieve BER performance superior to OFDM systems with constant loading. This supports the conclusions in chapter 5.

This chapter aims to evaluate the contribution of Adaptive OFDM to UWB systems and to discuss some practical challenges associated with its deployment. Firstly, the performance of the adaptive OFDM in the empirical channels from chapter 3 is presented as a motivation and justification for the investigation of the UWB systems with adaptive OFDM subcarrier loading. Secondly the chapter discusses the state-of-the-art channel estimators for OFDM systems because all the references above stress the importance of channel estimation as a prerequisite for adaptive loading of subcarriers in OFDM symbols. Thus this chapter reviews the available channel estimation algorithms for OFDM and discusses their suitability for WiMedia UWB systems. The choice of estimator type has implications on the system performance. Hence the spatial stationarity of the channel is discussed. Finally, the performance of adaptive OFDM scheme in an office environment is shown and compared with fixed OFDM similar to the WiMedia standard in order to show the superiority of the approach.

6.1 Initial Evaluation of UWB Systems with Adaptive OFDM

As mentioned in the introductory paragraph of this chapter, the idea of adaptive bit loading in UWB OFDM systems is not new and has been proposed before. References [122], [124], and [126] describe the increase of data rate and the increase of efficiency associated with the adaptive bit loading. However, references [122] and [126] present only simulations using the channel impulse responses from the IEEE802.15.4a channel model [21]. Reference [124] presents results for a real measurement but only for 8 measurements obtained for 2 distances, 2 orientations of planar monopole antennas (”face-to-face” and ”side-by-side” [121]) and 2 conditions (LOS and NLOS). References [123] and [125] consider MIMO systems, which will not be considered at this stage of the thesis because chapter 7 is devoted solely to UWB MIMO OFDM systems. In contrast to works [122], [124], and [126], this section presents the statistical performance evaluation of a sample adaptive OFDM system based on investigation of multiple frequency bands for 9,600 measurement points. The channel measurements used in chapter 3 and described in detail in appendix C are used. The data consists of six measurement sets, each of which provides information about 1,600 channels. The performance of a UWB OFDM system with adaptive subcarrier loading was studied for all these channels. Before the results are presented, UWB OFDM systems with adaptive subcarrier loading is introduced in the next paragraph.

Perhaps the main motivation for this chapter is to show how minor modifications can improve the performance of the WiMedia system. Hence, the theoretical system considered for the evaluation here is strongly inspired by the WiMedia OFDM standard. The OFDM symbols have 128 subcarriers spaced by 4.125 MHz and the positions of guard, pilot and data subcarriers is the same as in the WiMedia standard (described in detail in chapter 5). It is assumed that perfect knowledge of the properties of the wireless channel is available at the transmitter and at the receiver. The transmitter selects the modulations scheme for each subcarrier based on the knowledge of its E_s/N_0 at the receiver. E_s is the energy per symbol, N_0 is the noise spectral density at the receiver. Noise level of $N_0 = -101.3$ dBm/MHz is selected. This is selected based on the sensitivities of the receivers in the WiMedia standard and also because it corresponds to values typically considered in evaluations of performance of UWB systems [6]. The level is 12.7 dB above the -114 dBm/MHz noise floor, such a level is certainly achievable with the available UWB amplifiers with noise figures in the range 4-5 dB, e.g. [127],[128]. The modulation scheme for each subcarrier is selected out of four options:

- $E_s/N_0 < 10.5$dB - subcarrier switched off
- $10.5\text{dB} \leq E_s/N_0 < 17$dB - QPSK
- $17\text{dB} \leq E_s/N_0 < 24$dB - 16-QAM
- $24\text{dB} \leq E_s/N_0$ - 64-QAM

These values for E_s/N_0 were determined so that the BER in any subcarrier does not exceed 10^{-2}. The BER of 10^{-2} is selected as a limit because it appears that the codes in the WiMedia standard are capable of correcting BER below this level as was shown in the example in chapter 5. The BER performance for each of these modulation schemes given in [34], [94] is:

$$BER_{QPSK} = 0.5 \cdot \mathrm{erfc}\sqrt{\frac{1}{4}\frac{E_s}{N_0}} \tag{6.1}$$

$$BER_{MQAM} = \frac{2}{\log_2 M}\left(1 - \frac{1}{\sqrt{M}}\right) \cdot \mathrm{erfc}\sqrt{0.75\frac{\log_2 M}{4(M-1)}\frac{E_s}{N_0}} \tag{6.2}$$

where erfc is the complementary error function, M is the number of modulation points in the M-QAM grid.

The performance of such a UWB system with adaptive subcarrier loading is presented in Fig.6.1. Fig. 6.1 shows the achieved data-rate and corresponding BER for the measurement grid 2 with mean distance between transmitter and receiver of 1.05 m (see appendix C). The figure presents 8 graphs arranged in 4 rows and 2 columns. Each graph shows either the data-rates or BERs. The values in the graphs are colour-coded, each point in each graph corresponds to a single measurement point, the plots have size 40×40 data-points which corresponds to a grid with a physical size 23.4×23.4 cm. The achieved data-rates are presented in the left column, the BERs are in the right column. Each row corresponds to a different frequency band. The bands shown are WiMedia band 2 (f_c = 3.96 GHz [13]), WiMedia band 5 (f_c = 5.544 GHz [13]), WiMedia band 8(f_c = 7.128 GHz [13]), and WiMedia band 14 (f_c = 10.296 GHz [13]). The mean data-rates and the centre frequencies are in the title of each graph. It is noted that the BER is the gross BER excluding channel coding and the data-rates do not consider packet preambles and headers.

The following observations can be made based on the graphs. The data-rate achieved for the WiMedia band 2 reaches a mean of 877 Mbps. However the data-rates drop significantly with the frequency. For the highest WiMedia band there are even points for which the data-rate is zero. For these points, none of the subcarriers had sufficient energy to enable at least the QPSK modulation. This is not surprising because the increase of frequency by a factor of 3.4 between 3.1 GHz and 10.6 GHz corresponds in free-space to a path loss increase of 10.6 dB. There is

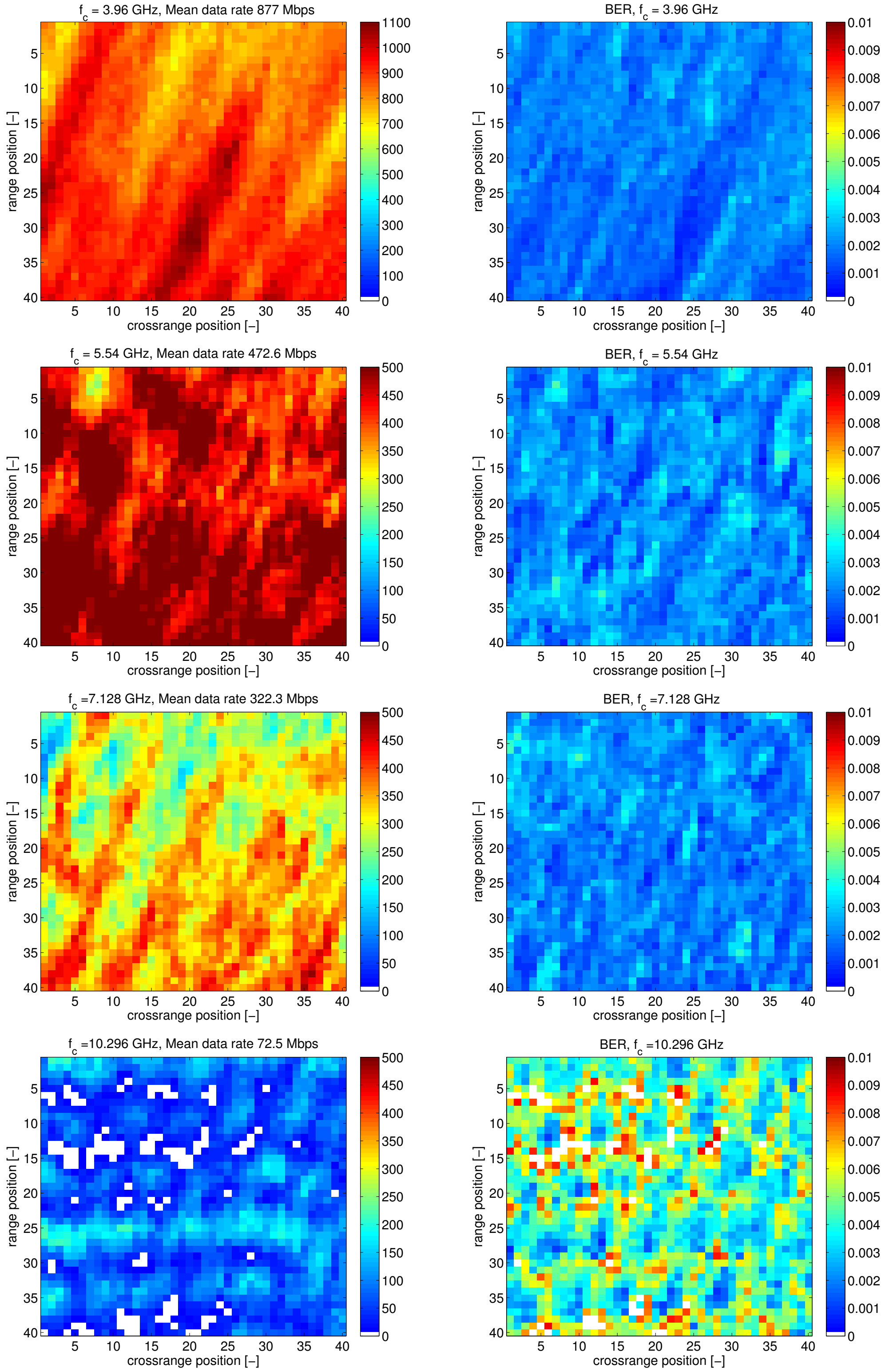

Figure 6.1: The theoretical data-rate and BER of a UWB system with adaptive OFDM for a grid of 1,600 measured channels for a TX-RX distance of 1.05 m. For the white positions in the last row no subcarrier met the minimum requirement E_s/N_0 for QPSK modulation.

also a change in the radiation pattern of the antennas. The gain increases but the maximum direction of radiation elevates as shown in Fig. B.9, hence the gain in the direction of the direct path remains constant or even decreases. A change of path loss by 10 dB is significant for a system with dynamic range of 60 dB as is the case for this theoretical UWB system with adaptive OFDM.

However, the performance of the system seems to be satisfactory - for instance in the band 8 at $f_c = 7.128$ GHz which approximately corresponds to the centre frequency of the EU UWB band, the system would still provide a mean output of 322 Mbps.[1]

Apart from the issue for highest frequencies, it can be observed that the system performance is almost independent of the position with approximately the same data-rate across the entire measurement grid. The same applies to the BER which remain safely below the selected target level of 10^{-2}. In fact in most cases the BER is below $5 \cdot 10^{-3}$. The main observation that can be seen in Fig. 6.1 are:

- The data-rate of an adaptive OFDM system can significantly outperform the systems with fixed OFDM, this confirms conclusions from [122]-[125].
- The data rate achieved by a system is stable within a grid of 23.4×23.4 cm.
- The performance deteriorates significantly with the increase of centre frequency.

The impact of the centre frequency is further investigated in Fig. 6.2. Fig. 6.2 presents the achievable data-rate for position 2 from appendix C (TX-RX distance of 1.05 m) for all 14 WiMedia bands [13]. The centre frequencies of each band are plotted on the horizontal axis. The vertical axis presents the achieved data-rate. The square represents the mean data rate and the crosses below and above show the mean +/- the standard deviation determined over the 23.4×23.4 cm grid.

The following observations can be made based on Fig. 6.2. Firstly, the figure confirms that the mean achievable data-rate decreases with the frequency, but it can be noticed that with the exception of the band 5-7 GHz, the performance difference between adjacent bands is almost

[1]This appears low given the commercial UWB development kit provided 480 Mbps for a mean transmission range of 1.5 m. However, it must not be forgotten that the kit operated only in the lowest three WiMedia bands. Band 8 corresponds to doubling of the centre frequency which in free-space would correspond to a path loss increase by 6 dB. Also, no frequency hopping is considered, i.e. the radiated power is 4.7 dB below the WiMedia development kit.

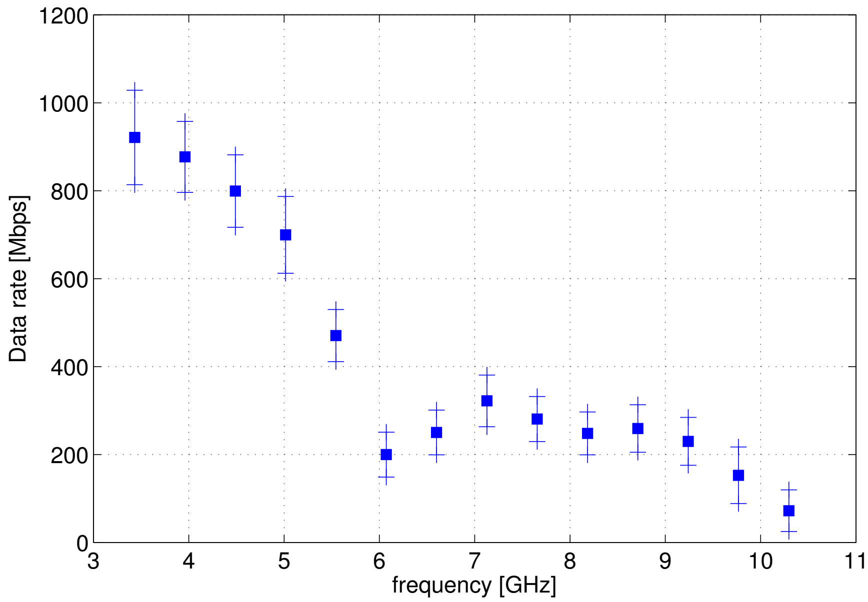

Figure 6.2: The theoretical data-rates of a UWB system with adaptive OFDM for a grid of 1,600 measured channels for a TX-RX distance of 1.05 m for all 14 WiMedia bands. The mean is presented by the squares, the mean+/-standard deviation by the crosses.

negligible. The performance drop for 6 GHz is noted and explained by Fig. 6.3.

Fig. 6.3 shows the channel transfer function measured at the centre of the grid investigated in Fig. 6.2. It explains performance dip at 6 GHz in Fig. 6.2. Firstly, a 5 dB step in the transfer function can be seen at approx. 5.4 GHz. This dip is believed to be caused by the change in

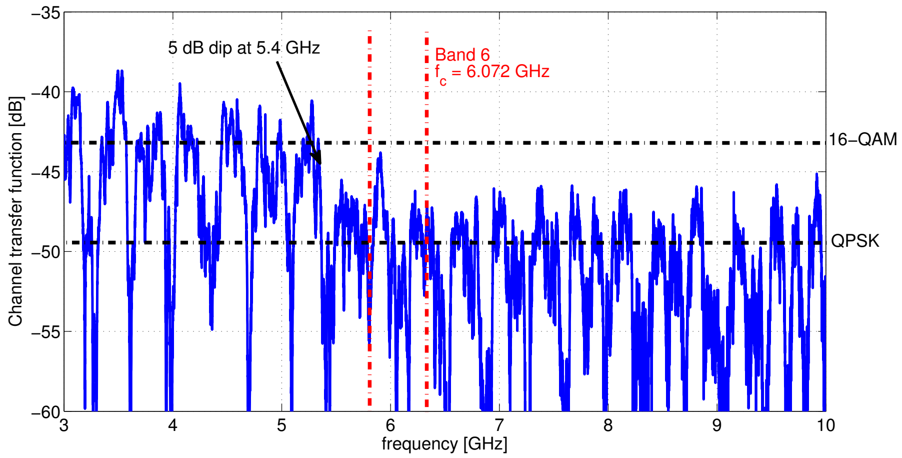

Figure 6.3: Example of channel transfer function for a position in the centre of the measurement grid. The decision levels for QPSK and 16-QAM are highlighted by the horizontal black lines, WiMedia band 6 is highlighted by the red vertical lines.

the radiation pattern of the antenna, when the radiation maximum elevates (see Fig. B.9) and the maximum gain does not cover the direct path anymore. This dip can also be compared to the horizontal lines that show the selected levels for the selection of QPSK and for the selection of 16-QAM. As can be seen, there is no subcarrier above 5.4 GHz that would enable the 16-QAM modulation. Secondly, the 6 GHz band is highlighted by red vertical lines and it can be seen that there is a large 200 MHz wide deep fade just around the centre frequency which causes a number of subcarriers to be switched off/not used. The position of the fade and its width are given mainly by the combination of antenna radiation pattern and by the time- and angle-of-arrival of individual paths. It is true that similar fades are in other bands as well but this one is the widest. Also for other bands, the fades are often divided between two adjacent WiMedia bands whereas this fade is fully in band 6. It is believed that in the case of a system with antennas more suitable for radiation around 6 GHz, i.e. main radiation direction would remain in the horizontal plane, the system performance would improve. Analysis of Fig. 6.3 also shows that further performance improvement, especially for frequencies above 5.4 GHz, could be achieved if an additional level for 8-QAM is introduced. This additional level will be considered in subsequent sections of this thesis.

Fig. 6.2 also allows us to comment on the stability of the achieved data-rate for a small local displacement. The standard deviation decreases with the frequency but this is mainly due to the fact that so does the mean. In fact the relative ratio of standard deviation-to-mean increases from about 10% for 3 GHz to about 35% for 10 GHz. There are two main causes for the variation: the path gain change and the change of the wavelength. The distance between TX-RX was varied by +/- 12 cm around the grid centre. This represents 10% of the mean distance of 1.05 m which impacts the path loss. The relative change of the path loss within the grid (between the closest and farthest points from the receiver) is the same for all frequency bands. However, for the higher frequencies this change of path loss is sufficient to enable more subcarriers to be switched on for the close measurement points than for the far measurement points. This is then reflected by a larger relative spread.

Additionally, the grid corresponds to two wavelengths at 3 GHz but it is 6-7 wavelengths at 10 GHz. This means that for each subcarrier there will be more maxima and minima within the grid at 10 GHz than at 3 GHz. As a result, the relative variation of data-rate will increase with frequency. However, for the bands 1 - 12 the achieved data-rate is stable above 200 Mbps which confirms the feasibility of the adaptive approach. With regards to the value, it is also noted that this performance is achieved for typical mean BER below $5 \cdot 10^{-3}$ as was shown in Fig. 6.1. If an increase of the gross (uncoded) BER was allowed, it would also help to significantly improve the data-rate performance. However, it would also reduce the system's robustness to channel changes due to temporal fading as will be discussed in section 6.3.

So far, the performance over frequency has been studied. In Fig. 6.4 the peformance of the system for the WiMedia band 2 (f_c = 3.96 GHz [13]), WiMedia band 5 (f_c = 5.544 GHz [13]), WiMedia band 8 (f_c = 7.128 GHz [13]), and WiMedia band 14 (f_c = 10.296 GHz [13]) is presented as a function of distance. Fig. 6.4 shows the mean achieved data-rate and the standard deviations for all six sets of measurements that are presented in appendix C. The horizontal axis presents mean distance of each measurement grid. For each position, four data-sets have been measured for each one of the above mentioned frequency bands. The reduction of the data-rate with distance is not surprising. However, if the result for the 3.96 GHz is observed the results still confirm that even for a distance of 2.8 metres, the data-rate is significantly above the empirical performance of a WiMedia system for which 3 m represents the maximum range for 400 Mbps for a system with frequency hopping (see Table 5.3) whereas here no hopping has been considered.

This section has showed that a realistic UWB system with adaptive loading of the OFDM symbol is poised to exceed the performance of current WiMedia systems. Thus, it justifies further investigation that will be presented in this chapter. These examples enable one to understand the limitations of the system as well as to suggest improvements. For instance, based on these observations in subsequent sections, the performance will be optimised by the introduction of a further decision level for subcarrier loading by 8-QAM.

6.2 Channel Estimation Algorithms

Channel estimation in OFDM systems has been of interest since the beginnings of the OFDM systems because channel estimation is required for coherent detection with non-constant symbol

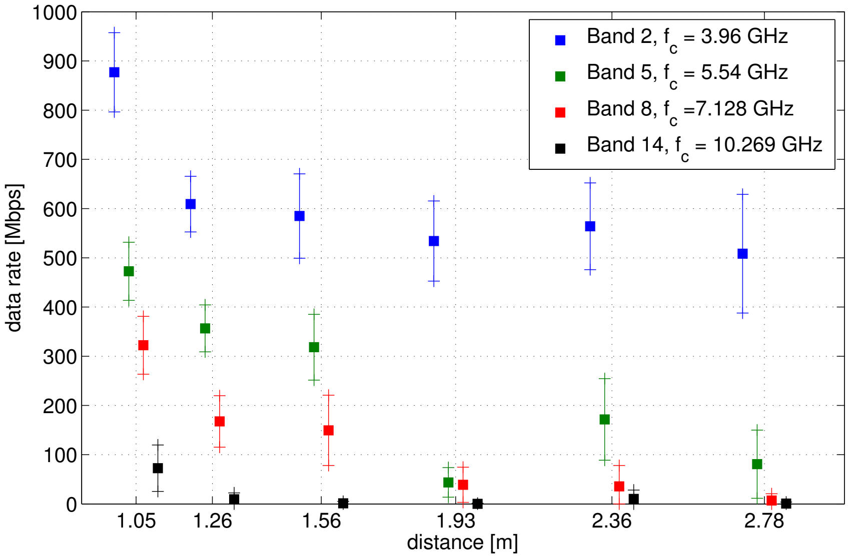

Figure 6.4: The theoretical data-rates of a UWB system with adaptive OFDM for a grid of 1,600 measured channels for a variable TX-RX distance. The mean is presented by the squares, the mean+/-standard deviation by the crosses.

amplitude (e.g. 16-QAM) [129].[2] As a result a number of approaches can be found in the open literature. They can be divided into two groups [130]: comb-type pilot arrangement and block-type pilot arrangement, both introduced in Fig. 6.5.

In the **comb-type pilot arrangement** systems, a number of subcarriers in every transmitted OFDM symbol and the information about the channel at these fixed pilot frequencies is used to estimate the channel at frequencies between the 'comb's teeth' [130]. The **block-type pilot arrangement** systems periodically transmits a single or multiple OFDM symbols as a pilot. Channel estimation from this pilot is then used for all subsequent OFDM symbols until a new pilot is sent [130].

The main advantage of the comb-type pilot arrangement over the block-type pilot arrangement is the fact that the channel estimate corresponds exactly to the current state of the channel and it can react to temporal fading[3] , because the block-type systems have no means to react to slow

[2] In systems with constant amplitude (e.g. QPSK), full channel estimation is not necessary. In these system coherent detection requires only phase shift information which can be obtained from pilot subcarriers with significantly less complexity than in the case of full channel estimation [13],[111].

[3] Temporal fading is the change of channel properties in time [8]. There are two types of temporal fading - slow fading and fast fading. In slow fading, the channel properties do not change during transmission of a symbol [8] (some studies even consider the channel constant for the packet duration [131]). In fast fading the channel properties change during the transmission of a single symbol. It is noted that chapter 3 discussed only a static channel, i.e. the environment did not change. However, the spatial fading characteristics in chapter 3 can be used for characterisation of temporal fading because both phenomena are connected, i.e., the main

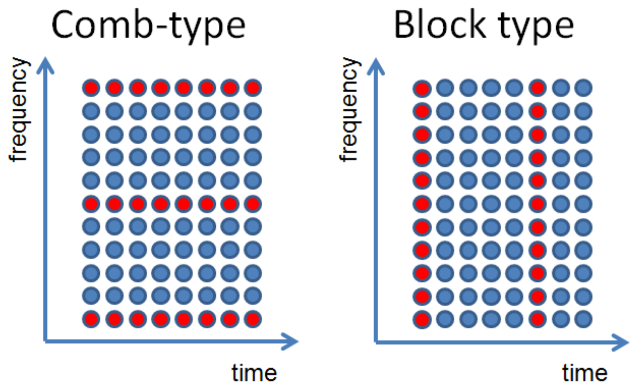

Figure 6.5: The position of pilots (red dots) and data symbols (blue dots) in an OFDM symbol for block-type and comb-type channel estimators.

fading that alters the channel between the transmission of the pilot OFDM symbols. On the other hand, the block-type has access to the full channel state information for every frequency and its 'momentary' estimates can therefore be more precise. In this section we discuss the performance of both methods in UWB systems with adaptive OFDM modulation.

The WiMedia systems are 'ready' for both approaches. As discussed in chapter 5, each symbol contains 12 pilot subcarriers that are used for phase correction [13]. The packet structure also foresees a preamble that contains six pilot OFDM symbols for channel estimation (in case of frequency hopping over three bands, there are two pilot OFDM symbols for each frequency band) [13]. The WiMedia systems also foresee channel estimations using these pilot symbols because they need phase estimation for QPKS symbols and amplitude estimation for the Mode 3 with Dual-Carrier-Modulation [13], however the standard does not specify the estimation [111]. The following subsections, review the comb-type and the pilot-based estimation algorithm and their suitability for UWB WiMedia systems is discussed.

6.2.1 Comb-Type Pilot Channel Estimators

At first, the comb-type estimators seem to be more suitable for WiMedia UWB systems because the standard already defines 12 pilot subcarriers spaced by 41.25 MHz [13] and it would seem natural to use these subcarriers as an approach to eliminate the issue of temporal fading. However, as will be discussed here there are some issues with the application of the comb-type

cause of temporal fading is the movement of transmitter/receiver which corresponds to spatial fading.

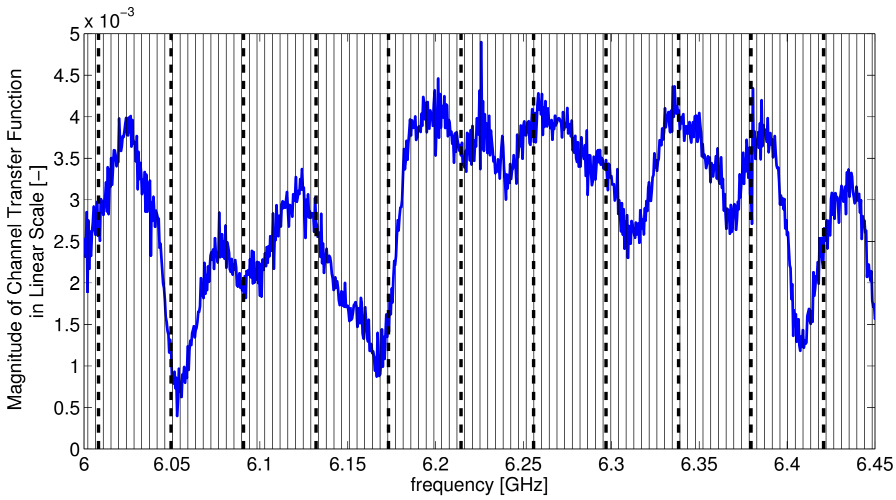

Figure 6.6: An example measured magnitude of channel transfer function measured in linear scale. The thick black dashed line represent the pilot spacing of subcarriers in WiMedia UWB systems. The thin solid black line represent the subcarrier spacing in an IEEE802.11.a system.

estimators in the UWB framework. This will be shown on the example of three comb-type estimators that are most common in the literature. These are [130],[129],[132]:

- Interpolation Algorithms
- Autocorrelation Matrix Algorithms
- Parametric Channel Modeling

The **Interpolation Algorithms** represent the most simple method for channel estimation. As the name already suggests, the channel between the known pilots is obtained by the means of interpolation. The interpolation methods used in literature are [130], [132]: linear, second order interpolation, low-pass interpolation, spline cubic interpolation, and time domain interpolation. According to [130], the time domain interpolation is not suitable for UWB WiMedia systems because of time domain signal aliasing after the Fourier Transform.[4]

Even though the performance of the Interpolation Algorithm is considered good in [130], they do not provide enough performance for WiMedia UWB OFDM. This is caused mainly by the UWB bandwidth. For a IEEE802.11a system there are 4 pilots spaced by 4.375 MHz [104]. For such frequency spacing, the channel transfer function is highly correlated and the interpolation

[4]The duration of the Fourier Transform based on 12 subcarriers is approx. 22.7 ns (= 12 × 1.89ns where 1.89ns is system's sampling time). The maximum delays in UWB channels often exceed this duration thus the periodic property of the Discrete Fourier Transform results in time domain aliasing [34], which is called a 'leakage effect' in [132] .

methods represent a strong channel estimation tool [130]. However, for UWB the subcarrier spacing is 4.125 MHz and the pilots are spaced by 41.25 MHz [13]. As a result interpolation over such bandwidth simply cannot describe the full channel information. This is illustrated in Fig. 6.6 which shows an example of measured channel transfer function and the corresponding spacing of subcarriers for WiMedia UWB (thick dashed black line) and for IEEE802.11 (thin solid black line). As can be seen, the pilot spacing for the WiMedia case is simply too far to gather the information about the 'fine' channel behaviour. This can be compared to signal sampling below the Nyquist rate. For such sampling full signal reconstruction is not possible.

The **Autocorrelation Matrix Algorithms** use the fact that the correlation properties between the subcarriers in a wireless channel are known and therefore can be used in a autocorrelation matrix R_{HH} [131]. There is a number of algorithms that can be used for channel estimation using the inversion of the Autocorrelation matrix. One of the best algorithms, known to the author, with performance close to perfect channel estimation is presented in [131]. The algorithm has an iterative structure. In the first iteration, a Wiener filter is used to estimate the full channel transfer function $\mathbf{\hat{H}_1}$ (vector of frequencies, index 1 marks the first iteration) using the vector of pilot symbols $\mathbf{Y}^P$ and the knowledge of the autocorrelation matrix $R_{HH} = \mathrm{E}\{\mathbf{HH}^H\}$ (where ^{H} stands for Hermitian operand). This channel estimate is used to estimate the full vector of received symbols $\mathbf{\hat{Y}}_1$, which is then used again by the Wiener Filter for the next iteration.

The system has been applied on WiMedia system and it was shown that within 6 iterations, the system is comparable to perfect channel estimation [131]. However, the issue of this algorithm is the computational complexity. The actual estimation by the Wiener filter for the n-th iteration is the following:

$$\mathbf{\hat{H}_n} = \mathbf{R_{HY}R_{YY}^{-1}\hat{Y}_{n-1}} \tag{6.3}$$

where $R_{HY} = \mathrm{E}\{\mathbf{HY}^H\}$ and $R_{YY} = \mathrm{E}\{\mathbf{YY}^H\}$ with $\mathbf{Y}$ standing for the vector of received symbols.

In [131], it is assumed that all the subcarriers have the same modulation scheme. As a result, it is possible to express $\mathbf{R_{HY}}$ and $\mathbf{R_{YY}}$ as [131]:

$$\mathbf{R_{HY}} = E_s \mathrm{E}\{\mathbf{H}\mathbf{H}^H\} = E_s R_{HH} \tag{6.4}$$

$$\mathbf{R_{YY}} = E_s^2 \mathrm{E}\{\mathbf{H}\mathbf{H}^H\} + E_s N_0 \mathbf{I} = E_s^2 R_{HH} + E_s N_0 \mathbf{I} \tag{6.5}$$

where E_s is the energy per symbol, N_0 is the noise power spectral density and $\mathbf{I}$ is identity matrix with dimensions corresponding to the length of $\mathbf{H}$.

With the *a priori* knowledge of the channel autocorrelation matrix R_{HH}, it is possible to calculate $\mathbf{R_{HY}}$ and $\mathbf{R_{YY}^{-1}}$ offline provided the SNR is known [131].

Unfortunately, due to the adaptive loading of subcarriers, the matrix of symbols does not contain the same symbols. There are two options. Firstly, the modulations applied on the subcarriers have the same symbol energy. This is possible, e.g. for M-PSK (Phase Shift Keying) which is suggested for a UWB adaptive OFDM in [126]. For such a choice of modulation, the offline implementation as presented in [131] could be used. However, it is well known that for the same SNR, M-PSK systems perform significantly worse than M-QAM [34],[94].[5] Also, some of the deeply faded subcarriers will have a power level comparable to the noise level in the receiver. Hence, it seems to be better to have the opportunity to switch off these subcarriers because their BER would be too high even for QPSK or BPSK. If a subcarrier is switched off, the sizes of the matrices in (6.3) change which effectively disables the possibility of offline calculations.

Secondly, for the use of subcarrier loading by more efficient M-QAM, the simplified offline processing is not possible and the implementation would require multiple generation inversions of matrices 112×112. It is believed that such implementation would be highly computationally complex and the cost of such a device would probably not be feasible.[6]

[5] It is noted that this is valid for higher order modulations with M>4 because 4-PSK (QPSK) and 4-QAM are the same modulation

[6] Theoretically, it would be possible to calculate the matrices offline for every possible combination of subcarrier loading and SNR level. However, 100 subcarriers and 3 different modulation schemes would yield in $3^{100} = 5.2 \cdot 10^{47}$ variants of matrix $\mathbf{R_{YY}}$ for every SNR level. It is apparent that such solution is as cumbersome as the online matrix calculation.

To conclude, the Autocorrelation Matrix Algorithms are highly interesting for OFDM systems with fixed subcarrier loading. As was shown, their use for systems with adaptive subcarrier loading seems to require high computational complexity which is already an issue for UWB WiMedia systems due the large FFT. Therefore, it is believed that at the moment these algorithms are not suitable for the use in adaptive OFDM systems.

The **Parametric Channel Modeling** is a channel estimation technique that utilises the knowledge of the channel model to estimate the model parameters of a specific channel [129]. These parameters are the parameters of the channel impulse response [129]: number of rays, the ray delays and the ray amplitudes. Reference [129] claims that such estimation is less complex than 'blind' estimations that make no assumption about the channel.[7]

Reference [129] presents the performance of such an estimator that uses four steps. Firstly, it estimates the number of rays. Then the delays of the rays are estimated using the ESPRIT algorithm. This is the core of the estimator. A tracking algorithm than increases the precision of delay estimates. Finally a MMSE estimator determines the amplitudes. However, a more detailed analysis reveals that this estimator is not suitable for UWB WiMedia systems. Reference [129] gives a condition for the ESPRIT algorithm that the duration of the Inverse Fourier Transform of the vector $\mathbf{H}^P$ (channel transfer function vector at pilot subcarriers) must be longer than the rms delay spread of the channel. The length of the Inverse Fourier Transform based on 12 subcarriers in WiMedia system is only about 22.7 ns which is less than the expected multipath delays in UWB indoor channels, see chapter 3 or [21]. As a result, the ESPRIT algorithm cannot be used for channel estimation. The reason why is briefly explained in the next two paragraphs.

The original ESPRIT algorithm was intended to determine Angle-of-Arrivals (AoA) of plane waves at an antenna array [133]. The core idea behind the algorithm is that each wave has its unique AoA ϕ. Signals from the same wave therefore manifest the same phase shift between adjacent elements. In the frequency domain this phase shift corresponds to a term $\propto e^{j\cos\phi}$.

[7] It must be noted that this statement is not completely correct. It is true that the Autocorrelation Matrix Algorithms do not estimate the model parameters. They estimate the vector of the channel transfer function $\mathbf{H}$ and at the beginning they make no assumption about its form. However, they use the knowledge of the channel autocorrelation matrix R_{HH} which includes information about the channels because the autocorrelation properties in the frequency domain are determined from the knowledge of the parametric channel model and its typical parametric values [131].

The algorithm can also be applied on estimation of the time-of-arrival because the impact of the i-th ray on the adjacent values in the vector $\mathbf{H}^P$ is $\propto e^{-j2\pi\tau_i\Delta f}$ where Δf is the frequency spacing between adjacent pilots and τ_i is the delay of the i-th ray. In other words, the pilots correspond to the antennas in an array and the delays to the AoAs. The AoAs are obviously limited only on the interval from 0 to 2π. Hence, the term $2\pi\tau_i\Delta f$ must also be confined to this interval.

If the duration of the inverse Fourier Transform is shorter than the maximum multipath delay, aliasing in the time domain occurs and late rays with delay τ_i will appear to have a delay $\tau_i - T_{IF}$ where T_{IF} is the length of the inverse Fourier transform. In WiMedia UWB, $T_{IF} = 22.7$ ns. Thus the algorithm would assume phase shifts between adjacent pilots to be $2\pi(\tau_i - T_{IF})\Delta f$ whereas the real phase shifts would be $(2\pi\tau_i\Delta f)$. Similar issues would occur even for enhanced algorithms such as MUSIC.

In other words the estimators using parametric channel models are not suitable for UWB WiMedia because of the bandwidth of the OFDM symbols, the basic condition for the algorithm is not met. It is noted that if the estimation is performed over three adjacent WiMedia bands for a system hopping over three bands, the time domain condition would be met as the duration of such impulse response would increase by a factor 3 to 68.1 ns. However, this is associated with a few issues. Firstly, the recent reduction of UWB in Europe, Japan, and Korea to some level prohibits systems from frequency hopping if multiuser access should be secured. Four single WiMedia bands fit in Europe's 2.5 GHz UWB band but a single system hopping over 3 bands would occupy effectively the full band. Furthermore, throughout the thesis we make the assumption that the channel parameters within a single OFDM symbol are not influenced by the frequency dependency of the pathloss and/or the antenna gains. This assumption does not necessarily hold over three bands covering 1.5 GHz. Additionally, symbols from different bands are downconverted individually. This introduces different attenuation and phase shift for each symbol. Each of these issues would have an impact on performance of the systems.

To conclude the section on **Comb-Type Pilot Channel Estimators** it has been shown that these estimators do not appear suitable for UWB systems with adaptive OFDM. For the interpolation algorithms and the parameter estimators, this is due to the bandwidth of the

OFDM symbol, which is 25 times higher than in the case of IEEE802.11 systems. Therefore the algorithms that work well for narrowly spaced pilots, lose their performance for increased pilot spacing. The algorithms that use an inversion of the autocorrelation matrix require fixed loading of the subcarriers. For a loading with M-QAM as proposed in the introduction of this chapter, the computational effort of these algorithms is too high. As a result it appears that the UWB WiMedia systems would have to resort to block-type algorithms.

It is noted though that this conclusion is not necessarily conclusive. It is possible that the development of faster chips will remove/mitigate the issue of computational complexity. Also new channel estimation algorithms with a fundamentally different strategy may appear. The conclusion about the comb-type algorithms is based on the analysis described in this section and it is limited by the author's knowledge of the state-of-the-art algorithms for channel estimation.

6.2.2 Block-Type Pilot Channel Estimators

As mentioned above the Block-Type Estimation uses all subcarriers in a single OFDM symbol as pilots. The estimated channel is then used for several subsequent OFDM symbols. For slow temporal fading it is assumed that the channel does not change between two subsequent pilot OFDM symbols.

The easiest way to determine the channel when all the symbols in the subcarrier are known is the use zero-forcing [132], [134]. For zero forcing it is assumed that the received symbol vector $\mathbf{Y}$ is:

$$\mathbf{Y} = \mathbf{X}\mathbf{H} + \mathbf{n} \tag{6.6}$$

where $\mathbf{X}$ is a diagonal matrix of known pilot input symbols, $\mathbf{H}$ is the channel vector that is supposed to be estimated, and $\mathbf{n}$ is a noise vector.

Zero forcing uses the inverse of $\mathbf{X}$ [132], [134]:

$$\mathbf{X}^{-1}\mathbf{Y} = \mathbf{H} + \mathbf{X}^{-1}\mathbf{n} \tag{6.7}$$

The second term is effectively an inverted SNR. Thus for high SNR values, zero-forcing represents a remarkably simple and precise estimation technique. Unfortunately, the SNR levels in

UWB systems are low and therefore better methods are used [134]. Reference [134] presents the Linear Minimum Mean Squared Error (LMMSE) and Singular Value Decomposition.

In principle, the estimators can use the same algorithms in the case of the comb-type estimators (excluding the interpolation algorithms) with the difference that many issues are alleviated by the increased number of known subcarriers. The larger number of subcarriers enables the use of the ESPRIT algorithm [129] because the length of the inverted Fourier transform exceeds the length of the channel impulse response [13].

The algorithms using the inversion of the autocorrelation matrix can also be deployed because the input vector $\mathbf{X}$ can easily be set to have the same modulation on all subcarriers so that offline calculated matrixes can be used. One of the best candidates appears the iterative algorithm using the Wiener filter [131]. According to reference [131], this iterative algorithm achieves perfect estimation after about 6 iterations.

To conclude, this section shows that many algorithms that cannot be used for the comb-type estimator can be used for the block-type estimator. The literature also reports that iterative approaches to channel estimation can achieve performance close to the perfect estimation. Thus, the first pre-requisite for the use of adaptive bit loading in OFDM symbols can be fulfilled when the block-type pilot channel estimators are used. However, these estimators are influenced by the temporal fading that might change the channel properties between two pilot symbols. This limitation is discussed in the next section.

6.3 Stationary Region and Pilot Repetition Rate

The objective of this chapter is to discuss the repetition rate of pilot symbols for channel estimation. It firstly defines the minimum rate of the symbol and justifies that the channel is stationary between subsequent pilot symbols by the means of estimated maximum displacement. Secondly, channel measurements are used to show that the proposed pilot repetition rate is sufficient and in fact could be potentially further reduced.

The pilot symbol repetition rate is given by the packet length. The packet structure was described in chapter 5. The maximum packet length is approximately 700 OFDM symbols (42 symbols for header and preamble, 4095 Bytes and short suffix equal to about 656 symbols for the Mode 1 which uses frequency and time spreading). The symbol duration in the WiMedia standard is 312.5 ns [13]. Similarly to the discussion in chapter 4 it can be assumed that the maximum velocity of the mobile terminal will not exceed 10 m/s. Then during a single symbol the displacement of the terminal can be assumed to be below 3 μm. Considering this it is suggested that sending a pilot OFDM symbol every 700 symbols would seem satisfactory. Over 700 symbols the terminal displacement will be approximately 2.1 mm. This is nearly $\lambda/15$ for the highest UWB frequencies at 10 GHz. As will be shown next, for such displacement the change of channel properties will not significantly impact the BER performance of receivers. It is noted that this is the maximum displacement for a packet with maximum length and for a movement corresponding to the average speed of 10 m/s (=36 km/h). For the default packet length with payload of 1024 Bytes [13] and slower movements, the displacement will be lower.

It is noted here that the author is aware that the packet length in the WiMedia standard was selected with the stationarity of the channel in mind, thus the investigation in this section may appear unnecessary. However, the standard was designed for fixed OFDM where the bits are spread over multiple subcarriers either directly (Modes 1 and 2) or by the means of the Dual-Carrier-Modulation (Mode 3). This use of channel diversity reduces the BER. Here, we aim to confirm that this rate is satisfactory even for adaptive OFDM.

The impact of temporal/spatial fading on the performance of UWB systems with adaptive OFDM symbol loading is investigated by the analysis of the BER increase associated with displacement of the transmitter/receiver.

Evaluation of the impact of the temporal changes by measurement is extremely difficult, because most channel sounding experiments for UWB are performed by the means of Vector Network Analyser that sequentially determines the channel transfer function at individual frequencies [135]. A duration of a single frequency measurement is about 1-5 ms [136]. With several hundreds/thousands of frequency points within the UWB frequency range[8], a single channel measurement can last even a few minutes. Hence, the measurements are typically performed in a static environment [135].

However, the spatial fading and the temporal fading are closely related (see channel energy

[8]Our measurements were performed with frequency step width of 0.5 MHz

variations in Fig. 3.8). Hence one can estimate impact of temporal fading using the spatial fading and the movement of the transmitter/receiver. The evaluation performed in this section has three steps. Firstly, the change of BER as a function of displacement is observed to define the maximum displacement radius. Secondly, the impact of selection levels for loading on the maximum displacement radius is explored. Finally, the results are used to confirm that the lowest repetition rate possible in the WiMedia system is sufficient to ensure that the channel does not change during the symbols that follow the pilot sequence.

The first step is empirically shown in Fig. 6.7 which shows the BER as a function of displacement. It is assumed that the communication link has perfect channel estimate and sets the subcarrier loading similarly as in the beginning of this chapter. Here the bit loading is enhanced by the introduction of another decision level for 8-QAM:

- $E_s/N_0 < 10.5$dB - subcarrier switched off
- $10.5\text{dB} \leq E_s/N_0 < 14$dB - QPSK
- $14\text{dB} \leq E_s/N_0 < 17$dB - 8-QAM
- $17\text{dB} \leq E_s/N_0 < 24$dB - 16-QAM
- $24\text{dB} \leq E_s/N_0$ - 64-QAM

Then the same subcarrier loading is applied on adjacent channels and the corresponding BER is calculated. The results are plotted and colour-coded. The blue colour shades represent positions for which the BER is below 10^{-2}, the red colour shades represent positions with BER above 10^{-2}. The left column shows data for the band around the centre frequency of 3.96 GHz (WiMedia band 2), the right column shows data for the band around 7.128 GHz (WiMedia band 8). The rows represent different measurement positions.

Two main observations can be made based on plots in Fig. 6.7. Firstly, the area in which the BER remains below 10^{-2} significantly decreases with frequency. This conclusion is not surprising, because the spatial correlation of a narrowband channel is known to be $\propto \mathrm{J}_0\left(\frac{2\pi d}{\lambda}\right)$ (e.g. [137]) where J_0 is the Bessel function of 0-th order, and d is the displacement. This means that for the same displacement the correlation drops faster at higher frequency. This observation itself is not innovative but the statistical analysis of this phenomena over multiple measurements will allow one to estimate the required repetition rate of the pilot symbol and potentially to express it as a function of centre frequency.

The second observation is with regards to the shape of the area. The coloured areas show directionality. This is believed to be determined by the angle of arrival of the dominant multipath components. As discussed in Section 3.3, the fading of a narrowband channel is determined mainly by the delay between the dominant multipaths. The delay between the dominant components is dependent on the direction of the displacement and on the angle-of-arrivals of the multipaths, hence the relatively larger increase of BER in one direction. This fact causes some inconvenience for the estimation of how far can the receiver/transmitter move without significant performance deterioration (here chosen as BER$> 10^{-2}$) and will result in approximation in the next steps.

So far Fig. 6.7 shows only two frequencies and two positions which is not enough to reach

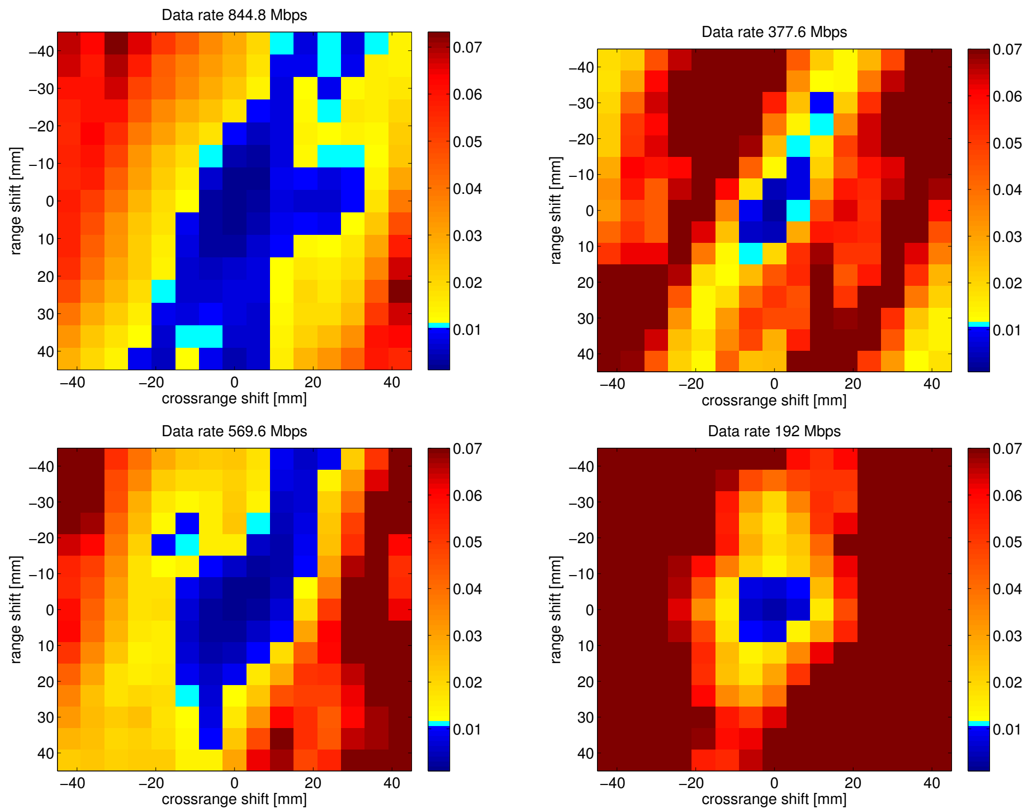

Figure 6.7: The BER of UWB system OFDM with adaptive subcarrier loading as a function of displacement. The bit loading is performed for the position in the centre of the grid. The upper row shows results for TX-RX distance of 1.05 m, the lower row shows results for TX-RX distance of 1.56 m. (Positions 2 and 4, see appendix C). The left column is for the WiMedia band 2, the right column for the WiMedia band 8. The spacing of adjacent points is by 6 mm.

a statistically relevant conclusion. A statistical analysis over a large number of channels will be presented next. Fig. 6.7 will be referred back for visualisation of the problem. The main objective of the second step is to determine the mean maximum displacement for which the BER does not exceed a selected threshold. The mean maximum displacement will be investigated as a function of data-rate and centre frequency. Prior to the investigation, the mean maximum distance must be defined, because so far it has only been introduced intuitively.

The mean maximum displacement for this work will be determined as follows. Each out of six measurement positions presented in appendix C provides 1,600 positions in a 40×40 grid spaced by 6 mm. For an inner grid of 400 positions (20×20) the perfect loading is calculated and the BER for displacement by up to +/-7 positions in each direction is calculated. As a result a grid 15×15 with BERs is obtained (as in plots Fig. 6.7). For each of these grids area A for which the BER is below the 10^{-2} threshold is determined (this corresponds to counting dark blue squares in Fig. 6.7). The mean area $\overline{A}$ over all 400 positions is calculated. Then, it is assumed that the area $\overline{A}$ is enclosed by a circle and the radius R of the circle is determined:

$$R = \sqrt{\frac{\overline{A}}{\pi}} \tag{6.8}$$

It is noted that such calculation is an approximation. If the area's shape is deformed in one direction, the radius R overestimates the possible movement in one direction and underestimates in another. However, the objective is only to estimate mean maximum shift for indoor channels. Hence, this error can be neglected as it averages out over the large number of channels. Fig. 6.9 shows that the error due to this approximation is not significant. It plots corresponding 'stationary circles' into the original Fig. 6.7.

The next step is to investigate the impact of frequency and data-rate on the radius R. The investigation of the frequency is apparent - the calculation is run over multiple frequency bands and the dependency of R is observed. Decrease of R is assumed based on Fig. 6.7. The dependency on data-rate might not be as obvious at first and is therefore explained here.

The decision levels are introduced at the beginning of this section. They have an impact on the data-rate and on the maximum displacement. If the decision levels are increased, the

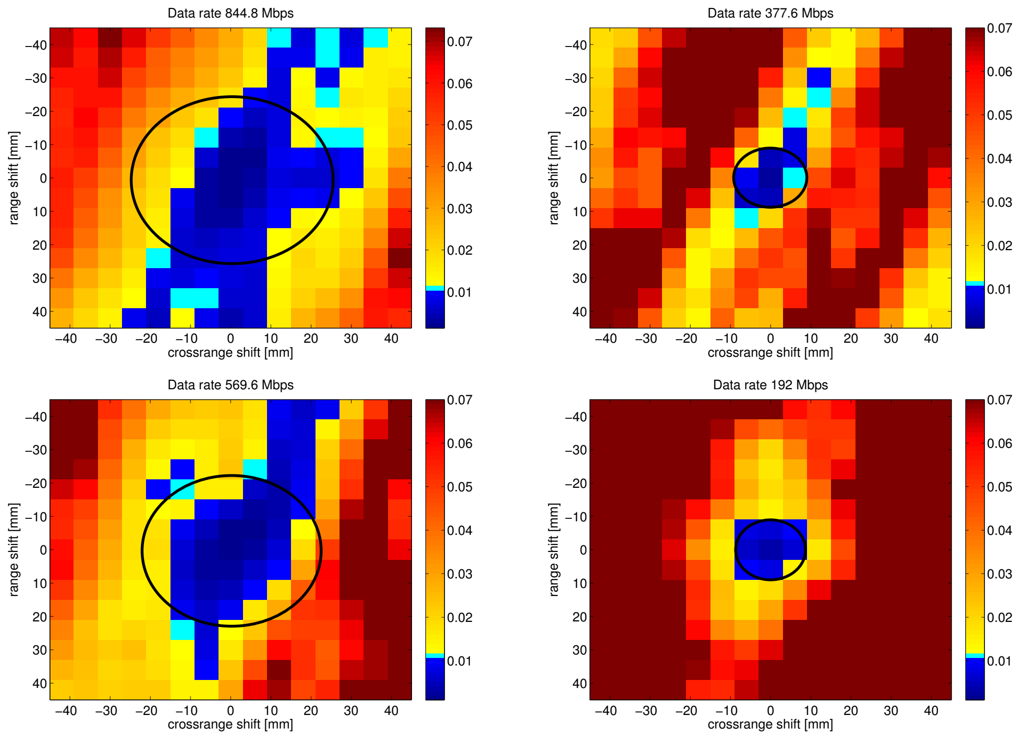

Figure 6.8: The BER of UWB system OFDM with adaptive subcarrier loading as a function of displacement. Compared to the 'stationary circle' with radius R.

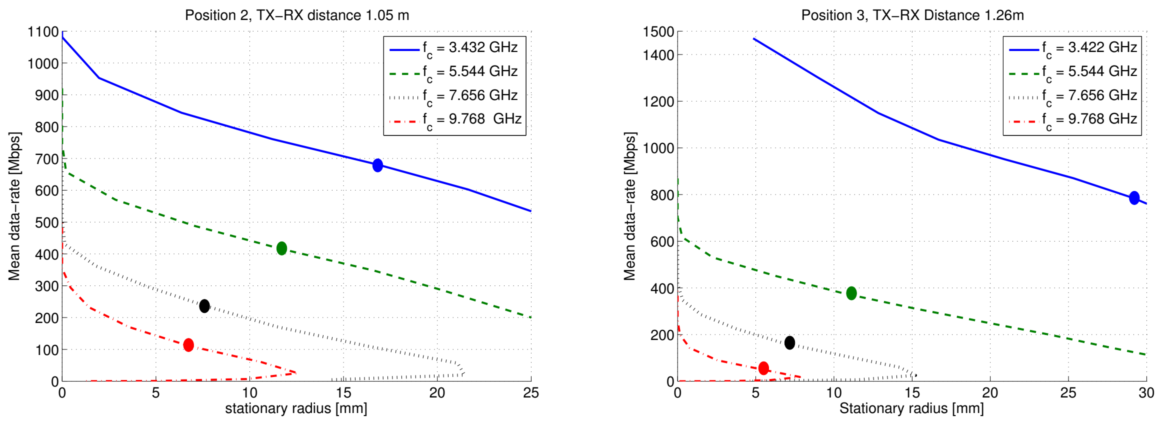

Figure 6.9: The relationship between data-rate, frequency and the stationary radius. The circles represent data-points for which the decision levels were as defined on page 143. Points to the left correspond to lower levels, points to the right to higher levels.

data-rate is reduced. At the same time the higher decision levels means each subcarrier is guaranteed lower BER for the position of channel estimation because it either meets the more strict decision level or uses a lower modulation scheme. As a result, the area of the 'stationary circles' increases because it will be possible to displace the transmitter/receiver farther without violating the selected performance limit (BER$< 10^{-2}$). This effect is investigated in Fig. 6.9.

Fig. 6.9 shows how the radius of stationarity circles increases when the decision levels for bit loading are increased and correspondingly the mean data-rate. This is shown for two example measurement positions but the behaviour was the same for the remaining 4 positions from appendix C as well. It can be seen that the line describing the property is a hypotenuse of a triangle spanned by the two axis. The area of this triangle is reduced with increased centre frequency but the angle of the hypotenuse remains approximately the same. In fact the angle was approximately constant for all positions and the mean drop rate was determined to be -15 Mbps/mm, i.e. if the decision levels are increased the data-rate drops by 15 Mbps but at the same time the radius of the stationarity region increases by 1 mm.

The situation for low data-rates also needs a comment. When the bit loading decision level increases it reaches a point where no subcarrier satisfies the criteria as a result communication will not be established and the mean radius of the circles goes to zero because no circles exist. Hence, the sudden change of trend and reduction of the radius can be observed for low data-rates at higher centre frequencies.

The conclusion of a -15 Mbps/mm slope of the curve in Fig. 6.9 which is found to hold for all positions is an interesting finding that may well be used in some application aiming to maximise the stationarity region. However, for the sake of this thesis the main conclusion based on the curves in Fig. 6.9 is that even for the lowest pilot repetition rate the shift of a mere 2.1 mm, the BER will not increase above 10^{-2} for neither of the measurements and for neither of the centre frequencies. As a result, it can be concluded that even at the lowest rate of pilot blocks foreseen by the WiMedia standard the system will not be significantly influenced by temporal fading. In other words, the WiMedia systems already foresee channel estimation and the repetition rate of pilot OFDM symbols is sufficient to reduce the impact of temporal fading. Thus, the introduction of adaptive OFDM is possible as the system already has all the pre-requisites. This is a positive finding and the performance of UWB systems with adaptive OFDM will be discussed in more detail in the subsequent section.

6.4 Performance Comparison Adaptive and Fixed OFDM

In this section, the performance of the proposed adaptive sytem will be evaluated and compared to the performance of a 'WiMedia-like' fixed OFDM system. The comparison will be performed using channel measurements in the office environment that were presented in chapter 5 to explain the range limitations of WiMedia systems. A quick performance evaluation was already presented in section 6.1, which aimed to provide motivation for the rest of the chapter. Here the performance will be compared to an equivalent system with fixed OFDM. The adaptive and the fixed systems are presented first. The evaluation is performed only for the lowest three bands in WiMedia systems in order to enable a reasonable comparison with the practical WiMedia UWB kit.

For the **adaptive OFDM system**, it is assumed that the block-type channel estimator provides sufficiently precise channel state information. This is used to have variable loading of the subcarrier. The modulation scheme for each subcarrier is selected as follows:

- $E_s/N_0 < 10.5$dB - subcarrier switched off
- $10.5\text{dB} \leq E_s/N_0 < 14$dB - QPSK
- $14\text{dB} \leq E_s/N_0 < 17$dB - 8-QAM
- $17\text{dB} \leq E_s/N_0 < 24$dB - 16-QAM
- $24\text{dB} \leq E_s/N_0$ - 64-QAM

The sensitivity of the receiver (the noise floor at the receiver) is assumed to be -101.3 dBm/MHz so that the dynamic range of the system is 60 dB. This level corresponds to the sensitivity in realistic WiMedia systems [13] as well as to levels used for performance estimation in the open literature [6]. Two transmission modes are considered, without frequency hopping with EIRP of -41.3 dBm/MHz and with frequency hopping over three centre frequencies which enables increasing the EIRP by 4.7 dB to -36.6 dBm/MHz [13]. Only 100 subcarriers are considered for the transmission, with positions defined by the WiMedia standard [13]. For the case of no hopping, the centre frequency of the transmission was 3.96 GHz as in the WiMedia band 2 [13], in the case of frequency hopping, all the three lowest frequency bands were considered.

The **fixed OFDM system** is called 'WiMedia-like' because most of its parameters are the same as in the WiMedia standard. However, there is a difference in the dynamic range consideration. The same sensitivity as for the adaptive OFDM system is assumed: -101.3 dBm/MHz. The modulation scheme on all subcarriers is QPSK. The EIRP and the sensitivity are chosen to be the same as in the adaptive OFDM scheme. Transmission modes with and without frequency hopping are considered and again only 100 data-subcarriers as in the WiMedia scheme are considered. Also, a frequency spreading of information is assumed similarly to the WiMedia. A single bit is spread onto two subcarriers and the results are combined using a Maximum-Ratio-Combiner [13]. The Maximum-Ratio-Combiner does not increase the SNR because it sums the powers of two subcarriers, thus it also doubles the noise power. However, it is a diversity scheme and it reduces the spread of the subcarrier energies. In other words, it reduces the probability of a deep fade. As a result, the data-rate of this scheme is 320 Mbps (50 subcarriers $\times$ 2 bits per subcarrier $\times$ 3.2 Msymbols/s[9]). This is a gross data-rate which excludes the packet preamble, header and channel coding. The same gross data-rate will be considered for the adaptive system as well.

The measurements were performed in an office environment with In4Tel™ antennas and have been already introduced in chapter 5. There are 40 channel measurements for 10 distances, for each distance there are four transmitter positions (the transmitter was positioned in the corners of a 5×5 cm square). The performance of the systems are compared in Figs. 6.10-6.13.

Figs. 6.10-6.11 present the simulation results for the case with no frequency hopping (dynamic range of 60 dB only). The Data-throughput adaptive OFDM drops with distance. However, its BER is almost constant and below the highlighted limit of 10^{-2}. The fixed OFDM has a constant data-rate but a significant increase of BER can noticed. In fact the BER exceeds the limit of 10^{-2} (this level is selected as it corresponds to the code strength of WiMedia systems [13]), i.e. the communication stops, already for the distance of 2 m. For this distance the adaptive OFDM provides higher data-rate of approximately 400 Mbps. Hence Figs. 6.10-6.11 show that the adaptive OFDM can provides a performance increase. It enables an increase of the data-rate and of the range.

The transmission effectively ceases after 5 m. It is noted that for this distance, the free-space

[9] 3.2 Msymbols/s = 1/312.5ns, where 312.5 ns is the duration of the OFDM symbol.

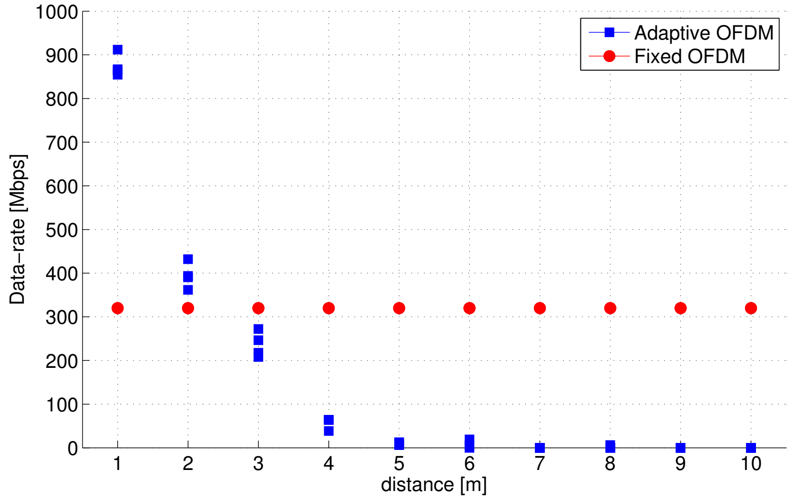

Figure 6.10: The comparison of the theoretical data-rate achieved by adaptive OFDM system with the fixed data-rate of a fixed OFDM system considering measurements of real channels. The case without frequency hopping.

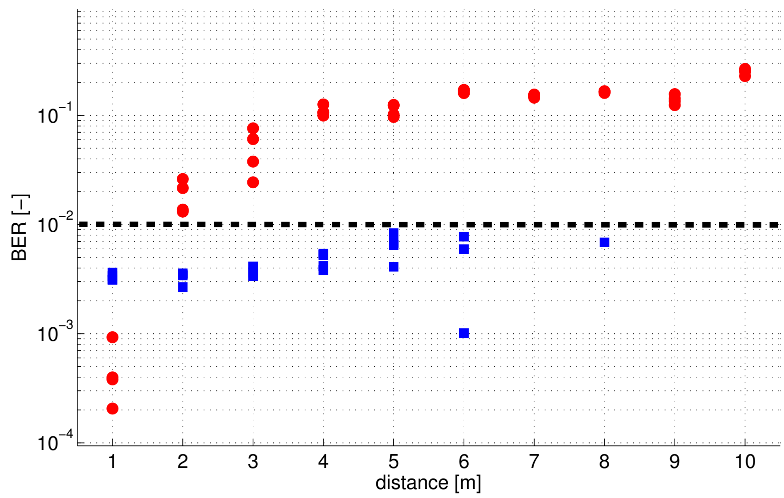

Figure 6.11: The comparison of the theoretical uncoded BER achieved by adaptive OFDM system with the BER of a fixed OFDM system considering measurements of real channels. The case without frequency hopping.

path-loss at 3.96 GHz for 5 meters is approximately 58.4 dB which is close to the dynamic range of 60 dB. This shows another practical advantage of adaptive OFDM, it is possible to estimate the range using a simple path-loss model. In fixed OFDM UWB systems such estimation does not work as was shown in chapter 5.

The missing data-points for adaptive OFDM's BER for ranges 7 - 10 m are due to the fact that for these ranges, no subcarrier met the minimum power requirement. Hence, the data-rate is zero and for such a data-rate the BER cannot be defined.

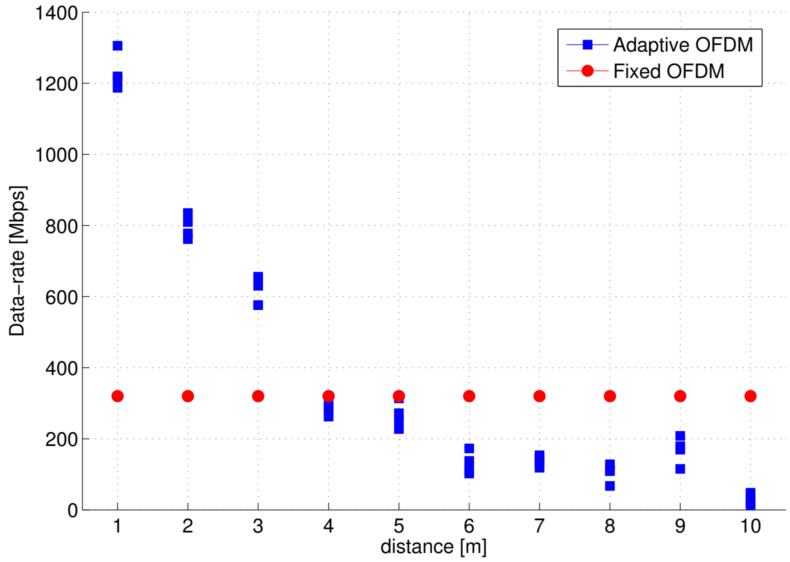

Figure 6.12: The comparison of the theoretical data-rate achieved by adaptive OFDM system with the fixed data-rate of a fixed OFDM system considering measurements of real channels. The case with frequency hopping.

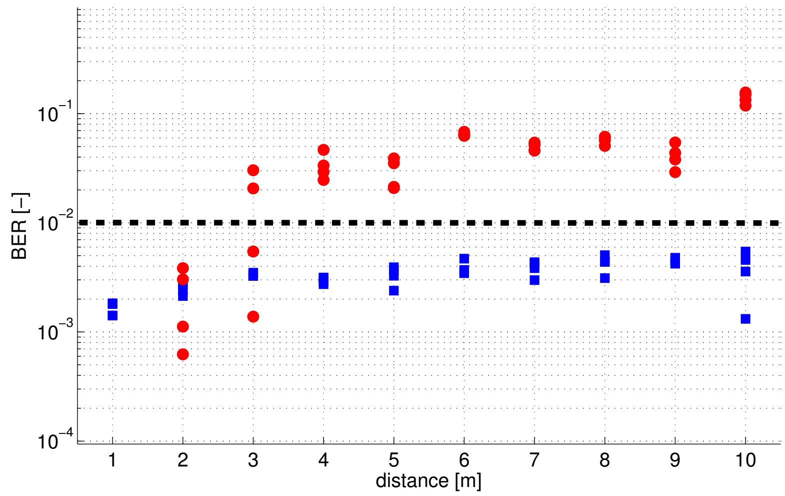

Figure 6.13: The comparison of the theoretical uncoded BER achieved by adaptive OFDM system with the BER of a fixed OFDM system considering measurements of real channels. The case with frequency hopping.

The results in Figs. 6.10-6.11 show an improvement but the range and data-rates may still appear insufficient because the high-speed communication is possible only up to the distance of 3 m, past this mark the performance drops. However, it is noted that these were results without frequency hopping. With frequency hopping, which enables increasing the EIRP by 4.7 dB [13], more improvement can be achieved as shown in Figs. 6.12-6.13.

As can be observed in Figs. 6.12-6.13, for the fixed OFDM the range was increased. The communication with BER below 10^{-2} is possible for a distance of 2 m. For the distance of 3 m, the BER is below 10^{-2} for two out of four cases. The improvement for the case of adaptive OFDM is even more significant. It enables communications at rates above 100 Mbps for distances of up to 9 m. Such a performance is significantly superior to the case of fixed OFDM or even to the performance of real WiMedia systems, where only the data-rate of 53.3 Mbps was available for the range of 9 m. Also significant is the increase of the data-rate for short-range. E.g. for the distance of 1 m, the achieved data-rates are above 1.2 Gbps.

6.5 Summary

To conclude the section on adaptive OFDM. It has been shown that adaptive OFDM opens the door towards higher performance and longer ranges. The improvements have been compared to the fixed OFDM scheme. The adaptive OFDM effectively removes the impact of frequency selective fading and the range is again limited almost entirely by the path loss.

Discussion of the channel estimation methods concluded that the block-type pilot positioning is more suitable for UWB systems and it was shown that even the lowest pilot repetition rate in WiMedia symbols enables up-to-date channel information.

The results in realistic simulations confirm the statement from the introduction of the thesis which claimed that an adaptation of the WiMedia scheme can deliver a performance improvement significant enough to make UWB systems a strong contender among the future wireless communication systems. However, the performance presented in this chapter is not the maximum achievable result and chapter 7 will show how multiple antenna systems can further increase the achievable data-rates and/or ranges.

CHAPTER 7

MIMO for UWB OFDM Systems

The aim of this chapter is to show how multiple antenna systems can be employed to improve the performance of both fixed and adaptive OFDM systems. The use of MIMO technology for enhancement of performance and range of OFDM systems has been studied excessively. A search for the keywords 'MIMO OFDM' in the IEEExplore$^{\text{TM}}$ database returns approximately 800 journal articles and 4,100 conference papers published since 1994. An overview of the-state-of-the-art technology in MIMO OFDM can be found in review works [138]-[139]. The success of MIMO OFDM is also highlighted by the fact that it is included in the IEEE802.11.n standard and its usage is further extended in the proposal of IEEE802.11.ac [104].

This chapter assesses the impact of MIMO techniques on realistic UWB systems and shows that a suitably chosen technique can deliver significant performance enhancement over equivalent SISO systems. Its structure is as follows. Firstly, some specific challenges for UWB MIMO systems are discussed and the basic difference between MIMO requirements for adaptive and fixed OFDM systems are explained. For fixed OFDM systems, antenna selection is considered as a candidate algorithm. A low complexity beamsteering technique for UWB systems with adaptive OFDM is then introduced. The technique does not require tight antenna spacing and it is proven to provide performance superior to Maximum-Ratio-Combining (MRC). Simulations show that in a 2×1 system performance of the low-complexity beam-steering is only marginally inferior to maximum gain combining.

7.1 Challenges for and objectives of MIMO in UWB systems

This section starts with a discussion of the challenges for UWB MIMO systems, and the objectives of the systems are then discussed. We discuss three main challenges for UWB OFDM systems: the regulatory framework; system complexity; and the antenna spacing.

The regulations for UWB limit the EIRP spectral density (given e.g. in [10]). In contrast, the IEEE802.11 is limited in the total radiated power (subject to maximum array gain) [140]. As a result, not all algorithms developed for IEEE802.11 MIMO OFDM systems can be directly applied to UWB systems. A UWB transmit array cannot increase the gain compared to a single antenna system. Transmit UWB arrays can still be used as spatial filters that eliminate the power transmission in unwanted directions, but they can not provide the transmit gain as in the case of IEEE802.11 since this would lead to the increase of EIRP. This is illustrated in Fig. 7.1. As a result, the Eigen-Beamforming cannot be used in UWB transmitting arrays [140].

Even though the Eigen-Beamforming can be used for a receiver array, this chapter focuses only on EIRP-bounded N×1 systems. This is mainly because the channel measurements performed in this thesis were conducted only for N×1 channels.[1] However, a majority of the UWB applications considers a complex base-station and low complexity mobile device with asymmetric data-flow towards the mobile device [6],[8], [13], and [37]. As a result, it can be assumed that in such scenarios the centre of gravity will be N×1 systems. As a result, the conclusions reached in this chapter are believed to be applicable to a large number of practical systems despite the limitation to N×1 EIRP-bounded systems.

[1] The theory in section 7.3 considers N×M systems but the performance comparison with empirical channels are limited solely to N×1 systems.

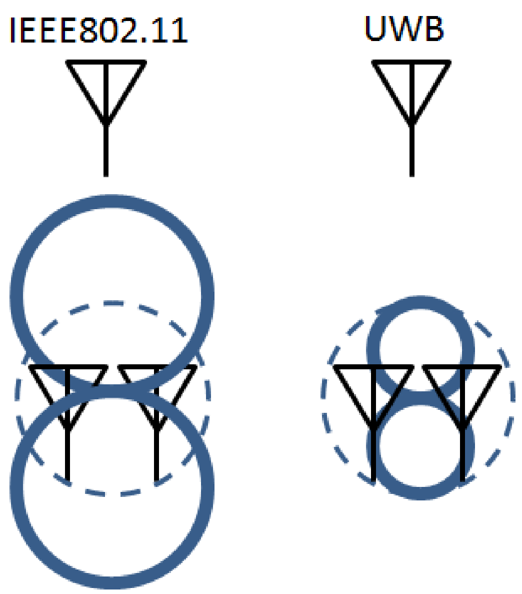

Figure 7.1: Illustration of the different strategies for multiple antenna transmitters for IEEE802.11 and UWB transmitters. The dashed line shows the radiation pattern of a single antenna. The solid lines show how this can be changed in a multiple antenna system.

Optimum beamforming in EIRP bounded systems has been investigated e.g. in [141]. As noted in [140], the optimum beamforming is achieved as a result of a convex optimisation problem. The numerical solutions of this problem are reported to be computationally complex [140]. As a result, suboptimal solutions are considered. Reference [140] discusses some of them. The first such solution is Scaled-Eigen-Beamforming, where Eigen-Beamforming is scaled to satisfy the EIRP [140], [141]. However, the cost for the simplicity of this solution is significant degradation of BER performance [140]. A remedy suggested in [140] is the use of the method proposed in [142]. The method in [142] takes advantage of the fact that the angles of the main lobes of Eigen-Beamforming are the same as in the case of the optimum solution. Thus, the algorithm starts with Eigen-Beamforming and uses more sophisticated scaling than in the case of Scaled-Eigen-Beamforming. As a result, the radiation pattern is closer to the optimum case and it is inherently associated with a superior BER performance [142].

However, even the approach from [142] has an issue. This arises from the wide available band for UWB systems. A system targeted for the world market should be capable of covering the full spectrum 3.1-10.6 GHz allowed by the US FCC [12]. This causes issues for the antenna spacing. All methods so far expect the absence of grating lobes. This leads to an issue briefly outlined in chapter 2. With an element spacing that does not allow the existence of grating lobes at 10 GHz, the directivity of such array at 3 GHz is close to a single antenna case. The conclusion of chapter 2 also is that grating lobes in a UWB antenna array disappear only for systems with relative bandwidth larger than 100%. This is not the case for OFDM systems such as WiMedia with a symbol bandwidth of 528 MHz.

As a result, it can be concluded that considering the large bandwidth of the UWB band, it is beneficial to use MIMO techniques that are not limited by the element spacing. Two such techniques, antenna selection and low complexity beamforming, will be discussed in the subsequent sections.

However, before we proceed to discuss these two techniques, the objectives of MIMO in UWB OFDM systems will be discussed. The top-level objectives are the maximisation of data-rate and/or minimisation of BER. However, the way this can be achieved depends strongly on the OFDM techniques used. For fixed OFDM modulation schemes, the main objective is to remove the deep fades from the transfer function because the deep fades limit the range of the system as shown and thoroughly discussed in chapters 5 and 6. In other words, the main objective is to 'flatten' the channel transfer function. Increase of the total power is of interest as well but the main priority is the removal of deep fades. Antenna Selection, which is discussed in section 7.2, is such a technique.

In adaptive OFDM systems, the algorithms 'flattening' the channel transfer function can be used as well simply because the 'flattening' enables the loading of more subcarriers. However, the maximisation of the total power has a higher priority, because for adaptive OFDM deep fades do not compromise the performance of the system. As will be demonstrated in section 7.3, the deep fades can in fact be advantageous because a presence of deep fade in one subcarrier means that there will be another subcarrier with very high SNR.

7.2 Antenna Selection - Low Complexity MIMO for UWB OFDM Systems

7.2.1 Antenna Selection - Introduction

At a basic level antenna selection can be considered a diversity scheme. For each subcarrier the transmitter or receiver selects one antenna which provides the highest level of channel transfer function (and consequently the highest SNR) and only this antenna is used for transmission or reception [140], [143]-[145]. As a result, at each frequency only one antenna in the antenna array is active and the EIRP corresponds to the single antenna case [140], [143]-[145].

The performance improvements are achieved because the scheme exploits the spatial diversity of the channel. This removes the issue of antenna spacing because the only objective is to ensure that the spacing is sufficient for the channels to be sufficiently de-correlated. Since at each frequency only one antenna from the array is used at any time, grating lobes cannot appear and if all the elements are identical, the gain is constant.

References [140], and [143]-[145] studied the performance of antenna selection in computer generated channels. In particular they studied the conditions for phase pre-coding. The issue of phase pre-coding can be explained using the following example. In an N×1 system, the transmitter preforms antenna selection based on its knowledge of the channel state information [140]. A WiMedia receiver uses the packet preambles for channel estimation and pilot subcarriers for phase corrections [13]. These algorithms assume phase continuity of the channel transfer function. The antenna selection at the transmitter, however, results in phase discontinuities in the phase of the transfer function as perceived by the receiver. Since the transfer functions of the channel are known at the transmitter (they must be known prior to the antenna selection) a phase pre-coding can be performed. In the rest of this thesis, the linear phase pre-coding is used because reference [140] reports it to have the best performance. The basic idea of linear phase pre-coding is to change the phase at individual antennas in a way so that the compound channel manifests linear phase at the receiver [140]. A compound channel is the channel 'seen by the receiver' in a N×1 system when the transmitter uses antenna selection.

This thesis will focus on the practical implementation and performance of this approach in measured UWB channels. In particular, the measured empirical wireless channels will be used to make a recommendation on the optimum selection of the array geometry. Then, the performance of an antenna selection system in an office environment is compared to a single antenna system and some complexity issues are pointed out.

7.2.2 Optimisation of Array Geometry for Antenna Selection

The objective of this section is to derive a recommendation of how to position N-antennas so that the BER performance of a N×1 antenna selection system operating in the full band 3.1-10.6 GHz is optimised. This section begins with theoretical discussion, which starts with the impulse response of a wireless channel. We use the simplified channel model presented in Eq. (3.20), which is repeated here for the sake of readability:

$$h(t) = \sum_{k=0}^{K_{DR}} \alpha_k e^{j\theta_k} \delta(t - \tau_k) \tag{7.1}$$

where K_{DR} is the number of multipaths; α_k,τ_k and θ_k stand for the amplitude, delay and phase of each multipath.

The corresponding channel transfer function $H(f)$ is then given as:

$$H(f) = \sum_{k=0}^{K_{DR}} \alpha_k e^{j\theta_k} e^{-j2\pi f \tau_k} \tag{7.2}$$

with total energy $|H(f)|^2$ given as:

$$|H(f)|^2 = \sum_{k=0}^{K_{DR}} \alpha_k^2 + \sum_{\substack{k=0 \\ k\neq l}}^{K_{DR}} \sum_{l=0}^{K_{DR}} \alpha_l \alpha_k \cos[2\pi f(\tau_k - \tau_l) - (\theta_k - \theta_l)] \tag{7.3}$$

As was shown in chapter 3, for a small displacement in a grid 23.4×23.4 cm, the amplitudes α_k and phases θ_l can be assumed constant. This means that the frequency selectivity at a single frequency is given mainly by the combinations of differences between path delays $(\tau_k - \tau_l)$.

Looking at (7.3) it is apparent that in a 2×1 system the objective is to position the second antenna in a way that the terms $2\pi f(\tau_k - \tau_l)$ differ significantly enough to change the amplitude and the sign of the cos-term. As a result, the total double sum result changes. The destructive multipath superposition changes into a constructive one and vice-versa. It is apparent that the spacing will depend on the wavelength $\lambda = \frac{c}{f}$. It also appears that due to the periodicity of the cos-function, the performance will show a 'pattern of periodicity' similar to the pattern appearing in Fig. 3.8. The 'pattern of periodicity' will depend on the angle-of-arrival/departure of the most significant multipaths. This may cause difficulties for array design because the periodicity pattern will depend on the wavelength and therefore optimisation of the array geometry must be performed jointly for all frequencies. This issue is explored in Fig. 7.2.

Fig. 7.2 explores the BER performance of a 2×1 'WiMedia-like' system with antenna selection. It shows how the BER performance varies with element spacing. The 'WiMedia-like' system is the same fixed OFDM as used in chapter 6 for comparison of the performance of the Adaptive and Fixed OFDM systems. The system employs QPSK modulation of the subcarriers and it has a dynamic range of 60 dB. The system also uses frequency spreading where each data bit is modulated on two subcarrier and the receiver uses Maximum-Ratio-Combining. The position of data subcarriers as well as the spreading is the same as in the WiMedia systems [13]. The performance is studied for three different centre frequencies (distinguished by colour) and for two array orientations (distinguished by line-type).

The lines were determined based on the empirical channel measurements in position 2 as presented in appendix C. The grid of 40×40 points was used to explore the behaviour of endfire and broadside arrays. The transfer functions of measurement points with defined spacing and selected orientation were used to determine the compound channel realisations using the antenna selection and linear phase pre-coding. For each array orientation and element spacing the maximum possible compound channel realisations were evaluated[2] and the BER was determined as a mean over all compound channel realisations. This mean BER is plotted as a function of the spacing. There are several conclusions based on Fig. 7.2.

Firstly, it is noted that the performance deteriorates with increasing centre frequency. This is due to the increased path-loss. For 10.296 GHz the mean SNR is lower than for 3.432 GHz and it remains so even after antenna selection removes the deep fades. The relatively high BER ($> 10^{-3}$) is due to the fact that here the frequency hopping is not considered.

Secondly, it confirms that there is a periodicity in the performance when the element spacing is increased. This is easier to observe for the higher frequencies. This shows the difficulty in

[2] This number depends on the element spacing. For an array with spacing by 1 measurement point (=6 mm), the number of compound channel realisations was 39×40, for an array with spacing by 2 measurement points (=12 mm), the number of compound channel realisations was 38×40 etc.

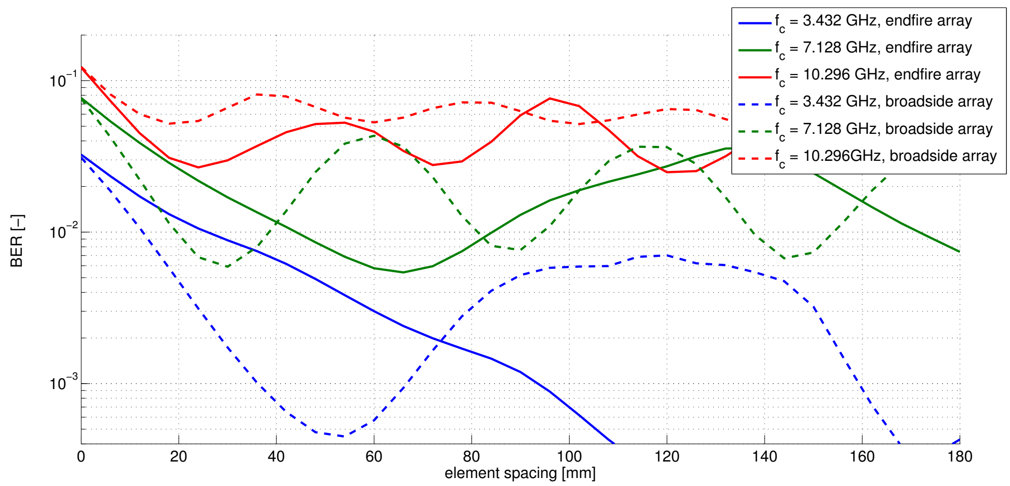

Figure 7.2: Analytical BER performance of a 2×1 'WiMedia-like' system with antenna selection in measured channels for various centre frequencies and for two orientations of the array as a function of element spacing. The BER for zero spacing shows the performance of a 1×1 system.

the choice of spacing because it can be seen that for the broadside case, the spacing of 50 mm is the optimum for the frequency of 3.432 GHz, but it is also almost the worst case for the frequency of 7.128 GHz.

Finally, it can be observed that the behaviour differs for broadside and endfire arrays. This is due to the fact that the 'periodic pattern' in Fig. 3.8 is caused by the angles-of-arrival/departure of the most significant multipaths and unless there is a significant symmetry in the environment, the performance changes with the rotation of the array. This is a positive result for the following reason. It is not surprising that further performance improvements can be achieved if more elements are used in the array, simply because more antennas add more diversity. This result suggests that the usage of circular arrays should be preferred over linear arrays because they can exploit the different 'periodicity' in different directions. Additionally, such arrays are more compact, i.e. a circular(square) 4-element array is easier to integrate than a 4-element linear array with the same spacing between adjacent elements.[3]

The better suitability of circular arrays over linear arrays is presented in Fig. 7.3 which shows the mean ratio of BER for the SISO case to the BER for antenna selection for a 4×1 system. The investigated arrays are 4-element linear arrays with a broadside and an endfire orientation and a 4-element circular array (square array). For each array, the BERs as a function of spacing are calculated for all 14 centre frequencies as was done in Fig. 7.2. For each centre frequency the ratio of BER for a SISO to BER for the antenna selection case is calculated and the mean over all 14 frequencies is plotted for the selected spacing. The spacing on the horizontal axis is the element spacing for the linear arrays and it is the length of the side of the square for the circular array.

It can be seen that the circular array outperforms the broadside array for all spacings above 20 mm. For spacings below 20 mm the performance is comparable. For the endfire array, the situation is more difficult. The endfire array outperforms the circular array for spacings over 36 mm. This suggests that the circular array is not universally advantageous. The reason for this is as follows. The measurement was performed for a mean range of 1.06 m. As the size of the endfire array increases, the four antenna elements eventually perceive the difference in

[3]It is noted that there is no difference between a 4-element circular and a 4 element square array. However, the investigation of the number of elements will follow and 'true' circular arrays will be considered.

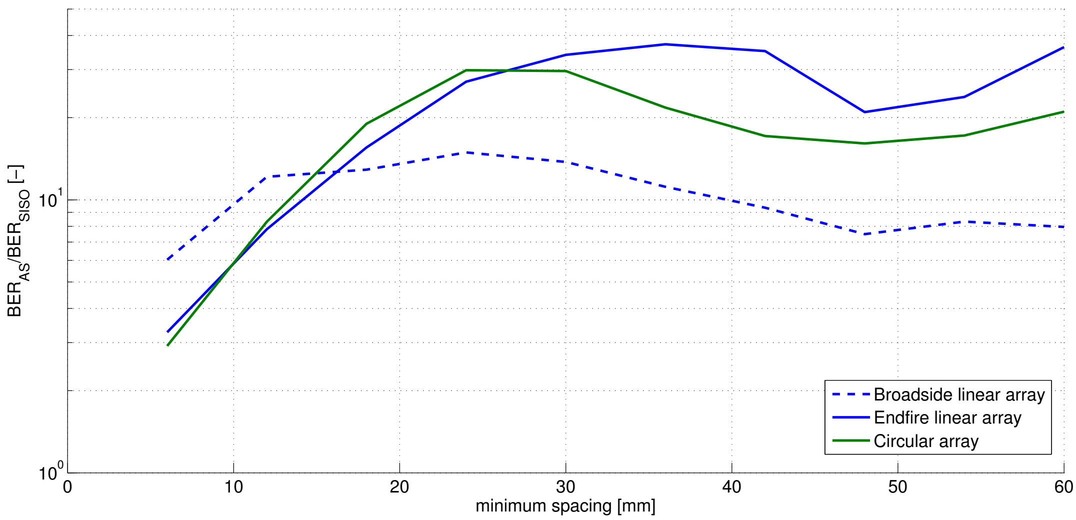

Figure 7.3: The mean BER improvement of a 4×1 antenna selection system compared to a SISO system for different array types. The mean is performed over all 14 WiMedia bands. The results are analytical using data from measured 4×1 wireless channels.

the path-loss between the elements. This distorts the results because then the elements with less path loss are preferred. However, it must be noted that even if the path-loss increase over the length of the array helps to improve the performance of the endfire arrays, in practical applications the position of the receiver will be arbitrary, hence it will alternate between the broadside and endfire case. The performance of the circular array is approximately the mean for the broadside and endfire case. At the same time, the circular arrays are also significantly more compact which is attractive in terms of integration into real devices.

So far, it has been demonstrated that the circular arrays are more compact and offer performance comparable to linear arrays. Now, the optimum diameter of the array and the number of the array elements are explored in Fig. 7.4 which shows the same measure as Fig. 7.3. It shows the mean BER improvement as a function of array diameter for arrays with different numbers of elements.

In terms of optimum diameter, Fig. 7.4 shows that the increase of the performance improvement is roughly independent of the diameter for diameters larger than 40 mm. This approximately corresponds to $\lambda/2$ at the lowest frequencies of the UWB band and it also corresponds to the knowledge that the correlation in a narrowband channel corresponds to the first order Bessel

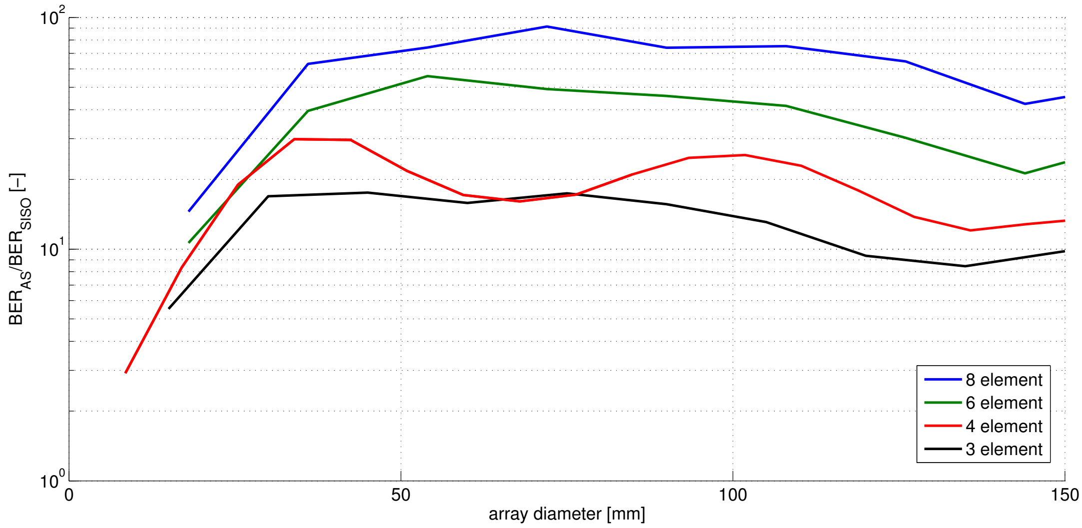

Figure 7.4: The mean BER improvement of a N×1 antenna selection system compared to a SISO system for different diameters of the circular arrays. The mean is performed over all 14 WiMedia bands.The results are analytical using data from measured N×1 wireless channels.

function [137]. In terms of the increasing number of elements, it can be observed that the performance improvement increases. However, this performance increase is associated with a linear complexity increase. Firstly, each transmit antenna in the system requires its own OFDM modulator. The issue of complexity of OFDM chips for UWB systems has been briefly outlined in chapter 5. Secondly, the complexity of the selection of the transmit antenna also increases linearly with the number of antennas.

To sum up the conclusions so far, it has been shown that antenna selection can significantly improve the performance of a UWB OFDM system. It's main advantages are the fact that it is insensitive to the element spacing, and it cannot violate the EIRP limits. It has been shown that the preferred choice should be circular arrays with diameters larger than 40 mm. The performance increases with the number of elements, but it is also associated with the linear increase in complexity.

The subsequent section shows how the transmission range of a fixed and adaptive OFDM UWB system with antenna selection increases compared to a SISO system.

7.2.3 Performance of Antenna Selection in an Office Environment

So far the recommendation for the array geometry for systems with antenna selection has been discussed. The metrics used for this evaluation was either the BER or the ratio of the mean BER improvement between the MIMO and SISO case. However, users of practical systems are interested in measures such as transmission range and/or data-rate. The BER is often fully remedied by the channel coding and 'hidden' from the user. Therefore in this section the measurements for 10 distances in an office environment are used to estimate the data-rate and range enhancement of UWB OFDM systems with antenna selection.

The measurements in an office are introduced in chapter 5 and they were also used for performance evaluation of an adaptive OFDM system in chapter 6. The measurements were used to evaluate the performance of two systems: a fixed 'WiMedia-like' OFDM system and an adaptive OFDM system. The systems are the same ones as used for performance evaluation of the adaptive OFDM system in chapter 6.

The fixed OFDM system in this investigation had 100 data-subcarriers with QPSK modulation spaced exactly as in the WiMedia system. Frequency spreading was employed so that each data-bit is spread on two subcarriers as in WiMedia systems [13] and the receiver combines them using Maximum-ratio-combining as in WiMedia systems [13]. The dynamic range of the system is 60 dB and the performance was evaluated only for the three lowest frequency bands so that the results can be representatively compared with the performance of real WiMedia system that was presented and in chapter 5. Such a system has a fixed data-rate of 320 Mbps (this is the gross data-rate without consideration of channel coding or packet preambles). The performance in terms of BER is presented in Fig. 7.5. Again, the BER of 10^{-2} indicates the limit of transmission range because it corresponds to the strength of channel codes used in WiMedia systems [13].

Fig. 7.5 shows performance for four cases: A SISO with fixed OFDM and a fixed OFDM 4×1 antenna selection system using antenna selection. For both systems the case of frequency hopped system (EIRP can be increased by 4.7 dB [13]) and a system without frequency hopping are considered. For the SISO systems, the measurement at four positions for each distance enabled plotting four data-points per distance. The performance of the 4×1 antenna selection

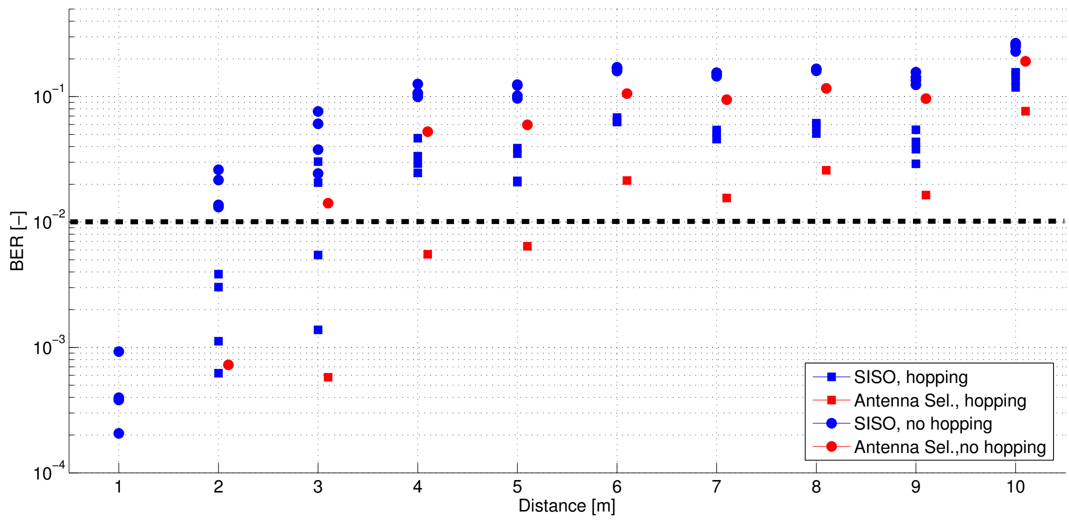

Figure 7.5: The BER dependency on range of 4×1 antenna selection system compared to a SISO system for systems with and without frequency hopping. The range is limited again by BER of 10^{-2} which is highlighted by a thick dashed line. The results are simulated using empirical wireless channels. The data for Antenna Selection were determined for the same distances as for the SISO system, the offset in the positions of the data-points is used for better clarity.

system is shown only by a single data-point because the measurement only provided 4 measurements. The antenna array was a circular (square) 4-element array with a diameter of 7.5 cm (square 5×5 cm).

As can be seen, the performance is improved for both cases with and without frequency hopping. For the case without hopping, the communication can be established even for the 2 m range, whilst it is only 1 m for the SISO system. With the frequency hopping, the range is up to 5 m, whereas the SISO system's boundary range was 3 m (2 out of 4 positions for 3 m have BER below 10^{-2}).

The performance of the adaptive OFDM system is presented in Fig. 7.6. The adaptive system is the same that used for the performance evaluation in chapter 6.4. It uses all 100 data-subcarriers and loads them with QPSK, 8-QAM, 16-QAM, and 64-QAM modulations based on the evaluation of their SNR. The data-rate is calculated by summation of the number of bits modulated on each subcarrier divided by the symbol duration (312.5 ns [13]).

Fig. 7.6 shows that for the case of frequency hopping, the data-rate can be increased by more than 100 Mbps for ranges of up to 9 m. If the range is defined by data-rate above 200 Mbps,

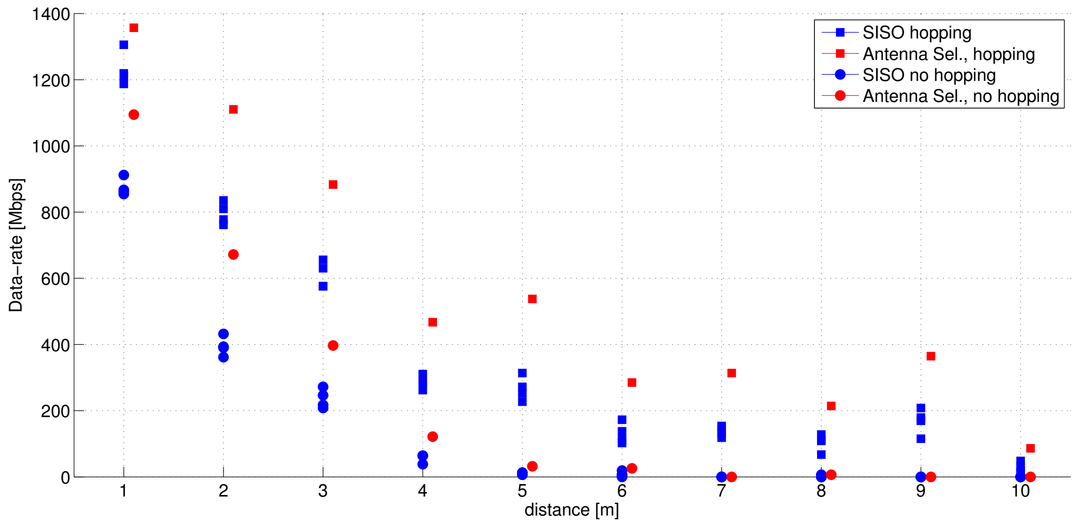

Figure 7.6: The data-rate dependency on range of a 4×1 antenna selection system compared to a SISO system for systems with and without frequency hopping. The results are simulated using empirical wireless channels. The data for Antenna Selection were determined for the same distances as for the SISO system, the offset in the positions of the data-points is used for better clarity.

antenna selection enables an increase from 5 m for SISO to 9 m for a 4×1 antenna selection system. For 400 Mbps it is an increase from about 3.5 m to about 6 m and for 1 Gbps, the range is increased from about 1 m to 2 m.

The range increase is lower for the case without hopping. Antenna selection still provides performance data-rate improvement by about 100 Mbps for the range of 3 m and by about 200 Mbps for ranges up to 2 m. However, the communication effectively ceases for a range of 5 m for both SISO and antenna selection systems. This is due to the fact that the performance is dominated by path-loss and for this range even the strongest subcarriers are below the minimum requirement of the adaptive system for loading by the lowest modulation scheme (QPSK). This is important to realise because it shows the limitation of antenna selection which is the path loss. Antenna selection can be used to 'flatten' the transfer function and to improve system's performance by removal of the deep fades but once the path-loss compares to the system's dynamic range, it does not provide any help, regardless of the number of antenna elements because it itself does not help to increase the system's dynamic range.

7.2.4 Antenna Selection: Conclusion

The antenna selection algorithm for UWB OFDM system has been introduced. Unlike other work that mostly focus on optimum phase pre-coding and simulations, here the impact of the array geometry was studied using empirical channels. It was concluded that circular arrays are advantageous. They provide performance comparable to the linear array. At the same time they are more compact and the performance is independent of the angle of arrival of the rays (rotation of the array will not impact its performance). The minimum array diameter required for a good performance over all 14 WiMedia bands is 40 mm and the performance remains unchanged for further increase of the diameter. The performance increases with the the number of elements but at the same time the complexity increases linearly and as noted in the performance evaluation, once the path-loss exceeds a certain level, additional antennas do not provide any performance improvement.

The results shown in Figs. 7.5 and 7.6 for both adaptive and fixed OFDM can be approximately translated as follows. By removal of deep fades, a 4×1 antenna selection enables the trading of a complexity increase of the system by a factor of four for approximately doubling the range of the system for the same data-rate. For more quantification of this conclusion, more measurements are required. These measurements are not available. However, at this stage the results in Fig. 7.5 are sufficient to illustrate how the understanding of the channel properties can be utilised for enhancement of the performance of UWB systems, which is the main objective of this thesis.

The main conclusion is that, for ranges where the performance of OFDM UWB systems is dominated by frequency selectivity and the mean path-loss is lower than the required dynamic range, the antenna selection is a powerful tool to enhance system's performance.

7.3 Low Complexity Beam Steering for UWB MIMO Systems with Adaptive OFDM

This section introduces an algorithm that exploits the channel properties provided by the UWB bandwidth. In short summary, the algorithm is a beam-forming method with the main lobe in the direction of the strongest multipath component, similar to the strategy used in 60 GHz systems [18]. As will be shown in this section, such a strategy is not suitable for narrowband systems with low number of antenna elements. For the UWB case, the large available bandwidth can be exploited. SNR of some subcarriers will be reduced whilst for some subcarriers the performance will be enhanced. However, it can be shown that on average over the large UWB bandwidth the performance is better than for Maximum-Ratio-Combining. This makes the algorithm an ideal candidate for adaptive OFDM UWB systems.

The section has the following structure. Firstly, analysis of the channel transfer function for a MIMO transmission will show that the statement about the properties of the algorithm, stated in the preceding paragraph, is justified. Secondly, the issue of grating lobes is discussed and it is shown that the properties of the algorithm are not significantly influenced by the presence of the grating lobes. Thirdly, its transmission range/data-rate performance in the office environment, used for performance evaluation in chapters 5 and 6, and in section 7.2, is explored. Finally, the implementation of the algorithm is briefly discussed.

7.3.1 Theory

The investigation of the properties of the algorithm begins with the channel impulse response $h_{i,j}(t)$ in a MIMO channel between the i-th antenna at the transmitter and the j-th antenna at the receiver.

$$h_{i,j}(t) = \sum_{r=1}^{R} \alpha_r e^{j\theta_r} \delta(t - \tau_r - \Delta_{i,r}^{T} - \Delta_{j,r}^{R} - \Delta_{BS,i}^{T} - \Delta_{BS,j}^{R}) \tag{7.4}$$

where t stands for time; R represents the number of multipaths; index r is the multipath number; α_r and θ_r stand for multipath attenuation and phase associated with path r;
τ_r stands for the delay that corresponds to the path (p_r) between the 'first elements' of the

array as depicted in Fig. 7.7 for multipaths 1 and 2;

$\delta(t)$ is a Dirac Delta Impulse function;

$\Delta^T_{i,r}$ represents the delay that incurs to the multipath r at the i-th antenna at the transmitter (noted by ^{T}) due to path difference given by the Angle-of-Departure (azimuth and elevation) of ray r;

$\Delta^R_{j,r}$ is a delay at the j-th antenna at the receiver (equivalent to $\Delta^T_{i,r}$);

$\Delta^T_{BS,i}$ and $\Delta^R_{BS,j}$ are delays introduced by the beam steerer at i-th (respectively j-th) antenna at the transmitter (resp. receiver). At this stage, $\Delta^T_{BS,i}$ and $\Delta^R_{BS,j}$ are not specified but they will be discussed at a later stage.

For the delays $\Delta^T_{i,r}$ and $\Delta^R_{j,r}$, it is assumed both arrays are in the far field, hence the delays are defined as a geometrical increase of length of parallel rays:

$$\Delta^T_{i,r} = (i-1)\frac{d_T}{c}\sin\phi^T_r \sin\vartheta^T_r \tag{7.5}$$

$$\Delta^R_{j,r} = (j-1)\frac{d_R}{c}\sin\phi^R_r \sin\vartheta^R_r \tag{7.6}$$

ϕ^T_r stands for azimuth angle of ray r at the transmitter; ϑ^T_r stands for elevation angle of ray r

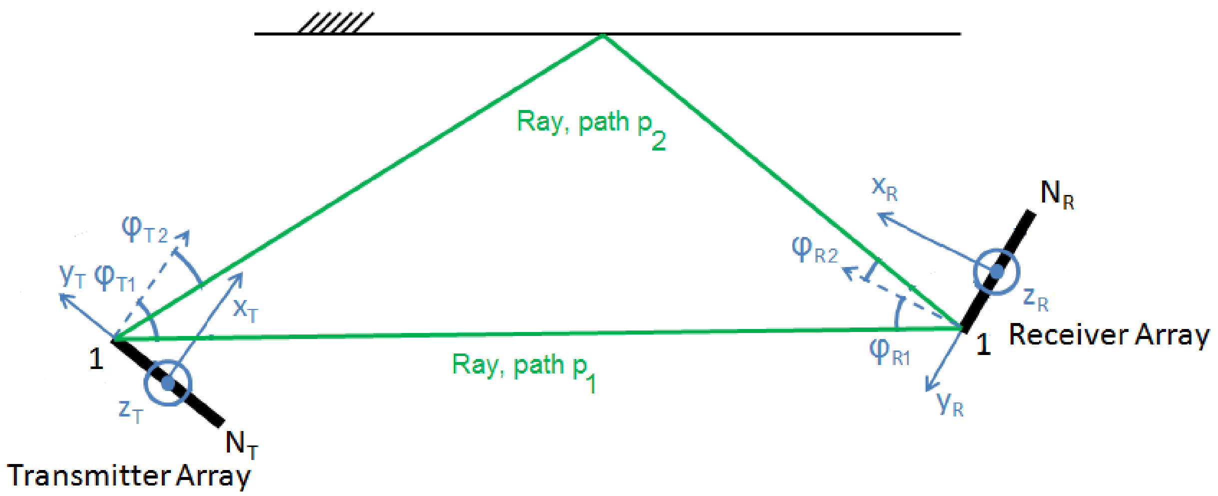

Figure 7.7: Definition of the 'first elements' in arrays and two example paths between these 'first elements'. The 'first element' is the element farthest from the centre of the array and placed on the positive y-axis of its corresponding coordinates. The opposite element on the negative y-axis has in general the number N_T for the transmit case and N_R for the receive case. Each array centre defines the coordinates' origin and the elements are on the y-axis.

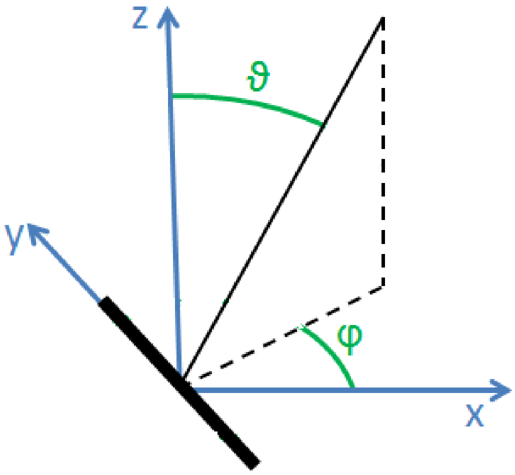

Figure 7.8: Definition of the coordinates set by an array (thick solid black line) and the definition of angles used in this thesis. (The definition is a standard definition for polar coordinates used in standard textbooks e.g. in [23])

at the transmitter; ϕ_r^R stands for azimuth angle of ray r at the receiver; ϑ_r^R stands for elevation angle of ray r at the receiver; c is the speed of light; d_T and d_R are the element spacings at the transmit and receive array respectively. The standard definitions of the azimuth and elevation angles are presented in Fig. 7.8. It is assumed that the choice of d_T and d_R is such that no grating lobes occur for the frequency band of observed OFDM symbol. The case for grating lobes will be discussed later in this section.

Fourier transform of (7.4) is:

$$H_{i,j}(f) = \sum_{r=1}^{R} \alpha_r e^{j\theta_r} e^{-j2\pi f(\tau_r + \Delta_{i,r}^T + \Delta_{j,r}^R + \Delta_{BS,i}^T + \Delta_{BS,j}^R)} \tag{7.7}$$

For later use, the expression for $|H_{i,j}(f)|^2$ is expressed here:

$$\begin{aligned} |H_{i,j}(f)|^2 = & \sum_{r=1}^{R} \alpha_r^2 + \\ + & \sum_{\substack{r1=1 \\ r1 \neq r2}}^{R} \sum_{r2=1}^{R} \alpha_{r1}\alpha_{r1} \cos[2\pi f(\tau_{r1} + \Delta_{i,r1}^T + \Delta_{j,r1}^R - \tau_{r2} - \Delta_{i,r2}^T - \Delta_{j,r2}^R) - (\theta_{r1} - \theta_{r2})] \end{aligned} \tag{7.8}$$

So far Eqs. (7.4) and (7.7) describe only the transmission contribution of the i-th transmitter and the j-th receiver antenna towards the total transmission. The total channel transfer function of the beam-steering, $H_{BS}(f)$, is defined as:

$$H_{BS}(f) = \sum_{i=1}^{N_T} \sum_{j=1}^{N_R} H_{i,j}(f) \tag{7.9}$$

where N_T and N_R stand for the number of antennas at the transmitter and the receiver respectively.

For the evaluation of the performance of such a system, it is necessary to know $|H_{BS}(f)|^2$ which can be calculated as follows:

$$|H_{BS}(f)|^2 = H_{BS}(f)H^*_{BS}(f) \tag{7.10}$$

where * stands for the complex conjugate.

Substituting (7.9) and (7.7) into (7.10) one obtains:

$$|H_{BS}(f)|^2 = \sum_{i1=1}^{N_T} \sum_{j1=1}^{N_R} \sum_{r1=1}^{R} \sum_{i2=1}^{N_T} \sum_{j2=1}^{N_R} \sum_{r2=1}^{R} \alpha_{r1}\alpha_{r2}e^{j(\theta_{r1}-\theta_{r2})}$$
$$e^{-j2\pi f[(\tau_{r1}+\Delta^T_{i1,r1}+\Delta^R_{j1,r1}+\Delta^T_{BS,i1}+\Delta^R_{BS,j1})-(\tau_{r2}+\Delta^T_{i2,r2}+\Delta^R_{j2,r2}+\Delta^T_{BS,i2}+\Delta^R_{BS,j2})]} \tag{7.11}$$

Using the relationship $0.5(e^{jx} + e^{-jx}) = \cos x$, Eq. (7.11) can be turned into:

$$|H_{BS}(f)|^2 = \sum_{i1=1}^{N_T} \sum_{j1=1}^{N_R} \sum_{r1=1}^{R} \sum_{i2=1}^{N_T} \sum_{j2=1}^{N_R} \sum_{r2=1}^{R} \alpha_{r1}\alpha_{r2}$$
$$\cos[2\pi f(\tau_{r1} + \Delta^T_{i1,r1} + \Delta^R_{j1,r1} + \Delta^T_{BS,i1} + \Delta^R_{BS,j1} - \tau_{r2} - \Delta^T_{i2,r2} - \Delta^R_{j2,r2} - \Delta^T_{BS,i2} - \Delta^R_{BS,j2})-$$
$$- (\theta_{r1} - \theta_{r2})] \tag{7.12}$$

In the next step, the six-duple is split to identify special cases. Firstly, the case $i1 = i2$ AND $j1 = j2$ is isolated into a separate term:

$$|H_{BS}(f)|^2 = \sum_{i=1}^{N_T}\sum_{j=1}^{N_R}\{\sum_{r=1}^{R}\alpha_r^2 \quad +$$

$$+\sum_{\substack{r1=1 \\ r1\neq r2}}^{R}\sum_{r2=1}^{R} \cos[2\pi f(\tau_{r1}+\Delta_{i,r1}^T+\Delta_{j,r1}^R-\tau_{r2}-\Delta_{i,r2}^T-\Delta_{j,r2}^R)-(\theta_{r1}-\theta_{r2})]\}+$$

$$+\sum_{i1=1}^{N_T}\sum_{i2=1}^{N_T}\sum_{\substack{j1=1 \\ i1\neq i2 \text{ OR } j1\neq j2}}^{N_R}\sum_{j2=1}^{N_R}\sum_{r1=1}^{R}\sum_{r2=1}^{R} \alpha_{r1}\alpha_{r2}\cdot$$

$$\cdot\cos[2\pi f(\tau_{r1}+\Delta_{i1,r1}^T+\Delta_{j1,r1}^R+\Delta_{BS,i1}^T+\Delta_{BS,j1}^R-\tau_{r2}-\Delta_{i2,r2}^T-\Delta_{j2,r2}^R-\Delta_{BS,i2}^T-\Delta_{BS,j2}^R)-(\theta_{r1}-\theta_{r2})] \tag{7.13}$$

In the first two lines of (7.13), the term $|H_{i,j}(f)|^2$ can be identified. Thus, the equation can be rewritten as:

$$|H_{BS}(f)|^2 = \sum_{i=1}^{N_T}\sum_{j=1}^{N_R}|H_{i,j}(f)|^2+$$

$$+\sum_{i1=1}^{N_T}\sum_{i2=1}^{N_T}\sum_{\substack{j1=1 \\ i1\neq i2 \text{ OR } j1\neq j2}}^{N_R}\sum_{j2=1}^{N_R}\sum_{r1=1}^{R}\sum_{r2=1}^{R} \alpha_{r1}\alpha_{r2}\cdot$$

$$\cdot\cos[2\pi f(\tau_{r1}+\Delta_{i1,r1}^T+\Delta_{j1,r1}^R+\Delta_{BS,i1}^T+\Delta_{BS,j1}^R-\tau_{r2}-\Delta_{i2,r2}^T-\Delta_{j2,r2}^R-\Delta_{BS,i2}^T-\Delta_{BS,j2}^R)-(\theta_{r1}-\theta_{r2})] \tag{7.14}$$

In Eq. (7.14), the first term corresponds to the Maximum-Ratio-Combining (MRC) in an $N_T \times N_R$ system:

$$|H_{MRC}(f)|^2 = \sum_{i=1}^{N_T}\sum_{j=1}^{N_R}|H_{i,j}(f)|^2 \tag{7.15}$$

In other words, it can be seen that in Eq. (7.14) $|H_{BS}(f)|^2$ corresponds to the value obtained for MRC changed by the second term that is represented by the six-duple sum. The second sum can further increase or reduce the result. It is similar to the impact fading in a narrowband channel on the mean path-gain in Eq. (3.28) in chapter 3.3. However, the terms $\Delta_{BS,i}^T$ and $\Delta_{BS,j}^R$ can be used to ensure maximisation of $|H_{BS}(f)|^2$.

Here we study the performance of a low-complexity beam steering system, hence $\Delta_{BS,i}^T$ and

$\Delta^R_{BS,j}$ are set to correspond to the delays of the first multipath[1]:

$$\Delta^T_{BS,i} = -\Delta^T_{i,1} = -(i-1)\frac{d_T}{c}\sin\phi^T_1\sin\vartheta^T_1 \tag{7.16}$$

$$\Delta^R_{BS,j} = -\Delta^R_{j,1} = -(j-1)\frac{d_R}{c}\sin\phi^R_1\sin\vartheta^R_1 \tag{7.17}$$

If the definition of the beam-steering delays is introduced (7.14), a further term for $r1 = 1$ AND $r2 = 1$ can be extracted out of the six-duple sum:

$$\begin{aligned}|H_{BS}(f)|^2 = \sum_{i=1}^{N_T}\sum_{j=1}^{N_R}|H_{i,j}(f)|^2 + [N_T(N_T-1)\cdot N_R(N_R-1) + N_T N_R(N_R-1) + N_R N_T(N_T-1)]\alpha_1^2 \\ + \underbrace{\textstyle\sum_{i1=1}^{N_T}\sum_{i2=1}^{N_T}\sum_{j1=1}^{N_R}\sum_{j2=1}^{N_R}\sum_{r1=1}^{R}\sum_{r2=1}^{R}}_{[i1\neq i2\ \text{OR}\ j1\neq j2]\ \text{AND}\ [(\text{IF}\ r1=1,\ r2\neq 1)\ \text{OR}\ (\text{IF}\ r2=1,\ r1\neq 1)]} \alpha_{r1}\alpha_{r2}\cdot \\ \cdot\cos[2\pi f(\tau_{r1}+\Delta^T_{i1,r1}+\Delta^R_{j1,r1}+\Delta^T_{BS,i1}+\Delta^R_{BS,j1}-\tau_{r2}-\Delta^T_{i2,r2}-\Delta^R_{j2,r2}-\Delta^T_{BS,i2}-\Delta^R_{BS,j2})-(\theta_{r1}-\theta_{r2})]\end{aligned} \tag{7.18}$$

It noted in the introduction of this chapter that the same algorithm is used for beam-steering in 60 GHz systems [18]. However, in such systems the N_T and N_R are significantly larger than in the UWB case [18]. For instance, [146] suggests an 8-antenna array and [147] discusses a 16-element array. Hence, for the same transmitter and receiver the amplification $N_T(N_T-1)\cdot N_R(N_R-1)$ yields 3136 and 57600 so that the first and the last term in (7.18) can be completely neglected and the communication can be perceived as a point-to-point single path link. For UWB with lower numbers of antenna elements N_T and N_R are typically less or equal to 4. The systems can also be N×1 UWB systems. Hence, all three terms in (7.18) yield roughly the same values and therefore none of them can be neglected.

The analysis of Eq. (7.18) for the UWB case leads to the following conclusion. The resulting value of $|H_{BS}(f)|^2$ for the low-complexity beam-steering corresponds to the MRC $|H_{MRC}(f)|^2$ increased by the amplification of the power of the first ray and finally the value is changed by the rest of the six-duple sum. The rest of the six-duple sum is a random variable because its total value depends on a number of random variables - the multipath-delays τ_r, the multipath

[1] It is noted that the beamsteering does not need to be towards the first multipath. The best results are obtained for the strongest multipath, which is typically the first one.

amplitude α_r, the multipath AoAs and AoDs (defining the delays $\Delta^T_{i1,r}$ and $\Delta^R_{j1,r}$), the multipath phases θ_r. The random variable is zero-mean. The principles of the proof now follow. Random variables in the cos-terms along with the phase-wrapping property of the cos-terms mean that the cos-terms are uniformly distributed random variables on the interval -1 to 1. Once this is shown, the sum of such a large number of such variables amplified by α_rs gives, owing to the central limit theorem [34], a zero mean Gaussian distribution.

The random variable further increases or reduces the value of $|H_{MRC}(f)|^2 + N_T(N_T-1)\cdot N_R(N_R-1)\alpha_1^2$. This makes such beam-steering unsuitable for narrowband systems with a low number of antenna elements, because the resulting $|H_{BS}(f)|^2$ can vary significantly. Unless the N_T and/or N_R are large like in the 60 GHz cases, it cannot be guaranteed that the level of $|H_{BS}(f)|^2$ will be above the MRC $|H_{MRC}(f)|^2$.

However, OFDM UWB systems have an $|H_{BS}(f)|^2$-value for each subcarrier. The spread over large frequencies helps to reduce the impact of the six-duple sum because over the frequency span of 500 MHz, the impact of the zero mean Gaussian random variable on each $|H_{BS}(f)|^2$ evens out as zero. In other words, the mean over the frequencies of the entire OFDM symbol $\mathrm{E}\left\{|H_{BS}(f)|^2\right\}$ yields:

$$\mathrm{E}\left\{|H_{BS}(f)|^2\right\} = \mathrm{E}\left\{|H_{MRC}(f)|^2\right\} + [N_T(N_T-1)\cdot N_R(N_R-1) + N_T N_R(N_R-1) + N_R N_T(N_T-1)]\alpha_1^2 \tag{7.19}$$

which is an improvement over Maximum-Ratio-Combining because the term $N_T(N_T-1)\cdot N_R(N_R-1)\alpha_1^2$ increases the mean SNR.

It is still valid that some subcarriers in the OFDM symbols may be below the level of MRC, but on average the received energy of all subcarriers is more. This is an optimal situation that can be exploited by adaptive OFDM.

This is shown in Figs. 7.9 and 7.10. Fig. 7.9 presents an example of an empirical channel transfer function $|H_{BS}(f)|$ and $|H_{MRC}(f)|$ obtained by measurement of both channels in a 2×1 system. The transmitter antennas were spaced 42 mm apart. The channel pair was randomly selected from the measurement grid at position 1 as presented in appendix C. The spacing is selected as approximately half-wavelength at the investigated frequencies. The frequency

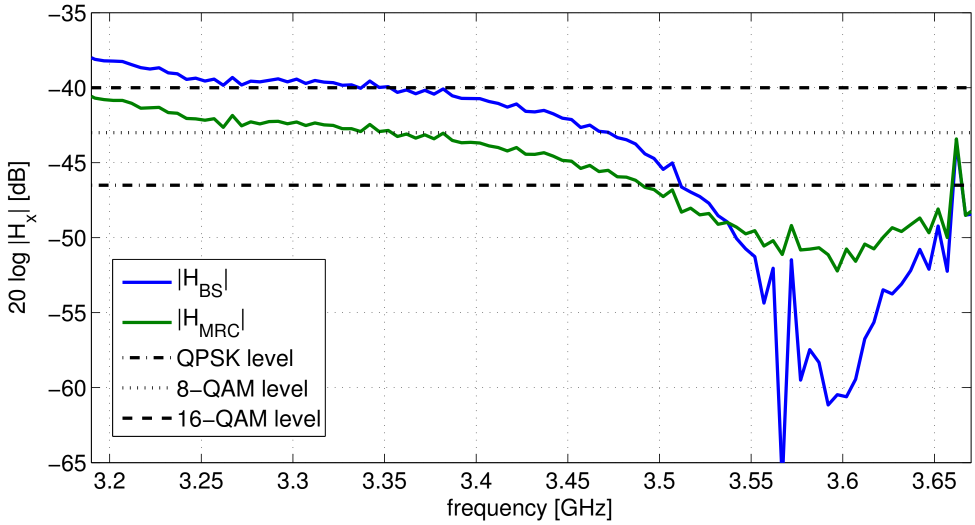

Figure 7.9: An example of $|H_{BS}(f)|$ and corresponding $|H_{MRC}(f)|$ to illustrate the performance of the proposed beam-steering algorithm.

band corresponds to the WiMedia band 1 [13]. The plot illustrates what has been discussed above. There are frequencies at which the $|H_{BS}(f)|$ outperforms the $|H_{MRC}(f)|$ and frequencies where the situation is opposite. The claim that an average of $|H_{BS}(f)|$ over frequency is above $|H_{MRC}(f)|$ will be shown in Fig. 7.10.

However, Fig. 7.9 can also be used to show why the $|H_{BS}(f)|$ is more suitable than the $|H_{MRC}(f)|$ in the case of the adaptive OFDM. Fig. 7.10 also plots the decision levels for QPSK, 8-QAM and 16-QAM of the system presented in chapter 6. These levels were determined assuming a dynamic range of 57 dB. The reduction of the 60 dB dynamic range from chapter 6 is due to the fact that the noise power is doubled by both schemes. Fig. 7.10 shows that for the case when the $|H_{BS}(f)|$ is below the $|H_{MRC}(f)|$, the power is below the QPSK level anyway and the adaptive system would not use these subcarriers even for the MRC. Hence, the deeper fades do not matter whilst the constructive superpositions are highly advantageous. The power increase by about 3 dB enables more subcarriers to be loaded with higher order modulation. In contrast, the beam-steering is not suitable for fixed OFDM techniques, because the deterioration of deep fades contributes the most to the overall BER and is the main limitation for the system's performance as discussed in chapter 5.

Fig. 7.10 confirms the validity of Eq. (7.19). The graph shows the ratio between the $\mathrm{E}\{|H_{BS}(f)|^2\}$ and $\mathrm{E}\{|H_{MRC}(f)|^2\}$ averaged over frequencies of the WiMedia band 1 [13] for

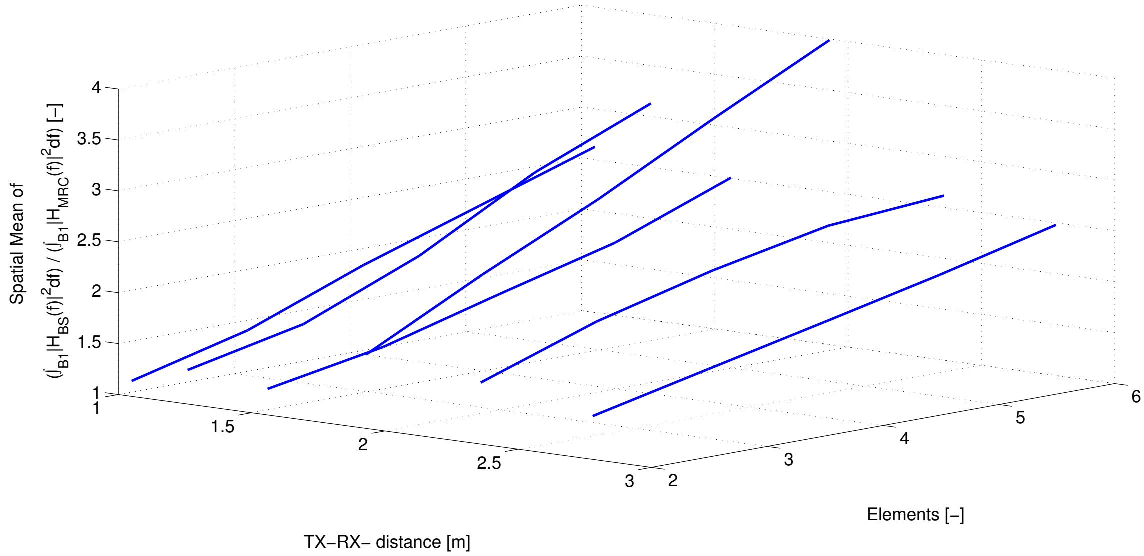

Figure 7.10: Comparison of the performance of the presented beam-steering compared to the MRC for six measurement positions as a function of number of elements in the array. The results are based on the use of measured channel transfer functions. For all measurement positions and number of elements, the ratio is above 1 which confirms Eq. (7.19).

arrays with 2 to 6 elements spaced by 42 mm. The measurement grids for all six measurement positions from appendix C were used. Each line in Fig. 7.10 stands for data from one measurement positions. They are differentiated by the axis with the mean TX-RX distance. For each measurement grid, the ratio $\frac{\mathrm{E}\left\{|H_{BS}(f)|^2\right\}}{\mathrm{E}\{|H_{MRC}(f)|^2\}}$ was calculated for all possible positions of the array within the measurement grid. Each data-point in Fig. 7.10 was obtained by spatial averaging over all measurement positions.

Fig. 7.10 confirms Eq. (7.19). The mean over all the frequencies in an OFDM symbol $\mathrm{E}\left\{|H_{BS}(f)|^2\right\}$ is higher than the mean performance of MRC $(\mathrm{E}\left\{|H_{MRC}(f)|^2\right\})$ and the difference increases with the number of elements in the array.

To conclude, this section has derived a low-complexity beam-steering algorithm suitable for UWB systems with adaptive OFDM. Due to the large UWB bandwidth the algorithm performs better than MRC. The theoretical results were confirmed by investigations in empirical channels. The discussion so far was limited to arrays with element spacing that does not allow the existence of grating lobes. The issue of element spacing is discussed in the next section.

7.3.2 Impact of Element Spacing

One of the issues of UWB MIMO systems is the fact that a fixed element spacing is suboptimal for spatial filtering algorithms. A tight spacing does not provide sufficient spatial filtering ability at the lower end of the UWB band, whereas sparser arrays result in the existence of grating lobes at the higher frequency end.

For the beam-steering algorithm introduced in the preceding section, the spacing has not been discussed. It was only assumed that the spacing is such that no grating lobes appear. The optimum spacing is discussed here. If Eqs. (7.14) and (7.18) are analysed, it can be seen that the first two terms in (7.18) are independent of the spacing. If the delays between adjacent elements are tuned so that all elements receive the first ray in-phase, the algorithm will on average perform better than MRC. The spacing has an impact on the last term in (7.18) and the frequency selectivity will change with the spacing. The explanation here is that the change of spacing will move the side-lobes and the nulls in the pattern at each frequency. This will have an impact on the attenuation/amplification of later multipaths at an individual frequency.

However, the adaptation to these changes is managed by the adaptive OFDM algorithm. In other words the core of the performance is independent of the spacing, even for spacings that enable the existence of grating lobes. Also, the position of the grating lobes differs with frequency as discussed in chapter 2.2. This makes the reception through the main lobe, with position fixed for all frequencies, unique and optimal. If grating lobes occur they have an impact on $|H_{BS}(f)|^2$ at individual frequencies but they do not impact the properties of the algorithm. This statement is confirmed by Fig. 7.11.

Fig. 7.11 investigates the same quantity as Fig. 7.10 for a two-element array with variable spacing for three different centre frequencies of the WiMedia bands 1, 8, and 14 [13]. The results are plotted on the scale of relative spacing. It can be observed that the performance varies with the spacing but remains above 1 at all times, i.e. the average performance is better than that of MRC. A periodicity can be observed in the curves, caused by the correlation in narrowband channels which is known to be $\propto \mathrm{J}_0\left(\frac{2\pi d}{\lambda}\right)$ (e.g. [137]) where J_0 is the Bessel function of 0-th order. This behaviour dictates to what extent the MRC can exploit the channel diversity.

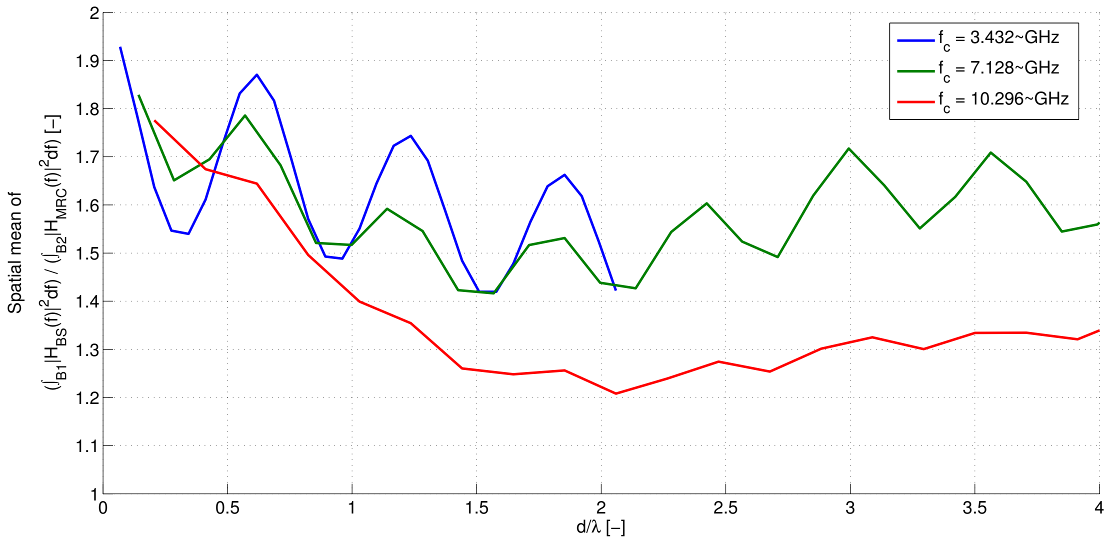

Figure 7.11: Comparison of the performance of the presented beam-steering compared to the MRC as a function of element spacing for a two-element array and various centre frequencies. The results are analytical using the data from measured channel.

Hence it can be concluded that the transfer function $|H_{BS}(f)|^2$ changes with the element spacing but overall the beam-steering algorithm does not lose its properties because the changes in $|H_{BS}(f)|^2$ are smeared by the averaging over the entire frequency band and by the adaptive OFDM. In other words, the spacing of the array elements can be selected based on other aspects such as the compactness of the design rather than by the impact of spacing on the performance.

7.3.3 Performance

The performance of the suggested algorithm in the office environment is presented in this section. The performance is studied only for the adaptive OFDM system, described in detail in chapter 6. Fixed OFDM is not presented, as discussed in the theory above, this algorithm is suitable for adaptive OFDM because it maximises the total energy over all subcarriers. The cost for the low complexity is the fact that whilst the total energy is maximised, some subcarriers suffer from deep fading.

The performance is now evaluated for a 2×1 system and for a 4×1 system. For each system, the cases without frequency hopping and with frequency hopping (increase of dynamic range by 4.7 dB [13]) are evaluated. The performance evaluation begins with the systems without frequency hopping which is presented in Fig. 7.12.

Fig. 7.12 presents the performance of the new algorithm for the 2×1-case (blue circles) and 4×1-case (blue squares). This performance is compared to the SISO case (black circles) of the same adaptive system and to two other MIMO techniques: MRC in red, and Maximum-Gain-Combining (MGC) in green. Similarly to the new algorithm the data-point shape for the 2×1 MRC and MGC is a circle and the data-point shape for the 4×1 MRC and MGC is a square. Since there are four measured channels available for each distance, there are 6 data-points plotted for the two-antenna-systems (given as $\binom{4}{2}$) and only one for four-antenna-systems.

The MRC algorithm has been introduced in (7.15), where the receiver sums the powers of signals from each antenna. For MGC the receiver sums the amplitudes of the signals from different antennas, e.g. [34]:

$$|H_{MGC}(f)|^2 = \left(\sum_{i=1}^{N_T} \sum_{j=1}^{N_R} |H_{i,j}(f)| \right)^2 \tag{7.20}$$

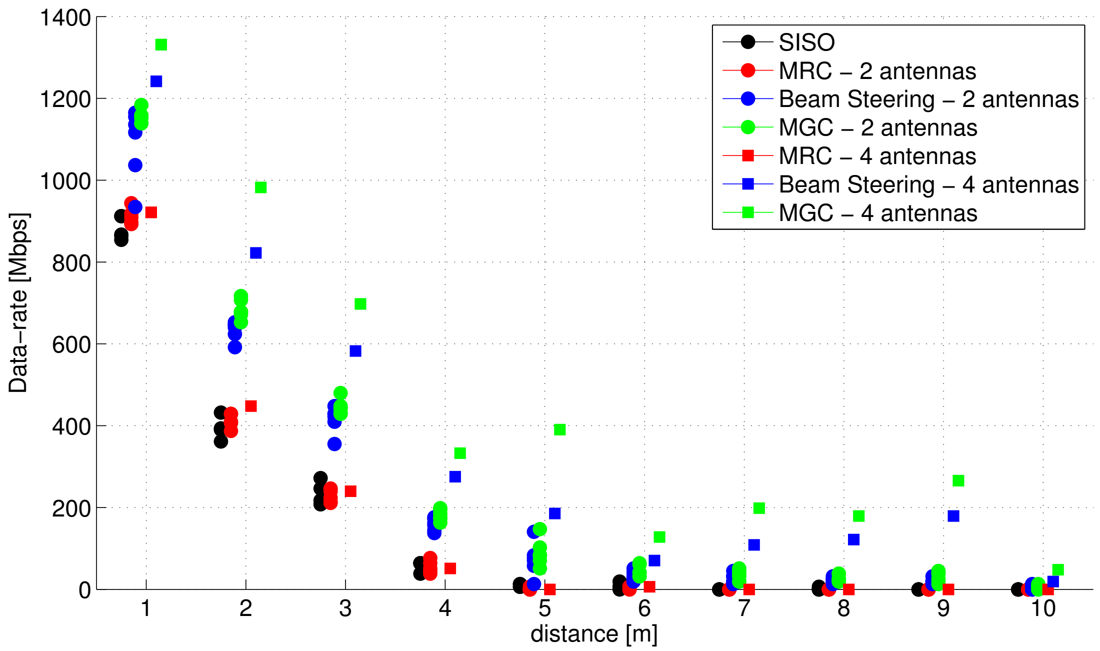

Figure 7.12: The data-rate dependency on range of adaptive UWB OFDM system for the SISO case and 2×1 (circles), and 4×1 (squares) MISO systems. The data points for the MISO systems are red for the MRC, blue for the new algorithm, and green for the MGC. The system do not use frequency hopping. The results are analytical using the data from measured channel.

A number of observations can be made based on Fig. 7.12. Firstly, the new algorithm provides an improvement in performance over the SISO case and also over the MRC case. For the two-antenna-case, it performs closely to the MGC case but the gap increases for the four-antenna-case.

Secondly, the performance of MRC should be discussed. It can be seen that the system does not improve the performance compared to the SISO case. This might seem surprising but is a result of the nature of the adaptive OFDM system. In an N×1 system, MRC does not increase the mean SNR because the power combining of N signals at the receiver increases the power on average by factor N but this factor is also applied to the noise. For transmitter precoding in UWB the transmit power has to be reduced to comply with the EIRP. Hence, MRC is an algorithm for 'flattening' of the transfer function and is suitable for fixed OFDM systems. For adaptive OFDM systems, it removes the deep fades but at the same time it tends to reduce the SNR for the strong subcarriers. Thus it might seem that plotting the MRC values in Fig. 7.12 does not make any sense. These data-points are included only to further confirm the superiority of the presented beam-steering.

The main source of improvement in the new algorithm is the increase of the SNR. This increase is caused by the term $N_T(N_T-1)\cdot N_R(N_R-1)\alpha_1^2$ in (7.19). As discussed in the theory, the variance of the subcarrier powers inherent to the algorithm is not suitable for fixed OFDM systems, but the adaptive OFDM UWB systems can exploit this property to their benefit. The performance of the MGC is superior to the new algorithm because it increases the signal power by the factor N^2 whereas the noise is amplified only by the factor N. As a result it 'boosts' the dynamic range of the system by $10\log N$[dB]. This is more than the increase by $N_T(N_T-1)\cdot N_R(N_R-1)\alpha_1^2$ in (7.19) and it is why the MGC's superiority is more apparent for the four-antenna case.

Finally, the improvement of the performance is quantified. The data-rates for the two-antenna system are superior to the SISO system. The range of the system is not significantly improved but for the range of 5 m, the two-antenna system enables data-rates of about 100 Mbps, whereas the SISO case effectively ceases the communication. This is due to the fact that the term $N_T(N_T-1)\cdot N_R(N_R-1)\alpha_1^2$ yields $2\alpha_1^2$. The improvements are more interesting for the

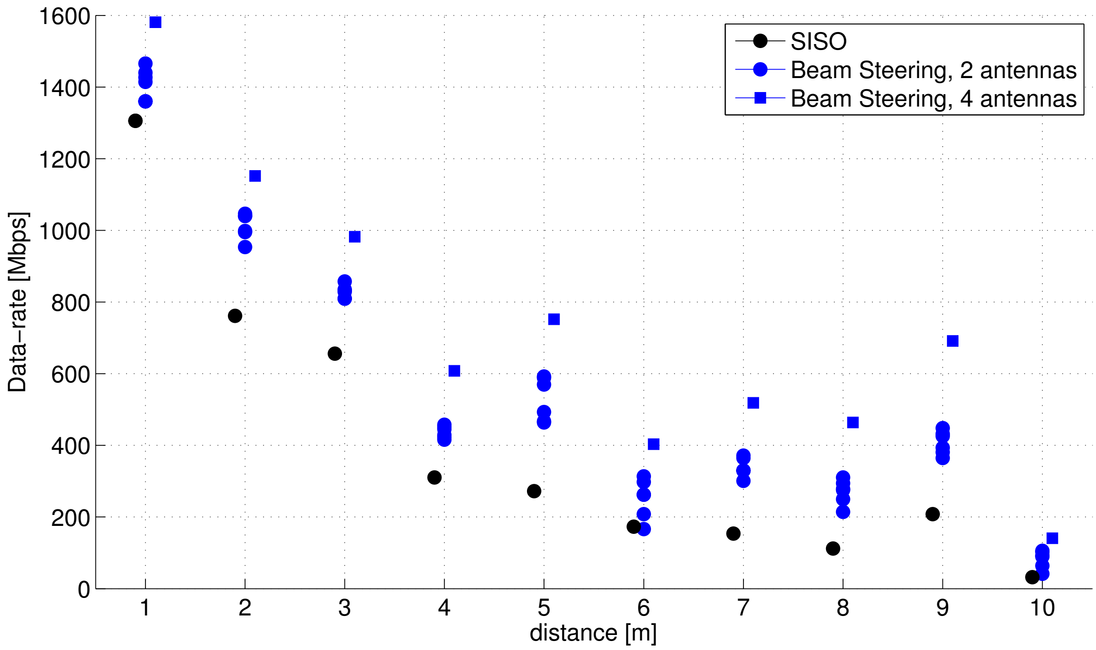

Figure 7.13: The data-rate dependency on range of adaptive UWB OFDM system for the SISO case and 2×1 (circles), and 4×1 (squares) MISO systems using the new algorithm. The systems use frequency hopping increasing dynamic range by 4.7 dB.

4-antenna case where the term $N_T(N_T-1) \cdot N_R(N_R-1)\alpha_1^2$ yields $12\alpha_1^2$. As a result, the 4×1 system enables communication for ranges of up to 9 m with data-rates above 100 Mbps.[4] This described performance increase confirms the theoretical expectations based on Eq. (7.19).

For frequency hopping, the performance of the new algorithm is investigated in Fig. 7.13. Fig. 7.13 does not include the MRC and MGC systems because the results would be similar as in Fig. 7.12. Again a significant performance improvement can be observed especially for the 4×1 system that allows data-rates above 400 Mbps for ranges of up to 9 m. The main conclusion based on Fig. 7.13 shows that a 4×1 system UWB system with adaptive OFDM can provide high data-rates (hundreds of Mbps) over distances of up to 10 m.

7.3.4 Implementation

The performance of the beam steering system aiming the beam at the first ray as discussed so far is very good, however it is only attractive if its implementation does not add excessive system complexity. In this section, the implementation of the new beam-steering algorithm is

[4]With the exception of the range of 6 m where due to higher path loss the data-rate was 70 Mbps.

briefly discussed. The discussion is structured around two main points:

- Discrete Beam-steering
- Implementation complexity of the OFDM

The beam-steering algorithm as described above assumes perfect in-phase combining between the adjacent elements. However, implementation of such precise in-phase combining is complex. Instead, it is possible to use beam-steering with a limited number of discrete steps that cover the entire area of interest. Such approach is not new and is considered e.g. in 60 GHz systems [146],[148]. The switching between a limited number of fixed beam-steering position for the UWB applications significantly reduces the space for the optimisation. The advantage of the arrays with a low number of elements (compared to 60 GHz systems) is the fact that systems with lower number of elements have smaller aperture, thus larger beamwidth [23]. As a result, a lower number of beam positions is required to cover the full space and the beam-steering is therefore less complex than for 60 GHz systems.

The final issue discussed in this section is the OFDM implementation of beam-steering. As pointed out in chapter 5, the implementation complexity of the FFT required for the OFDM increases linearly with the bandwidth and the chip complexity for UWB. The implementations of OFDM MIMO systems for UWB and IEEE802.11 (including antenna selection, MRC and MGC) almost entirely assume an OFDM chipset for each individual antenna and the MIMO operation is then performed in the frequency domain [47],[138],[139],[140]. The processing in the frequency domain is important, especially for complex algorithms such as Singular-Value-Decomposition [34]. The result of MIMO implementation is the linear increase of complexity with the increase in the number of the antenna elements.

However, the proposed beam-steerer is low-complexity, and as briefly mentioned similar to the beamsteering used in 60 GHz systems. Therefore, it is possible to use a pre-OFDM implementation. In principle, two implementations of the beam-steering are possible. Assuming the discrete beam-steering between a limited number of beams, the beam-steering can be implemented in the analogue domain using switched delay lines and/or Butler Matrix such as presented for a 60 GHz system in [146], and for a 5.8 GHz system in [148]. The advantage of this approach is the use of a single mixer and a single Digital-Analogue-Conversion (for transmit case, the convertor is Analogue-Digital). The challenge is the implementation of delay lines with a constant delay over the large UWB bandwidth. The beam-steering in the digital domain requires a mixer and Digital-Analog-Convertor for each antenna array. The FFT chip for the OFDM can be shared. The delays can be implemented in the digital domain, e.g. through a concatenation of invertors. The advantage is a constant delay step across the entire UWB band, but at the cost of increased complexity.

Ultimately, the actual implementation will depend on considerations for a specific system and will be influenced by factors such as - the choice of the total active UWB bandwidth (2.5 GHz for EU or 7.5 GHz for USA), the number of the discrete beam-steering steps and the associated cost factor. Discussion of this trade off is beyond the scope of this thesis which does not focus on implementation. The brief discussion about implementation of the beam-steering is presented here to show that the proposed beam-steerer is low-complexity not only in its principle but also in its implementation.

7.4 MIMO Systems Summary

In this section the specifics of UWB MIMO such as fixed EIRP were introduced. The importance of the selection of MIMO strategy matching with the system's modulation was explained. For OFDM systems with fixed subcarrier loading, the main objective should be to 'flatten' the transfer function so that deep fades limiting the system performance are eliminated. For adaptive OFDM systems, deep fades can be avoided thanks to bit loading. Hence, the main objective should be the maximisation of the total energy.

Two strategies were studied in realistic simulations using measured channels. It is shown that a 4×1 antenna selection can double the range of a WiMedia-like fixed OFDM system. A 4×1 low-complexity beam-steering in an office environment combined with a realistic adaptive OFDM system enables data-rates above 400 Mbps for ranges of up to 9 m.

This last chapter of this thesis justifies the statement from the introduction claiming that, when the understanding of the UWB wireless channel is used to modify existing UWB systems, it is possible to achieve significant improvements of the performance, and that the UWB systems remain realistic contenders to 60 GHz and Visible-Light-Communication systems.

CHAPTER 8

Conclusions and Future Work

The main objective of this thesis was to explore the impact of the properties of the UWB channel on the performance of UWB systems. It also aims to show how the relationship can be exploited in order to develop UWB systems providing more data-rate and/or range. This has been achieved and the thesis demonstrates performance enhancements that can be achieved by modifications to the impulse radio systems and to the OFDM WiMedia system. However, the conclusion that UWB communication systems can competitively deliver the 'Gigabit Wireless' systems is not the only significant contribution of this thesis. The other significant contributions of this thesis are briefly summarised here. This chapter begins with a summary of the contribution that links the findings, not only to UWB systems, but also to other systems. Future work is then discussed.

8.1 Major contributions

The main objective of the thesis was to understand the wireless channel and its impact on the performance of and other parameters in UWB systems. Hence the thesis began with discussions and explorations of the channel which consists of antennas and wireless propagations for indoor environments. For both the antennas and the wireless propagation, there are two cases - the classical narrowband case where the signal durations are significantly longer than the duration of the channel impulse response, and the extreme UWB case with extremely short sub-nanosecond signals. Both cases have been thoroughly investigated by previous work, however this thesis noted that not much attention had been paid to the transition between both cases even though practical UWB systems fall exactly into this category. For instance, WiMedia signals have a bandwidth of 528 MHz. By definition, such a signal is a UWB signal. However the channel properties of a 500 MHz channel differ from a channel with bandwidths in excess of several GHz. Hence, the first two chapters studied the transition between the two extreme cases.

Firstly, the impact of **antennas** on transmitted signals has been studied because, whilst the impact of antennas is neglected for the narrowband cases, the distortion of short UWB baseband pulses required the development of a new framework for antenna description. It was shown how the distortion of the signal caused by antennas can be quantified and evaluated. It was also concluded that the distortion of signals by antennas can be neglected for situations when the current distribution on the antenna is approximately constant for the entire bandwidth of the signal. It was shown that practical UWB antennas covering the entire US UWB spectrum (3.1-10.6 GHz) do not cause significant distortion to bandpass signals with bandwidths below 1 GHz.

Secondly, the properties of **antenna arrays** were investigated. Previous works investigating antenna arrays receiving extremely short sub-nanosecond pulses report interesting properties such as sparse arrays without grating lobes. However, this thesis concluded that for bandpass signals with bandwidths below 1 GHz the classical narrowband descriptors of antenna arrays can be used and that for such signals, sparse antenna arrays manifest significant grating lobes. In fact, it was shown that the requirement for the suppression of grating lobes is that the relative bandwidth of the signal needs to be 100% or more.

In the investigation of **wireless propagation**, firstly the **channel impulse response** from the IEEE802.15.4a channel model was studied and it was shown that the model incorrectly assumes that manifestations of antenna impulse responses are independent multipath components. Removal of this error significantly simplifies the channel model by reducing the number of independent multipath components by a factor of four or five.

Secondly, the spatial **frequency selective fading** of wireless channels was studied in great detail, especially the scaling of its impact with increasing bandwidth. The transition between the narrowband and UWB case was quantified in terms of standard deviations (called fade depth) and in terms of probability distribution function.

Briefly it can be concluded that whilst antennas treat signals with the 'transition bandwidths' from 100 MHz to 1 GHz in the same way as they treat the narrowband signals, the wireless propagation for signals with these bandwidths manifests properties similar to the channel for sub-nanosecond UWB signals.

All these conclusions about the properties of the antennas and wireless propagation were relevant for later chapters and were linked to specific properties and performance limitations of

UWB communication systems. However, their contribution goes far beyond this. Firstly, the full understanding of the transition between the classical narrowband and the extreme UWB worlds helps us to fully understand phenomena such as fading of the wireless propagation in the 'narrowband case'. These phenomena are given by properties that can only be observed in the 'UWB case'. Secondly, the currently planned IEEE802.11ac standard envisions the use of signals with bandwidth of 160 MHz. Such a bandwidth is closer to the 528 MHz of the WiMedia systems than to the original 20 MHz of the IEEE802.11a or any other narrowband system. Thus a lot of the findings about the transition between the 'two cases' is relevant to systems other than just UWB.

The third chapter of the thesis discussed the **impulse radio systems**. It is shown that, even though these systems do not suffer from frequency selective fading, as their bandwidth enables them to resolve individual multipath components, the multipath propagation limits their performance as it forces them to include guard intervals. The knowledge of the scaling of fading enabled weighing the BER performance with the duty cycle of the system. As a result, it was possible to find an optimum compromise for signal duration so that the signal remains resistant to erasure by fading but it does not require operation with very low duty cycle. It was shown that such signals should have bandwidths between 150 and 400 MHz and that they can be used in multicarrier impulse radio systems. A performance of one such system was investigated in measured channels. It was shown that such a system can achieve data-rates significantly higher than other state-of-the-art impulse radio systems.

The last three chapters studied the impact of the channel on **UWB OFDM system**, especially on the WiMedia systems. It was shown that the transmission range of WiMedia systems is significantly below values marketed by commercial vendors and the frequency selective fading was identified as the main cause. Frequency selective fading causes the energies of individual subcarriers in an OFDM symbol to vary by up to 20 dB, which is an issue for UWB systems with a dynamic range of approximately 60 dB. It was shown that even strong channel coding and sophisticated information spreading cannot fully remedy this issue. Consequently, modifications to the systems were investigated. The antenna selection MIMO technique that 'flattens' the spread of the subcarrier energies was shown to improve the transmission range of a WiMedia system. It was shown that a 4×1 antenna selection system can double the range of a WiMedia-like OFDM system with gross data-rate of 320 Mbps.

The second modification is the use of adaptive OFDM, which loads only subcarriers based on their SNR. Systems with adaptive OFDM avoid the deep fades. Instead they exploit frequencies for which the frequency selective fading is manifested as constructive superposition of multipaths. Such a system can easily be implemented in the WiMedia framework because the protocol already foresees pilot sequences for channel estimation in the packet preamble. Thus, investigation of such a system seems highly attractive.

The idea of adaptive OFDM symbols is not new, but to our best knowledge this thesis is the first work that evaluated performance of such an UWB system in measured channels. Also, the resistance of the adaptive system to spatial displacement was explored. It was concluded that for speeds below 10 m/s (which can be safely assumed for most indoor applications) a system with symbol duration the same as the WiMedia OFDM system can use the channel estimate based on a pilot OFDM symbol for 700 subsequent symbols (corresponding to the maximum duration of the packet) without a significant performance deterioration. In other words, the data-rate of the systems will not be compromised by excessive transmission of pilot sequences for channel estimation.

Furthermore, low-complexity beam-steering for such an adaptive OFDM system was explored. The beam-steering aims the main lobe in the direction of the strongest multipath. It is therefore similar to the beam-steering in a 60 GHz wireless system. However, compared to the 60 GHz systems, UWB systems are expected to have a lower number of antenna elements. Hence, other multipath components have to be considered. These multipath components cause frequency selectivity, therefore such a beam-steering is not suitable for narrowband systems because it may well attenuate rather than amplify the received signal. However, the frequency selectivity is compatible with the adaptive subcarrier loading and it was shown that, on average, such UWB systems perform better than a Maximum-Ratio-Combiner.

It was shown that a realistic 4×1 system with low-complexity beam steering and adaptive OFDM can offer data-rates above 400 Mbps for ranges of up to 9 m. Compared to a real WiMedia system, this is an improvement by almost a factor of 5 and it is believed that the added complexity is well compensated by the performance increase.

To conclude, the thesis fulfilled its objective which was to show how understanding of the wireless channel can be used to significantly enhance performance of existing and future broader bandwidth UWB systems when justifiable modifications are made.

Again, some of these conclusions are transferable beyond UWB. IEEE802.11 systems have higher dynamic range. Hence they are not strongly influenced by the frequency selective fading as was shown in chapter 5. However, IEEE802.11ac foresees a modulation of 256-QAM. For such a high-order modulation scheme, the fading of individual subcarriers may well become important and the conclusions from this thesis can be applied. Also the 160 MHz bandwidth of the IEEE802.11ac systems may already be able to benefit from the properties of the low-complexity beam steering.

8.2 Future work

The conclusions of this thesis will be used in further work of the Communications Research Group and it is believed that it will also feed into research conducted elsewhere. The work in the Communications Research Group will mostly focus on further investigation of adaptive OFDM UWB systems. The system design will be further optimised based on further analysis of its performance. Adaptation of the scheme for various environments is envisioned. As shown in chapter 3 of this thesis, the frequency selectivity is more severe in confined environments. Therefore, the adaptive OFDM UWB system seems like the ideal candidate for confined environments such as cars, trains, planes, or inside computers (the Communications Research Group has been performing studies of the use of UWB as a cable replacement inside desktop computers and servers).

Furthermore, it is envisioned to proceed from simulations presented in this thesis to real implementations. The works on the implemenation have started and the first results are expected in the near future.

The properties of the beam-steering algorithm will also be further studied. In this thesis, it has been shown that for the bandwidths used in WiMedia systems, the algorithm smears out the frequency selectivity and outperforms the Maximum-Ratio-Combining. However, it remains to answer what is the minimum bandwidth required to benefit from this property for a low number of antenna elements. Also, the link to the 60 GHz beam-steering has been shown. It was shown that for a large number of antennas the performance is dominated by the main beam. Further research is planned to explore the transition in order to tell what is the minimum number of antennas so that the beam-steering can be feasible for OFDM systems with fixed subcarrier loading as well.

Apart from the investigations of adaptive OFDM for UWB systems, future work is also intended on further the analysis of UWB antennas and antenna arrays. This thesis has explored the pulse distortion by antennas as a function of bandwidth with the help of antenna impulse response in the time domain. However, the bandwidth limit for pulse distortion was found to be given mainly by the fact that the surface current distribution of an antenna is a function of frequency. Therefore the investigation of the relationship between antenna descriptors in frequency domain (such as antenna transfer function and antenna group delay), the distribution of the surface current and the distortion of transmitted pulses appears to be an interesting research avenue for the future.

For UWB antenna arrays, Eq. (2.20), which is repeated here for better readability, defines the directional properties of an arbitrary array processing an arbitrary bandpass signal:

$$\epsilon(\varphi_0,\varphi) = N + \frac{2\sum_{i=1}^{N-1}(N-i)\Re\left[R_{bb}\left(i\frac{d}{c}(\sin\varphi - \sin\varphi_0)\right)\right]\cos\left(2\pi f_c i\frac{d}{c}(\sin\varphi - \sin\varphi_0)\right)}{R_{bb}(0)} \quad (8.1)$$

As can be seen, these properties depend also on the value of $R_{bb}(\tau)$, the autocorrelation function of the envelope of the bandpass signal. As was discussed in chapter 2, as the bandwidth increases, the impact of this function increases. The transition was studied in chapter 2 in great detail. However, chapter 2 did not discuss the following idea. For a fixed bandwidth, the envelope of the bandpass signal could theoretically be changed so that $R_{bb}(\tau)$ changes the radiation properties in a selected direction, e.g. introducing an additional null in the radiation pattern. It is intended to study this property of the arrays in order to understand what is the limit on the bandwidth so that a required change in the pattern can be achieved. This could enable a reduction the multiuser interference by assigning different signal envelopes to different users in impulse radio localisation applications, e.g. [149].

APPENDIX A

Definition of Baseband Signal Waveforms

Multiple chapters in this thesis, in particular chapters 2 and 4, use bandpass signals $s(t)$ described as:

$$s(t) = b(t) \cdot \cos(2\pi f_c t) \tag{A.1}$$

where $b(t)$ is the baseband envelope signal, f_c is the centre frequency, and t is time.

Chapter 2 compares performance of antennas and antenna arrays for five different waveforms of pulses $b(t)$. These pulses are:

- Rectangular Pulse
- Gaussian Pulse
- Triangular Pulse
- Raised Cosine Pulse
- Double Exponential Pulse

The properties of these pulses are well known and their properties in time and frequency domain are described in the literature e.g. [34]-[37]. There is no novelty about these pulses, this thesis employed them as tools to evaluate various properties of UWB antennas and systems. However, since various authors often choose different parameters in the pulse description or different definitions of bandwidth, the pulses are introduced in this attachment for the sake of completeness and in order to avoid confusion. The framework for the pulse definition from [34] has been chosen. The bandwidth of the pulse has been defined as the -10 dB bandwidth of the bandpass signal $s(t)$.

A.1 Rectangular Pulse

The definition of the rectangular pulse $s_{rect}(bt) = \mathrm{rect}(bt)$ in the time domain is the following [34]:

$$\mathrm{rect}(bt) = \begin{cases} 1, & \text{if } |bt| < 0.5 \\ 0, & \text{else} \end{cases} \tag{A.2}$$

where t stands for time and b is a pulse length parameter associated with bandwidth.

The corresponding Fourier transform of this pulse is [34]:

$$S_{rect}\left(\frac{f}{|b|}\right) = \mathcal{F}\left\{s_{rect}(bt)\right\} = \frac{1}{|b|}\mathrm{sinc}\left(\frac{f}{b}\right) \tag{A.3}$$

where f stands for frequency, and $\mathrm{sinc}(x) = \frac{\sin(\pi x)}{\pi x}$.

The relationship between the -10 dB bandwidth B and the pulse length coefficient b is then given as:

$$b = \frac{B}{2 \cdot 0.7381} \tag{A.4}$$

The example rectangular pulse $\mathrm{rect}(t)$ and its corresponding Fourier transform are shown in Fig. A.1

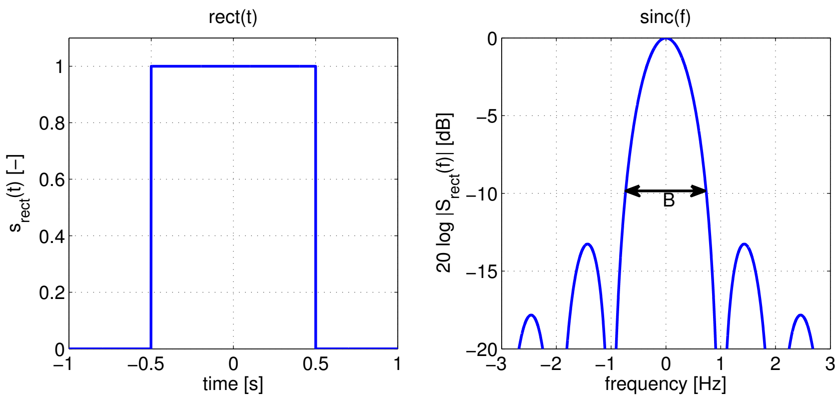

Figure A.1: The rectangular pulse and its Fourier transform

A.2 Gaussian Pulse

The definition of the Gaussian pulse $s_{Gauss}(\frac{t}{T_p})$ in the time domain is the following[34]:

$$s_{Gauss}\left(\frac{t}{T_p}\right) = e^{-\pi\left(\frac{t}{T_P}\right)^2} \tag{A.5}$$

where t stands for time, the time constant T_P defines the pulse length and is defined by bandwidth.

The corresponding Fourier transform of this pulse is [34]:

$$S_{Gauss}(T_p f) = \mathcal{F}\left\{s_{gauss}(t)\right\} = T_p \cdot e^{-\pi(T_P f)^2} \tag{A.6}$$

where f stands for frequency.

The relationship between the -10 dB bandwidth B and the time constant T_P is then given as:

$$T_P = \frac{2\sqrt{\ln(\sqrt{10})/\pi}}{B}. \tag{A.7}$$

The example Gaussian pulse $s_{Gauss}(t)$ and its corresponding Fourier transform are shown in Fig. A.2

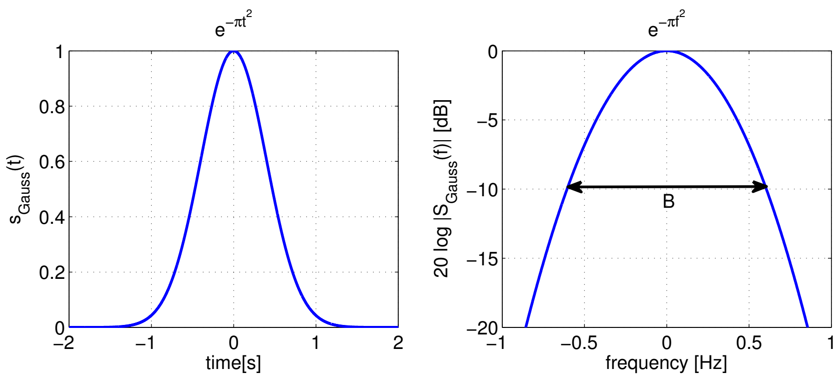

Figure A.2: The Gaussian pulse and its Fourier transform

A.3 Triangular Pulse

The definition of the triangular pulse $s_{tri}(bt) = \text{tri}(bt)$ in the time domain is the following [34]:

$$\text{tri}(bt) = |b|\text{rect}(bt) * \text{rect}(bt) = \begin{cases} 1 - |bt|, & \text{if } |bt| < 1 \\ 0, & \text{else} \end{cases} \tag{A.8}$$

where t stands for time, b is a pulse length parameter associated with bandwidth and $*$ represents convolution.

The corresponding Fourier transform of this pulse is [34]:

$$S_{tri}\left(\frac{f}{|b|}\right) = \mathcal{F}\left\{s_{tri}(bt)\right\} = \frac{1}{|b|}\text{sinc}^2\left(\frac{f}{b}\right) \tag{A.9}$$

where f stands for frequency, and $\text{sinc}(x) = \frac{\sin(\pi x)}{\pi x}$.

The relationship between the -10 dB bandwidth B and the pulse length coefficient b is then given as:

$$b = \frac{B}{2 \cdot 0.557} \tag{A.10}$$

The example triangular pulse $\text{tri}(t)$ and its corresponding Fourier transform are shown in Fig. A.3

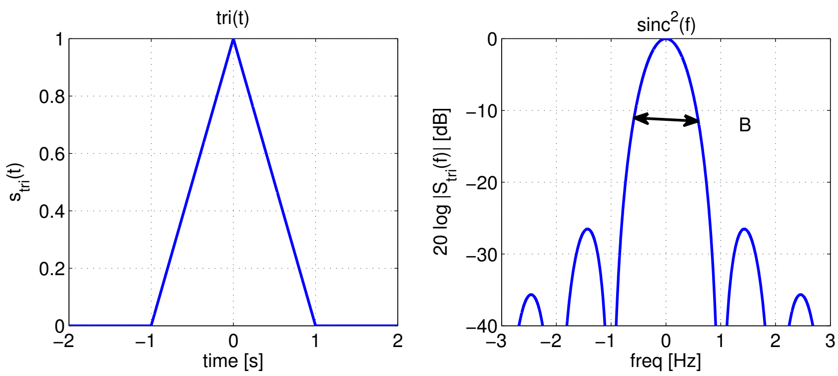

Figure A.3: The triangular pulse and its Fourier transform

A.4 Raised Cosine Pulse

The definition of the raised cosine pulse $s_{RC}(bt)$ in the time domain is the following [34]:

$$s_{RC}(bt) = \mathrm{rect}(bt) \cdot \cos(\pi bt) = \begin{cases} \cos(\pi bt), & \text{if } |bt| < 0.5 \\ 0, & \text{else} \end{cases} \tag{A.11}$$

where t stands for time, b is a pulse length parameter associated with bandwidth.

The corresponding Fourier transform of this pulse is [34]:

$$\begin{aligned} S_{RC}\left(\frac{f}{|b|}\right) = \mathcal{F}\left\{s_{RC}(t,b)\right\} = \frac{1}{|b|}\mathrm{sinc}\left(\frac{f}{b}\right) * 0.5\left[\delta\left(f - \frac{b}{2}\right) + \delta\left(f + \frac{b}{2}\right)\right] = \\ = \frac{1}{2|b|}\left[\mathrm{sinc}\left(\frac{f - \frac{b}{2}}{b}\right) + \mathrm{sinc}\left(\frac{f + \frac{b}{2}}{b}\right)\right] \end{aligned} \tag{A.12}$$

where f stands for frequency, $\mathrm{sinc}(x) = \frac{\sin(\pi x)}{\pi x}$, and $*$ represents convolution.

The relationship between the -10 dB bandwidth B and the pulse length coefficient b is then given as:

$$b = \frac{B}{2.04} \tag{A.13}$$

The example raised cosine pulse pulse $s_{RC}(t)$ and its corresponding Fourier transform are shown in Fig. A.4

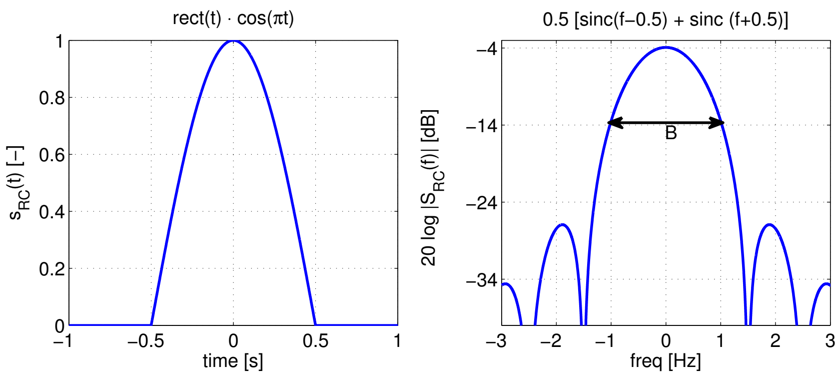

Figure A.4: The Raised Cosine pulse and its Fourier transform

A.5 Double Exponential Pulse

The definition of the double exponential pulse $s_{DE}(\frac{t}{T_p})$ in the time domain is the following [34]:

$$s_{DE}\left(\frac{t}{T_p}\right) = \frac{1}{2T_p} e^{-\frac{|t|}{T_P}} \tag{A.14}$$

where t stands for time, the time constant T_P defines the pulse length and is defined by bandwidth.

The corresponding Fourier transform of this pulse is [34]:

$$S_{Gauss}(T_p f) = \mathcal{F}\left\{ s_{DE}\left(\frac{t}{T_p}\right)\right\} = \frac{1}{1+(2\pi t f)^2} \tag{A.15}$$

where f stands for frequency.

The relationship between the -10 dB bandwidth B and the time constant T_P is then given as:

$$T_P = \frac{\sqrt{\sqrt{10}-1}}{\pi B} \tag{A.16}$$

The example double exponential pulse $s_{DE}(t)$ and its corresponding Fourier transform are shown in Fig. A.5

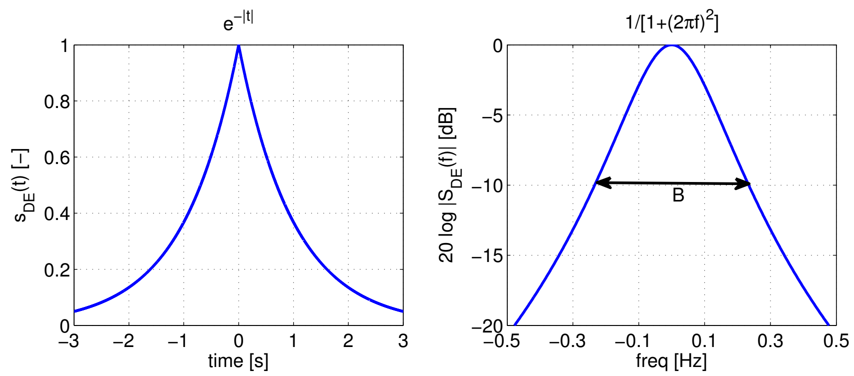

Figure A.5: The double exponential pulse and its Fourier transform

APPENDIX B

Extremely Wideband Channel Sounder

Experimental sounding of a wireless channel was an important part of this thesis. The measurements of the wireless channel presented in this thesis were conducted using state-of-the-art channel sounding equipment for frequencies of 3 - 20 GHz. The equipment that was designed and assembled as part of this thesis work is introduced here. Measurements over such wide frequency range are typically conducted with the use of VNA which performs measurement sequentially for single frequency steps from the band [135]. The VNA used for the work in this thesis was the HP8722ES covering the frequencies 50 MHz - 40 GHz [136].

The biggest challenge of wideband wireless channel measurement is the available dynamic range of the VNA especially for the high frequencies above 10 GHz. Not only does the path loss of free space propagation increase with the frequency but the system also manifests increasing losses in the cables that are part of the setup. In a coaxial cable, there are two types of losses, conductive losses and dielectric losses. The conductive losses are caused by the skin effect which reduces the effectively used cross-section of the conductor [150]. This results in the increase of the resistance of the cable. The associated losses are $\alpha_R \propto \sqrt{f}$ [150], where f stands for frequency. The dielectric losses appear because the dipole moments of polar molecules rotate to follow the changing electric field. This rotation is associated with losses. These losses are $\alpha_G \propto f$ [150]. To avoid these losses, our channel sounder employed a Radio-over-Fibre (RoF) link which provides a frequency flat response for all frequencies in its pass-band. This RoF can be used as stand-alone (used for measurements in office environment) or incorporated with a positioner (measurements in laboratory environment). The setup with the positioner table is introduced in Fig. B.1. The individual components introduced in Fig. B.1 are now introduced in more detail.

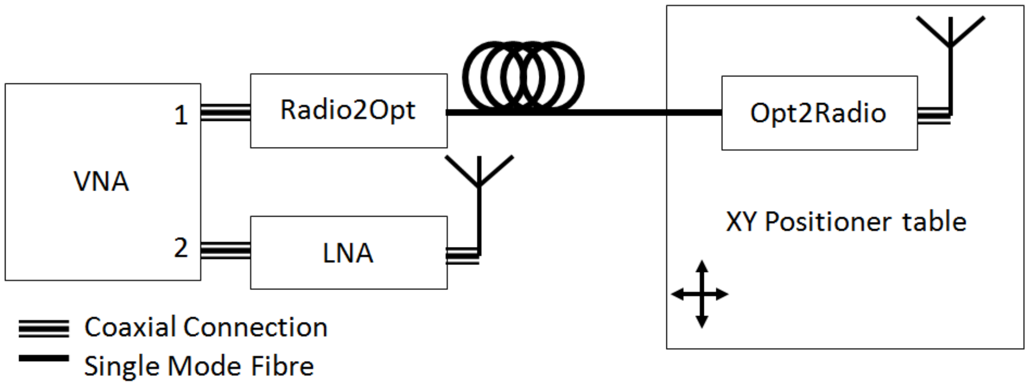

Figure B.1: Setup for channel measurement with positioner table

B.1 Radio-over-Fibre Link

As mentioned above, the RoF is a crucial component as it enables one to replace frequency selective coaxial cables with a system that provide a frequency flat response across the entire frequency band. For the sounder presented here we used a RoF link designed by a previous member of the Communication Research Group [83],[151]. As part of the work on this thesis, the link was analysed and its performance was improved by the means of pre-amplification. This description of the link as well as its performance will be presented here.

A generic RoF consists of three elements: a transmitter unit, optical fibre and a receiver unit. The transmitter turns an electrical signal into a modulated optical signal. The receiver is a photodetector that recovers the electrical signal from the modulated optical signal. Recent work confirms that the transmitter unit with laser and external modulator is a better option because of the superior gain and noise figure compared to links with directly modulated laser sources [152], [153]. According to [152], there are two main potential candidates for modulators in RoF links: Mach-Zehnder modulator, semiconductor Electro-Absorption Modulator (EAM). References [83],[151] selected EAM. For a low power laser source (optical power in magnitude of milliwatts), its performance is comparable to the performance of a Mach-Zehnder Modulator [153], [152]. The Mach-Zehnder Modulator performs better than the EAM for high power lasers (optical power in magnitude of watts) [152],[154]. However, such a laser could not be used due to health and safety considerations [83]. The RoF used in [83] is presented in Fig. B.2. The components used in the transmitter part of the link are Anritsu Bias Tee K250 [155], 1550 nm

Laser QPhotonics QDFBLD-1580-20 [156], CIP Photonics EAM 40G-SR-EAM-1550 [157], and Anritsu 28K50 50Ω termination. The optical fibre was a single mode optical fibre with length of 100 m. The receiver photo-detector was $\mu 2t$ Photonics XPDV2020 [158].

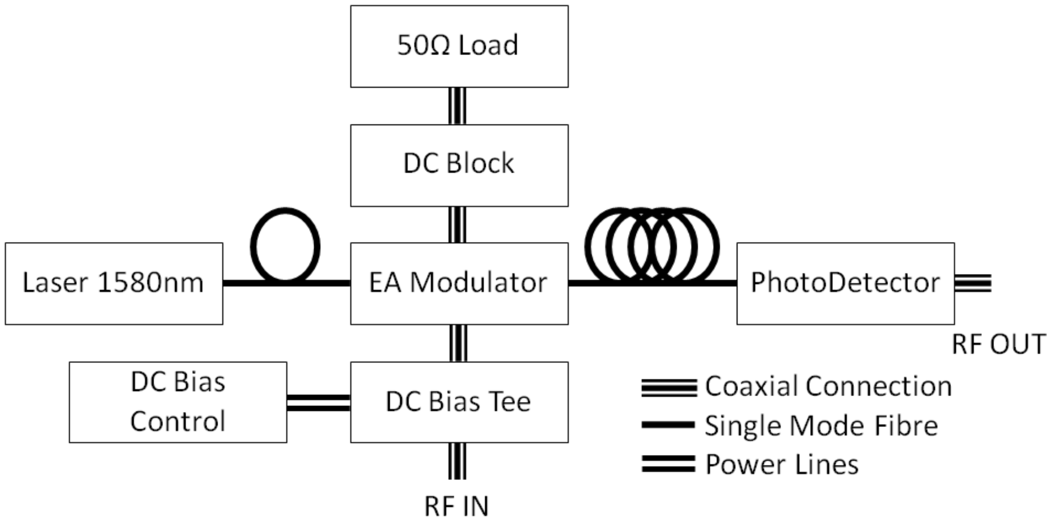

Figure B.2: Block diagram of the Radio-over-Fibre Link

Similarly to most electronic components for transmission, there are two main descriptors of RoF links: gain, and noise figure. For RoF links with EAM the gain g is given as [153]:

$$g = \left(\frac{P_I T_{fm} T_{mf} r_d \pi}{2V_{\pi e}}\right)^2 \cdot \left(\frac{1}{1 + \frac{P_I T_{fm} r_m \pi}{2V_{\pi e}}\left(R_M + \frac{R_L R_S}{R_L + R_S}\right)}\right)^2 \cdot R_D R_L \tag{B.1}$$

where P_I is the input optical power, T_{fm} is the transmission coefficient from fibre to modulator ('optical impedance matching'); T_{fm} is the transmission coefficient from modulator to fibre; r_m is the responsivity of the modulator; r_D is the responsivity of the photodetector; $V_{\pi e}$ is the effective on-off switch voltage for electro-optic transfer function versus the bias voltage at bias point; R_D is the load at the photodetector; R_L is the load at the modulator; R_S is the input impedance of the RF signal generator; R_M is the modulator resistance in series with the modulator junction. The load and input resistances are considered in order to include impedance matching in (B.1) [153].

Analysis of (B.1) reveals the reason why EAM are not suitable for high power optical sources. For low P_I, the second term can be neglected so the gain increases at the rate of 20dB per decade. However, as P_I increases the second term cannot be neglected and the system saturates

[153]. This behaviour was measured and is presented in Fig. B.3. Values of P_I were measured only to 20 mW because that is the maximum optical power provided by the employed laser QDFBLD-1580-20 from QPhotonics^{TM} [156].

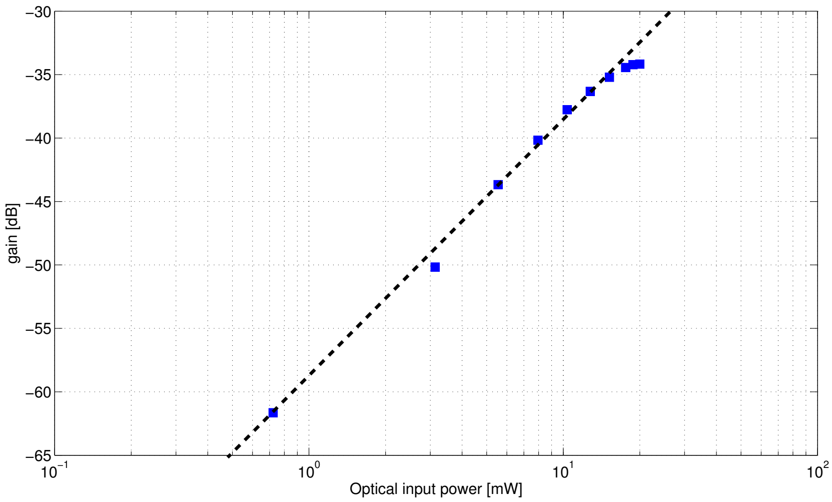

Figure B.3: Gain of RoF link from [83] as a function of input optical power. The dashed line represent the 20dB per decade increase. The gain was determined as a mean gain measured by VNA over the frequency span 4 - 15 GHz.

The second descriptor of the link's performance is its noise figure F_{ROF} given as [153]:

$$F_{ROF} = 1 + \frac{f_R}{g} + \frac{2eP_I T_{fm} T_{mf} t_B r_d R_D}{gkT_0} + \frac{eP_I T_{fm} T_{mf}(1-t_B) r_m R_S \left[1 + \frac{R_M(R_L+R_S)}{R_L R_S}\right]^2}{2kT_0} \tag{B.2}$$

where f_R represent the noise figure of the receiver; e is elementary charge; k is the Boltzmann's constant; T_0 is operating temperature; t_B is the bias point of the EAM; the remaining variables have been explained under (B.1).

As can be seen in (B.2) the noise figure is inversely proportional to the gain of the link. This is an issue because for a low gain of - 35 dB as presented above, the noise figure can yield very large values. In fact a measurement of the noise figure using a Hewlett Packard noise figure meter Hewlett-Packard 8970B shows that the noise figure of the link increases with frequency from approx 36 dB for 2 GHz to 44 dB for 9 GHz. However, it must be noted that for a coaxial cable with similar attenuation, the noise figure would yield a similar value.

Both the attenuation and the noise figure are not good results in terms of use in extremely wideband measurements. Therefore, the link from [83],[151] has been improved by pre-amplification with a broadband Centellax^{TM} amplifier UA0L30VM that covers the band from 100 kHz to 30 GHz providing gain in excess of 30 dB with mean noise figure of 5.5 dB [128]. Pre-amplification has been chosen as it can reduce the link's overall noise figure F_{tot} according to the Friis formula [150]:

$$F_{tot} = F_{amp} + \frac{F_{ROF}}{g_{amp} - 1} \tag{B.3}$$

where g_{amp} is the amplifier's gain and F_{amp} its noise figure.

As can be observed from (B.3) the impact of the link's noise figure is reduced by the amplifier's gain (i.e. by factor 1000). This is presented in Figs. B.4 and B.5 which present the performance of the link with and without pre-amplification. A significant improvement in both gain and noise figure can be observed. The resulting link provides a gain of approximately -2 dB over the frequency range of the measurement (3 - 20 GHz) and with it's noise figure of 9 dB it seems like a good candidate for extremely wideband channel sounding outperforming even the best coaxial cables.

With regards to the performance of the pre-amplifier the maximum input power of the link needs to be limited so that the EAM is not overloaded. To evaluate this, the 1 dB compression point for the link was determined. At 1 dB compression the EAM is not yet overloaded but the input power should not unnecessarily exceed this limit. For measurement with a vector network analyser, the higher harmonics caused by the non-linear distortion do not represent a significant issue because they are filtered by the VNA's receiver. However, they cannot be present in situations when the link would be used as a part of a communication system. The measured 1 dB compression point is presented in Fig. B.6. As can be observed, if the EIRP spectral density limits of -41.3 dBm/MHz are not exceeded, the signal power remains well below the 1 dB compression point of the link, even for the case of pre-amplification by 30 dB.

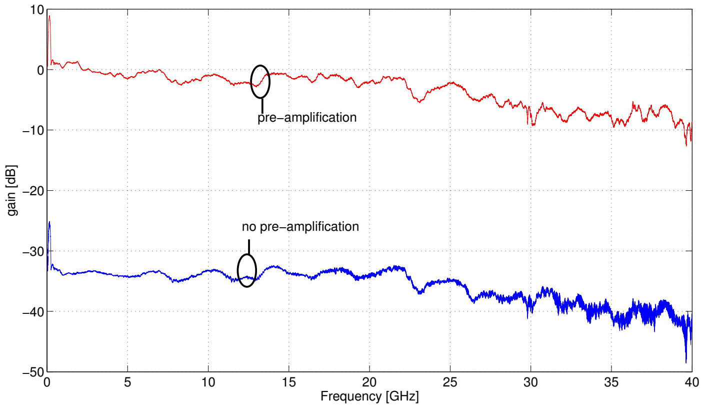

Figure B.4: Gain of the experimental RoF link with and without pre-amplification

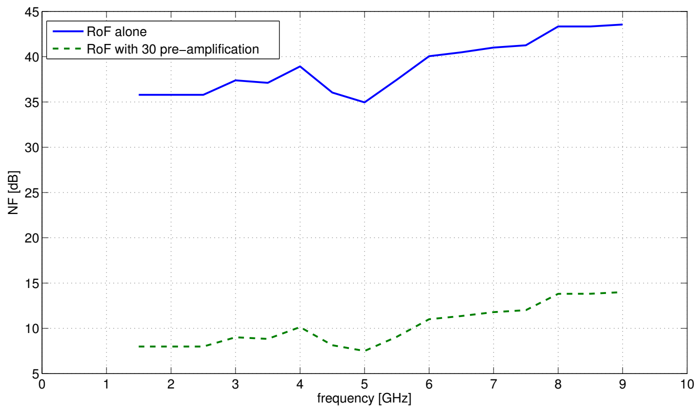

Figure B.5: Gain of the experimental RoF link with and without pre-amplification. The noise figure is measured only in the interval 2 - 9 GHz due to the frequency span of available noise figure meter Hewlett-Packard 8970B and available mixers.

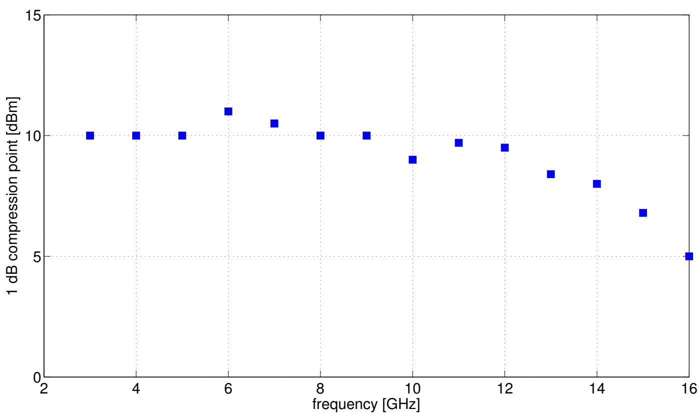

Figure B.6: 1 dB compression point of the RoF link (without the pre-amplifier)

B.2 Positioner Table

The positioner table represents an essential part of the apparatus for sounding of a wireless channel. It allows one to automatically alter the position of the antenna. The results can be used e.g. to study frequency selective fading, to synthesise virtual antenna arrays. The table used in this thesis allows a movement of the antenna in a square 1×1 m. The position of the platform, to which the antennas can be fastened, is set by three stepping motors (Parker Series 850). Two motors for the x-axis and one motor for the y-axis. The minimum step of the motor is 1.2 mm. This provides sufficient resolution for most wireless channel measurement experiments including high resolution radio imaging. The table with attached RoF link is presented in Fig. B.7.

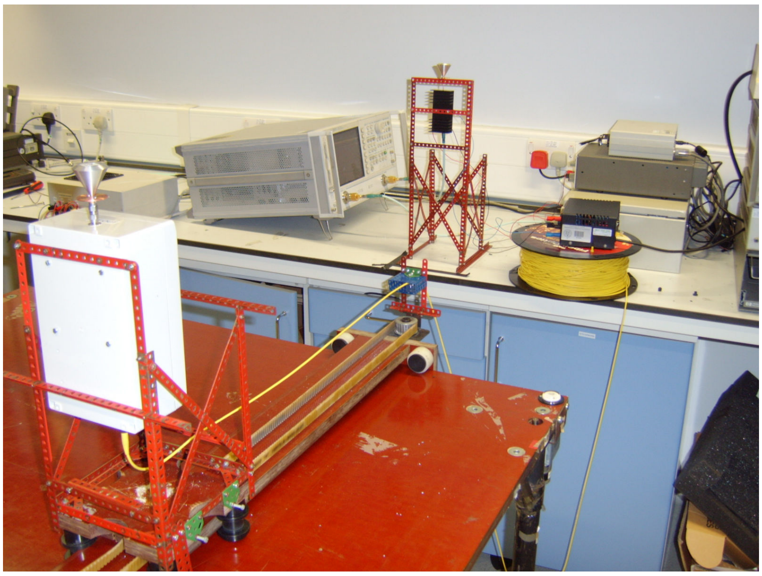

Figure B.7: Photo of the experimental apparatus from $B.1$ - positioner table, RoF link and VNA

Each of the stepping motors is controlled by a Parker VIX500M Drive Controller which are connected in a Daisy Control chain. The first drive controller is connected to a computer's serial port. The commands can be sent via a serial port e.g. from LabVIEW^{TM} environment. For most measurements according to Fig. B.1 the control computer is also connected to the vector network analyser via a GPIB bus. This limits the range of the measurements because there is a maximum acceptable length of GPIB cable (typical requirement of average 2 m between devices) and serial cable (typically 15 meters).

Such a length was acceptable for measurements presented in this thesis but they might represent a limitation in some special long range measurements. Since the RoF link easily allows separation of up to hundreds of metres, the table has been equipped with an alternative Bluetooth RS232 Adapter from LM Technologies^{TM} which offers significantly more range than a serial cable.

B.3 Antennas

For the channel sounding, two types of antennas were used. Most measurements were conducted with discone antennas but some were conducted with commercial In4Tel$^{\mathrm{TM}}$ antennas that were provided with the Wisair$^{\mathrm{TM}}$ UWB development kit which is described in Appendix D.

B.3.1 Discone antennas

The discone antennas were designed and manufactured as part of the research project. They were designed to operate with lower cut off frequency of approximately 2.4 GHz. The antenna dimensions and the reflection coefficient of the two antennas used for channel sounding is presented in Fig. B.8. The ripples in the s_{11} for frequencies above 4 GHz are believed to be caused by the fact that the SMA connector represents a short piece of transmission line (about 1 cm) that neither matches perfectly to the impedance of the VNA nor to the antenna. Therefore, some standing waves can occur. Despite this, it is apparent that the antennas are well matched for the entire bandwidth of interest 3 - 20 GHz.

As mentioned in chapter 2, the reflection coefficient is an important measure but it is not the only one. The antenna's radiation is another important aspect and it is shown in Fig. B.9. Fig. B.9 shows the gain of the antenna simulated by the CST Microstripes$^{\mathrm{TM}}$ full-wave simulation package. It is presented in this form because it provides better insight into the radiation properties than E-Plane and H-Plane cuts. It is noted that the good agreements between the measured antenna impulse responses and their simulated counterparts as presented in chapter 3.2 support the assumption that the quality of the simulations is satisfactory and the plots of the radiation patterns are reliable. Furthermore, an E-Plane measurement of the antenna was performed and compared with the E-Plane simulation and good agreement could be confirmed.

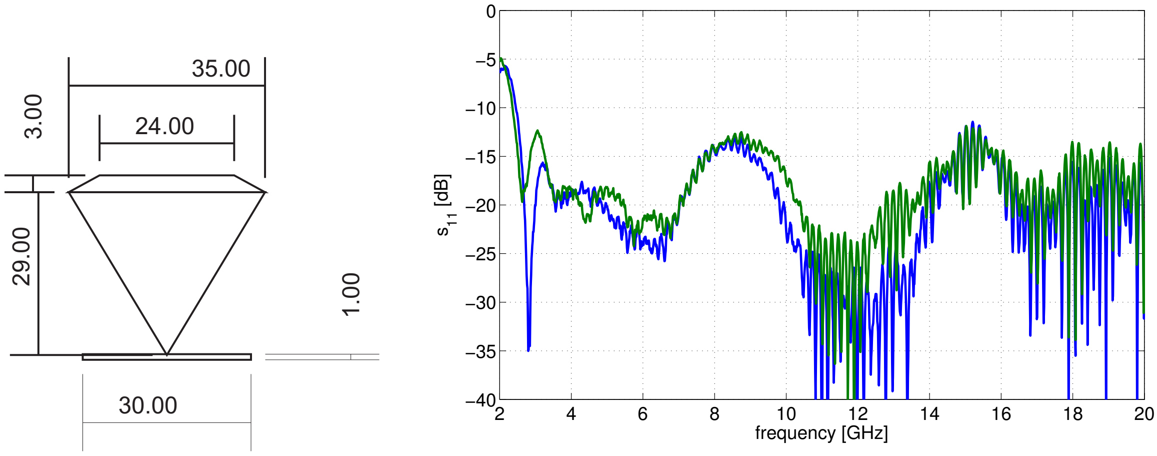

Figure B.8: Dimensions of the discone antennas (in mm) and the s_{11} of the two discone antennas used for channel sounding

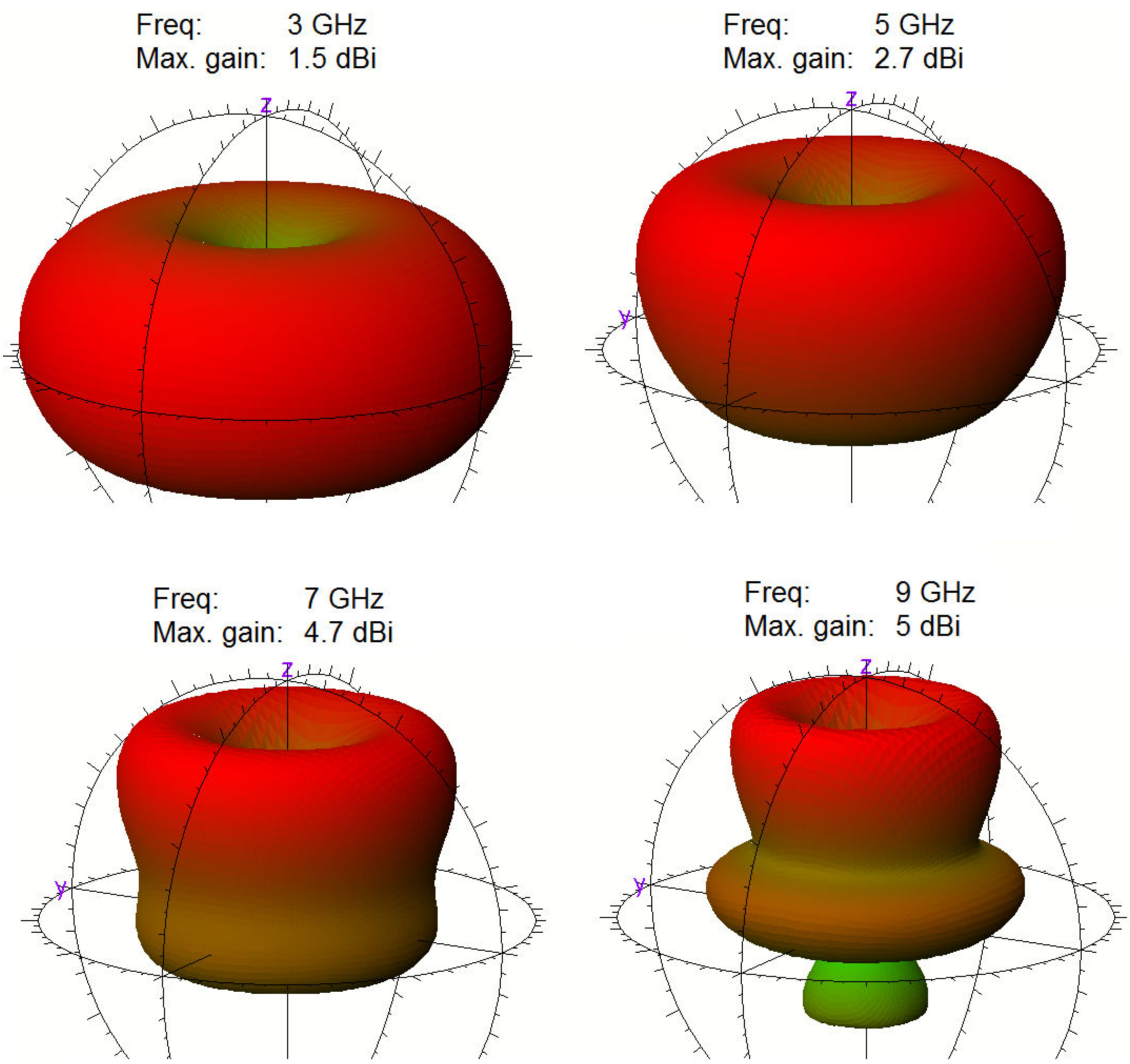

Figure B.9: Simulated gain of the discone antenna for some example frequencies.

B.3.2 In4Tel Antennas

The In4Tel antenna was delivered with the Wisair DV9110 UWB development kit for testing of the WiMedia standard. The antenna is an array of two dipole antennas and should cover the WiMedia Band Group ♯1 3.168 - 4.752 GHz [13] (see chapter 5 for details). Unfortunately, it was neither possible to obtain a full description of the Int4Tel antennas from the manufacturer, nor was it possible to fully explore the geometry structure as it was hidden under a layer of colour. However, it was possible to measure the antenna parameters. The reflection coefficient of the antennas is presented in Fig. B.10. It can be observed that the required WiMedia is covered with $s_{11} < -5$dB. This shows that the antenna can operate in the required band but it also suggests that the matching of the antenna has potential for improvement as the s_{11} effectively means that at 3.29 GHz about 25% of the energy from the transmitter gets reflected and is not radiated.

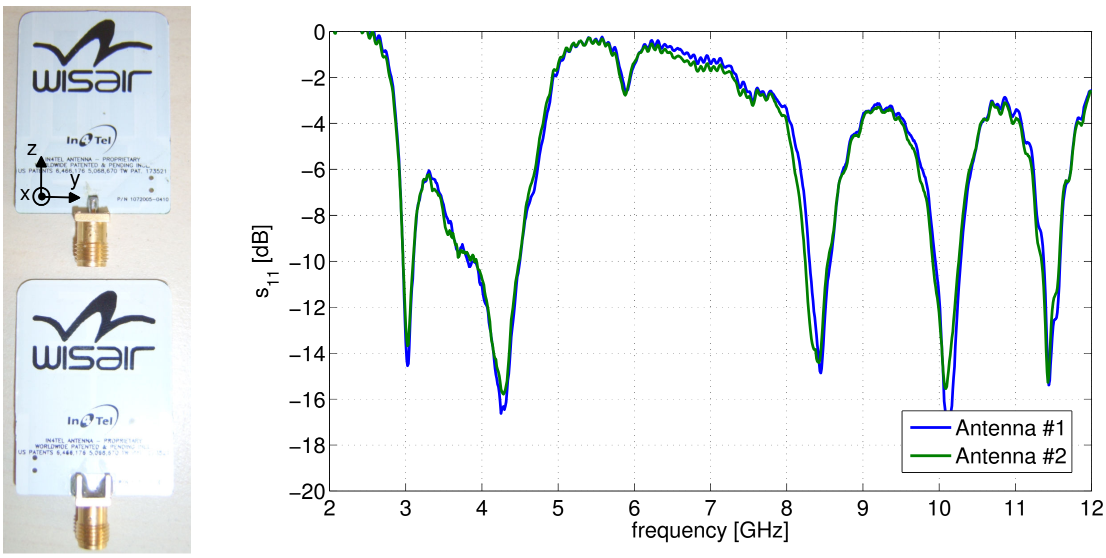

Figure B.10: The photo of the In4Tel antenna (front view and back view) with definition of coordinates and the measured s_{11} of the two In4Tel antennas used for some channel sounding experiments and with the UWB development kit

The directivity of the antenna in the E-Plane and H-Plane was measured and it is presented in Fig. B.11. The maximum gain of the antenna is reported by the manufacturer to be 3 dBi and was confirmed by measurement. The measurements are presented for the frequency of 3.75 GHz (centre of the antenna's pass-band) but measurements at other frequencies did not manifest much change. The antenna radiation pattern in the H-Plane does not manifest axis symmetry along the x- and y-axis. The same is valid for the E-plane where there is no symmetry along the xy-plane. This is not due to the misalignment of the measurement (the measurement was carefully repeated to exclude this error) but rather due to the fact that the antenna itself does not appear to have any symmetry plane.

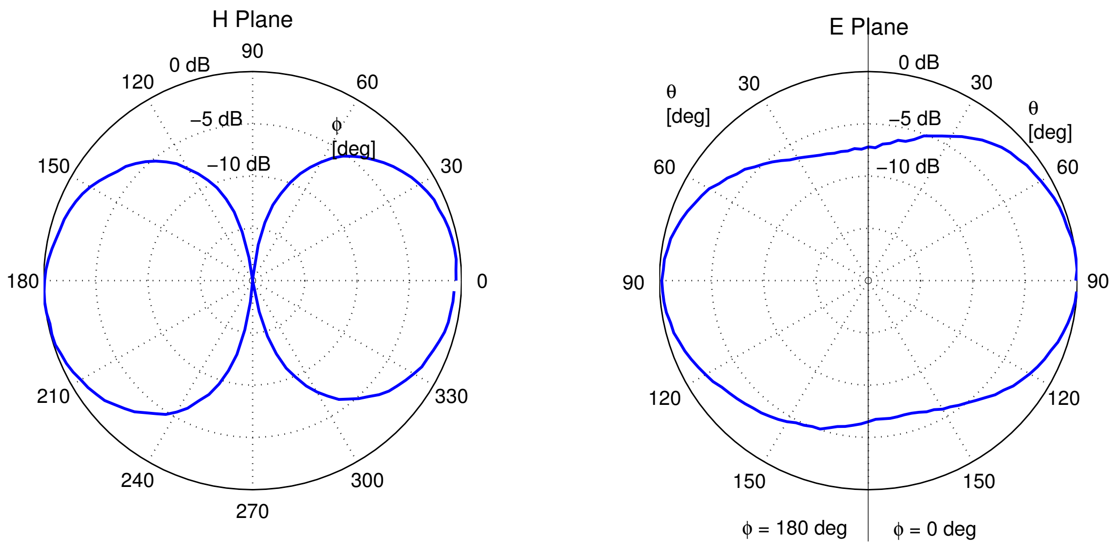

Figure B.11: The directivity of the In4Tel antennas used for some channel sounding experiments measured at 3.75 GHz. The coordinates are the same as defined in Fig. B.10

APPENDIX C

Laboratory for Channel Sounding

This appendix introduces the laboratory environment in which the measurements of 9,600 wideband wireless channels was performed. The laboratory is depicted in Fig. C.1. The room is located in a basement laboratory, the walls are from reinforced concrete. Fig. C.1 defines the position of the positioner table and also all six measurement sets. The LOS for each measurement set is presented by a line with its specific colour. Each line begins in a left bottom corner of a box which represents the measurement grid 40×40 points in which the position of the transmitter was varied. The other end of the line represents the position of the receiver.

The measurements were performed over the bandwidth 3-20 GHz with a frequency step of 0.5 MHz. As a result, a measurement at a single position lasted approximately 2.5 minutes. Therefore, it was necessary to ensure that the channel does not change during the measurements. Hence, the laboratory was closed and unattended by anyone during the measurements which lasted about 3 days. There also were no fans or other moving objects in the laboratory therefore, the impact of Doppler shift of some multipath components could be neglected.

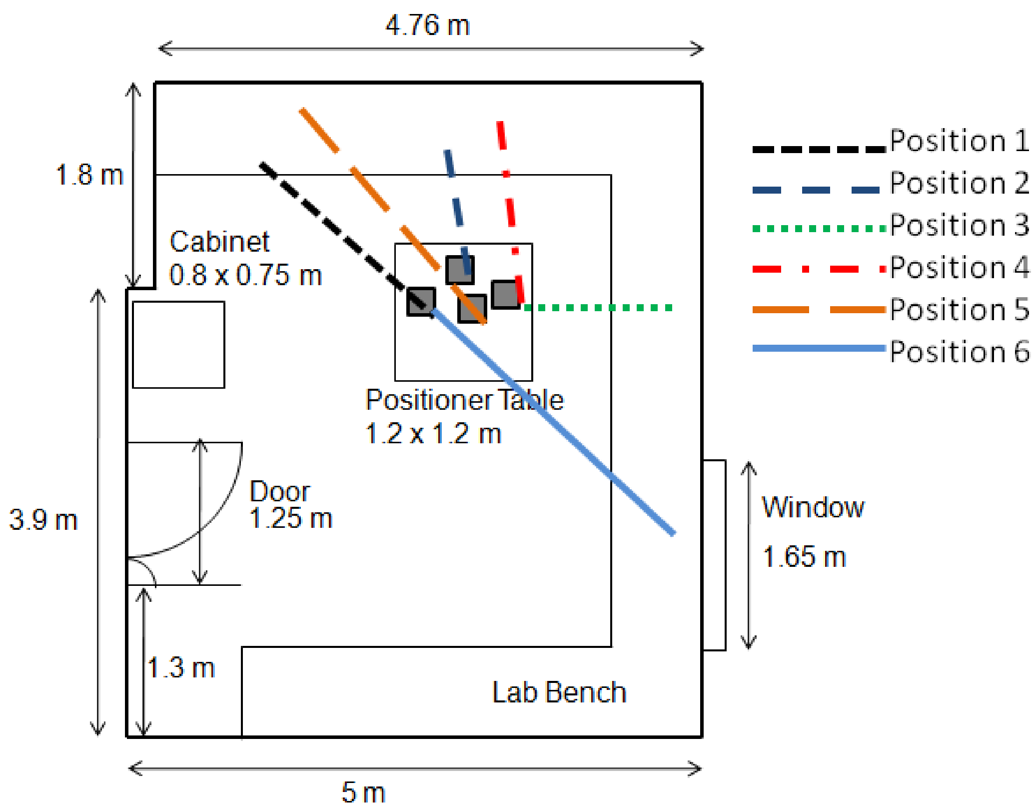

Figure C.1: Plan of the laboratory used for the measurement of the wireless channel. The positions for each measurement sets are defined by lines representing the direct multipath between the receiver and the first position of the transmitter in the corner of a 40×40 grid. These grids are depicted by grey squares.

APPENDIX D

UWB Development Kit - Wisair DV9110

As part of the thesis a performance evaluation of a commercial WiMedia system was performed. The system employed was the Wisair^{TM} DV9100M development kit. The kit is depicted in Fig. D.1. It consists of three basic components, the In4Tel antennas, introduced already in Appendix B.3.2, the actual development kit Wisair^{TM} DV9100M [159], and the controlling FPGA board developed by HW Communications Ltd. [160]. Here, the properties of the kit and the development board are briefly introduced.

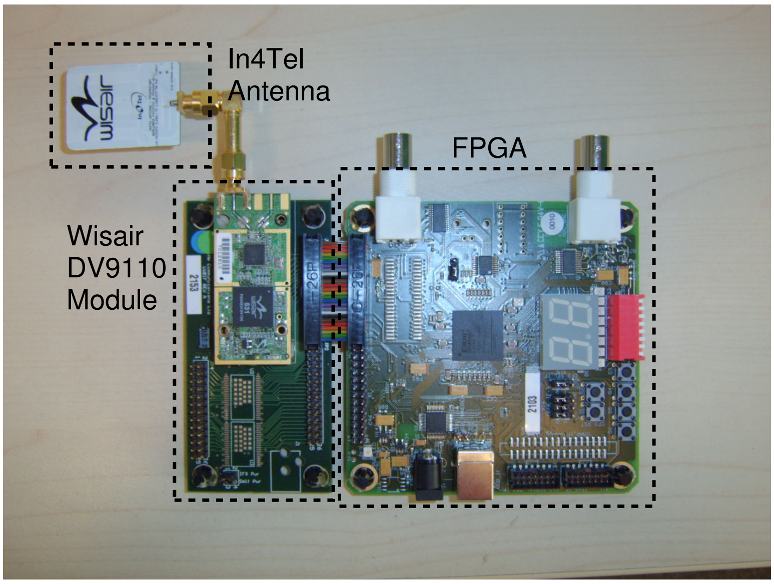

Figure D.1: The development kit, the three basic components are marked by dashed rectangles.

Wisair^{TM} DV9100M is a development module for data transmission using the WiMedia standard. The kit can operate as a transmitter, receiver, or a transceiver. It does not cover all the 14 bands as defined by the WiMedia standard [13], in fact it only covers the three lowest bands falling into band group ♯1 covering the frequency band 3.168 - 4.752 GHz [13].

The kit enables the choice of all eight WiMedia datarates from 53.3 - 480 Mbps [159]. Frequency hopping is over the individual bands is included but it is possible to alter it and use non-standard hopping schemes [159]. Finally, the kit is equipped with an attenuator that enables one control the output power by up to 20 dB with 1 dB steps [159].

The **HW Communications UWB-IF FPGA Board** developed by HW Communications Ltd. can be used to control the development kit. The board has two basic tasks [160]:

- Setting up the Development Kit
- Performance Evaluation

The FPGA board can be connected to a computer via USB cable and the control software enables setting all allowed options of the Wisair^{TM} DV9100M development board [159]. Once the setup is complete, the computer can be disconnected and the board operates as a mobile unit (provided available power supply).

In terms of performance evaluation, the FPGA board is equipped with a generator of pseudo-random bit packets. These are transmitted via the wireless link and since the receiver board knows the packet generator, it can be used to evaluate the real transmission data-rate and the PER. Because of the limited processing power of the FPGA, it does not allow data-rates over 220 Mbps. The real data-rate through the wireless channel can be up to 480 Mbps but the FPGA can only generate/process lower data-rate [160]. Thus, the UWB kit does not run at full duty-cycle but it can still be used to empirically evaluate performance of the WiMedia systems. Unfortunately, the access to the BER is not possible [159],[160]. Regardless, the PER is deemed as a sufficient performance measure for the sake of this thesis where the kit was used mainly to demonstrate the practical range of a WiMedia UWB system.

LIST OF FIGURES

LIST OF TABLES

BIBLIOGRAPHY

[1] C. Susskind, “Heinrich Hertz: a short life,” *Microwave Theory and Techniques, IEEE Transactions on*, vol. 36, no. 5, pp. 802 –805, May 1988.

[2] G. Falciasecca and B. Valotti, “Guglielmo Marconi: The pioneer of wireless communications,” in *Microwave Conference, 2009. EuMC 2009. European*, Oct 2009, pp. 544–546.

[3] E. Herron, *Miracle of the air waves: a history of radio.* Messner, 1969.

[4] A. Goldsmith, S. Jafar, I. Maric, and S. Srinivasa, “Breaking Spectrum Gridlock With Cognitive Radios: An Information Theoretic Perspective,” *Proceedings of the IEEE*, vol. 97, no. 5, pp. 894 –914, May 2009.

[5] D. Cabric, S. M. Mishra, D. Willkomm, R. Brodersen, and A. Wolisz, “A Cognitive radio approach for usage of virtual unlicensed spectrum, Dresden, Germany,” in *14th IST Mobile Wireless Communications Summit*, 2005, pp. 331 –334.

[6] S. Roy, J. R. Foerster, V. S. Somayazulu, and D. G. Leeper, “Ultrawideband radio design: the promise of high-speed, short-range wireless connectivity,” *Proceedings of the IEEE*, vol. 92, no. 2, pp. 295–311, 2004.

[7] L. Fullerton, “UWB waveforms and coding for communications and radar,” in *Telesystems Conference, 1991. Proceedings. Vol.1., NTC ’91., National*, mar 1991, pp. 139 –141.

[8] B. Allen, M. Dohler, E. Okon, W. Malik, A. Brown, and D. Edwards, *Ultra Wideband Antennas and Propagation for Communications, Radar and Imaging.* John Wiley & Sons, 2006.

[9] M. Win and R. Scholtz, “Impulse radio: how it works,” *Communications Letters, IEEE*, vol. 2, no. 2, pp. 36–38, Feb 1998.

[10] ECC, “Decision to make the Wireless Telegraphy (Ultra-Wideband Equipmemt) (Exemption) Regulations 2009,” ECC, Tech. Rep., 2009.

[11] F. Berens, “The European flexible DAA approach towards an open UWB regulation,” in *Ultra-Wideband, 2008. ICUWB 2008. IEEE International Conference on*, vol. 3, sept. 2008, pp. 71 –75.

[12] U. FCC, “Ruling Part 15,” US FCC, Tech. Rep., Feb. 2002.

[13] G. Heidari, *WiMedia UWB - technology choice for wireless USB and Bluetooth.* John Wiley & Sons, 2008.

[14] M. W. Paper, “Ultrawideband: High-speed, short-range technology with far-reaching effects,” Multiband OFDM Alliance, Tech. Rep., September 2004.

[15] M. Halper, “Future Focus,” *Time*, Dec. 6 2004.

[16] G. Fleishman, “UWB group shutters, sends tech to Bluetooth, USB groups,,” *Ars Technica*, Mar. 2009.

[17] R. Merrit, “UWB start-up Radiospire shuts down,” *EE Times*, April 2009.

[18] J. Laskar, S. Pinel, D. Dawn, S. Sarkar, P. Sen, B. Perunama, D. Yeh, and F. Barale, “60 GHz entertainment connectivity solution,” in *Ultra-Wideband, 2009. ICUWB 2009. IEEE International Conference on*, sept. 2009, pp. 17 –21.

[19] D. O’Brien, L. Zeng, H. Le-Minh, G. Faulkner, J. Walewski, and S. Randel, “Visible light communications: Challenges and possibilities,” in *Personal, Indoor and Mobile Radio Communications, 2008. PIMRC 2008. IEEE 19th International Symposium on*, sept. 2008, pp. 1 –5.

[20] F. Mlinarski, “Wireless HD video: Raising the UWB throughput bar (again),” *EE Times*, Feb. 2008.

[21] A. F. M. et.al., "IEEE 802.15.4a channel model - final report," IEEE, Tech. Rep., 2004.

[22] T. Kaiser, F. Zheng, and E. Dimitrov, "An Overview of Ultra-Wide-Band Systems With MIMO," *Proceedings of the IEEE*, vol. 97, no. 2, pp. 285 –312, Feb. 2009.

[23] C. Balanis, *Antenna Theory: Analysis and Design*, 3rd ed. Wiley-Blackwell, May 2005.

[24] R. DuHamel and D. Isbell, "Broadband logarithmically periodic antenna structures," pp. 119–128, 1957.

[25] R. DuHamel and F. Ore, "Logarithmically periodic antenna designs," pp. 139–151, 1958.

[26] C.-C. Chen, *Antenna Engineering Handbook*, 4th ed. McGraw Hill, 2007, ch. Ultrawide Bandwidth Antenna Design, pp. 19–1 – 19–20.

[27] D. Lamensdorf and L. Susman, "Baseband-pulse-antenna techniques," *Antennas and Propagation Magazine, IEEE*, vol. 36, no. 1, pp. 20–30, Feb 1994.

[28] J. McLean, H. Foltz, and R. Sutton, "Pattern descriptors for UWB antennas," *Antennas and Propagation, IEEE Transactions on*, vol. 53, no. 1, pp. 553–559, Jan. 2005.

[29] D. Lamensdorf and L. Susman, "Picosecond Pulse Antenna Techniques," RADC, Tech. Rep., May 1971.

[30] ——, "An analysis of some directive antennas using time domain measurements," in *Antennas and Propagation Society International Symposium, 1971*, vol. 9, Sep 1971, pp. 307–310.

[31] A. Shlivinski, E. Heyman, and R. Kastner, "Antenna characterization in the time domain," *Antennas and Propagation, IEEE Transactions on*, vol. 45; 45, no. 7, pp. 1140–1149, 1997.

[32] J. Liang, C. Chiau, X. Chen, and C. Parini, "Study of a printed circular disc monopole antenna for UWB systems," *Antennas and Propagation, IEEE Transactions on*, vol. 53, no. 11, pp. 3500–3504, Nov. 2005.

[33] N. Behdad and K. Sarabandi, "A compact antenna for ultrawide-band applications," *Antennas and Propagation, IEEE Transactions on*, vol. 53; 53, no. 7, pp. 2185–2192, 2005.

[34] J.-R. Ohm and L. H.-D., *Signalubertragung: Grundlagen der digitalen und analogen Nachrichtenubertragung*, 10th ed. Springer, 2006.

[35] R. Bracewell, *The Fourier-Transform and Its Applications*. McGraw-Hill, 1986.

[36] F. Coulon de, *Signal Theory and Processing*. Artech House, 1986.

[37] M.-G. Di Benedetto, K. T., M. A.F., O. I, C. Politano, and D. Porcino, *UWB Communication Systems: A Comprehensice Overview*. EURASIP, 2006.

[38] H. Schantz, "Planar elliptical element ultra-wideband dipole antennas," in *Antennas and Propagation Society International Symposium, 2002. IEEE*, vol. 3, 2002, pp. 44–46.

[39] H. Schantz and L. Fullerton, "The diamond dipole: a gaussian impulse antenna," in *Antennas and Propagation Society International Symposium, 2001. IEEE*, vol. 4, 2001, pp. 100–103 vol.4.

[40] J. Bourqui and E. Fear, "Shielded UWB Sensor for Biomedical Applications," in *IEEE International Symposium on Antennas and Progagation and USNC/URSI National Radio Science Meeting, APS-URSI 2012*, Chicago, July 2012, pp. 1–2.

[41] K. Vaddagiri, S. Monni, and A. Netp, "A Leaky Wave Antenna for Radar Medical Imaging," in *IEEE International Symposium on Antennas and Progagation and USNC/URSI National Radio Science Meeting, APS-URSI 2012*, Chicago, July 2012, pp. 1–2.

[42] R. Kazemi and K. Toosi, "An Eight-Element Dielectric Rod Antenna Array Integrated to a Substrate Integrated Waveguide Feed for Wideband Applications," in *IEEE International Symposium on Antennas and Progagation and USNC/URSI National Radio Science Meeting, APS-URSI 2012*, Chicago, July 2012, pp. 1–2.

[43] G. Southworth, "Certain Factors Affecting the Gain of Directive Antennas," *Proceedings*

of the Institute of Radio Engineers, vol. 18, no. 9, pp. 1502 – 1536, Sept. 1930.

[44] R. M. Wilmotte and J. McPetrie, “A Theoretical investigation of the phase relations in beam systems,” *Wireless Section, Institution of Electrical Engineers - Proceedings of the*, vol. 3, no. 9, pp. 182 –187, September 1928.

[45] J. Schelleng, “Some Problems in Short-Wave Telephone Transmission,” *Proceedings of the Institute of Radio Engineers*, vol. 18, no. 6, pp. 912a – 938, June 1930.

[46] J. L. Volakis, *Antenna Engineering Handbook*, 4th ed. McGraw Hill, 2007.

[47] M. Jensen and J. Wallace, “A review of antennas and propagation for MIMO wireless communications,” *Antennas and Propagation, IEEE Transactions on*, vol. 52, no. 11, pp. 2810 – 2824, Nov. 2004.

[48] C. Chen and M. Jensen, “Secret Key Establishment Using Temporally and Spatially Correlated Wireless Channel Coefficients,” *Mobile Computing, IEEE Transactions on*, vol. 10, no. 2, pp. 205 –215, Feb. 2011.

[49] S. Ries and T. Kaiser, “Ultra wideband impulse beamforming: It is a different world,” *Signal Processing*, vol. 86, no. 9, pp. 2198 –2207, Feb. 2006.

[50] M. Hussain and A. Al-Zayed, “Aperture-Sparsity Analysis of Ultrawideband Two-Dimensional Focused Array,” *Antennas and Propagation, IEEE Transactions on*, vol. 56, no. 7, pp. 1908 –1918, July 2008.

[51] A. Shlivinski, “Kinematic properties of short-pulsed sparse transmitting arrays,” *Progress in Electromagnetic Research*, vol. 115, pp. 11 –33, 2011.

[52] V. Sipal, B. Allen, and D. Edwards, “Bandwidth Requirement for Suppression of Grating Lobes in Ultrawideband Antenna Arrays,” in *International Conference on UWB (ICUWB), 2012*, Sep. 2012, pp. 1–5.

[53] A. F. Molisch, “Ultrawideband propagation channels-theory, measurement, and modeling,” *Vehicular Technology, IEEE Transactions on*, vol. 54; 54, no. 5, pp. 1528–1545, 2005.

[54] A. F. Molisch, K. Balakrishnan, D. Cassioli, C.-C. Chong, S. Emami, A. Fort, J. Karedal, J. Kunisch, H. Schantz, and K. Siwiak, “A comprehensive model for ultrawideband propagation channels,” p. 3653, 2005.

[55] A. Durantini, W. Ciccognani, and D. Cassioli, “UWB propagation measurements by PN-sequence channel sounding,” pp. 3414–3418 Vol.6, 2004.

[56] B. M. Donlan, S. Venkatesh, V. Bharadwaj, R. M. Buehrer, and J.-A. Tsai, “The ultra-wideband indoor channel,” pp. 208–212 Vol.1, 2004.

[57] S. S. Ghassemzadeh, R. Jana, C. W. Rice, W. Turin, and V. Tarokh, “Measurement and modeling of an ultra-wide bandwidth indoor channel,” *Communications, IEEE Transactions on*, vol. 52; 52, no. 10, pp. 1786–1796, 2004.

[58] ——, “A statistical path loss model for in-home UWB channels,” pp. 59–64, 2002.

[59] S. S. Ghassemzadeh and V. Tarokh, “UWB path loss characterization in residential environments,” pp. 501–504, 2003.

[60] D. R. McKinstry and R. M. Buehrer, “UWB small scale channel modeling and system performance,” vol. 58. Affiliation: Mobile/Portable Radio Res. Group, Virginia Tech, Blacksburg, VA, United States, 2003, pp. 6–10.

[61] R. C. Qiu and I.-T. Lu, “Wideband wireless multipath channel modeling with path frequency dependence,” pp. 277–281 vol.1, 1996.

[62] A. Saleh and R. Valenzuela, “A Statistical Model for Indoor Multipath Propagation,” *Selected Areas in Communications, IEEE Journal on*, vol. 5; 5, no. 2, pp. 128–137, 1987.

[63] V. Sipal, B. Allen, and D. Edwards, “Analysis and mitigation of antenna effects on wideband wireless channel,” *Electronics Letters*, vol. 46, no. 16, pp. 1159 –1160, 5 2010.

[64] ——, “Effects of antenna impulse response on wideband wireless channel,” in *Antennas*

and Propagation Conference (LAPC), 2010 Loughborough, Nov. 2010, pp. 129 –132.

[65] R. Scholtz, "Multiple access with time-hopping impulse modulation," in *Military Communications Conference, 1993. MILCOM '93. Conference record. 'Communications on the Move'., IEEE*, vol. 2, Oct 1993, pp. 447–450 vol.2.

[66] V. Sipal, B. Allen, and D. Edwards, "Modelling Of Antenna Pattern Descriptors for Antenna Performance Evaluation," in *International Conference on Modelling and Simulation, 2010. MS 10 Prague*, June 2010.

[67] D. Shutin, "Clustering wireless channel impulse responses in angular-delay domain," in *Signal Processing Advances in Wireless Communications, 2004 IEEE 5th Workshop on*, July 2004, pp. 253 – 257.

[68] V. Sipal, J. Gelabert, B. Allen, C. Stevens, and D. Edwards, "Frequency-selective fading of ultrawideband wireless channels in confined environments," *Microwaves, Antennas Propagation, IET*, vol. 5, no. 11, pp. 1328 –1335, 19 2011.

[69] W. Q. Malik, B. Allen, and D. J. Edwards, "Fade depth scaling with channel bandwidth," *Electronics Letters*, vol. 43; 43, no. 24, pp. 1371–1372, 2007.

[70] W. Malik, B. Allen, and D. Edwards, "Bandwidth-dependent modelling of smallscale fade depth in wireless channels," *Microwaves, Antennas Propagation, IET*, vol. 2, no. 6, pp. 519 –528, Sep. 2008.

[71] W. Q. Malik, D. J. Edwards, and C. J. Stevens, "Frequency Dependence of Fading Statistics for Ultrawideband Systems," *Wireless Communications, IEEE Transactions on*, vol. 6; 6, no. 3, pp. 800–804, 2007.

[72] V. Sipal, B. Allen, and D. Edwards, "Exploration and analysis of fade depth scaling," in *Antennas and Propagation Conference (LAPC), 2010 Loughborough*, Nov. 2010, pp. 125 –128.

[73] G. Llano, J. Reig, and L. Rubio, "Analytical Approach to Model the Fade Depth and the Fade Margin in UWB Channels," *Vehicular Technology, IEEE Transactions on*, vol. 59, no. 9, pp. 4214 –4221, Nov. 2010.

[74] C. Spiliotopoulos and A. Kanatas, "Path-loss and time-dispersion parameters of uwb signals in a military airplane," *Antennas and Wireless Propagation Letters, IEEE*, vol. 8, pp. 790 –793, 2009.

[75] C. Spiliotopoulos, A. Kanatas, and G. Efthymoglou, "UWB channel parameters in a C130 airplane," in *Personal, Indoor and Mobile Radio Communications, 2009 IEEE 20th International Symposium on*, Sept. 2009, pp. 1766 –1770.

[76] A. Skrebtsov, A. Burnic, D. Xu, A. Waadt, and P. Jung, "Uwb applications in public transport," in *Communications, Computing and Control Applications (CCCA), 2011 International Conference on*, March 2011, pp. 1 –4.

[77] I. Garcia Zuazola, J. Elmirghani, and J. Batchelor, "High-speed ultra-wide band in-car wireless channel measurements," *Communications, IET*, vol. 3, no. 7, pp. 1115 –1123, July 2009.

[78] M. Schack, R. Geise, I. Schmidt, R. Piesiewiczk, and T. Kurner, "UWB channel measurements inside different car types," in *Antennas and Propagation, 2009. EuCAP 2009. 3rd European Conference on*, March 2009, pp. 640 –644.

[79] M. Schack, J. Jemai, R. Piesiewicz, R. Geise, I. Schmidt, and T. Kurner, "Measurements and Analysis of an In-Car UWB Channel," in *Vehicular Technology Conference, 2008. VTC Spring 2008. IEEE*, May 2008, pp. 459 –463.

[80] J. Gelabert, D. Edwards, and C. Stevens, "Experimental evaluation of UWB wireless communication within PC case," *Electronics Letters*, vol. 47, no. 13, pp. 773 –775, 23 2011.

[81] J. Gelabert, A. Kavatjikidis, D. Edwards, and C. Stevens, "Experimental UWB channel

characterisation of an electromagnetically small environment," in *Antennas Propagation Conference, 2009. LAPC 2009. Loughborough*, Nov. 2009, pp. 381 –384.

[82] J. Gelabert, D. Edwards, and C. Stevens, "UWB wireless interconnect scheme for communicating devices within small conducting enclosure," in *Antennas and Propagation (EUCAP), Proceedings of the 5th European Conference on*, April 2011, pp. 1743 –1747.

[83] A. Kavatjikidis, "Measurement Analysis and Capacity Performance of Ultra-Wideband Radio Propagation Channels," Ph.D. dissertation, University of Oxford, Sep 2008.

[84] C. Kapagerof and C. Oikonomopoulos-Zachos, "Simulative investigation of parameters influencing the reception characteristicsof integrated automobile glass antennas," in *POSTER 2008,Pragye*, May 2008, pp. 1 –4.

[85] V. Sipal, B. Allen, and D. Edwards, "Exploration of nakagami fading in ultra-wideband wireless channels," *Electronics Letters*, vol. 47, no. 8, pp. 520 –521, 14 2011.

[86] G. Llano, J. Reig, and L. Rubio, "The UWB-OFDM Channel Analysis in Frequency," in *Vehicular Technology Conference, 2009. VTC Spring 2009. IEEE 69th*, April 2009, pp. 1 –4.

[87] V. Sipal, B. Allen, and D. Edwards, "Multi-tone frequency shift keying for ultrawideband wireless communications," *Communications, IET*, vol. 6, no. 10, pp. 1170 –1178, 3 2012.

[88] N. He and C. Tepedelenlioglu, "Performance analysis of non-coherent UWB receivers at different synchronization levels," *Wireless Communications, IEEE Transactions on*, vol. 5, no. 6, pp. 1266 –1273, June 2006.

[89] W. Lovelace and J. Townsend, "The effects of timing jitter and tracking on the performance of impulse radio," *Selected Areas in Communications, IEEE Journal on*, vol. 20, no. 9, pp. 1646 – 1651, Dec 2002.

[90] V. Lottici, A. D'Andrea, and U. Mengali, "Channel estimation for ultra-wideband communications," *Selected Areas in Communications, IEEE Journal on*, vol. 20, no. 9, pp. 1638 – 1645, Dec 2002.

[91] Y. Wang, X. Dong, P. Wittke, and S. Mo, "Cyclic prefixed single carrier transmission in ultra-wideband communications," in *Communications, 2005. ICC 2005. 2005 IEEE International Conference on*, vol. 4, May 2005, pp. 2862 – 2866 Vol. 4.

[92] M. Sahin, I. Guvenc, and H. Arslan, "Optimization of energy detector receivers for UWB systems," in *Vehicular Technology Conference, 2005. VTC 2005-Spring. 2005 IEEE 61st*, vol. 2, June 2005, pp. 1386 – 1390 Vol. 2.

[93] R. Zhang and X. Dong, "Synchronization and Integration Region Optimization for UWB Signals with Non-coherent Detection and Auto-correlation Detection," *Communications, IEEE Transactions on*, vol. 56, no. 5, pp. 790 –798, May 2008.

[94] J. Proakis, *Digital Communications*, 4th ed. McGraw-Hill, 2000.

[95] A. D'Amico, U. Mengali, and E. Arias-de Reyna, "Energy-Detection UWB Receivers with Multiple Energy Measurements," *Wireless Communications, IEEE Transactions on*, vol. 6, no. 7, pp. 2652 –2659, July 2007.

[96] Y. Nakache, P. Orlik, W. Gifford, A. Molisch, I. Ramachandran, G. Fang, and J. Zhang, "Low-complexity ultrawideband transceiver with compatibility to multiband-ofdm," in *Ultra Wideband Systems, 2004. Joint with Conference on Ultrawideband Systems and Technologies. Joint UWBST IWUWBS. 2004 International Workshop on*, May 2004, pp. 151 – 155.

[97] C. Luo, M. Medard, and L. Zheng, "On approaching wideband capacity using multitone FSK," *Selected Areas in Communications, IEEE Journal on*, vol. 23, no. 9, pp. 1830 – 1838, Sep. 2005.

[98] C. Luo, "Communication for wideband fading channels: on theory and practice," Ph.D. dissertation, MIT, 2006.

[99] T. Hosman, M. Yeary, and J. Antonio, "Design and Characterization of an MFSK-Based Transmitter/Receiver for Ultrasonic Communication Through Metallic Structures," *Instrumentation and Measurement, IEEE Transactions on*, vol. 60, no. 12, pp. 3767 –3774, Dec. 2011.

[100] R. W. Chang, "Synthesis of band-limited orthogonal signals for multi-channel data transmission," *Bell System Technical Journal*, vol. 46, pp. 1775–1796, 1966.

[101] R. Chang and R. Gibby, "A Theoretical Study of Performance of an Orthogonal Multiplexing Data Transmission Scheme," *Communication Technology, IEEE Transactions on*, vol. 16, no. 4, pp. 529 –540, August 1968.

[102] S. Weinstein and P. Ebert, "Data Transmission by Frequency-Division Multiplexing Using the Discrete Fourier Transform," *Communication Technology, IEEE Transactions on*, vol. 19, no. 5, pp. 628 –634, October 1971.

[103] S. G. Johnson and M. Frigo, "A Modified Split-Radix FFT With Fewer Arithmetic Operations," *Signal Processing, IEEE Transactions on*, vol. 55, no. 1, pp. 111 –119, Jan. 2007.

[104] IEEE, "IEEE 802.11: Wireless LAN Medium Access Control (MAC) and Physical Layer (PHY) Specifications," IEEE, revision 2007, 2007.

[105] M. Shin and H. Lee, "A high-speed four-parallel radix-24 FFT/IFFT processor for UWB applications," in *Circuits and Systems, 2008. ISCAS 2008. IEEE International Symposium on*, May 2008, pp. 960 –963.

[106] S. Cho and K. Kang, "A Low-Complexity 128-Point Mixed-Radix FFT Processor for MB-OFDM," *ETRI Journal*, vol. 32, no. 2, pp. 1 –10, Feb. 2010.

[107] R. Sherratt, O. Cadenas, and N. Goswami, "A low clock frequency FFT core implementation for multiband full-rate ultra-wideband (UWB) receivers," *Consumer Electronics, IEEE Transactions on*, vol. 51, no. 3, pp. 798 – 802, Aug. 2005.

[108] IEEE, "IEEE 802.15.3c-2009 Ammendment 2:Milimeter-wave-based Alternative Physical Layer Extension," IEEE, Tech. Rep., 2009.

[109] ECMA, "Standard ECMA-387 v.2, High Rate 60 GHz PHY, MAC and PALs," ECMA, Tech. Rep., 2010.

[110] WirelessHD, "WirelessHD Specification, Version 1.1 Overview," WirelessHD, Tech. Rep., 2010.

[111] E. International, "High Rate Ultra Wideband PHY and MAC Standard," ECMA International, Tech. Rep.

[112] M. Wylie-Green, P. Ranta, and J. Salokannel, "Multi-band OFDM UWB solution for IEEE 802.15.3a WPANs," in *Advances in Wired and Wireless Communication, 2005 IEEE/Sarnoff Symposium on*, April 2005, pp. 102 –105.

[113] M. O. Alliance, "Ultrawideband: High-speed, short-range technology with far-reaching effects," Multiband OFDM Alliance, MBOA White Paper, September 2004.

[114] Z. Qiyue, A. Tarighat, and A. Sayed, "Performance Analysis of Multiband OFDM UWB Communications With Application to Range Improvement," *Vehicular Technology, IEEE Transactions on*, vol. 56, no. 6, pp. 3864 –3878, Nov. 2007.

[115] Ellisys, "WiMedia Ultra-wideband:Efficiency Considerations of the Effects of Protocol Overhead on Data Throughput," Ellisys, Technical Report, Jan. 2009.

[116] A. Rahimian and F. Mehran, "RF link budget analysis in urban propagation microcell environment for mobile radio communication systems link planning," in *Wireless Communications and Signal Processing (WCSP), 2011 International Conference on*, Nov. 2011, pp. 1 –5.

[117] L. Liu, X. Dong, Z. Tian, and A. Schwartz, "Link Budget Analysis and Throughput Measurement for Multi-Antennas WiMedia UWB Systems," in *Vehicular Technology Confer-*

ence Fall (VTC 2009-Fall), 2009 IEEE 70th, Sep. 2009, pp. 1 –5.

[118] V. Sipal, B. Allen, and D. Edwards, "On the Range of WiMedia OFDM UWB Wireless," in *International Conference on UWB (ICUWB), 2012*, Sep. 2012, pp. 1–5.

[119] A. Czylwik, "Adaptive OFDM for wideband radio channels," in *Global Telecommunications Conference, 1996. GLOBECOM '96. 'Communications: The Key to Global Prosperity*, vol. 1, Mov 1996, pp. 713 –718 vol.1.

[120] ——, "Comparison between adaptive OFDM and single carrier modulation with frequency domain equalization," in *Vehicular Technology Conference, 1997, IEEE 47th*, vol. 2, May 1997, pp. 865 –869 vol.2.

[121] T. Keller and L. Hanzo, "Adaptive multicarrier modulation: a convenient framework for time-frequency processing in wireless communications," *Proceedings of the IEEE*, vol. 88, no. 5, pp. 611 –640, May 2000.

[122] L. Zeng, S. McGrath, and E. Cano, "Rate Maximization for Multiband OFDM Ultra Wideband Systems Using Adaptive Power and Bit Loading Algorithm," in *Telecommunications, 2009. AICT '09. Fifth Advanced International Conference on*, May 2009, pp. 369 –374.

[123] L. Jie and W. Yiwen, "Adaptive Resource Allocation Algorithm Based on Sequence Strategy of Modulated MIMO-OFDM for UWB Communication System," in *Measuring Technology and Mechatronics Automation (ICMTMA), 2010 International Conference on*, vol. 1, March 2010, pp. 424 –427.

[124] M. Magani, L. Guo, and X. Chen, "Improved BER performance on MB-OFDM UWB system using adaptive bit loading," in *Ultra-Wideband (ICUWB), 2010 IEEE International Conference on*, vol. 1, Sept. 2010, pp. 1 –4.

[125] M. Baek and H.-K. Song, "Performance Evaluation of Adaptive UWB System with Multiple Antennas," *Progress In Electromagnetics Research C*, vol. 5, pp. 1 – 12, 2008.

[126] J. Pascual and R. Gonzalo Llano, "Perfomance of Ultra-Wideband OFDM Systems Using Adaptive MPSK Modulation over Nakagami-m Channels," in *Wireless Communication Systems, 2006. ISWCS '06. 3rd International Symposium on*, Sep. 2006, pp. 631 –634.

[127] Hittite, "HMC-ALH102," Hittite Microwave Corp., Tech. Rep., 2010.

[128] Centellax, "UA0L30VM Datasheet," Centellax, Tech. Rep., 2010.

[129] B. Yang, K. Letaief, R. Cheng, and Z. Cao, "Channel estimation for OFDM transmission in multipath fading channels based on parametric channel modeling," *Communications, IEEE Transactions on*, vol. 49, no. 3, pp. 467 –479, Mar 2001.

[130] S. Coleri, M. Ergen, A. Puri, and A. Bahai, "Channel estimation techniques based on pilot arrangement in OFDM systems," *Broadcasting, IEEE Transactions on*, vol. 48, no. 3, pp. 223 – 229, Sep 2002.

[131] F. Munier and T. Eriksson, "Time-Frequency Channel estimation for MB-OFDM UWB Systems," in *Personal, Indoor and Mobile Radio Communications, 2006 IEEE 17th International Symposium on*, Sept. 2006, pp. 1 –5.

[132] R. Tesi, M. Hamalainen, and J. Iinatti, "Channel Estimation Algorithms Comparison for Multiband-OFDM," in *Personal, Indoor and Mobile Radio Communications, 2006 IEEE 17th International Symposium on*, Sep. 2006, pp. 1 –5.

[133] R. Roy and T. Kailath, "ESPRIT-estimation of signal parameters via rotational invariance techniques," *Acoustics, Speech and Signal Processing, IEEE Transactions on*, vol. 37, no. 7, pp. 984 –995, Jul 1989.

[134] O. Edfors, M. Sandell, J.-J. van de Beek, S. Wilson, and P. Borjesson, "OFDM channel estimation by singular value decomposition," *Communications, IEEE Transactions on*, vol. 46, no. 7, pp. 931 –939, Jul. 1998.

[135] A. Street, L. Lukama, and D. Edwards, "Use of VNAs for wideband propagation mea-

surements," *Communications, IEE Proceedings-*, vol. 148, no. 6, pp. 411 –415, Dec 2001.

[136] A. Technologies, *Reference Guide Agilent Technologies 8719ET/20ET/22ET 8719ES/20ES/22ES Network Analyzers*, Agilent Technologies, 2002.

[137] W. Malik, "Spatial correlation in ultrawideband channels," *Wireless Communications, IEEE Transactions on*, vol. 7, no. 2, pp. 604 –610, Feb. 2008.

[138] G. Stuber, J. Barry, S. McLaughlin, Y. Li, M. Ingram, and T. Pratt, "Broadband MIMO-OFDM wireless communications," *Proceedings of the IEEE*, vol. 92, no. 2, pp. 271 – 294, Feb 2004.

[139] A. PAULRAJ, D. GORE, R. NABAR, and H. BOLCSKEI, "An overview of MIMO communications - a key to gigabit wireless," *Proceedings of the IEEE*, vol. 92, no. 2, pp. 198 – 218, Feb 2004.

[140] C. Vithanage, M. Sandell, J. Coon, and Y. Wang, "Precoding in ofdm-based multi-antenna ultra-wideband systems," *Communications Magazine, IEEE*, vol. 47, no. 1, pp. 41 –47, Jan. 2009.

[141] P. Zetterberg, M. Bengtsson, D. McNamara, P. Karlsson, and M. Beach, "Performance of multiple-receive multiple-transmit beamforming in WLAN-type systems under power or EIRP constraints with delayed channel estimates," in *Vehicular Technology Conference, 2002. VTC Spring 2002. IEEE 55th*, vol. 4, 2002, pp. 1906 – 1910 vol.4.

[142] C. Vithanage, Y. Wang, and J. Coon, "Spatial PAPR Reduction Based Beamforming Scheme for EIRP Constrained Systems," in *Global Telecommunications Conference, 2008. IEEE GLOBECOM 2008. IEEE*, Dec 2008, pp. 1 –5.

[143] C. Vithanage, S. Parker, and M. Sandell, "Antenna Selection with Phase Precoding for High Performance UWB Communication with Legacy WiMedia Multi-Band OFDM Devices," in *Communications, 2008. ICC '08. IEEE International Conference on*, May 2008, pp. 3938 –3942.

[144] M. Sandell and C. Vithanage, "Per-Tone Transmit Antenna Selection with Phase Precoding for OFDM," *Communications, IEEE Transactions on*, vol. 59, no. 6, pp. 1514 –1518, June 2011.

[145] Y. Zhu and Y. Fang, "Optimization of transmit-antenna selection / equal gain transmission in Rayleigh fading channels," in *Wireless, Mobile and Multimedia Networks, 2006 IET International Conference on*, nov. 2006, pp. 1 –4.

[146] W. Moulder, W. Khalil, and J. Volakis, "60-GHz Two-Dimensionally Scanning Array Employing Wideband Planar Switched Beam Network," *Antennas and Wireless Propagation Letters, IEEE*, vol. 9, pp. 818 –821, 2010.

[147] B. Razavi, "Design of millimeter-wave cmos radios: A tutorial," *Circuits and Systems I: Regular Papers, IEEE Transactions on*, vol. 56, no. 1, pp. 4 –16, jan. 2009.

[148] M. Nedil, T. Denidni, and L. Talbi, "Novel butler matrix using CPW multilayer technology," *Microwave Theory and Techniques, IEEE Transactions on*, vol. 54, no. 1, pp. 499 –507, jan. 2006.

[149] S. Gezici, Z. Tian, G. Giannakis, H. Kobayashi, A. Molisch, H. Poor, and Z. Sahinoglu, "Localization via ultra-wideband radios: a look at positioning aspects for future sensor networks," *Signal Processing Magazine, IEEE*, vol. 22, no. 4, pp. 70 – 84, july 2005.

[150] D. Pozar, *Microwave Engineering*, 2nd ed. John Wiley and Sons, 1998.

[151] A. Kavatjikidis, D. J. Edwards, and C. J. Stevens, "A Long Range UWB Channel Sounding System Exploiting UWB over Fibre Technology," in *European Eelectromagnetics, 2008. Lausanne, Switzerland*, 2008.

[152] I. Cox, C.H., E. Ackerman, G. Betts, and J. Prince, "Limits on the performance of RF-over-fiber links and their impact on device design," *Microwave Theory and Techniques, IEEE Transactions on*, vol. 54, no. 2, pp. 906 – 920, Feb. 2006.

[153] G. Betts, X. Xie, I. Shubin, W. Chang, and P. Yu, "Gain Limit in Analog Links Using Electroabsorption Modulators," *Photonics Technology Letters, IEEE*, vol. 18, no. 19, pp. 2065 –2067, Oct 2006.

[154] H. Roussell, M. Regan, J. Prince, C. Cox, J. Chen, W. Burns, G. Betts, E. Ackerman, and J. Campbell, "Gain, Noise Figure and Bandwidth-Limited Dynamic Range of a Low-Biased External Modulation Link," in *Microwave Photonics, 2007 IEEE International Topical Meeting on*, Oct. 2007, pp. 84 –87.

[155] Anritsu, "Anritsu Bias Tees K250,V250," Anritsu, Tech. Rep., 2000.

[156] Qphotonics, "Wavelength stabilized single mode fiber coupled laser diode 20mw at 1580nm, qdfbld-1580-20," Qphotonics, Tech. Rep., 2010.

[157] CIPhotonics, "40G-SR-EAM-1550 - 1550nm 40Gbit/s Electro Absorption Modulator (EAM)," CIPhotonics, Tech. Rep., 2010.

[158] μ $2t$ Photonics, "Ultrafast 1.55 μm photodetector xpdv," $\mu 2t$ Photonics, Tech. Rep., 2003.

[159] Wisair, *Wisair Development Kit (DVK) DV9110M, User's Manual*, rev1.13 ed., Wisair, 2006.

[160] H. C. Ltd., "UWB-IF System Specification," HW Communications Ltd., Tech. Rep., 2008.